Mode Locking of Fiber Lasers at High Repetition Rates

by

Nicholas G. Usechak

Submitted in Partial Fulfillment

of the

Requirements for the Degree

Doctor of Philosophy

Supervised by

Professor Govind P. Agrawal

The Institute of Optics
The College
School of Engineering and Applied Sciences

University of Rochester
Rochester, New York

2006

In memory of my grandmother Ellen van Winkle Fox and to my wife Susan

Curriculum Vitae

The author was born in Long Branch, NJ in 1976 and grew up in nearby Holmdel and then Shrewsbury. He graduated from Lehigh University in 2000 with high honors, obtaining BS degrees in both Electrical Engineering and Engineering Physics. During college he participated in Lehigh University's Co-Op program where he worked full time at Binney & Smith developing a system to assist in the optimization of the machines on the company's production floor during the fall of 1997 and the summer 1998. In the summer of 1999 he participated in the National Science Foundation's Research experience for undergraduates (REU) program for physics majors at the University of California, Irvine working for professor Steven Barwick on the Antarctic muon and neutrino detector array (AMANDA) project. During his final year at Lehigh, he conducted research on optical switching devices under Professor Michelle Malcuit, of Lehigh's Physics Department. In this work, polymer-dispersed liquid crystal gratings were fabricated and the effect of shear stress on the gratings was characterized. After graduating college in 2000, he began his graduate studies at the Institute of Optics, University of Rochester where he received a MS degree in optics in 2003. Under the supervision of Professor Govind P. Agrawal and Jonathan D. Zuegel, he carried out his doctoral research in mode-locked fiber lasers.

Publications

Nicholas G. Usechak and Govind P. Agrawal, "An investigation of FM mode-locking using the moment method," *J. Opt. Soc. Am. B* **22**, 2570-2580 (2005)

Nicholas G. Usechak, Govind P. Agrawal, and Jonathan D. Zuegel, "FM mode-locked fiber lasers operating in the Autosoliton regime," *IEEE J. Quantum Electron.* **41**, 753-761 (2005)

Nicholas G. Usechak and Govind P. Agrawal, "Semi-analytic technique for analyzing mode-locked lasers," *Opt. Express* **13**, 2075-2081 (2005)

Nicholas G. Usechak, Govind P. Agrawal, and Jonathan D. Zuegel, "Tunable, high-repetition-rate, harmonically mode-locked, Ytterbium fiber laser," *Opt. Lett.* **29**, 1360-1362 (2004)

E. Andrés *et al*, "Observation of high-energy neutrinos using Cerenkov detectors embedded deep in Antarctic ice," *Nature* **410**, 441-443 (2001)

E. Andrés *et al*, "Recent results from AMANDA," *Int. J. Mod. Phys. A.* **16**, 1013-1015 (2001)

Presentations

J. Bromage, C. Dorrer, I. A. Begishev, N. Usechak, and J. D. Zuegel, “Single-Shot Pulse Characterization from 0.4 to 85 ps Using Electro-Optic Shearing Interferometry,” ICUIL, Cassis, France, September 2006

R. Dekker, E. Klein, J. Niehusmann, M. Först, F. Ondracek, J. Ctyroky, N. Usechak, and A. Driessen, “Self Phase Modulation and Stimulated Raman Scattering due to High Power Femtosecond Pulses Propagation in Silicon-on-Insulator Waveguides,” LEOS, Mons, Belgium, December 2005.

Nicholas G. Usechak and Govind P. Agrawal, “An analytic technique for investigating mode-locked lasers,” CLEO, Baltimore, MD, May 2005.

Nicholas G. Usechak and Govind P. Agrawal, “Pulse switching and stability in FM mode-locked fiber lasers,” CLEO, Baltimore, MD, May 2005.

Nicholas G. Usechak, Govind P. Agrawal, and Jonathan D. Zuegel, “Analysis of FM mode-locking in fiber lasers,” OSA Annual Meeting, Rochester, NY, October 2004.

Nicholas G. Usechak, Govind P. Agrawal, and Jonathan D. Zuegel, “Tunable, High-Repetition-Rate, Harmonically Mode-Locked, Ytterbium Fiber Laser,” ASSP, Albuquerque, NM, February 2003.

Acknowledgments

A doctoral degree means different things to different people and I am grateful to have been advised by two people who allowed me to pursue what it meant to me. I was able to explore different aspects of my field (and of other fields) that I would not have otherwise been exposed to. This has enabled me to become a more well-rounded scientist, not only with a broader view of optics, but also with a broader range of scientific skills outside of optics.

Professor Govind P. Agrawal, who advised me during this work, is curious about everything from science to computer software. In many groups it is the students who introduce their advisors to new programming languages and software packages. Yet, it is frequently the opposite case in his group. His encyclopedic knowledge of fiber optics, numerical techniques, and scientific literature is a great asset not only to members of his own group but also to students in other groups who periodically consult him on such issues. Perhaps his strongest asset, however, is not scientific. He is a kind and caring person who treats his students fairly, is well liked, and can always make himself and others laugh.

Jonathan D. Zuegel supported this work and advised me on experimental issues. His interests lie more in the practical than the theoretical, which mirrors my own mentality. Although he obtained a PhD from the Institute of Optics, he also holds multiple degree's in electrical engineering, which gives him a practical perspective. This hands-on approach to optics was nice for someone with an electrical engineering background

in an otherwise physics dominated department. Dr. Zuegel is caring, smart, and humorous; moreover, he was a pleasure to work under and inspired me every time I talked with him.

Although not one of my advisors, John Marciante deserves a special thank you for his many useful and motivational discussions that helped add to this work. These conversations were most appreciated during my final year in graduate school when I spent the majority of my time at the laser lab.

I would also like to thank a few other members of Jon Zuegel's group at the laser lab. In particular, I would like to thank Jake Bromage for whom I characterized some FM modulators for a short pulse characterization tool he built (EO-SPIDER), Vincent Bagnoud for his all-around humor, Ildar Begishev for helping me find things in the laser development lab, and Christope Dorrer for a few useful discussions relating to spectral interferometry.

I would also like to thank my committee: Wayne Knox, Nick Bigelow, and Chunlei Guo for their guidance and time. Moreover, I would also like to thank Professor Knox for allowing me to use his lab during the completion of some of the experimental work reported in this thesis.

As a graduate student, I had positive interactions with so many people that it would not be possible nor would it be pragmatic to list them all here. Such a statement is a testament to the Laboratory for Laser Energetics and its employees as well as the Institute of Optics, its professors, and students. However, I am most indebted to the interactions I've had with my group members both current and former, specifically Qiang Lin and Fatih Yaman, who are both excellent scientists. Qiang possesses a powerful understanding of nonlinear fiber optics and physics in general. Not only is he an excellent theoretician, but he is also an excellent experimentalist — a rare quality. Since he is curious about other fields of science, he is always a pleasure to discuss problems with due to his vast knowledge base and unique prospective. Fatih has an innate understanding of nonlinear phenomenon and is able to easily break complicated processes down using

simple physical analogies, making them easy to understand and digest. Conversations I have had with both Qiang and Fatih have helped me get out of a number of “ruts” during my thesis work, and I am extremely grateful for their support.

In her thesis, Jayanthi Santhanam gave such a detailed introduction to the moment method that she saved me a great deal of time in applying it to mode-locked lasers as I do in part of this thesis. It is with her work in mind that I have tried to make this thesis of some use to students in the future.

My conversations with various members of professor Boyd’s group, in particular John Heebner, Vincent Wong, Giovanni Perieda, Colin O’Sullivan-Hale, and George Gehring, have also been rewarding. I must also acknowledge members of Professor Wayne H. Knox’s group: Fei Lu and, in particular, Yujun Deng for the time I spent working in their lab where I built my first mode-locked laser.

My conversations with Per Adamson, whether they were personal, carpentry-related, or scientific, have also benefited me and my house in many ways. I am also grateful to his encouraging me to “update” one of the optics labs. This forced me to learn windows API programming in visual C++, work with stepper motors, and build a circuit to interface with a computer.

I am indebted to Joseph Henderson who runs the student machine shop at the Laboratory for Laser Energetics (LLE) and Richard Fellows who runs the professional machine shop at the LLE for their expert instruction in machining, use of their own personal equipment, and other shop resources.

I would like to Alexander Maltsev, an optician at the LLE, who assisted me in polishing fiber ferrules so they could have a dichroic mirror deposited on them. Unfortunately, the mirrors were not deposited as expected and a wavelength shift crippled this work. As a result, it is not mentioned in this thesis.

I appreciate all of the help Wade Bittle, an RF engineer at the LLE, gave me on circuit issues, network analyzers, and pulse-train timing jitter.

Robert Keck, a scientist at the laser lab, helped get me past a few hurdles I ran into

when programming in Visual C++ in the Windows environment. He also gave me a copy of Microsoft's DirectX 9.0 SDK, which is the most current version still compatible with Visual C++ 6.0 (the platform I have), when I was learning how to create 3D computer games. I am thankful for his with these issues; it allowed me to greatly improve my programming ability in C++.

I would also like to thank Joan Christian, Betsy Benedict, Gina Kern, Gayle Thompson, and Noelene Votens for countless discussions about everything except optics.

John Siminson and, in particular, Brian McIntyre, who probably found themselves hiding from me on more than one occasion, helped me in my extracurricular programming activities using the department's server and PHP.

Finally, I would like to thank my wife for all of her support. Not only did she leave all of her friends and her job in New York City to move, with her dog, to Rochester to be with me, but she is also my best friend. I would also like to thank her for her help proofreading this thesis.

Abstract

Mode-locked fiber lasers have become indispensable tools in many fields as their use is no longer relegated to the optics community. In the future, their size will decrease and their applications will become far more prevalent than they are today. At present, the field is undergoing a cardinal shift as these devices have become commercially available in the last decade. This has put an emphasis on long-term performance and reliability as these devices are beginning to be integrated into complex systems in areas as diverse as medical optics, micro-machining, forensics, and tracking as well as their obvious use as laboratory tools or sources in telecommunications. This is also resulting in a transition from research to engineering.

Since the field of mode-locked lasers has been extensively studied for over forty years, one may expect that little has been overlooked. However, since the mode locking phenomena is governed by nonlinear partial differential equations, a rich degree of effects exist and the field has not yet been exhausted. During the past two decades, the main emphasis has been on short-pulse generation; however, the main thrust of research is likely to change to producing high-power devices, which will result in limiting effects and thermal issues that are currently ignored for low-power sources. Finally, detailed studies have generally been performed numerically as analytic solutions only exist in limiting cases.

In this thesis, mode-locked fiber lasers are studied experimentally, numerically, and theoretically. The experimental work focuses on high-repetition rate, mode-locked cavities, which are then modeled numerically. A semi-analytic tool, which goes beyond the

prior theories and includes all of the effects experienced by steady-state, mode-locked pulses as they propagate in a laser cavity, is also derived. The only caveats to this approach are an assumption of the pulse shape and the requirement that it not change during propagation through the laser cavity. Despite these limitations, it is found that the parameters predicted by our method deviate from those found through rigorous numerical simulations by 10% or less.

Table of Contents

List of Tables

List of Figures

1 A Historical Introduction to Mode Locking

This chapter gives a brief historical introduction to the vast field of mode-locked lasers. Particular emphasis is placed on the birth of mode-locked lasers and various mode-locking techniques. In order to motivate this thesis, some potential applications illustrating the need for high-repetition-rate mode-locked lasers with operating wavelengths $\sim 1\mu$m are noted. The particular philosophy under which this thesis was written as well as its intended goal is also highlighted in this chapter along with our research contributions. Finally, a brief summary of the subsequent chapters and an overview of the appendices is presented.

1.1 Early Work

Mode-locked lasers have a long history that can be traced back to the work of Gürs and Müller in 1963.[6] However, the first statement of the basic phenomena was found a year later in Lamb's work, where he investigated the frequency locking of three modes.[7] During this time period, lasers were analytically investigated in the frequency domain, where it was well known that a laser has multiple longitudinal modes, similar to those of a Fabry–Perot étalon. It is with this picture in mind that DiDomenico predicted

mode locking by noting that if a cavity's modes could be made to have a constant phase relationship with one another, that is, if they could be "locked" together — thus, the origin of the term "mode-locked laser" — one would obtain a short pulse in time via the Fourier-transform relationship between the two domains.[8] Independently of DiDiomenico's work, the first mode-locked laser was experimentally demonstrated when Hargrove, Fork, and Pollack used an acousto-optic modulator to modulate the loss (AM mode locking) inside a laser cavity at a rate coincident with the cavity's own repetition rate; yielding pulsed operation.[9] An intracavity frequency modulator was used the same year by Harris and Targ to obtain FM mode locking.[10] Theoretical work directly followed the first experimental demonstration of FM mode locking, with Harris and McDuff providing a detailed investigation the following year.[11] In 1965, Mocker and Collins demonstrated the first passively mode-locked laser when they found that the saturable dye used to Q-switch a ruby laser could also be used to mode lock the laser.[12] In this work, Mocker and Collins found that their Q-switched pulse split into short pulses separated in time by the the cavity's round trip time. However, this type of passive mode locking was unpredictable and transient in nature. McClure investigated how laser performance was effected by cavity length and the placement of the modulator in the cavity, and he was probably the first to obtain mode locking at a higher harmonic.[13] The mode locking of lasers at a repetition rate higher than the cavity's fundamental was investigated in greater detail in 1968 by Hirano and Kimura.[14] Their work presented the three most useful ways to increase the repetition rate — decrease the cavity length, build a coupled cavity, or drive a modulator at a higher harmonic of the cavity's fundamental repetition rate. Finally, seven years after the first experimental demonstration of passive mode locking, Ippen, Shank, and Dienes were the first to demonstrate a passively mode-locked laser with a stable pulse train in 1972.[15]

All of the early theoretical works treated mode locking exclusively in the frequency domain. Although such a treatment of lasers had brought excellent results in the past for continuous wave (cw) lasers (for example Lamb was able to predict Doppler broad-

ening and explain hole burning[7]) and even for mode locking (DiDomenico was able to predict AM mode locking[8] and Harris and McDuff were able to explain FM mode locking[11]), it should have a time domain corollary as well. In 1970, Kuizenga and Siegman presented such a time-domain treatment of active mode locking.[2] Their approach allowed them to predict the shape and width of the mode-locked pulses in a simple fashion and was also confirmed experimentally.[16] Using Kuizenga and Siegman's time domain approach, Kim, Marathe, and Rabson showed that the pulse should be a Hermite-Gaussian function[17] and thus the Gaussian pulse shape assumed by Kuizenga and Siegman was only one of a family of potential solutions. Two years later, however, Haus showed that the higher-order Hermite-Gaussian functions were linearly unstable[18] and thus only the fundamental Gaussian pulse is physically realizable. In the same work, Haus also sought to reconcile the time- and frequency-domain descriptions of mode locking noting that one is often preferable to the other. Later that year, Haus developed the first analytical treatment for the passively mode-locked cw laser by assuming a fast saturable absorber and using Siegman's time-domain approach.[19]

Finally, spatial-temporal effects were leveraged in 1991 to produce 60 femtosecond pulses by using a Titanium:sapphire (Ti:Al_2O_3) crystal both as a gain medium and a mode locker.[20] In this technique, referred to as Kerr-lens mode locking (KLM), higher gain is either concentrated in a small spatial region (soft-aperture KLM) or an aperture is placed after the gain medium (hard-aperture KLM) to block light that is not tightly localized. The nonlinear effect of self-focusing is used to overcome the passive effect of diffraction-induced broadening for intense powers. By introducing an aperture, hard or soft, pulse operation is favored over cw operation and the laser is mode locked passively. This mode-locking technique is credited with producing the shortest pulse directly from a resonator to date ($\sim$ 5 fs at 780 nm),[21] is usually associated with repetition rates $<$ 100 MHz,[21] and is extremely popular and Ti:sapphire lasers based on it can be found in hundreds if not thousands of research laboratories today.

1.2 Mode-Locked Fiber Lasers

Although the first fiber laser was experimentally demonstrated in 1961 using a large-core Nd-doped fiber,[22] the first mode-locked fiber laser was not demonstrated until 1983.[23] In this laser, a flashlamp produced transient color centers which acted as an effective saturable absorber that, in turn, passively mode locked the laser. In 1984, Mollenauer and Stolen added an auxiliary fiber cavity to a mode-locked laser and were able to generate 210-fs pulses.[24] This so-called "soliton laser" used self-phase modulation in the optical fiber to produce an intensity-dependent phase on the pulse passing through the fiber; when the chirped pulse re-entered the main cavity, it interfered with its un-chirped replica. By adjusting the cavity lengths (they must be matched with interferometric precision which limits the practicality of this laser), constructive interference can me made to occur at the pulse center and destructive interference in the pulse wings. At the time, the operating principle behind this laser was theoretically believed to require soliton formation and thus only thought to be useful in the anomalous-dispersion regime. Later, however, investigations by Blow and Wood revealed that anomalous dispersion was not required.[25] Finally, a detailed analytic investigation was made[26,27] and this entirely new type of mode locking was dubbed additive-pulse mode locking (APM) due to the interference (which results from the addition of the fields) at the beam splitter, which essentially results in a fast intensity dependent loss, similar to the effect of a fast saturable absorber. Moreover, just as saturable absorption based mode locking produces hyperbolic-secant pulses, APM does as well.

In the 1980s, it was also realized that the pulse shapes produced by actively mode-locked lasers were frequently more consistent with a hyperbolic secant profile than with a Gaussian profile — as predicted by the earlier theories. There was no great mystery as to why either; the effects of dispersion and nonlinearity within a laser cavity were playing a role in the pulse shaping. In 1986, Haus and Silberberg tried to analytically incorporate these effects in AM mode-locked lasers operating in the anomalous disper-

sion regime.[3] Their work assumed that the pulse shape was only determined by the cavity elements; the effect of the modulator was ignored. Although developed for AM mode-locked lasers, their results are also applicable to FM mode-locked lasers as we will show in chapter 5 of this thesis using numerical simulations.[28]

The first FM mode-locked fiber laser was reported by Geister and Ulrich in May of 1988.[29] Within a year, Phillips, Ferguson, and Hanna also demonstrated an FM mode-locked fiber laser.[30] In 1989, Kafka, Baer, and Hall built the first AM mode-locked fiber laser using a ring geometry.[31] In the years following, fiber laser development exploded with the demonstration of various other cavity designs. In 1990, Duling reported the "figure-eight" laser, which relies on APM and an auxiliary Sagnac interferometer to form mode-locked pulses.[32–34] In this laser, a fiber coupler splits a pulse into two replicas which propagate in opposite directions through the Sagnac loop interfering in the coupler before re-entering a unidirectional ring cavity.

An ingenious implementation of APM mode locking was demonstrated by Hofer *et al.* in 1991 by using an elliptically polarized pulse inside a standard single-mode fiber.[35] In this laser, a linearly polarized pulse is converted into an elliptically polarized pulse using waveplates or another polarization rotation device. The two polarization components of the pulse then propagate under the influence of self- and cross-phase modulation in the optical fiber inside the laser cavity. Next, the pulse is passed through a polarizer, which is aligned such that the wings of the pulse experience large losses, yet the peak experiences only minimal losses. Although this type of laser relies on the APM mechanism (between the two polarizations of the pulse), it is commonly referred to as a nonlinear-polarization rotation (NLPR) mode-locked laser in reference to the action of the fiber on the pulse.* An all-fiber, unidirectional, mode-locked ring laser was first constructed using the NLPR mechanism a year later by Tamura, Haus, and Ippen in 1992.[36] The most important advantage of the figure-eight and ring fiber lasers over

*we will use NLPR loosely throughout this thesis to denote this type of mode locking although it is not strictly a mode-locking mechanism; just an implementation of APM

Mollenauer and Stolen's original APM laser is that they are self-stabilizing. Since the optical paths for the two pulses are the same, these lasers do not require feedback loops or active stabilization to operate. Furthermore, they all rely on fiber nonlinearity, which has a nearly instantaneous response time allowing for femtosecond pulse generation; as a point of interest, the current fiber laser record of 33 fs is held by a ytterbium fiber laser built at Cornell in 2006.[37]

In 1993, the first stretched-pulse fiber laser was built by Tamura, Ippen, and Haus.[38] This laser incorporated a section of normal-dispersion fiber in an otherwise anomalously dispersive cavity.[38] The pulses produced by this dispersion-managed laser are generally more consistent with a Gaussian shape than with a hyperbolic-secant, however, they can carry roughly 100 times more power than their anomalous cousins before the onset of Kerr-nonlinearity induced instabilities. Therefore, this scheme is attractive to those seeking higher power fiber lasers. The stretched-pulse fiber laser gets its name from the fact that the pulses temporally stretch and compress twice as they circumnavigate the cavity.

Almost a decade after Haus and Silberberg's work on AM mode-locked lasers in the presence of dispersion and nonlinearity, Kärtner *et al.* tried to analytically include not only the effect of dispersion and nonlinearity in an AM mode-locked laser, but the effect of the modulator as well.[39] The resulting treatment relies on soliton perturbation theory, is mathematically involved, and is only valid in the anomalous-dispersion regime. Moreover, unlike Kuizenga and Siegman's work, this result has not proven to be a useful tool; undoubtedly due to its complexity.

Finally, came the surprising result of Ilday and co-workers. In 2004, it was found that through careful cavity design, guided by numerical simulations and proper optimization, an otherwise conventional stretched-pulse fiber laser with a net normal dispersion could operate in a different mode where the the shortest pulses are found in the opposite location in the cavity as normally expected in stretched-pulse operation.[40] This laser, dubbed the similariton fiber laser by its creators, gets its name from simi-

laritons; which are defined as pulses that propagate self-similarly. The amplitude and phase of similaritons, also referred to as self-similar pulses, retain their shape (but not width or peak power) under propagation. In other words, pulses at any (spatial) location can be represented as scaled versions of the pulses at any other (spatial) location. In an optical amplifier, the pulse's spectral and temporal profiles take a parabolic shape while the pulse has a linear chirp.[41] However, some clarification is warranted since, based on the definition of a similariton, the creation of a true similariton laser is not possible as the cavity would quickly deteriorate into cw operation. In Ilday's laser, NLPR was used to achieve mode-locked operation, yet the pulses propagated in a manner constant with similaritons in the cavity. The presence of a mode-locking mechanism insures pulse formation and means that the pulses inside this laser can not be true similaritons despite the presence of the similariton-like pulse shaping observed.

1.3 High Repetition-Rate Mode-Locked Lasers

Since this thesis focuses on high repetition-rate mode-locked lasers, prior "high" repetition-rate lasers deserve some discussion. Restricting our focus to diode-pumped, ion-doped, solid-state lasers, we first review passively mode-locked high-repetition rate lasers and then address high-repetition rate actively mode-locked lasers.

In 1998, Collings, Bergman, and Knox demonstrated an erbium/ytterbium fiber laser with a fundamental repetition rate of 235 MHz by using a saturable Bragg reflector (SBR) to passively mode lock the cavity.[42] By increasing the pump power, the laser harmonically mode locked: the number of pulses circulating in the cavity increased from one to eleven and the repetition rate increased to 2.6 GHz.[42] Although other fiber lasers have archived similar repetition rates, they relied on longer cavities mode locked at much higher harmonics. For example, Gray *et al.* had achieved a 526 MHz pulse train in 1995 by increasing the pump power in a NLPR mode-locked erbium/ytterbium

fiber laser till it operated at its $\sim 50^{\text{th}}$ harmonic.[43] Two years later, Grudinin and Gray used a semiconductor saturable absorber mirror (SESAM) to help increase the repetition rate to > 2 GHz; this laser operated at its 369^{th} harmonic.[44]

There are, however, inherent drawbacks to high harmonic mode locking: it tends to increase timing jitter and amplitude fluctuations, it is susceptible to deleterious pulse-pulse interactions, and it may lead to dropped pulses, etc. The allure of a short cavity, passively mode-locked, laser is that its immune to some of these issues and the others may be mitigated to varying extents. In terms of short-cavity fiber lasers, the layout presented by Collings, Bergman, and Knox[42] remains the most compact and so we have chosen to focus on it here. Of the mode-locking mechanisms already discussed in this chapter, we point out that those relying on fiber nonlinearity (APM and NLPR) require that nonlinear effects be important. This mandates that the fiber lengths be large enough that nonlinear effects accrue to a non-trivial extent. In optical fibers, high-power pulses are prone to Kerr-nonlinearity induced instabilities, such as wave breaking,[45] which prohibits the realization of either of these mechanisms in cavities short enough (1-10 cm) to yield gigahertz operation. Moreover, (conventional) APM and NLPR lasers require waveplates or auxiliary cavities which places an additional limit on cavity size. Therefore, if we ignore semiconductor lasers and active mode locking, passive mode locking via a SBR or SESAM appears to be the best approach for producing short cavity lasers.

Indeed, by removing the fiber from the cavity, Krainer *et al.* passively mode locked a Nd:YVO_4 laser at a fundamental repetition rate above 10 GHz and have even demonstrated mode locking at 160 GHz.[46,47] These lasers produce up to 500-mW of average output power in 12-ps pulses, have small footprints, and are likely to become commercially available in the near future.

Actively mode-locked lasers are generally more easily able to produce high-repetition rate pulse trains and have done so for more than a decade; however, this is always accomplished by high-harmonic mode locking. In 1994, Longhi *et al.* demonstrated a

2.5-GHz FM mode locked laser with a pulse width of 9.6 ps.[48] Using rational harmonic mode locking,[49] Yoshida and Nakazawa demonstrated one of the highest repetition rates to-date in 1996 with a FM mode-locked erbium doped fiber laser operating at 80–200 GHz.[50] Rational harmonic mode locking is achieved by driving the modulator at a frequency disparate with a higher harmonic of the cavities fundamental frequency. By properly detuning the two frequencies, the repetition rate of the pulses in the cavity may be increased. This method, however, suffers from pulse-train non-uniformity, jitter, and stability.[51]

In the late 1990s, Abedin and co-workers investigated higher-order FM mode locking in a series of papers where they demonstrated 800-fs transform-limited pulse trains at repetition rates as high as 154 GHz.[52–55] In higher-order FM mode locking, an FM modulator is heavily driven such that it produces many higher-order FM sidebands. The laser cavity must also contain a high-finesse Fabry-Perot filter whose free-spectral range is a harmonic of the modulation frequency. By filtering out some of the spectral components, the filter, in conjunction with the FM modulator, multiplies the lasers repetition rate. Yu *et al.* used a FM modulator in conjunction with fiber nonlinearity to produce 500-fs pulses at a 1-GHz repetition rate.[56] Other groups have demonstrated FM mode locking at 40 GHz with pulse widths of 1.37 ps[57] and 850 fs.[58]

Of course high repetition rates may also be achieved with AM mode locking; 30-ps pulses were produced by an AM mode-locked all-fiber laser operating at 14 GHz as early as 1992.[59] In the same year, 5-ps pulses were demonstrated in another fiber laser mode locked at a higher repetition rate, 20 GHz.[60] In 1996, a sigma fiber laser incorporating a Mach-Zehnder amplitude modulator driven at 10-GHz produced 1.3 ps pulses.[61,62] Other groups have demonstrated AM mode locking at repetition rates as high as 40 GHz with pulse widths around 1.5 ps.[63] In fact, rationally AM mode-locked fiber lasers have even operated at repetition rates as high at 80 GHz.[51] It is interesting to note that the pulses obtained from FM mode-locked lasers are generally shorter than those obtained from AM mode-locked lasers.

There are still other schemes of mode locking lasers at higher repetition rates. For example, a clever injection mode-locking technique was demonstrated in 1992 where cross-phase modulation in a section of fiber inside the cavity was exploited to perform FM mode locking producing 30-ps pulses at 1GHz.[64] A similar technique that used the all-optical equivalent of AM mode locking was also demonstrated the same year.[65] However, we will not address these types of lasers again since they essentially require that a mode-locked laser exist at another wavelength, and we are interested in self-contained laser systems. Moreover, since rational harmonic mode locking and higher-order harmonic mode locking create trains of pulses susceptible to large fluctuations, we do not discuss them in the rest of this thesis.

In their pioneering work, Kuizenga and Siegman predicted[2] and found[16] that FM mode-locked lasers are prone to a switching instability where the mode-locked pulses would locate themselves under the two different extrema of the modulator. This type of behavior does not arise in passive mode locking or AM mode locking. The consequences of this seemed to go unnoticed until 1996 when Nakazawa *et al.* began experiments with high repetition-rate, FM mode-locked, fiber lasers.[66] Since they did not observe any switching they surmised that it had been suppressed by the cavity dispersion,[66] a conclusion which was actually speculated on in Kuizenga and Siegman's original work (Ref. [2]). In order to verify their experimental claim, they extended Kuizenga and Siegman's results by incorporating dispersion and then perturbatively considering the effect of nonlinearity.[4] In 1996, Haus *et al.* investigated the effects of small detunings between an FM modulator and a cavity's fundamental repetition rate.[67] The effects of large detunings between the repetition rate of an FM modulator and that of (a harmonic of) the cavities fundamental repetition rate were numerically modeled and experimentally confirmed in 1998.[68]

1.4 Motivation for this Thesis

The overview presented in this chapter seeks to give the reader a general idea of some of the milestones in mode-locked lasers and a prospective for where the field is today; yet, it is far from exhaustive, since there are now well over a thousand papers on mode-locked lasers. At the onset of this thesis work, however, only two mode-locked ytterbium fiber lasers had been demonstrated,[69,70] both passively mode locked and operating at a repetition rate of $\sim$30 MHz. Additionally, none of the analytic techniques that existed for actively mode-locked lasers were able to incorporate the effects of third-order dispersion. Moreover, those that accurately treated second-order dispersion and nonlinearity, for example Refs. [3, 39], failed in the normal-dispersion regime. This thesis was motivated to overcome some of these shortcomings.

Prior to the work presented in this thesis, the mode locking of ytterbium fiber lasers focused only on passive techniques.[69,70] These lasers provided short pulse widths, taking advantage of ytterbium's large gain bandwidth; however they resulted in repetition rates $<$100 MHz due to the requirement that the cavity lengths be a few meters or longer. There is, however, a need for ytterbium sources with repetition rates in the gigahertz regime. Such lasers can be used to synchronize systems or work as an optical clock for timing applications. Other applications involving frequency metrology may also require such sources and would also be a useful source of the ultrafast picket-fence pulse trains that have been proposed to improve the performance of fusion laser systems.[71] In this scheme, shaped nanosecond pulses are replaced by a train of ultrafast picket pulses that deliver the same average power while increasing the third-harmonic conversion efficiency. A high-repetition-rate and broadly tunable source would also be useful for synchronously pumping multigigahertz optical parametric oscillators.[72]

There are a few different ways in which the repetition rate of a mode-locked laser can be increased. The simplest approach consists of reducing the cavity length.[14] Another common way in which the repetition rate of the laser can be multiplied is by

increasing the number of pulses circulating in the cavity.[14,73–75] In this approach, the fundamental repetition rate remains the same while additional pulses circulate in the cavity; ideally, they are equally spaced from one another. This may be done passively, by increasing the pump power until a bifurcation point is reached,[74,76–79] or actively, by driving an active mode locker at a higher harmonic of the cavity's fundamental repetition rate.[61,66,73] Recent work has investigated the location and stability of passively mode-locked lasers operating with multiple pulses circulating in the cavity;[80–82] however, such lasers are generally noisy, since the pulse locations can shift and are not suitable for time-sensitive applications. One particular exception is coupled-cavity lasers which can be used to decrease the timing jitter in high-harmonic passively mode-locked lasers. Yet these cavities need to have repetition rates that are multiples of one another and their lengths must be maintained with interferometric precision for these lasers to live up to their potential.[14,24] Nevertheless, a non-interferometric coupled-cavity laser, which had good noise performance and did not require interferometric control was recently demonstrated by Deng *et al.* at the Institute of Optics.[83]

Actively mode-locked lasers, operating with multiple pulses in the cavity, enjoy far better jitter performance then their passive counterparts, since their pulses are continuously gated by a modulator. Nevertheless, the performance of these lasers ultimately suffers due to the inescapable noise in the electronics which drive the modulators and pulse-pulse interactions are still a concern.[84–86]

In this thesis, high repetition-rate mode-locked lasers are investigated experimentally and numerically. Experimentally, mode-locked high-repetition rate fiber lasers are demonstrated by changing the cavity parameters in a NLPR mode-locked laser to force a single mode-locked pulse to split into many pulses, actively mode locking at a high harmonic, and by building a short cavity passively mode-locked fiber laser. Analytically, we develop a new approach for treating mode-locked lasers in the presence of dispersion and nonlinearity. This is accomplished by sacrificing an exact knowledge of the pulse shape for a more precise knowledge of the pulse parameters. Using this

method, this thesis presents a new time-domain approach to mode locking. In many respects, it is more general than its predecessors, especially if one notes that its results collapse to the prior theories in the appropriate limits.

Although it is possible to satisfy the requirements for a thesis simply by rehashing the work and results obtained during one's tenure as a graduate student, it generally makes for a less than useful manuscript. As a graduate student, I have had the opportunity to read a few theses and it has been my experience that those which provide basic information and details are valuable whereas those that simply summarize results, while informative, are less useful.

It is with this approach that this thesis has been written. Although it is highly detailed and textbook-like at times, it has been done so intentionally in the hope that it may, perhaps, benefit someone else in the future.

1.5 Thesis Outline and Research contributions

This thesis is organized in the following manner. Chapter 2 reports on some of the experimental results obtained as part of this thesis work. Specifically, a harmonically mode-locked erbium fiber laser operating at 210 MHz is demonstrated. Following the investigation of that laser, an actively mode-locked ytterbium fiber laser operating at 10.3 GHz is reported.

Chapter 3 summarizes some of the experimental techniques which should be mastered by anyone working in the field of mode-locked lasers. Although these techniques may be found in other works, this chapter provides a good introduction with sufficient information so that one would be able to perform them without consulting the primary works. In this sense, it serves as a brief overview for these experimental techniques.

Chapter 4 gives a basic introduction to nonlinear fiber optics starting from Maxwell's equations and deriving the generalized nonlinear Schrödinger equation (GNLSE). The

nonlinear Schrödinger equation (NLSE) is shown to be a simplification of the more general case and is valid for pulses whose widths are > 100 fs. The effect of finite-bandwidth saturable gain is then introduced and the Ginzburg–Landau equation is "derived." This chapter then glosses over fiber amplifiers with a focus on ytterbium before providing a cursory introduction to lasers. Finally, a mathematical introduction to mode locking is given where a simple analytic treatment for the main mode-locking mechanisms is presented along with the expected pulse shapes.

Chapter 5 introduces the numerical modeling approach used in this thesis by applying it to one of the mode-locked lasers demonstrated in chapter 2. Aside from obtaining good agreement with the experimental results, the model predicted a new pulse shifting mechanism in FM mode-locked lasers.[28] Moreover, this chapter concludes by extending the work of Haus and Silberberg[3] to FM mode-locked lasers.[28]

In chapter 6 the moment method is introduced as a useful tool for investigating nonlinear pulse propagation. This method is then applied to the basic equation governing mode locking in the time domain: the Ginzburg–Landau equation. This result provides us with rate-equations which serve as the building block for our theoretical contribution to mode-locked lasers.

Chapter 7 applies our rate-equation approach to lasers mode locked by saturable absorbers. The results obtained are then compared with full simulations to show their accuracy.

Chapter 8 applies the rate-equation approach to an AM mode-locked laser and compares it with the full numerical solution.

Chapter 9 applies the rate-equation approach to an FM mode-locked laser and compares it with the full numerical solution. By focusing on the equations governing frequency shift and temporal shift, we are able to map out the expected location for pulse formation analytically for the first time.

Chapter 10 summarizes the results obtained in this thesis and predicts a few directions the field of mode-locked lasers is likely to move in.

Finally, as well as providing supplemental material, the appendices give a detailed derivation of the numerical techniques required to model basic nonlinear pulse propagation. The appendices are more thoroughly introduced throughout this manuscript when their content is required.

2 Experiments on Mode-Locked Fiber Lasers

In this chapter, some of the experiments performed as part of this thesis are discussed. These experimental works are primarily comprised of fiber laser fabrication, pulse and pulse train measurement, and the characterization of laser cavities. In chapters 5, 7, 8, and 9, we will revisit some of these lasers through numerical simulations.

2.1 High-Repetition Rate Mode-Locked Lasers

As noted in the introduction, there are three well-known ways in which the repetition rate of a mode-locked laser can be increased: decreasing the cavity length, increasing the number of pulses in the cavity (known as harmonic mode locking), or by employing a coupled-cavity architecture which also increases the number of pulses in the main cavity. In this chapter, we will focus on achieving high repetition rates through some of these approaches.

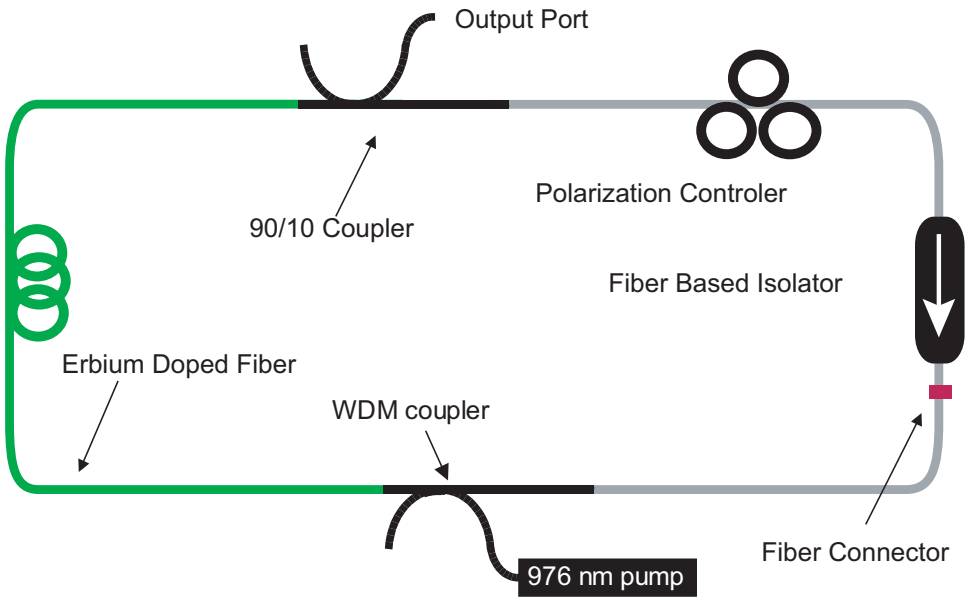

Figure 2.1: Passively mode-locked all-fiber erbium laser.

2.1.1 Passive Harmonic Mode Locking

The number of pulses in passively mode-locked lasers can be increased by increasing the pump power, increasing the fiber's nonlinearity, or changing the dispersion within the cavity since solitons can be shown to obey an area-like theorem; their peak power P_0 is related to their width T_0 by the soliton condition $\gamma P_0 T_0^2/|\beta_2|$, where γ and $|\beta_2|$ are the nonlinear and dispersion parameters of the fiber (see Chapters 3 and 4). In a NLPR mode-locked fiber laser the nonlinear polarization rotation mechanism can be over-driven,[78,87] which places a limit on the pulse power/energy and leads to such effects as optical wave breaking.[87] Therefore, the combination of these two effects means that a single pulse circulating in a laser cavity can be forced to split into multiple pulses by changing the cavity parameters.[76,78,79] In this section, we exploit this effect by building an erbium-doped fiber ring laser, pumping it with powers $\sim$ twice the threshold power, and introducing a $\sim$5 m section of anomalous dispersion fiber into the cavity. By adjusting the polarization controller (mode locker), we are also able to demonstrate this feature.

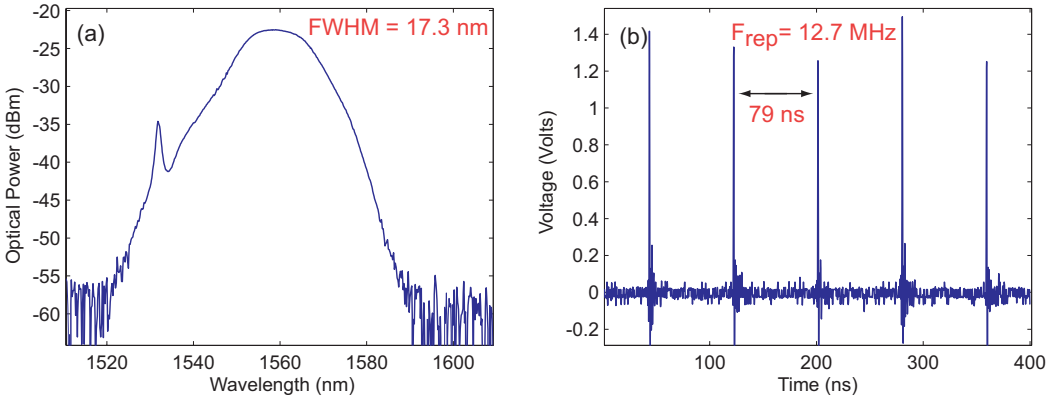

Figure 2.2: (a) Passively mode-locked optical spectrum produced from the laser of Fig. 2.1 (b) shows the mode-locked pulse train recorded on an oscilloscope.

To achieve mode locking in a passively mode-locked laser, consider the ring cavity shown in Fig. 2.1. The polarization controller allows the experimentalist to optimize the polarization such that the peak of the pulse travels through the isolator. In our setup, the isolator also acts as an analyzer since it has a large polarization-dependent loss. As a consequence of NLPR, the center of the pulse acquires a different polarization than its wings. Therefore, the isolator shortens the pulses by acting, in conjunction with this rotation mechanism, as an artificial fast saturable absorber.

We point out that all of the results appearing in this section were obtained by injecting 70 mW of 976-nm pump power into the laser cavity depicted in Fig. 2.1, although the laser could be mode locked with pump powers as low as 40 mW. For example, Fig. 2.2(a), which was obtained using an optical spectrum analyzer (OSA; Ando AQ-6315A), shows the spectrum produced by mode locking this laser at its fundamental frequency of 12.7 MHz.

If we assume the pulses are transform-limited and use the relation for a hyperbolic secant pulse from Appendix A, the spectrum's 17.3-nm full width at half maximum (FWHM) implies the laser produces 150-fs pulses (FWHM). The narrow peak seen in Fig. 2.2 is known as a Kelly sideband[88] and is a consequence of the soliton radiating through dispersive waves.[89] In a dispersion-managed laser, a soliton is continuously

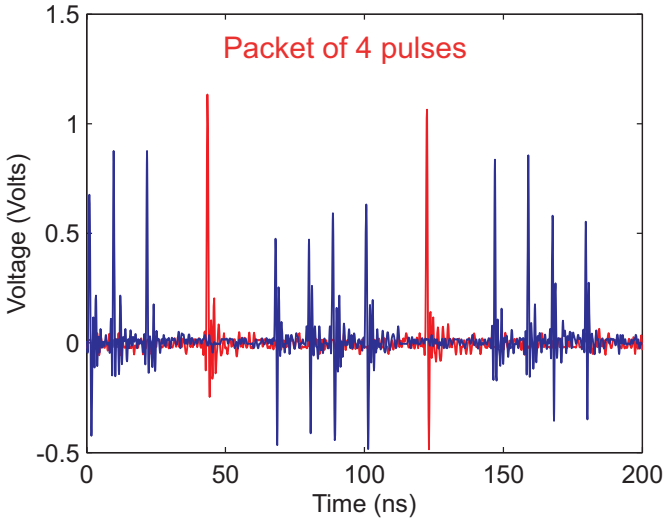

Figure 2.3: Pulse train obtained when the polarization controller is adjusted and the pulse splits into 4 pulses (blue). For comparison the pulse train obtained under fundamental mode locking is also shown (red).

perturbed by the different cavity elements, which causes the soliton to radiate. If the difference between the phase delay of the soliton and the radiated light is a multiple of 2π, these sidebands appear. Generally, they are unwanted; however, they do provide a means by which one can get an indication of the cavity dispersion.[89]

The mode-locked pulse train shown in Fig. 2.2(b) was obtained by using a 2.5 GHz bandwidth detector (ThorLabs Model D400FC InGaAs Detector) in conjunction with an oscilloscope (Tektronix TDS 3064B). This figure reveals large pulse-to-pulse amplitude fluctuations. Although the quality of the mode-locked pulse train can be improved by careful adjustment of the dispersion map within the cavity and the pump power, the goal of this work was to achieve higher harmonic mode locking. To that end, the noisy pulse train we find is actually a good sign since it indicates that the pulse is subject to oscillations.

By carefully adjusting the polarization controllers, each mode-locked pulse in Fig. 2.2(b) can be split into 4 pulses which travel around the cavity as a packet. This regime is depicted in Fig. 2.3. Through an even more careful adjustment, each mode-locked pulse

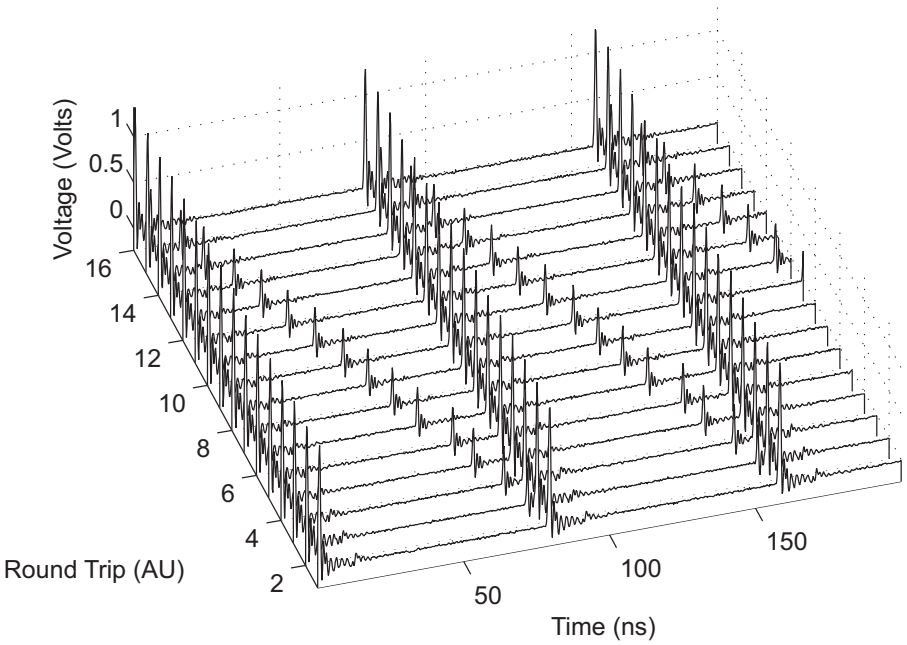

Figure 2.4: Two simultaneously mode-locked pulses with different carrier frequencies pass one another in the time domain because of cavity dispersion.

can be made to split in two where, in contrast to the preceding result, the two resulting pulses have slightly different carrier frequencies. As a consequence of dispersion, these two pulses complete a single cavity round trip in slightly different times; of course, they also have different repetition rates. Figure 2.4 shows the experimental data taken from an oscilloscope showing how pulses cross one another on a slow time scale. The speed with which the pulses pass each other is related to the respective carrier frequencies and the cavity dispersion. Experimentally, it was found to vary from much $\ll 1$ second to around 20 seconds. Although this observation is interesting, it does not help us achieve our goal of a high-repetition rate; however, it is relevant to this topic and will be discussed later.

In an effort to pursue higher repetition rates, a $\sim$5 m section of Corning SMF-28 is inserted into the laser cavity at the location of the fiber connector. By introducing extra fiber into the cavity, the fundamental repetition rate will have decreased. In order to determine the new repetition rate, the laser is again fundamentally mode locked. In this

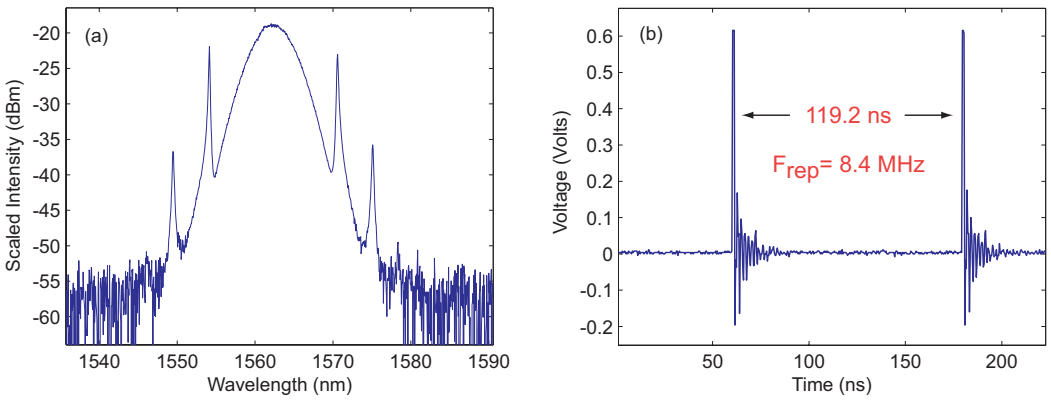

Figure 2.5: Effect of a section of extra fiber on the fundamental mode locking. (a) The optical spectrum now includes more dispersive side waves due to the increased cavity dispersion. (b) As a result of the increased fiber both the pulse-to-pulse spacing has increased and, as a consequence, the repetition rate has decreased.

case, the pulse spectrum develops four very noticeable peaks, which have already been identified as Kelly side bands. As expected, the pulse-to-pulse spacing has increased to $\sim$120 ns. As a consequence, the repetition rate has decreased to 8.4 MHz. Figure 2.5 reveals that the bandwidth of these pulses is three times smaller than that of the pulses formed by the previous cavity. This is related to the large excess anomalous dispersion that was introduced into the laser cavity by the fiber.

By adjusting the polarization controllers, we are able to obtain more pulses simultaneously circulating in the laser cavity than with our shorter cavity. Figure 2.6 shows two pulse trains obtained from this cavity. In Fig. 2.6(a), a packet of 15 pulses was obtained; almost four times more pulses than what was obtained in the same laser devoid of the extra section of fiber. Figure 2.6(b) shows the best pulse spitting archived for this laser where a total of 48 pulses circulated in the cavity.

Although these results are interesting in their own right, our goal is to obtain a uniform pulse train, where the pulse-to-pulse spacing is constant between any two adjacent pulses. This situation represents a special case of mode locking with multiple pulses present in the cavity and is known as harmonic mode locking since the repetition rate is increased by a factor equal to the number of pulses in the cavity. Once again, through

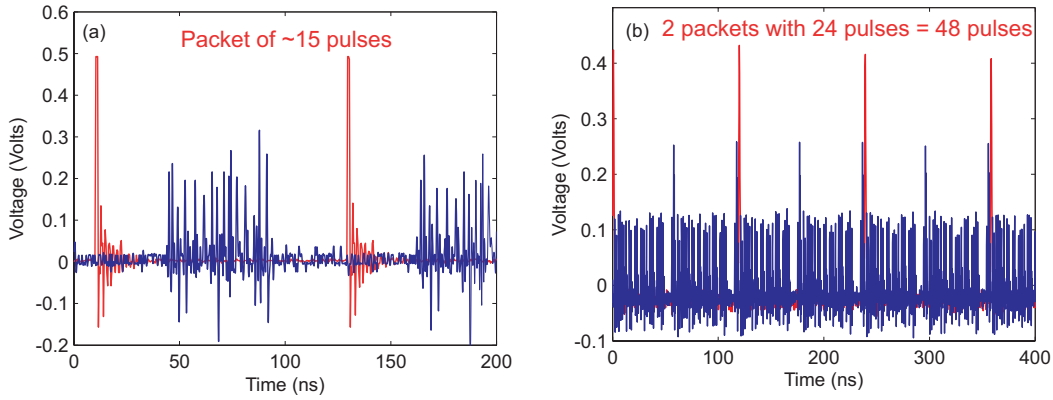

Figure 2.6: Effect of an extra $\sim$ 5 meter intracavity section of SMF-28 fiber on packet mode locking. (a) Shows the formation of a single packet consisting of $\geq$ 15 individual pulses whereas (b) shows the interesting case where two similar packets consisting of $\sim$ 24 pulses each were obtained.

careful adjustment of the polarization controllers, the pulse-to-pulse spacing can be equalized among all of the neighboring pulses. This situation is shown in Fig. 2.7(a) where 25 pulses with equal spacings are simultaneously obtained within the cavity. Although this increased the repetition rate of the laser from 8.4 MHz to 210 MHz, careful inspection of Fig. 2.7(a) reveals pulse-to-pulse fluctuations which still occur at 8.4 MHz. As a consequence of these fluctuations, there are large pulse-to-pulse fluctuations in amplitude and temporal separation and the quality of this pulse train is limited. Figure 2.7(b) is an example of subharmonic mode locking, an interesting regime of operation that challenges the conventional wisdom regarding a mode-locked laser. In this type of mode locking, the pulse does not repeat itself every round trip as all of the analytic treatments of mode locking assume. Instead, a mode-locked pulse repeats its shape only after multiple round trips in the cavity. By adjusting the polarization controllers, this laser was found to mode lock at its $\frac{1}{2}$ harmonic, as shown in Fig. 2.7(b). Mathematically, we can consider such a mode-locked laser as having converged to a limit cycle. In this case, a phase diagram relating any two (or more) orthogonal pulse parameters (such as pulse width and chirp or center frequency and arrival time) converges to an ellipse as opposed to a single point.

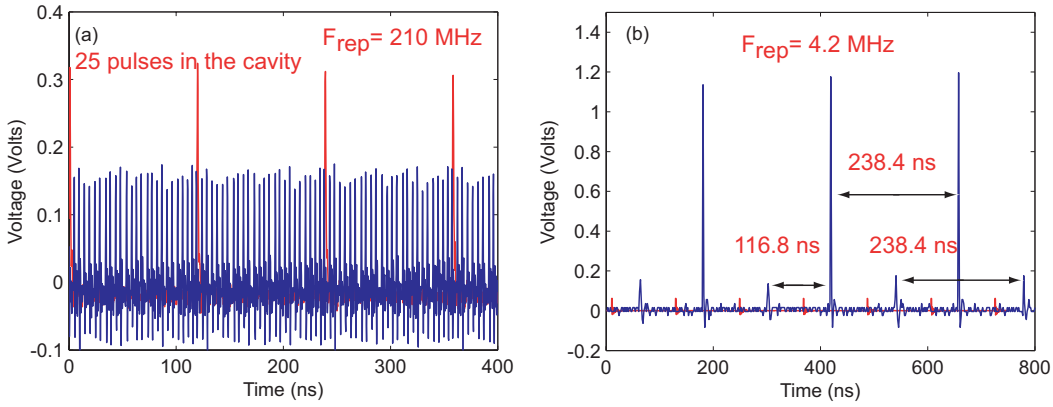

Figure 2.7: Effect of a $\sim$ 5 meter intracavity section of SMF-28 fiber on (a) harmonic and (b) subharmonic mode locking.

The drawbacks of using this approach to produce a high-repetition-rate mode-locked laser are limited pulse contrast, pulse-to-pulse variations, dropped pulses, stability issues, timing jitter, and amplitude fluctuations. In fact, the microwave spectrum of the mode-locked pulse train from this laser (not shown here) reveals that the laser has an excessive amount of amplitude fluctuations. Although these fluctuations could be minimized by using a spectral filter,[4] we did not pursue such a solution. In fact, the main reason for showing the wide variety of results that can be achieved using this laser in Figs. 2.2– 2.7 was to give the reader an appreciation for the difficulty in making such a laser operate in a chosen state. With such a plethora of operating regimes, it is hard to guarantee that this laser will self-start in a particular regime and continue to operate in that regime. Nevertheless, there are schemes that can be employed to mitigate some of the stability issues this laser is susceptible to. Still operation at repetition rates $\sim$ 10 GHz would require hundreds of pulses to simultaneously exist in the laser cavity. Therefore, although it is possible to fabricate high-repetition-rate passively mode-locked lasers, the low contrast is usually an impediment that must be addressed. Moreover, issues with timing jitter and pulse location inherent in high-harmonic passively mode-locked lasers must be countered with some type of active stabilization scheme in practice.

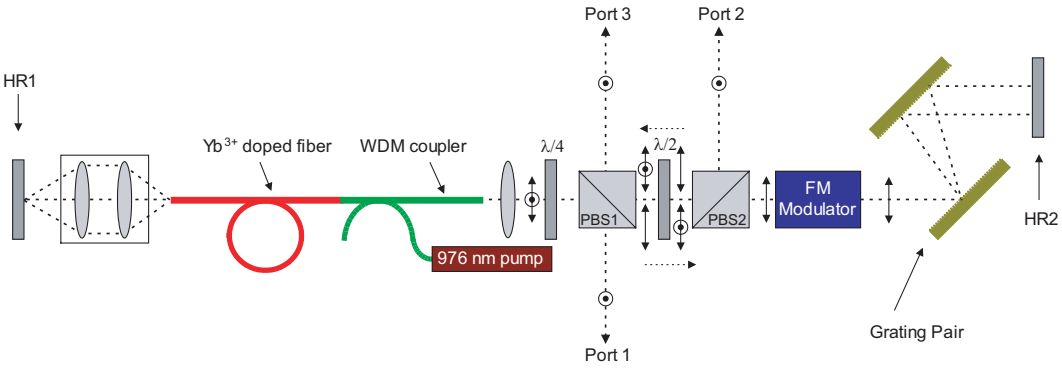

Figure 2.8: Laser cavity configuration: HR, high-reflectivity mirrors; PBS, polarizing beam splitters; WDM, 976/1050-nm wavelength division multiplexer. The double-sided arrows and the dots surrounded by circles represent the horizontal and vertical polarizations respectively.

2.1.2 Active Harmonic Mode Locking

An alternative to using passive mode-locking techniques, that reduces jitter and allows for synchronization, is to simply use high-harmonic active mode locking. To accomplish this, an active modulator is driven at a multiple of the cavity's fundamental repetition rate. Therefore, each pulse is gated or temporally stabilized by the modulator and timing jitter is reduced.* By using active mode locking one also has the ability to synchronize a laser to an external clock or electronic signal. We now demonstrate a high-repetition rate FM mode-locked laser operating at 1053 nm using a ytterbium doped fiber as a gain media.[73]

Figure 2.8 shows the cavity layout of the ytterbium fiber laser. In this design the $\lambda/2$ waveplate and PBS2 create a variable output port that is not necessary to achieve mode locking but allows us to extract more power from the cavity. Even though the laser works without the $\lambda/4$ waveplate, it was included to allow for better performance and adjustability.

A bulk phase modulator[90] actively FM mode locks this laser, enabling synchro-

*In actuality, the jitter is now limited by the electronics. This may or may not be acceptable in a given application.

nization to an external reference frequency. Velocity matching between the optical and microwave fields in the modulator's $LiNbO_3$ crystal, in conjunction with a resonant design, offers efficient phase modulation at the device's resonance frequency ($\approx$ 10.3 GHz). A synthesized microwave signal generator (HP model 83732B) amplified by a travelling-wave tube amplifier (Hughes model 8010H) provides up to 10 W of microwave power to the modulator, which was measured to have a single-pass modulation depth of ≈ 0.45 radians using a technique described later in this chapter. To reduce intracavity loss, the crystal facets were antireflection coated, resulting in an insertion loss of $< 1\%$ at 1053 nm.

The mode-locking threshold was measured to be as low as 30 mW, but the pump laser was operated at a power of 150 mW in an effort to maximize the output power and facilitate autocorrelation measurements. All of the following results were obtained using this pump power and the output from port 1, where the laser has a slope efficiency of 32% (if all three ports are considered the slope efficiency is 40%). Since conventional fibers do not exhibit anomalous dispersion below 1.3 μm, the cavity also incorporates a grating pair, which compensates the normal dispersion introduced by 1 m of ytterbium-doped fiber and 1.2 m of fiber associated with the 976/1050 WDM coupler. The overall second- and third-order cavity dispersions were measured using an *in situ* technique[†92,93] to be -6.3×10^4 fs^2 and 130.6×10^4 fs^3 respectively, revealing that this laser is within the soliton regime.

A typical mode-locked pulse spectrum, shown in Fig. 2.9 and measured with an OSA, reveals a bandwidth of 0.8 nm. This spectrum is best fit by a sech^2 function, shown by the dashed curve. The dotted curve shows a Gaussian fit for comparison. Considering the pulse spectrum to be a hyperbolic secant, a 0.8-nm bandwidth (FWHM) implies a 1.5-ps (FWHM) transform-limited sech pulse. According to simple FM mode-locking theory, an FM modulator in a purely linear dispersionless cavity

[†]To use this technique HR1 was replaced with a SESAM[91] and the laser was passively mode locked. A detailed discussion regarding this measurement is provided in Section 3.5

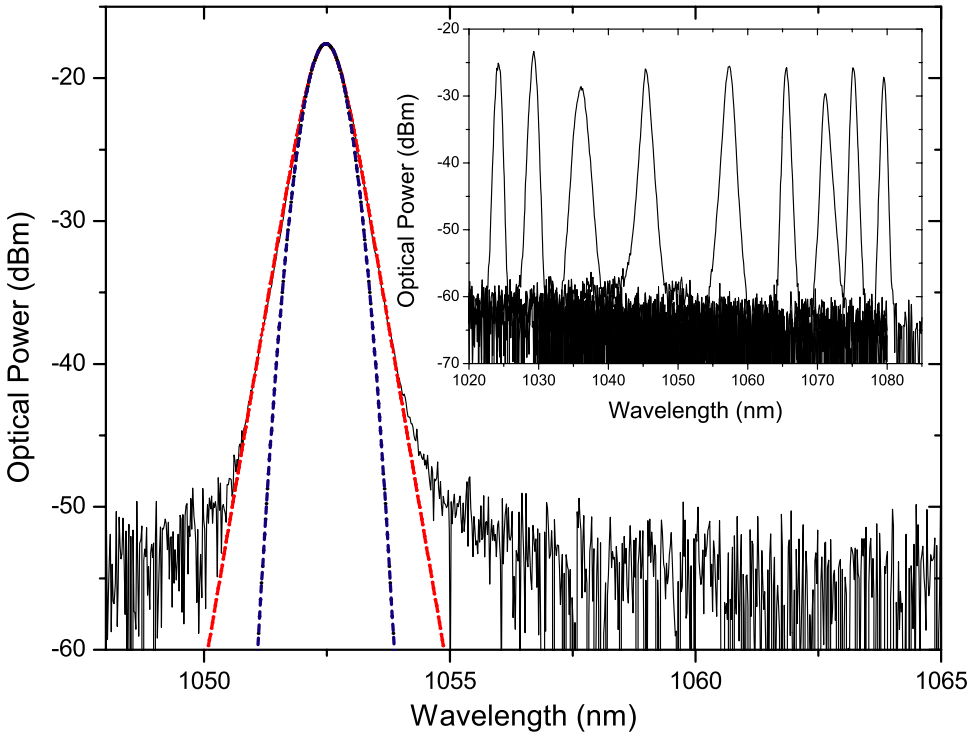

Figure 2.9: Mode-locked optical pulse spectrum and its associated sech^2 fit [shown by the (red) dashed trace]. The dotted (blue) trace shows the corresponding Gaussian fit for comparison. The inset contains superimposed mode-locked spectra illustrating the 1022- to 1080-nm tuning range.

should produce chirped Gaussian output pulses with Gaussian spectra.[2] In light of this, our spectral measurements suggest that cavity dispersion, fiber nonlinearity, and modulator induced chirp play a significant role in shaping the laser pulses.[3,31]

Aside from normal laser optimization practices, actively mode-locked lasers can be mode locked by carefully adjusting the modulation frequency applied to the modulator. For an FM modulator, as the applied frequency gets close to a harmonic of the cavity's fundamental frequency, the cw output spectrally broadens and the laser enters into the so-called FM oscillation regime.[68] Under this type of operation the temporal output of the laser looks like a noisy pulse train superimposed on a cw background.[68] In the frequency domain, the spectrum corresponding to this regime of operation takes on a double-peaked appearance, as experimentally found for a detuning of ~ -94 kHz in Fig. 2.10. As the modulation frequency is tuned onto a harmonic of the cavity, the

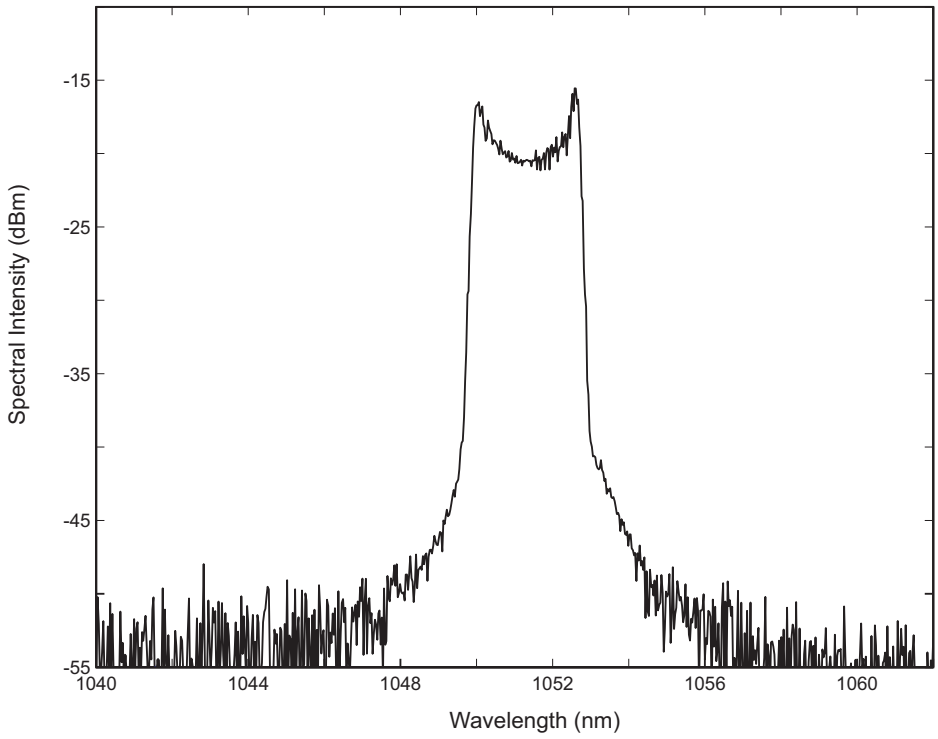

Figure 2.10: Optical spectrum when the FM modulation frequency is slightly detuned from a higher harmonic of the cavity's fundamental frequency.

spectral shape changes until it becomes similar to the result shown in Fig. 2.9 and the laser enters into the mode-locked regime.

An interferometric autocorrelator employing two-photon absorption (TPA) in the photocathode of a photomultiplier tube was used to perform autocorrelation measurements (Fig. 2.11).[‡][94] This sensitive diagnostic was required to determine the width of the pulses, whose low energy ($\leq$ 4 pJ) resulted from the large number of pulses simultaneously circulating in the laser cavity. The autocorrelation trace was best fit[95] by the TPA response to a sech pulse, indicating a pulse width of 2.0 ± 0.2 ps (FWHM) and revealing that this laser's time-bandwidth product is 0.43 ± 0.04. As a consequence of the low peak power, not only was it difficult to obtain autocorrelation traces, but they had signal to noise ratios of about 5.

[‡]Please see 3.1 for a detailed discussion of interferometric TPA autocorrelation.

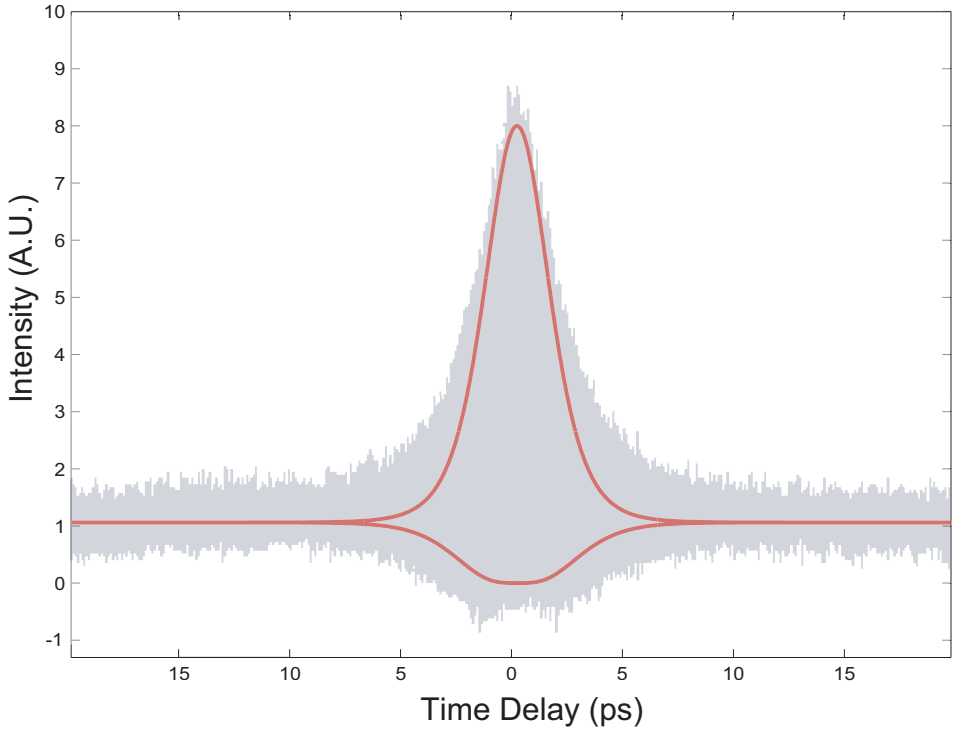

Figure 2.11: Autocorrelation Results. The fit shown in this figure was obtained by using the two-photon absorption response to a 2-ps hyperbolic-secant pulse.

Mode-locked operation was achieved with central wavelengths ranging from 1022 nm to 1080 nm by inserting a knife edge (not depicted in Fig. 1) in front of HR2 and adjusting its position. The central wavelength also depended on the driving modulation frequency, the cavity length, and the angular position of mirror HR2. The effect of tuning on the pulse spectrum is shown in the inset of Fig. 2.9, where several different spectra in the tuning range of 1022 to 1080 nm have been superimposed on one another. The spectral shape varies little over the tuning range, although the spectra centered around 1030 nm have the largest bandwidth.

Side-mode suppression and timing jitter are two common figures of merit used to evaluate the quality of a mode-locked pulse train. These quantities are derived from the pulse-train power spectrum shown in Fig. 2.12 and were obtained using a 25-GHz photodetector with a nominally flat frequency response (New Focus model 1414)

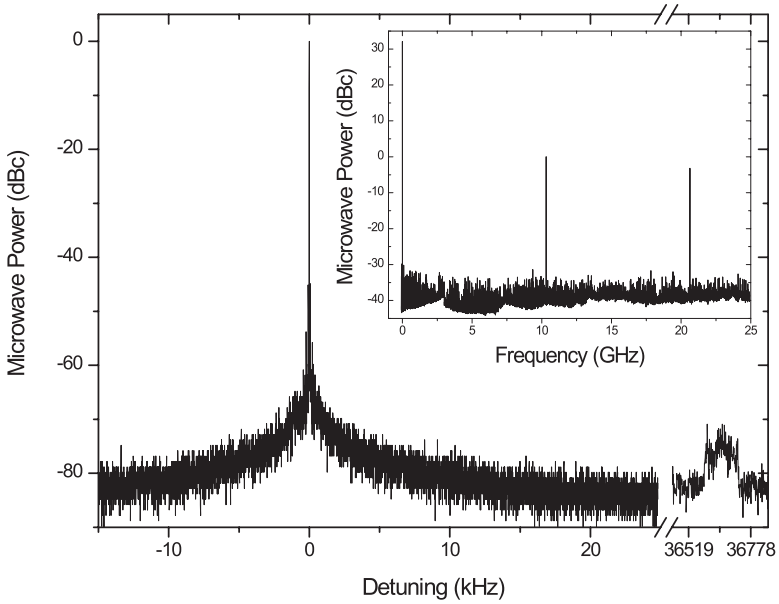

Figure 2.12: The microwave spectrum of the laser versus detuning from the 10.31455-GHz modulation frequency. The horizontal axis is broken to show the closest supermode noise peak, which is detuned from the carrier by the fundamental repetition rate of the laser. The inset shows the DC contribution, verifies the $\approx$ 10.3-GHz mode-locked repetition rate, and shows the repetition-rate's first harmonic located at $\approx$ 20.6 GHz. Note that the strength of the noise floor has increased in the inset as a result of the reduced resolution required to display such a broad frequency range.

and a 26.5-GHz microwave spectrum analyzer (Agilent model E4407B). As expected, the microwave spectrum shown in the inset of Fig. 2.12 is composed of peaks at the 10.31455-GHz driving frequency, its harmonics, and much weaker structures spaced by the 36.65-MHz fundamental repetition rate of the laser cavity (not visible in the inset), which are due to supermode noise.[96] A side-mode suppression of greater than 72 dB was measured with respect to the largest of these side modes as shown in the main figure.[§] Dividing the laser's mode-locked repetition rate by its fundamental repetition rate reveals that there are 281 pulses simultaneously circulating in this cavity.

[§]By way of comparison, the side-mode suppression for the passively mode-locked laser reported in the previous section was $\sim$ 40 dB when fundamentally mode locked and far worse ($\leq$ 10 dB) when the laser was harmonically mode locked. The improved performance of actively mode-locked lasers is due to the temporal gating each pulse receives as it passes through the laser's modulator.

Since the inset of Fig. 2.12 shows that each peak is δ-function like, having a FWHM narrower than the minimum resolution (1 Hz) of the spectrum analyzer, the timing jitter and pulse energy fluctuations of the output pulse train were characterized.[¶] An upper bound on root mean square (rms) timing jitter is related to the integrated spectral power over the offset frequency range $f_l - f_h$[‖97]

$$\sigma = \frac{1}{2\pi f_m}\left[2\int_{f_l}^{f_h} L(f)df\right]^{1/2}, \tag{2.1}$$

where σ is the rms timing jitter, f_m is the frequency of the m$^{\text{th}}$ harmonic around which this measurement is made, and $L(f)$ is the single-sided phase-noise spectral density detuned from f_m. Integration of the 20.6-GHz peak over an offset range from 10 Hz to 12 kHz yields an upper bound on rms timing jitter of 370 fs, which is only slightly larger than the 283-fs jitter measured for the microwave signal generator using the same range. Above 12 kHz, the noise floor of the spectrum analyzer dominated $L(f)$, which prohibited an accurate jitter quantization over the typically quoted range (10 Hz to 10 MHz). The rms energy fluctuations were not limited by the spectrum analyzer and were quantified[97] over the 10-Hz to 10-MHz range, indicating an rms fluctuation of 16.9 fJ, which corresponds to an energy fluctuation of 0.85% for the 2-pJ pulses.

2.2 Chapter Summary

This chapter presented some of the experimental results obtained as part of this thesis. A high-repetition rate passively mode-locked erbium fiber laser was presented. Many different regimes of operation were demonstrated showing both the versatility of this laser and hinting at the difficulty in keeping the laser operating in a single regime. Indeed, this laser was found to produce non-uniform pulse trains when operating under

[¶]Please see 3.4 for details about how the jitter can be determined from the microwave spectrum and as to how characterization was performed.

[‖]See Section 3.4 for a detailed discussion of timing jitter and a derivation of this result.

harmonic mode locking. To achieve a high-repetition rate and mitigate some of the pulse-to-pulse fluctuations encountered in the passively mode-locked laser and actively mode-locked ytterbium fiber laser was demonstrated for the first time. Although the pulse train could not be viewed on an oscilloscope, due to the high repetition rate, analysis of the microwave spectrum indicated that the pulse train was of high quality. In addition to reporting on some of the lasers built as part of this work this chapter serves to motivate subsequent chapters as they investigate the lasers presented in this chapter analytically and computationally to varying extents.

3 Measurement of Parameter Values

Without experimental work to supplement it, theory would be all but useless, since its goal is to explain and predict observable phenomena. Therefore, it is the interplay between theory and experiments that reveal new or unexplained results and motivate one another. It is with the explanation of such results that our understanding of science is increased, allowing us to go beyond today's horizon as we transition to tomorrow's reality. In order to accurately apply a theoretical treatment to an experimental setup or device, one must bridge the two different worlds by using experimental values in theoretical models. Although understanding and insight can be gained by using heuristically obtained parameters, often times the parameters used can change the parameter space of the system such that one thing is observed in the laboratory while a completely different thing may be found numerically/analytically. For this reason, this chapter deals with the experimental measurement of various parameters that will be used numerically and theoretically in subsequent chapters. This chapter also serves as a repository for some of the most commonly used techniques in mode-locked laser characterization and should be a good starting point for those new to this field.

3.1 Pulse Characterization using Autocorrelation

Since cutting-edge detectors and electronics are not available at frequencies above $\sim$ 80 GHz,[98] it becomes impossible to characterize short optical pulses, which have bandwidths in the THz regime, using direct detection. Although this limitation is primarily applicable to pulses shorter than $\sim$ 50 picoseconds, it has implications for broader pulses that posses any fine structure resulting in higher frequency components. It is possible to detect pulse trains at frequencies up to $\sim$ 50 GHz; however, the cost associated with these setups becomes prohibitive for most research groups and they provide little information about the pulse shape.

Historically, streak cameras were used to characterize 10-ns to 10-ps pulses, yet for pulses shorter than 100 ps, autocorrelators are used extensively. Direct electric field reconstruction techniques, such as frequency resolved optical gating (FROG),[99] spectral phase interferometry for direct electric-field reconstruction (SPIDER),[100,101] or their variants, require powers sufficient to produce reasonable nonlinear responses and are difficult to use with GHz pulse trains for which the peak powers are often less than a Watt. Although temporal analysis by dispersing a pair of light e fields (TADPOLE)[102] completely overcomes the power issue, it requires a well-characterized source. Therefore, it is not generally useful. Electro-optic SPIDER also partially overcomes the power limitation.[103] However, all of these more sophisticated schemes require bandwidths in the nanometer regime to produce accurate results (if used in conjunction with an OSA). Since the pulses experimentally generated in this thesis have low peak powers and $\leq$ 1 nm bandwidths, we will only focus on two-photon absorption (TPA) based autocorrelation due to its excellent sensitivity and use for low peak-power pulses.

An autocorrelator, as the name implies, allows one to characterize the autocorrelation of a pulse in a slow time scale, thus overcoming any difficulties associated with high-speed electronics. This approach, however, has an inherent limitation; it allows one to characterize the autocorrelation function, not the pulse. Since what we are inter-

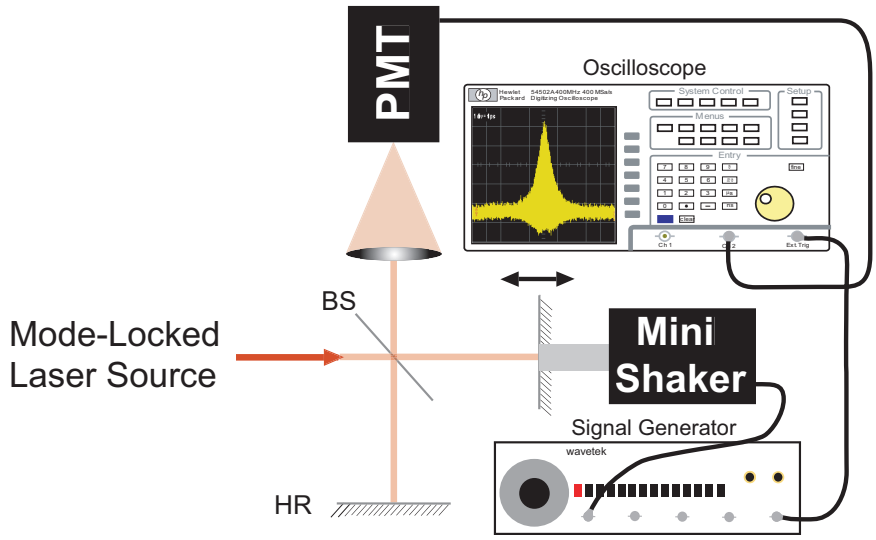

Figure 3.1: Setup for a typical two-photon absorption based autocorrelator. HR: highly reflective (broadband) mirror; BS: (pellicle) beam splitter; PMT: photomultiplier tube.

ested in is the pulse itself, we must figure out the pulse shape from the autocorrelation data. This is an impossible feat for traditional autocorrelation schemes since any pulse asymmetry is removed. Regardless, autocorrelators are still widely used since they provide reasonable results and are more sensitive than any self-referencing electric field reconstruction technique for picosecond pulses.

In this section, we focus on an interferometric TPA-based autocorrelator since it is very sensitive and easy to align. Such an autocorrelator is depicted in Fig. 3.1 where a beam splitter is used to split the incoming pulse into two separate pulses. One of the pulses has a variable delay imparted upon it by either* a stepper motor driven stage (for 10-100 ps pulses), an actuator, such as the armature of an audio speaker (for 20-1000 fs pulses), or a permanent magnet vibrator also known as a shaker (for 20 fs-10 ps pulses). The two delayed pulses are then recombined at the beam splitter and focused onto a detector with a TPA response at the carrier wavelength. Although the figure depicts a lens, a parabolic mirror may be used as a low-dispersion alternative for focusing; likewise a cube-type beam splitter can be replaced with a pellicle beam splitter (as depicted in

*depending on the travel distance and accuracy required

Fig. 3.1) to reduce excess dispersion. The TPA detector should be selected such that its response to a mode-locked pulse is dominated by the TPA signal. This can even be archived with detectors that are insensitive to the carrier frequency (ω_0) of the pules so long as they are sensitive to light at $2\omega_0$.

An important point not addressed in Fig. 3.1 is that photodiodes, PMT's, and other optical detectors act as current devices not voltage devices. Therefore, to insure accuracy, the output of the detector used in the autocorrelator should serve as the input into a transimpedance amplifier[†] whose output is then connected to an oscilloscope. A common way around this is to use the oscilloscope's 50 Ohm internal load and drive the current through it or to use the oscilloscope's 1 MOhm termination but drop a resistor ($\ll$ 1 MOhms) across the wires to try to "convert" the current to a voltage. If one wishes to resolve the high-frequency structure, however, the ramifications of improper termination will cause problems and using a transimpedence amplifier is a more appropriate solution.

Mathematically, we can write the electronic response of the TPA detector as being the sum of two contributions, one from any light detected at ω_0 referred to here as the linear response[‡] or $i_L(t)$ and another contribution due to the nonlinear signal which depends on the overlap between the two pulses $i_{NL}(t)$. These two terms give the resulting current

$$i(t) = i_L(t) + i_{NL}(t) \tag{3.1}$$

$$= r_L I_L(t) + r_{NL} I_{NL}(t), \tag{3.2}$$

where

$$I_L(t) = \int_{-\infty}^{\infty} \left| e_a(\tau) e^{iw\tau} + e_b(\tau - t) e^{iw(\tau - t)} \right|^2 d\tau, \tag{3.3}$$

[†]A transimpedance amplifier is simple circuit involving an Operational Amplifier which converts a current source to a voltage source.

[‡]Note, for detectors which exhibit no linear response (such as the one used in our work) the linear term should be removed from our treatment of this problem ($r_L = 0$). However, in this section we keep this term to insure generality.

$$I_{NL}(t) = \int_{-\infty}^{\infty} \left[\left| e_a(\tau) e^{iw\tau} + e_b(\tau - t) e^{iw(\tau - t)} \right|^2 \right]^2 d\tau, \tag{3.4}$$

and r_L and r_{NL} are the detector's responsivity to the linear signal and the nonlinear signal respectively. Given this prescription, we now investigate the electric current produced by one of these devices when the optical pulse is of a well-known form.

3.1.1 Response to a Hyperbolic Secant Pulse

If the optical pulse is described by

$$e_a(t) = A\,\mathrm{sech}(t/T_0) \tag{3.5}$$

the linear response of the detector is given by

$$I_L(t) = \int_{-\infty}^{\infty} \left| A\mathrm{sech}(\tau/T_0) e^{iw\tau} + B\mathrm{sech}((\tau - t)/T_0) e^{iw(\tau - t)} \right|^2 d\tau \tag{3.6}$$

or

$$\begin{aligned} I_L(t) = \int_{-\infty}^{\infty} & \left[A^2 \mathrm{sech}^2(\tau/T_0) + B^2 \mathrm{sech}^2((\tau - t)/T_0) \right. \\ & \left. + \, 2AB\mathrm{sech}(\tau/T_0)\mathrm{sech}((\tau - t)/T_0)\cos(\omega t) \right] d\tau \end{aligned} \tag{3.7}$$

Performing these integrals results in:

$$I_1 = \int_{-\infty}^{\infty} \mathrm{sech}^2(\tau/T_0) d\tau = \int_{-\infty}^{\infty} \mathrm{sech}^2\left[(\tau - t)/T_0\right] d\tau = 2T_0 \tag{3.8}$$

$$I_2 = \int_{-\infty}^{\infty} \mathrm{sech}(\tau/T_0)\mathrm{sech}\left[(\tau - t)/T_0\right] d\tau = \frac{4te^{t/T_0}}{e^{2t/T_0} - 1} \tag{3.9}$$

Using these results, we find that the linear TPA response for a hyperbolic secant pulse is given by:

$$I_L(t) = A^2\phi_1 + B^2\phi_1 + 2AB\phi_2 \cos(\omega t) \tag{3.10}$$

The nonlinear response of the detector may be investigated in an analogous fashion

$$I_{NL}(t) = \int_{-\infty}^{\infty} \left\{ \left| A\mathrm{sech}(\tau/T_0) e^{iw\tau} + B\mathrm{sech}\left[(\tau - t)/T_0\right] e^{iw(\tau - t)} \right|^2 \right\}^2 d\tau \tag{3.11}$$

$$I_{NL}(t) = \int_{-\infty}^{\infty} \left\{ A^2 \mathrm{sech}^2(\tau/T_0) + B^2 \mathrm{sech}^2\left[(\tau - t)/T_0\right] + 2AB \mathrm{sech}(\tau/T_0)\mathrm{sech}\left[(\tau - t)/T_0\right]\cos(\omega t) \right\}^2 d\tau \tag{3.12}$$

$$\begin{aligned} I_{NL}(t) = \int_{-\infty}^{\infty} \{ & A^4 \mathrm{sech}^4(\tau/T_0) + B^4 \mathrm{sech}^4\left[(\tau - t)/T_0\right] \\ & + 2A^2B^2 \mathrm{sech}^2(\tau/T_0)\mathrm{sech}^2\left[(\tau - t)/T_0\right] \\ & + 4A^3B \mathrm{sech}^3(\tau/T_0)\mathrm{sech}\left[(\tau - t)/T_0\right]\cos(\omega t) \\ & + 4A^2B^2 \mathrm{sech}^2(\tau/T_0)\mathrm{sech}^2\left[(\tau - t)/T_0\right]\cos^2(\omega t) \\ & + 4AB^3 \mathrm{sech}(\tau/T_0)\mathrm{sech}^3\left[(\tau - t)/T_0\right]\cos(\omega t) \Big\} d\tau \end{aligned} \tag{3.13}$$

By carrying out the above integrals, we obtain the following results:

$$I_3 = \int_{-\infty}^{\infty} \mathrm{sech}^4(\tau/T_0) d\tau = \int_{-\infty}^{\infty} \mathrm{sech}^4\left[(\tau - t)/T_0\right] d\tau = \frac{4}{3} T_0 \tag{3.14}$$

$$\begin{aligned} I_4 &= \int_{-\infty}^{\infty} \mathrm{sech}^2(\tau/T_0)\mathrm{sech}^2\left[(\tau - t)/T_0\right] d\tau \\ &= \frac{16 e^{2t/T_0}\left[(t - T_0)e^{2t/T_0} + t + T_0\right]}{3e^{2t/T_0} - 3e^{4t/T_0} + e^{6t/T_0} - 1} \end{aligned} \tag{3.15}$$

$$\begin{aligned} I_5 &= \int_{-\infty}^{\infty} \mathrm{sech}(\tau/T_0)\mathrm{sech}^3\left[(\tau - t)/T_0\right] d\tau \\ &= \frac{-4 e^{t/T_0}\left[4te^{2t/T_0} - T_0 e^{4t/T_0} + T_0\right]}{3e^{2t/T_0} - 3e^{4t/T_0} + e^{6t/T_0} - 1} \end{aligned} \tag{3.16}$$

$$\begin{aligned} I_6 &= \int_{-\infty}^{\infty} \mathrm{sech}^3(\tau/T_0)\mathrm{sech}\left[(\tau - t)/T_0\right] d\tau \\ &= \frac{-4 e^{t/T_0}\left[4te^{2t/T_0} - T_0 e^{4t/T_0} + T_0\right]}{3e^{2t/T_0} - 3e^{4t/T_0} + e^{6t/T_0} - 1} = \phi_5 \end{aligned} \tag{3.17}$$

So we find that:

$$\begin{aligned} I_{NL} = & A^4 I_3 + B^4 I_3 + 2A^2B^2 I_4 + 4A^3B I_5 \cos(\omega t) \\ & + 4AB^3 I_5 \cos(\omega t) + 4A^2B^2 I_4 \cos^2(\omega t) \end{aligned} \tag{3.18}$$

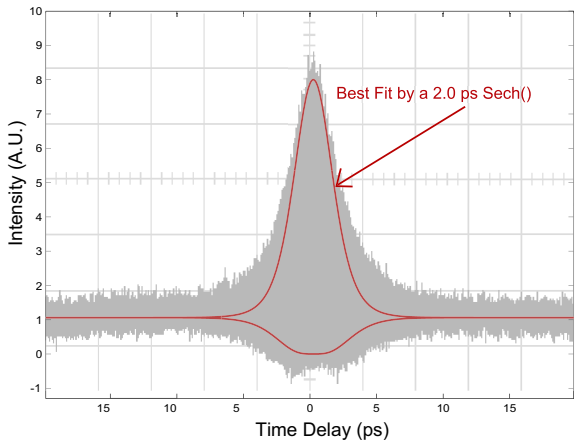

Figure 3.2: Experimentally obtained TPA-based autocorrelation trace and its TPA-based hyperbolic secant fit.

Since this result is generic, it can be simplified if we assume that the two arms of the interferometer have equal powers, a condition that is easy to satisfy experimentally and gives:

$$i(t) = 2r_L A^2 \left[I_1 + I_2 \cos(\omega t)\right] + 2r_{NL} A^4 \left[I_3 + I_4 + 2I_5 \cos(\omega t) + 2I_5 \cos(\omega t) + 2I_4 \cos^2(\omega t)\right]. \quad (3.19)$$

Figure 3.2 demonstrates an autocorrelation trace obtained from the device shown in Fig. 3.1. Since the device is interferometric in design, fringes are obtained. Although the fringes are predicted by Eq. (3.19) and have been used to gain information on pulse chirp,[95,104] it is not feasible to consider these fringes for pulse widths above 100 fs since it require an excessive amount of data to resolve them. As a consequence, it is common to use the minimum and maximum of Eq. (3.19) to fit the experimental data, as shown in Fig. 3.2. Analytically these can be obtained by splitting Eq. (3.19) up (where a $2A^2$ has been factored out):

$$i_{\text{top}}(t) = r_L \left(I_1 + I_2\right) + r_{NL} A^2 \left(I_3 + I_4 + 4I_5 + 2I_4\right) \quad (3.20)$$

$$i_{\text{bottom}}(t) = r_L \left(I_1 - I_2\right) + r_{NL} A^2 \left(I_3 + I_4 - 4I_5 + 2I_4\right) \quad (3.21)$$

3.1.2 Response to a Gaussian Pulse

The response to a Gaussian pulse may also be described analytically by starting with

$$e_a(t) = Ae^{-t^2/2T_0^2}. \tag{3.22}$$

Given this pulse shape, the linear response of the detector is found through

$$I_L(t) = \int_{-\infty}^{\infty} \left| Ae^{-\tau^2/2T_0^2} e^{iw\tau} + Be^{-(\tau-t)^2/2T_0^2} e^{iw(\tau-t)} \right|^2 d\tau \tag{3.23}$$

$$I_L(t) = \int_{-\infty}^{\infty} \left\{ A^2 e^{-\tau^2/T_0^2} + B^2 e^{-(\tau-t)^2/T_0^2} + 2ABe^{-[\tau^2+(\tau-t)^2]/2T_0} \cos(\omega t) \right\} d\tau \tag{3.24}$$

By performing the integrals we find

$$I_1 = \int_{-\infty}^{\infty} e^{-\tau^2/T_0^2} d\tau = \int_{-\infty}^{\infty} e^{-(\tau-t)^2/T_0^2} d\tau = \sqrt{\pi} T_0 \tag{3.25}$$

and

$$I_2 = \int_{-\infty}^{\infty} e^{-[\tau^2+(\tau-t)^2]/2T_0^2} d\tau = \sqrt{\pi} T_0 e^{-t^2/4T_0^2}. \tag{3.26}$$

This gives us

$$I_L(t) = A^2 I_1 + B^2 I_1 + 2ABI_2 \cos(\omega t). \tag{3.27}$$

The nonlinear response of the detector may be investigated in an analogous fashion

$$I_{NL}(t) = \int_{-\infty}^{\infty} \left[\left| Ae^{-\tau^2/2T_0^2} e^{iw\tau} + Be^{-(\tau-t)^2/2T_0^2} e^{iw(\tau-t)} \right|^2 \right]^2 d\tau \tag{3.28}$$

$$I_{NL}(t) = \int_{-\infty}^{\infty} \left\{ A^2 e^{-\tau^2/T_0^2} + B^2 e^{-(\tau-t)^2/T_0^2} + 2ABe^{-[\tau^2+(\tau-t)^2]/2T_0^2} \cos(\omega t) \right\}^2 d\tau \tag{3.29}$$

$$\begin{aligned} I_{NL}(t) = \int_{-\infty}^{\infty} \Big\{ & A^4 e^{-2\tau^2/T_0^2} + B^4 e^{-2(\tau-t)^2/T_0^2} + 2A^2B^2 e^{-[\tau^2+(\tau-t)^2]/T_0^2} \\ & + 4A^3 B e^{-[3\tau^2+(\tau-t)^2]/2T_0^2} \cos(\omega t) \\ & + 4AB^3 e^{-[\tau^2+3(\tau-t)^2]/2T_0^2} \cos(\omega t) \\ & + 4A^2B^2 e^{-[\tau^2+2(\tau-t)^2]/T_0^2} \cos^2(\omega t) \Big\} d\tau \end{aligned} \tag{3.30}$$

As before, all integrals can be performed analytically:

$$I_3 = \int_{-\infty}^{\infty} e^{-2\tau^2/T_0^2} d\tau = \int_{-\infty}^{\infty} e^{-2(\tau-t)^2/T_0^2} d\tau = \sqrt{\frac{\pi}{2}} T_0 \tag{3.31}$$

$$I_4 = \int_{-\infty}^{\infty} e^{-[\tau^2+(\tau-t)^2]/T_0^2} d\tau = \sqrt{\frac{\pi}{2}} T_0 e^{-t^2/2T_0^2} \tag{3.32}$$

$$I_5 = \int_{-\infty}^{\infty} e^{-\frac{1}{2T_0^2}[3\tau^2+(\tau-t)^2]} d\tau = \int_{-\infty}^{\infty} e^{-[\tau^2+3(\tau-t)^2]/2T_0^2} d\tau = \sqrt{\frac{\pi}{2}} T_0 e^{-3t^2/8T_0^2} \tag{3.33}$$

Using them we find that:

$$\begin{aligned} I_{NL} &= A^4 I_3 + B^4 I_3 + 2A^2 B^2 I_4 + 4A^3 B I_5 \cos(\omega t) \\ &\quad + 4AB^3 I_5 \cos(\omega t) + 4A^2 B^2 I_4 \cos^2(\omega t) \end{aligned} \tag{3.34}$$

As we did for the hyperbolic secant case, we assume that the two arms of the interferometer have equal powers and obtain

$$\begin{aligned} i(t) &= 2r_L A^2 \left[I_1 + I_2 \cos(\omega t)\right] \\ &\quad + 2r_{NL} A^4 \left[I_3 + I_4 + 2I_5 \cos(\omega t) + 2I_5 \cos(\omega t) + 2I_4 \cos^2(\omega t)\right]. \end{aligned} \tag{3.35}$$

Moreover, if we split this result into its maximum and minimum values (where a $2A^2$ has been factored out), we find

$$i_{\text{top}}(t) = r_L \left(I_1 + I_2\right) + r_{NL} A^2 \left(I_3 + I_4 + 4I_5 + 2I_4\right) \tag{3.36}$$

and

$$i_{\text{bottom}}(t) = r_L \left(I_1 - I_2\right) + r_{NL} A^2 \left(I_3 + I_4 - 4I_5 + 2I_4\right). \tag{3.37}$$

3.1.3 Response to an Arbitrary Pulse

The prescription for autocorrelation seems simple enough: it should be possible to automate so that it can be performed on an arbitrary pulse shape. This will enable us to compare computational results to those obtained experimentally.

Linear Response: Expanding the square in

$$I_L(t) = \int_{-\infty}^{\infty} \left| e_a(\tau) e^{iw\tau} + e_b(\tau - t) e^{iw(\tau - t)} \right|^2 d\tau, \tag{3.38}$$

we can write:

$$\begin{aligned} I_L(t) = &\int_{-\infty}^{\infty} |e_a(\tau)|^2 \, d\tau + \int_{-\infty}^{\infty} |e_b(\tau - t)|^2 \, d\tau \\ &+ e^{i\omega t} \int_{-\infty}^{\infty} e_a(\tau) e_b^*(\tau - t) d\tau + e^{-i\omega t} \int_{-\infty}^{\infty} e_a^*(\tau) e_b(\tau - t) d\tau. \end{aligned} \tag{3.39}$$

This expression can be re-written as

$$I_L(t) = I_a + I_b + e^{i\omega t} e_a(t) \otimes e_b^*(t) + e^{-i\omega t} e_a^*(t) \otimes e_b(t), \tag{3.40}$$

where $\otimes$ denotes convolution. Since we are dealing with autocorrelation, $e_a(t) = e_b(t - \tau)$ when the interferometer's arms are balanced, and we obtain

$$I_L(t) = 2 \int_{-\infty}^{\infty} |e(\tau)|^2 \, d\tau + 2 \, \mathscr{F}^{-1} \left\{ \mathscr{F} \left[e(t) \right] \cdot \mathscr{F} \left[e^*(t) \right] \right\} \cos(\omega t), \tag{3.41}$$

where $\mathscr{F}$ denotes a Fourier Transform and $\mathscr{F}^{-1}$ represents the inverse Fourier Transform.[§]

If we define

$$I_1 = \int_{-\infty}^{\infty} |e(\tau)|^2 \, d\tau, \tag{3.42}$$

$$I_2 = \mathscr{F}^{-1} \left\{ \mathscr{F} \left[e(t) \right] \cdot \mathscr{F} \left[e^*(t) \right] \right\} \tag{3.43}$$

this result can be written as

$$i_L(t) = 2 r_L \left[I_1 + I_2 \cos(\omega t) \right]. \tag{3.44}$$

[§]In the course of this thesis we heavily used Matlab's fast Fourier transform fft and inverse fast Fourier transform ifft. We point out that these functions use the opposite time-harmonic dependence as the ones of our analytic Fourier transform pair $\mathscr{F}$ and $\mathscr{F}^{-1}$. As a consequence, the ifft corresponds to the Fourier transform $\mathscr{F}$ and fft corresponds to the inverse Fourier transform $\mathscr{F}^{-1}$.

Nonlinear Response:

$$I_{NL}(t) = \int_{-\infty}^{\infty} \left[\left| e_A(\tau) e^{iw\tau} + e_b(\tau - t) e^{iw(\tau - t)} \right|^2 \right]^2 d\tau \tag{3.45}$$

$$\begin{aligned} I_{NL}(t) = \int_{-\infty}^{\infty} \Big[& |e_a(\tau)|^2 + |e_b(\tau - t)|^2 + e_a(\tau) e_b^*(\tau - t) e^{i\omega t} \\ & + e_a^*(\tau) e_b(\tau - t) e^{-i\omega t} \Big]^2 d\tau \end{aligned} \tag{3.46}$$

Expanding the square, we obtain:

$$\begin{aligned} I_{NL}(t) = \int_{-\infty}^{\infty} \Big[& |e_a(\tau)|^4 + 2 |e_a(\tau)|^2 |e_b(\tau - t)|^2 \\ & + 2 |e_a(\tau)|^2 e_a(\tau) e_b^*(\tau - t) e^{i\omega t} + 2 |e_a(\tau)|^2 e_a^*(\tau) e_b(\tau - t) e^{-i\omega t} \\ & + |e_b(\tau - t)|^4 + 2 |e_b(\tau - t)|^2 e_a(\tau) e_b^*(\tau - t) e^{i\omega t} \\ & + 2 |e_b(\tau - t)|^2 e_a^*(\tau) e_b(\tau - t) e^{-i\omega t} + e_a^2(\tau) e_b^{*2}(\tau - t) e^{i2\omega t} \\ & + 2 |e_a(\tau)|^2 |e_b(\tau - t)|^2 + e_a^{*2}(\tau) e_b^2(\tau - t) e^{-i2\omega t} \Big] d\tau. \end{aligned} \tag{3.47}$$

We can rewrite this equation in terms of the Fourier-transform operator as

$$\begin{aligned} I_{NL}(t) = & 2 \int_{-\infty}^{\infty} |e(\tau)|^4 d\tau + 4 \mathscr{F}^{-1} \left\{ \mathscr{F} \left[|e(t)|^2 \right]^2 \right\} \\ & + 2 \mathscr{F}^{-1} \left(\mathscr{F} \left[|e(t)|^2 e(t) \right] \cdot \mathscr{F} \left[e^*(t) \right] \right) e^{i\omega t} \\ & + 2 \mathscr{F}^{-1} \left(\mathscr{F} \left[|e(t)|^2 e^*(t) \right] \cdot \mathscr{F} \left[e(t) \right] \right) e^{-i\omega t} \\ & + 2 \mathscr{F}^{-1} \left(\mathscr{F} \left[e(t) \right] \cdot \mathscr{F} \left[|e(t)|^2 e^*(t) \right] \right) e^{i\omega t} \\ & + 2 \mathscr{F}^{-1} \left(\mathscr{F} \left[e^*(t) \right] \cdot \mathscr{F} \left[|e(t)|^2 e(t) \right] \right) e^{-i\omega t} \\ & + \mathscr{F}^{-1} \left(\mathscr{F} \left[e^2(t) \right] \cdot \mathscr{F} \left[e^{*2}(t) \right] \right) e^{i2\omega t} \\ & + \mathscr{F}^{-1} \left(\mathscr{F} \left[e^{*2}(t) \right] \cdot \mathscr{F} \left[e^2(t) \right] \right) e^{-i2\omega t}. \end{aligned} \tag{3.48}$$

If we define

$$I_3 = \int_{-\infty}^{\infty} |e(\tau)|^4 d\tau, \tag{3.49}$$

$$I_4 = \mathscr{F}^{-1}\left(\mathscr{F}\left[|e(t)|^2\right]^2\right), \tag{3.50}$$

$$I_5 = \mathscr{F}^{-1}\left(\mathscr{F}\left[|e(t)|^2 e(t)\right] \cdot \mathscr{F}\left[e^*(t)\right]\right), \tag{3.51}$$

$$I_6 = \mathscr{F}^{-1}\left(\mathscr{F}\left[|e(t)|^2 e^*(t)\right] \cdot \mathscr{F}\left[e(t)\right]\right), \tag{3.52}$$

$$I_7 = \mathscr{F}^{-1}\left(\mathscr{F}\left[e^2(t)\right] \cdot \mathscr{F}\left[e^{*2}(t)\right]\right), \tag{3.53}$$

we finally obtain

$$i_{NL}(t) = 2r_{NL}\left[I_3 + 2I_4 + 2I_5\cos(\omega t) + 2I_6\cos(\omega t) + I_7\cos(2\omega t)\right]. \tag{3.54}$$

So we find that the TPA photodetector response is given by:

$$\begin{aligned} i(t) = {} & 2r_L\left[I_1 + I_2\cos(\omega t)\right] + 2r_{NL}\left[I_3 + 2I_4 + 2I_5\cos(\omega t)\right. \\ & \left. + \; 2I_6\cos(\omega t) + I_7\cos(2\omega t)\right] \end{aligned} \tag{3.55}$$

The maximum and minimum values of $I(t)$ are found to be (where a 2 has been factored out):

$$i_{\text{top}}(t) = r_L\left(I_1 + I_2\right) + r_{NL}\left(I_3 + 2I_4 + 2I_5 + 2I_6 + I_7\right) \tag{3.56}$$

$$i_{\text{bottom}}(t) = r_L\left(I_1 - I_2\right) + r_{NL}\left(I_3 + 2I_4 - 2I_5 - 2I_6 + I_7\right). \tag{3.57}$$

To demonstrate the utility of this technique, consider the response of a TPA based interferometric autocorrelator that has no linear response at the wavelength of our field so $r_L = 0$. In this case, we assume a 220 fs Gaussian pulse with a chirp $C = 1$ is investigated with the autocorrelator. Figure (3.3) shows the predicted response (gray) in addition to the actual pulse intensity (black) and I_{top} (blue) and I_{bottom} (red) as defined in the above equations.

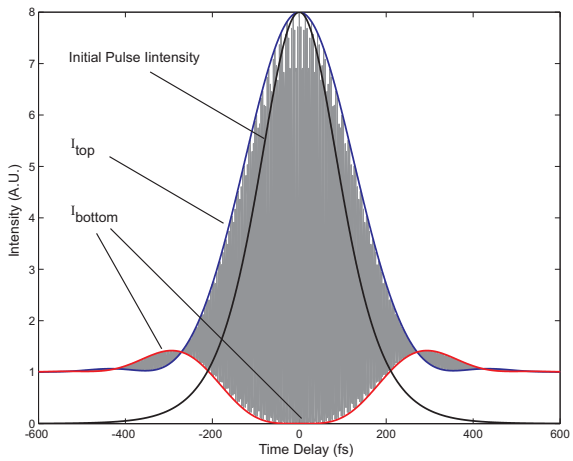

Figure 3.3: Numerically predicted TPA-based autocorrelation trace, the initial pulse intensity, and $I_{\text{top}}(t)$ and $i_{\text{bottom}}(t)$.

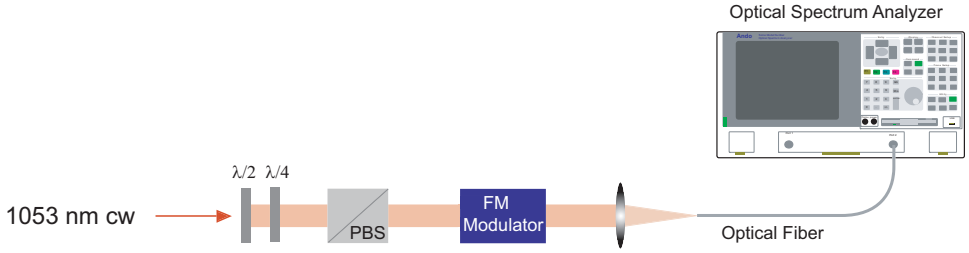

Figure 3.4: Experimental setup used to characterize the FM modulation depth. The polarizing beam splitter (PBS) insures the optimum polarization is used for the characterization and that the characterization is constant with how the device is used in the laser of Fig. 2.8.

3.2 Characterization of Modulators

For FM or AM modulators operating at speeds $\geq$ 10 GHz, quantifying the modulation depth is a straightforward task. Since a 10-GHz frequency can be resolved on an OSA, a cw laser operating at the carrier wavelength of interest can probe the modulation depth as depicted in Fig. 3.4.

The FM(AM) modulator imparts a time-dependent phase(loss) on the cw light, causing the optical spectrum to gain sidebands with a strength proportional to the modulation depth and a detuning from the optical carrier related to the driving frequency.

Mathematically, this can be written as

$$S_{\mathrm{FM}} \approx \left| \mathscr{F}\left[A_0 e^{i\omega_0 t} e^{-\delta + i\Delta\cos(\omega_{FM} t + \phi)} \right] \right|^2 \tag{3.58}$$

or

$$S_{\mathrm{AM}} \approx \left| \mathscr{F}\left[A_0 e^{i\omega_0 t} e^{-\delta - \Delta\cos(\omega_{FM} t + \phi)} \right] \right|^2 \tag{3.59}$$

where F represents the Fourier transform, A_0 is the input field strength, and $\delta \geq 0$ represents any losses due to the modulator and coupling into the fiber. This mathematical prescription is most conveniently carried out on a computer because it does not yield an analytically compact solution and because our cw source will generally have a finite spectral width that should be taken into account. That is, ω_0 is not a constant in Eq. (3.59), but varies over the spectral bandwidth of the cw laser. Figure 3.5 shows the experimental data used to characterize the modulation depth of the FM modulator used to mode lock the laser described in chapter 2.

Since the location of the sidebands necessary for this characterization (seen in Fig. 3.5 at 10.3 GHz) is fixed by the electronic driving frequency, the technique detailed above cannot be used in conjunction with an OSA for frequencies ≤ 1 GHz. Under lower driving frequencies OSA's lack the resolution needed to resolve the slightly detuned side modes. Moreover, the finite bandwidth of most cw probe sources can limit the usefulness of scanning Fabry–Perot étalons for characterizing modulators at lower frequencies.

Therefore, at lower frequencies, modulators must either be characterized using either a scanning Fabry-Perot étalon and a laser source with a very narrow linewidth, a high-speed detector and an oscilloscope, or a microwave spectrum analyzer.[¶] Since AM fluctuations may immediately be detected using a high-speed detector and an oscilloscope or a microwave spectrum analyzer, their characterization should be straightforward when these devices are driven with a sine wave. Since microwave spectrum

[¶]For low driving frequencies FM modulators must be placed in an arm of a Mach-Zehnder interferometer and characterized as an amplitude modulator.

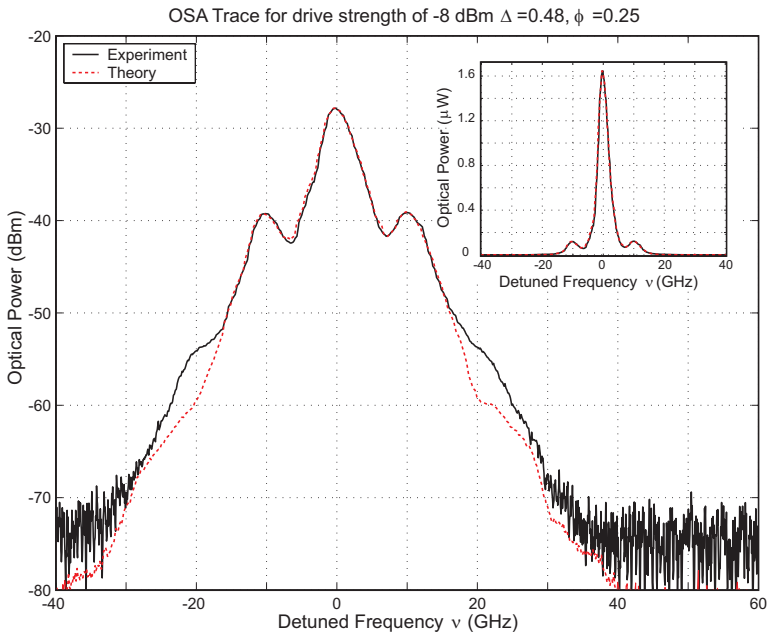

Figure 3.5: Experimentally obtained results and their theoretical fit, where the results predicted by Eq. (3.59) have been convolved with the optical spectrum of the cw source. The inset shows that the fit is quite good on a linear scale despite the fact that the strength of the 20.6 GHz components is underestimated; the discrepancy is most likely due to the finite resolution of the OSA.

analyzers are more sensitive than oscilloscopes this technique was also used to verify the characterization of the FM modulator.

3.3 Gain Measurements

Of all the measurements that need to be performed to characterize a mode-locked laser, those that involve doped-fiber are to be the most difficult. A simple theory predicting how to characterize the small-signal gain and the saturation coefficient for a doped-fiber amplifier starts with the following equation

$$\frac{\partial A}{\partial z} = \frac{g_0/2}{1+P/P_{sat}}A, \tag{3.60}$$

where A is our optical field, g_0 is the small-signal gain coefficient, $P = \int |A|^2 dt$ is the optical power, and P_{sat} is the saturation power of the gain medium. Multiplying this equation by A^* and integrating over time gives

$$\frac{\partial P}{\partial z} = \frac{g_0}{1 + P/P_{sat}} P. \tag{3.61}$$

This can be solved analytically by integrating over the amplifier length to give

$$G = G_0 \exp\left(-\frac{G-1}{G} \frac{P_{out}}{P_{sat}} \right), \tag{3.62}$$

where $G = P_{out}/P_{in}$ and $G_0 = \exp(g_0 L)$ for a fiber of length L. As P_{out} becomes comparable with P_{sat}, the gain fiber saturates and the gain exponentially drops from its small-signal value of G_0.

There are a few glaring errors with such a treatment of the doped-fiber in a laser cavity. For one thing, finite gain bandwidth is ignored; if it were to be included, no analytic solution would exist. Other shortcomings of this model are: it assumes the pump is exponentially absorbed, it ignores amplified spontaneous emission, it assumes pump absorption is independent of the signal being amplified, etc. See sections 4.2 for a further discussion.

Nevertheless, a simple experimental technique to acquire a ball-park idea for the macroscopic behavior of the small-signal gain of a section of fiber is to build an amplifier with a section of doped fiber of the same length and from the same spool as is in a given cavity, (see Fig. 3.6). This amplifier must then be pumped with the same power as the laser is, and care must be taken to avoid cw lasing since it will invalidate any results. By injecting a low-power broadband optical source into the amplifier, the input spectrum and output spectrum can be compared to yield an approximation to the small signal gain of the fiber. By performing such a measurement on a section of ytterbium-doped fiber similar to that used in 2.1.2, we obtained the results shown in Fig. 3.7.

By inspecting Fig. 3.7, one notes that outside of the 1030–1080 nm window the results are dominated by noise. Experimentally, this comes from a finite extent of the broadband source used in this experiment, making the data outside the 1030–1080 nm

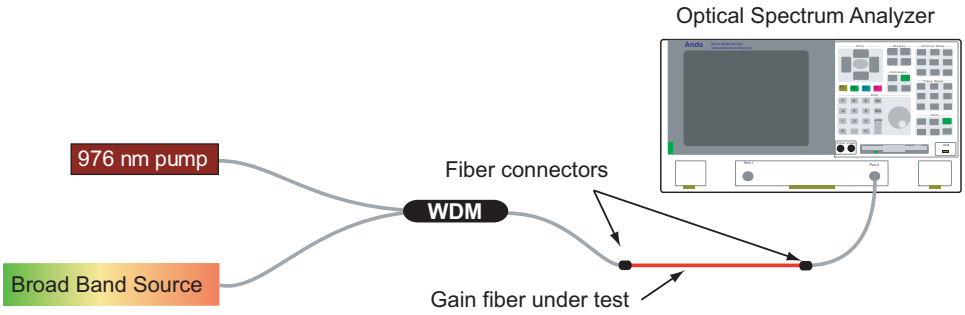

Figure 3.6: Setup for determining the parameters of a gain medium for computer simulations.

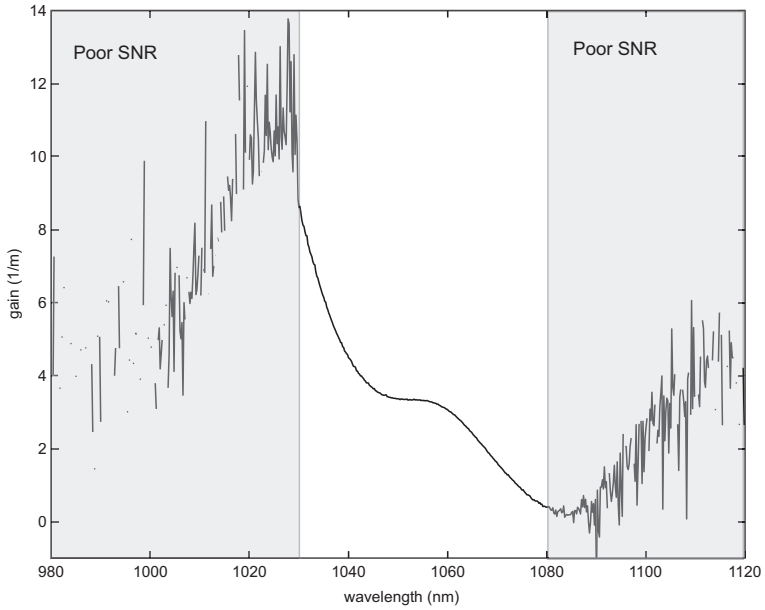

Figure 3.7: Small signal, wavelength dependent, gain coefficient for the laser of 2.1.2.

window unreliable. Indeed, by examining the gain and absorption cross-sections for ytterbium in a silica host [see Fig. 4.4(a)], one easily confirms this fact, since those figures indicate that the gain should fall to zero outside of the 950–1150 nm range.

Unfortunately, the onset of cw lasing prohibited us from performing this characterization with the pump power used in the actual laser of 2.1.2. Although Fig. 3.7 was obtained using a slightly lower pump power, it indicated a small-signal gain at 1053 nm of 3.3 m^{-1}. The small-signal value of 4.3 m^{-1} used in all of the computer simulations

was extrapolated using this data in conjunction with a simple cw characterization which amplified a low-power 1053 nm cw laser (see chapter 5).

In general, it should be possible to increase the power of the probe source in order to determine the saturation power of the gain medium. In our case, however, the probe source used was a superluminescent diode laser (SLED) unable to provide sufficient power to do so. Amplifying the output of the SLED using a ytterbium fiber amplifier caused the fiber under test to lase. This thwarted our efforts to determine the saturation power and so the saturation power was used as a fitting parameter in the numerical studies of chapter 5 where it was found to be $\sim$ 24 mW. This result is similar to the saturation powers expected for erbium-doped fiber lasers.

Thus far, we have only addressed a macroscopic characterization of the gain media which, in some instances, is woefully inadequate. The characterization presented here assumes that the gain follows an exponential profile inside the amplifier and in effect treats the gain medium as a black box. A more accurate way to characterize doped fibers is to use a rate-equation approach in conjunction with an experimental technique that allows one to "see" what is going on inside the pumped gain media; one such approach, which avoids the destructive "cut back" process, is discussed in Section 4.2. Yet, for the understanding and modeling of most mode-locked fiber lasers, a highly detailed rate-equation treatment would amount to overkill since the equations used to model these systems incorporate gain in a simple-minded fashion.

3.4 Characterization of Pulse Train Non-Uniformity

The output of an ideal mode-locked laser in the time domain would be a train of equally spaced identical pulses. In reality there are pulse-to-pulse fluctuations in shape, energy, and pulse-to-pulse spacing. Although quantifying changes in the pulse shape is difficult

and beyond the scope of this work,[‖] energy/amplitude fluctuations and changes in the pulse position, also known as timing jitter, may be characterized using a few different approaches. For example, one obvious way to characterize the timing jitter of a pulse train is to use optical cross correlation.[106] This technique involves an autocorrelator where one arm has a variable delay such that cross-correlation can be performed between temporally disparate pulses.[106] Since the characterization of low frequency jitter would require impractically long delays, this technique is best suited for determining high-frequency timing fluctuations and pulse-to-pulse timing jitter.

Electronically, well-known techniques such as phase-encoded sampling and differential edge detection may be used; however, these approaches can be difficult to implement, requiring high-speed phase-locked loops, high-speed electronics, and local oscillators. Moreover, the accuracy of such approaches are limited by the finite resolution of oscilloscopes ($\sim$1 ps), the finite response times of the detectors (usually $\gtrsim$ 10 ps), and the bandwidth and noise in the phase-locked loops. Finally, timing jitter can be determined by using optical power spectrum techniques. These tend to be the easiest to perform since they only require a high-speed detector and a microwave spectrum analyzer (MSA); unfortunately, they do not provide accurate information on the high-frequency jitter.[97]

In order to understand the jitter measurements performed in this thesis, we need to understand the assumptions used by our technique — the optical power spectrum approach of von der Linde. This technique provides an upper limit on amplitude and timing jitter by assuming that pulse-train fluctuations are correlated; this is the case in mode-locked fiber lasers. Recently, it has been shown that the correlated and uncorrelated jitter contributions to a pulse train can be determined.[107] However, such techniques are more involved and time-consuming and should only result in a slightly more accurate determination of the jitter in a mode-locked laser. In this work, we are not interested in the origin of timing jitter but would like to obtain quantitative estimate

[‖] The interested reader is referred to Ref. 105 for a more detailed treatment that addresses these issues.

of the jitter in a given laser. To this end, this section provides the mathematical foundation on which our experimental technique is based; this derivation essentially follows straight from von der Linde's work.[97]

3.4.1 Mathematical Framework

We can write a perfect (laser) pulse train as

$$F(t) \equiv F_0(t) = \sum_{n=-\infty}^{\infty} F(t+nT), \tag{3.63}$$

where $F(t)$ represents a voltage corresponding to the intensity of the pulse train. Optically, the intensity of a pulse train is detected with a square-law detector and, as a consequence, $F(t) \propto |E(t)|^2$. We also introduce T as the time between adjacent pulses.

Therefore, if we have a slightly imperfect pulse train, we could write it as a perturbed version of Eq. (3.63),

$$F(t) = F_0(t) + \delta F(t), \tag{3.64}$$

where $\delta F(t) \ll F_0(t)$ represents any fluctuations imprinted on the pulse train.

Next, we consider the case where the pulse shape is constant, but its timing and amplitude vary. Such an assumption simplifies the treatment and is frequently valid if we are dealing with short-pulse mode-locked lasers since high-speed detectors cannot resolve the pulse structure anyway (see appendix B for a more detailed discussion of this issue). To simplify the math, we investigate the effects of amplitude fluctuations and timing jitter separately.

In the the presence of amplitude fluctuations, we expect that our pulse train will simply be amplitude modulated. Therefore, by introducing a random function $A(t)$, which accounts for amplitude fluctuations, we can write the expected pulse train as

$$F(t) = F_0(t) + A(t)F_0(t). \tag{3.65}$$

Jitter will manifest itself by changing the temporal location of the pulses. This can be written as

$$F(t) = \sum_{n=-\infty}^{\infty} F(t + nT + \delta T_n), \tag{3.66}$$

where δT_n is a random function which characterizes the jitter.

Assuming that the jitter is small, compared to the normal pulse-to-pulse spacing T, we can Taylor expand the argument in Eq. (3.66) which gives

$$F(t + nT + \delta T_n) \simeq F(t + nT) + \dot{F}(t + nT)\delta T_n + \mathrm{O}(\delta T_n^2). \tag{3.67}$$

Now we introduce a continuous random function $J(t)$ such that $J(t) = \delta T_n / T$. This gives us

$$\begin{aligned} F(t) &= \sum_{n=-\infty}^{\infty} F(t + nT + \delta T_n) \\ &\simeq \sum_{n=-\infty}^{\infty} F(t + nT) + \sum_{n=-\infty}^{\infty} T\dot{F}(t + nT)J(t). \end{aligned} \tag{3.68}$$

Recalling that an ideal pulse train is given by Eq. (3.63), this result can be simplified to become

$$F(t) = F_0(t) + \dot{F}_0(t)TJ(t). \tag{3.69}$$

Combining the results just derived for amplitude fluctuations and timing jitter, we obtain

$$F(t) = F_0(t) + F_0(t)A(t) + \dot{F}_0(t)TJ(t). \tag{3.70}$$

The power spectrum associated with the non-ideal pulse train described above can now be investigated with the hope that it will enable us to identify the different contributions to experimentally observed power spectra. This should then allow us to quantify the degree to which an experimentally obtained pulse train suffers from amplitude fluctuations or timing jitter.

To proceed with our derivation, we must first understand what an (ideal) spectrum analyzer measures. Microwave spectrum analyzers (MSAs) measure the input power

(not amplitude) spectrum of an electrical signal. This may tempt us to write the response of the MSA as

$$\tilde{S}(\omega) = |F(\omega)|^2. \tag{3.71}$$

However, this treatment is mathematically flawed (it ends up giving essentially the same result but contains an extra Dirac delta function) since $F(t)$ fluctuates in time. As a result, $\tilde{S}(\omega)$ is, in reality, a random process that does not necessarily tend to zero as $\omega \to \pm\infty$. To circumvent such an issue, we introduce the Wiener-Khintchine theorem (see, for example, Ref. [108])

$$\tilde{S}(\omega) = \lim_{\Delta\to\infty} \frac{1}{2\Delta}|\tilde{V}(\omega,\Delta)|^2, \tag{3.72}$$

where we have introduced the Fourier transform of the truncated signal via

$$\tilde{V}(\omega,\Delta) = \int_{-\Delta}^{\Delta} V(t)e^{i\omega t}dt. \tag{3.73}$$

In order to keep our result general and account for the filtering effects that inevitably arise due to the finite response time of the detector or the spectrum analyzer, we have introduced a filter function $h(t)$ which acts on our actual signal $F(t)$ through

$$V(t) = \int_{-\infty}^{\infty} h(t-t')F(t')dt'. \tag{3.74}$$

We also define the spectrum of this filter function through

$$h(\omega) = \int_{-\infty}^{\infty} h(t)e^{i\omega t}dt \tag{3.75}$$

By substituting Eq. (3.74) into Eq. (3.73) and then substituting the result into Eq. (3.72), we find

$$\begin{aligned}
\tilde{S}(\omega) &= \lim_{\Delta\to\infty}\frac{1}{2\Delta}\int_{-\Delta}^{\Delta}\left[\int_{-\infty}^{\infty}F^*(t')h^*(t-t')dt'\right]e^{-i\omega t}dt \\
&\times \int_{-\Delta}^{\Delta}\left[\int_{-\infty}^{\infty}F(t_2')h(t_2-t_2')dt_2'\right]e^{i\omega t_2}dt_2 \\
&= \lim_{\Delta\to\infty}\frac{1}{2\Delta}\int_{-\Delta}^{\Delta}\int_{-\Delta}^{\Delta}F^*(t')F(t_2') \\
&\times \int_{-\infty}^{\infty}h^*(t-t')e^{-i\omega t}dt\int_{-\infty}^{\infty}h(t_2-t_2')e^{i\omega t_2}dt_2dt'dt_2' \\
&= \lim_{\Delta\to\infty}\frac{1}{2\Delta}\int_{-\Delta}^{\Delta}\int_{-\Delta}^{\Delta}F^*(t')F(t_2') \\
&\times \frac{2\pi}{2\pi}\int_{-\infty}^{\infty}h^*(\tau_1)e^{-i\omega\tau_1}d\tau_1e^{-i\omega t'}\int_{-\infty}^{\infty}h(\tau_2)e^{-i\omega\tau_2}d\tau_2e^{i\omega t_2'}dt'dt_2' \\
&= 2\pi H(\omega)\lim_{\Delta\to\infty}\frac{1}{2\Delta}\int_{-\Delta}^{\Delta}\int_{-\Delta}^{\Delta}F^*(t')F(t_2')e^{i\omega(t_2'-t')}dt'dt_2' \\
&= 2\pi H(\omega)\int_{-\infty}^{\infty}\lim_{\Delta\to\infty}\frac{1}{2\Delta}\int_{-\Delta}^{\Delta}F^*(t')F(t'+\tau)e^{i\omega\tau}dt'd\tau
\end{aligned} \tag{3.76}$$

where we introduced $\tau = t_2' - t'$, brought the limit inside the τ integral by evaluating its limits, and switched the limits on the integrals for $t \to t'$ and $t_2 \to t_2'$. We also introduced the detector and/or MSA transfer function as $H(\omega) \triangleq |h(\omega)|^2$.

By introducing the intensity autocorrelation function

$$\Gamma(\tau) = \langle F^*(t)F(t+\tau)\rangle \triangleq \lim_{\Delta\to\infty}\frac{1}{2\Delta}\int_{-\Delta}^{\Delta}F^*(t)F(t+\tau)dt \tag{3.77}$$

we can now write our spectrum in a far more concise form as

$$\tilde{S}(\omega) = 2\pi H(\omega)\int_{-\infty}^{\infty}\Gamma(\tau)e^{i\omega\tau}d\tau. \tag{3.78}$$

From this result, we notice that the MSA will measure the autocorrelation function of the input signal, and so we must now insert the expression we derived for a realistic pulse train [Eq. (3.70)] into our autocorrelation function [Eq. (3.77)] which gives us

$$\begin{aligned}
\langle F(t)F(t+\tau)\rangle = \big\langle &\left\{F_0(t+\tau)\left[1+A(t+\tau)\right]+\dot{F}_0(t+\tau)TJ(t+\tau)\right\} \\
&\times \left\{F_0(t)\left[1+A(t)\right]+\dot{F}_0(t)TJ(t)\right\}\big\rangle.
\end{aligned} \tag{3.79}$$

In writing this equation, we have taken advantage of the fact that $F(t)$ is real and the complex conjugate operation has been dropped. Expanding this result leads to

$$\begin{aligned}\langle F(t)F(t+\tau)\rangle &= \langle F_0(t+\tau)F_0(t)\,[1+A(t+\tau)]\,[1+A(t)]\rangle \\ &+ \left\langle \dot{F}_0(t+\tau)\dot{F}_0(t)T^2J(t+\tau)J(t)\right\rangle \\ &+ \left\langle \dot{F}_0(t+\tau)F_0(t)TJ(t+\tau)\,[1+A(t)]\right\rangle \\ &+ \left\langle \dot{F}_0(t)F_0(t+\tau)TJ(t)\,[1+A(t+\tau)]\right\rangle. \end{aligned} \tag{3.80}$$

Because we are dealing with stationary random processes, we argue that we can discount the $J(t)(1+A(t+\tau))$ terms since they are uncorrelated. With this simplification, we obtain

$$\begin{aligned}\langle F(t)F(t+\tau)\rangle \simeq \langle & F_0(t+\tau)F_0(t)+F_0(t+\tau)F_0(t)A(t+\tau) \\ &+ F_0(t+\tau)F_0(t)A(t)+F_0(t+\tau)F_0(t)A(t+\tau)A(t)\rangle \\ &+ T^2\left\langle \dot{F}_0(t+\tau)\dot{F}_0(t)J(t+\tau)J(t)\right\rangle. \end{aligned} \tag{3.81}$$

Since F and A are also independent, this can be further simplified to:

$$\begin{aligned}\langle F(t)F(t+\tau)\rangle \simeq & \langle F_0(t+\tau)F_0(t)\rangle + \langle F_0(t+\tau)F_0(t)\rangle\langle A(t+\tau)\rangle \\ &+ \langle F_0(t+\tau)F_0(t)\rangle\langle A(t)\rangle + \langle F_0(t+\tau)F_0(t)\rangle\langle A(t+\tau)A(t)\rangle \\ &+ T^2\left\langle \dot{F}_0(t+\tau)\dot{F}_0(t)\right\rangle\langle J(t+\tau)J(t)\rangle. \end{aligned} \tag{3.82}$$

Moreover, since A is a random variable with zero mean, we can drop the second and third terms from the previous equation. We also define the following quantities:

$$G_A(\tau) = \langle A(t+\tau)A(t)\rangle, \tag{3.83}$$

$$G_{F_0}(\tau) = \langle F_0(t+\tau)F_0(t)\rangle, \tag{3.84}$$

$$G_{\dot{F}_0}(\tau) = \left\langle \dot{F}_0(t+\tau)\dot{F}_0(t)\right\rangle, \tag{3.85}$$

$$G_J(\tau) = \langle J(t+\tau)J(t)\rangle, \tag{3.86}$$

which allow us to write our non-ideal autocorrelation function more concisely as

$$\langle F(t)F(t+\tau)\rangle = G_{F_0}(\tau)\,[1+G_A(\tau)] + T^2G_{\dot{F}_0}(\tau)G_J(\tau). \tag{3.87}$$

Now using Eq. (3.78), we can write the power spectrum displayed by the spectrum analyzer

$$\begin{aligned}\frac{\tilde{S}(\omega)}{2\pi H(\omega)} &= \int_{-\infty}^{\infty} G_{F_0}(\tau)\left[1+G_A(\tau)\right]e^{i\omega\tau}d\tau + T^2\int_{-\infty}^{\infty} G_{\dot{F}_0}(\tau)G_J(\tau)e^{i\omega\tau}d\tau \\ &= \left[\int_{-\infty}^{\infty} G_{F_0}(\tau)e^{i\omega\tau}d\tau\right]\otimes\left[\int_{-\infty}^{\infty}\left[1+G_A(\tau)\right]e^{i\omega\tau}d\tau\right] \\ &+ T^2\left[\int_{-\infty}^{\infty} G_{\dot{F}_0}(\tau)e^{i\omega\tau}d\tau\right]\otimes\left[\int_{-\infty}^{\infty} G_J(\tau)e^{i\omega\tau}d\tau\right], \end{aligned} \tag{3.88}$$

where $\otimes$ denotes convolution.

We now define

$$\tilde{P}_{F_0}(\omega) = \int_{-\infty}^{\infty} G_{F_0}(\tau)e^{i\omega\tau}d\tau, \tag{3.89}$$

$$\tilde{P}_A(\omega) = \int_{-\infty}^{\infty} G_A(\tau)e^{i\omega\tau}d\tau, \tag{3.90}$$

$$\tilde{P}_{F_0}(w) = \int_{-\infty}^{\infty} G_{F_0}(\tau)e^{i\omega\tau}d\tau, \tag{3.91}$$

$$\begin{aligned}\tilde{P}_{\dot{F}_0}(\omega) &= \int_{-\infty}^{\infty} G_{\dot{F}_0}(\tau)e^{i\omega\tau}d\tau \\ &= \int_{-\infty}^{\infty}\frac{\partial^2}{\partial\tau^2}G_{F_0}(\tau)e^{i\omega\tau}d\tau = \omega^2 P_{F_0}(\omega),\end{aligned} \tag{3.92}$$

$$\tilde{P}_J(w) = \int_{-\infty}^{\infty} G_J(\tau)e^{i\omega\tau}d\tau, \tag{3.93}$$

which allows us to concisely write the expected power spectrum of a pulse train in the form

$$\frac{\tilde{S}(\omega)}{2\pi H(\omega)} = \tilde{P}_{F_0}(\omega)\otimes\left[\delta(\omega)+\tilde{P}_A(\omega)\right] + \left[(\omega T)^2\tilde{P}_{F_0}(\omega)\right]\otimes\tilde{P}_J(\omega). \tag{3.94}$$

Although this is the microwave spectrum we expect to see due to a realistic pulse train, we are interested in characterizing the amplitude and jitter fluctuations in the pulse train. In order to determine these values, we must first compare the spectrum we observe to an ideal spectrum; one devoid of either amplitude or jitter fluctuations.

By substituting an ideal finite pulse train into Eq. (3.73), we arrive at

$$\begin{aligned}\tilde{F}(\omega,\Delta) &= \int_{-\infty}^{\infty}\sum_{n=-N}^{N} F(t+nT)e^{i\omega t}dt \\ &= \int_{-\infty}^{\infty} F(\tau)\sum_{n=-N}^{N} e^{-i\omega nT}e^{i\omega\tau}d\tau \\ &= \int_{-\infty}^{\infty} F(\tau)\frac{\sin[(2N+1)\omega T]}{\sin(\omega T)}e^{i\omega\tau}d\tau \\ &= \tilde{F}(\omega)\frac{\sin[(2N+1)\omega T/2]}{\sin(\omega T/2)},\end{aligned} \tag{3.95}$$

where we have taken advantage of the fact that the sum introduces the ultimate limit on the extent of the the signal and could therefore extend the limits of the integral to infinity. This approach, used by von der Linde,[97] seeks to avoid issues involving Dirac delta functions that otherwise crop up. Focusing on pulse trains generated by mode-locked lasers, we find that the spectral width of the individual pulses is given by $\Omega_{FWHM} = \frac{4\ln(\sqrt{2}\pm1)}{\pi T_0}$ (in the case of hyperbolic-secant pulses, see Appendix A). Now if we assume that the pulse width is $T_0 \leq 1$ ps in duration, we find that $\Omega_{FWHM} \geq$ 1.12 THz. Since cutting-edge MSA have bandwidths $\leq$ 80 GHz, we can, to a good approximation, perform the Fourier transform and then move the $\tilde{F}(w)$ out of the sum by first introducing $\tau = t+nT$, $d\tau = dt$. We also used the relation[109]

$$\sum_{n=-N}^{N} e^{-i\omega nT} = \frac{\sin[(2N+1)\omega T/2]}{\sin(\omega T/2)}. \tag{3.96}$$

By substituting our Eq. (3.95) into Eq. (3.72) and using the relation

$$\lim_{N\to\infty}\frac{1}{2N+1}\left(\frac{\sin[(2\Delta+1)\omega T/2]}{\sin(\omega T/2)}\right)^2 = \frac{2\pi}{T}\sum_{k=-\infty}^{\infty}\delta\left(\omega-\frac{2\pi k}{T}\right), \tag{3.97}$$

we obtain the response to an ideal pulse train

$$\begin{aligned}\tilde{P}_{F_0}(\omega) &= \lim_{N\to\infty}\frac{1}{(2N+1)T}|\tilde{F}(\omega)|^2\left(\frac{\sin[(2N+1)\omega T/2]}{\sin(\omega T/2)}\right)^2 \\ &= \frac{2\pi}{T^2}\left|\tilde{F}(\omega)\right|^2\sum_{k=-\infty}^{\infty}\delta\left(\omega-\frac{2\pi k}{T}\right),\end{aligned} \tag{3.98}$$

where we changed the limit variable from Δ to $(2N+1)T$; the extra T is required to maintain the proper units.

Now defining $\omega_k = w - \frac{2\pi k}{T}$ and inserting the above result into the power spectrum of a realistic laser with both amplitude and timing fluctuations [given by Eq. (3.66)], we find[**]

$$\tilde{S}(\omega) \approx \left(\frac{2\pi}{T}\right)^2 H(\omega)\left|\tilde{F}(\omega)\right|^2 \left[\sum_{k=-\infty}^{\infty} \delta(w_k) \otimes \delta(\omega) + \sum_{k=-\infty}^{\infty} \delta(\omega_k) \otimes P_A(\omega) + (\omega T)^2 \sum_{k=-\infty}^{\infty} \delta(\omega_k) \otimes P_J(\omega)\right]. \quad (3.99)$$

Performing the convolution integrals above gives our final result

$$\tilde{S}(\omega) \approx \left(\frac{2\pi}{T}\right)^2 H(\omega)\left|\tilde{F}(\omega)\right|^2 \sum_{k=-\infty}^{\infty} \left[\delta(\omega_k) + P_A(\omega_k) + (2\pi k)^2 P_J(\omega_k)\right], \quad (3.100)$$

where we pulled the $|\tilde{F}(\omega)|^2$ term out of the convolution integrals by assuming it is slowly varying.

3.4.2 Experimental Considerations

Now that we have derived the response of a MSA to a realistic pulse train containing both amplitude fluctuations and timing jitter, we explain how to quantify the fluctuations experimentally.

We first point out that the energy fluctuations (related to the amplitude fluctuations by a scale factor assuming the pulse shape is constant) are given by

$$\Delta E^2 = E^2 \int_{-\infty}^{\infty} P_A(\omega) d\omega, \quad (3.101)$$

[**]Comparing this result with Eq. (13) in Ref. 97, we see that there is a discrepancy of 2π, which is most likely due to a typo in that paper. Note that we have included detector/MSA filtering which adds a multiplicative $2\pi H(\omega)$ to our result; by substituting Eq. (13) into Eq. (8) of Ref. 97, this result could also be obtained (although it would still be off by 2π).

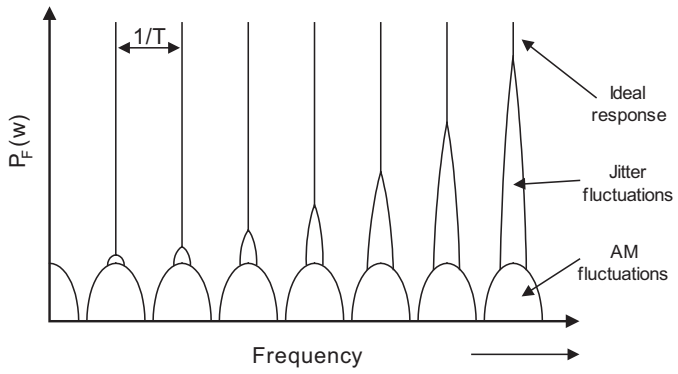

Figure 3.8: This cartoon provides a graphic depiction of the behavior of the higher harmonics of the pulse-train power spectrum as predicted by Eq. (3.100)

where E is the average pulse energy. In a similar fashion, the jitter fluctuations are given by

$$\Delta T^2 = T^2 \int_{-\infty}^{\infty} P_J(\omega) d\omega. \tag{3.102}$$

Using Eqs. (3.100)–(3.102) and a spectrum analyzer, we were able to use the pulse train power spectrum to characterize the rms energy fluctuations and the rms timing jitter of a pulse train emitted by a mode-locked laser.

Looking at Eq. (3.100), we note that losses arising from the detector's responsivity or any other static sources can easily be incorporated into $H(\omega)$. We also expand ω_k and re-state our result as

$$P_F(w) = \left(\frac{2\pi}{T}\right)^2 H(\omega)\left|\tilde{F}(\omega)\right|^2 \sum_{k=-\infty}^{\infty}\left[\delta\left(w-\frac{2\pi k}{T}\right)+P_A\left(w-\frac{2\pi k}{T}\right)\right.$$
$$\left.+\,(2\pi k)^2 P_J\left(\omega-\frac{2\pi k}{T}\right)\right]. \tag{3.103}$$

We first point out that the $k=0$ term is devoid of jitter content since the P_J term drops out of P_F when $k=0$ giving us

$$P_F(w,k=0) = \left(\frac{2\pi}{T}\right)^2 H(\omega)\left|\tilde{F}(w)\right|^2 [\delta(\omega)+P_A(\omega)]. \tag{3.104}$$

As shown in Eq. (3.100), the area under the $P_A(w)$ curve is related to the energy fluctuations. From Eq. (3.100) and the above result, we can see how we would experimentally

perform this operation. By converting our result centered on $\omega = 0$ to units of decibels below carrier (dBc) removes the constant coefficient and leaves us with:

$$L_F(\omega) \equiv \delta(\omega) + P_A(\omega). \tag{3.105}$$

In other words, only the ideal delta function response and the response due to the AM fluctuations is present. Because the delta function has a very well defined structure, we can easily subtract it out from the spectrum and we are left only with $P_A(\omega)$.

Of course, by subjecting MSAs to dc voltages, the mixer on the input of these devices may be damaged or blown out and so this should be avoided. Fortunately, by looking at higher harmonics, it is possible to determine the AM fluctuations and remove them since they are always constant. This leaves the term governing the pulse jitter, $P_J(w)$, which grows with harmonic number quadratically, as depicted in Fig. 3.9. When comparing data from higher harmonics, it is important that the different harmonics are compared correctly. Filtering, due to the finite response of the detector or MSA $[H(\omega)]$ or due to the finite spectrum of the optical pulse $|F(\omega)|^2$, is important to include when comparing different harmonic components.

By assuming the spectrum to be symmetric about any harmonic of the carrier frequency, all that is needed to determine the timing jitter is to compute a single-sided integral . This assumption is valid for passively mode-locked lasers; however, the spectrum will become asymmetric in actively mode-locked lasers if the modulation frequency is not properly matched with the cavity length. The reason this approach is chosen in practice is that by integrating from $\varepsilon > 0$ we remove the delta function from the data in a simple-minded fashion. In the following discussion we convert to units of frequency, where we are using $P_F(f)$ (in Watts over a 1 Hz resolution bandwidth) so that

$$\Delta T_{rms} = \frac{1}{2\pi f_k}\left[2\int_{\varepsilon}^{\infty} 10^{P_F(f)/10} df - 2\int_{\varepsilon}^{\infty} 10^{P_A(f)/10} df\right]^{1/2}. \tag{3.106}$$

Figure 3.9 explains the issues that come up experimentally when trying to figure out the different P's. Both parts in this figure are supposed to depict the same spectral

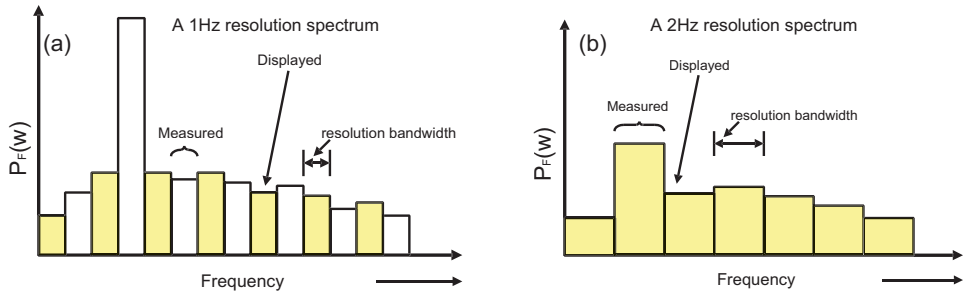

Figure 3.9: (a) This figure depicts the case where our spectrum analyzer has been set to a 1 Hz resolution bandwidth, but we are only able to display and/or save every other point within that region due to the finite number of points displayed by the device. (b) This figure shows the issues that arise when one does not use a 1 Hz resolution bandwidth. In this case, we must account for our larger bandwidth; otherwise we would be overestimating the result of the integral.

window of interest. In this case we are assuming we are only able to use 7 points to acquire data over this frequency range for displaying.

Of course, when we integrate the spectral density we must account for the resolution of the device. The measurements should be made using a 1 Hz resolution bandwidth. Finally, it is important to verify that one is measuring the signal and not the noise floor of the spectrum analyzer. This issue will be addressed in the following section where it interferes with our measurements.

3.4.3 Considerations for Harmonic Mode Locking

When a laser is harmonically mode locked, using either an AM or FM modulator, any difference between the pulses simultaneously circulating in the laser cavity will manifest itself as so-called supermode noise. Physically, a pulse-to-pulse fluctuation within a harmonically mode-locked pulse train will result in a non-zero signal at various integer multiples of the laser's fundamental repetition rate. In our FM mode-locked laser the supermode noise was found to be 72 dB below our peak value (see the contribution at 36.6 MHz in Fig. 2.12). Of course if one were to look at any other integer multiple

of the fundamental repetition rate a similar structure would be found.

The supermode noise causes a deterioration in the quality of the pulse train. If one is able to perform a jitter characterization from the mode-locked repetition rate (10.3 GHz in our laser) up to its second harmonic (20.6 GHz) then the jitter can be fully determined. However, it is often feasible to perform a partial characterization only; in which case these noise sources may not included in the measurement. This limitation is frequently encountered due to bandwidth issues or issues related to the noise floor of the microwave spectrum analyzer, as was our case. Nevertheless, it is possible to include the effects of the supermode noise in an approximate fashion by assuming that each supermode noise peak contributes the same quantity of noise.[96] In this case, the noise we expect is that found using the above mentioned technique over a bandwidth of the laser's fundamental repetition rate multiplied by the square root of the harmonic number. This is best written in the following approximate form:

$$\Delta T_{rms} = \frac{1}{\pi f_k}\left[\int_{\varepsilon}^{F_{rep}} 10^{P(f)/10} df\right]^{1/2} \approx \frac{\sqrt{n}}{\pi f_k}\left[\int_{\varepsilon}^{F_0} 10^{P(f)/10} df\right]^{1/2}, \quad (3.107)$$

where n is the number of pulses simultaneously circulating in the laser cavity, F_{rep} is the repetition rate the laser is mode locked at, F_0 is the fundamental repetition rate, and $P(f)$ is the the power spectrum detuned from the carrier in units of dBc/Hz. Furthermore, we point out that the relationship $F_{rep} = nF_0$ always holds for harmonic mode locking. If our data is examined using this fact our jitter values are immediately increased by a factor of $\sqrt{10.3\,GHz/36.6\,MHz} = 16.76$. This places the RMS jitter around 6.4 ps; however, this treatment is predicated on the fact that all the noise in the laser is correlated which is not always the case and our value could be better or worse than this number. Moreover, by using an intracavity Fabry–Perot etalon the supermode noise could be suppressed for jitter critical applications.

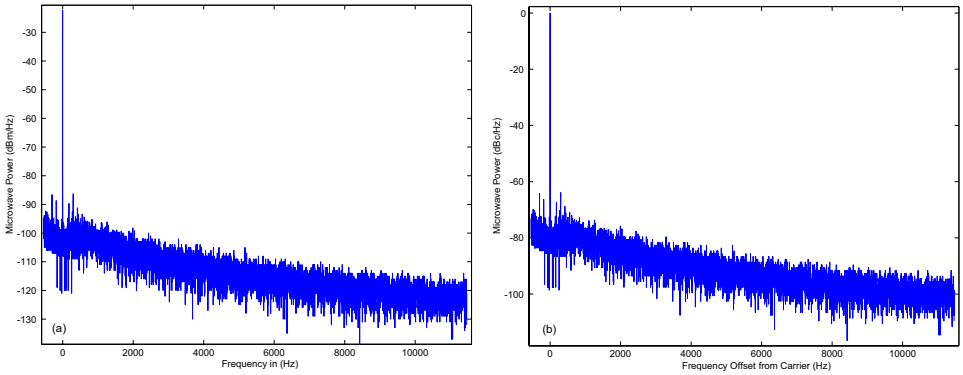

Figure 3.10: (a) Raw data spectrum seen on the spectrum analyzer. (b) Identical spectrum to (a) except it has been converted to units of dBc/Hz. Note the only difference is the offset has been removed and the carrier frequency has been changed to offset from carrier frequency.

3.4.4 Example of Jitter Measurements

To complete this discussion, we apply this technique to a set of acquired data. Figure 3.10 shows a microwave spectrum obtained from a MSA for the 10.3 GHz FM mode-locked laser of Section 2.1.2. In this case, the two parts show the dc part of the spectrum, i.e. the spectrum centered about 0 Hz.[††]

As described above, the δ response is "removed" by moving our window of integration slightly to the right side of it. Since our rms energy fluctuations are 16.201 fJ and we have a pulse energy of 2 pJ, we find that this corresponds to a fluctuation of 0.81%

Now we look at the spectrum centered on the carrier frequency of 10.3 GHz so that we can determine the timing jitter. As we did above, we convert the plot into units of dBc/Hz with respect to the offset from the 10.3 GHz carrier frequency. By integrating over the spectrum obtained, we find the noise due to timing jitter and amplitude fluctuations. To accurately quantify the timing jitter, we need only subtract out the contribution due to AM fluctuations. Had we not removed the AM contribution, our

[††]Generally this is a bad idea due to the input mixer, however the pulse train from this laser was very weak and (fortunately) the spectrum analyzer was not damaged.

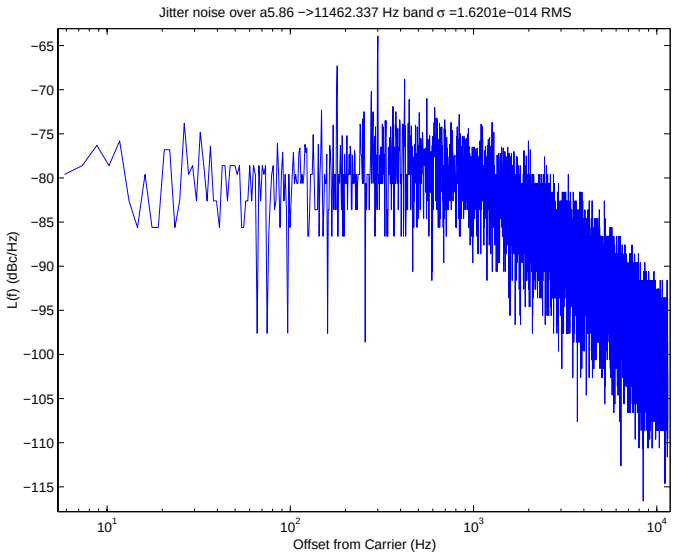

Figure 3.11: A plot of the spectral side band obtained in the above figures. Performing the integral we find that the rms energy fluctuations are 16.201 fJ for our 2 pJ pulse.

value would be artificially inflated and represent only an upper bound on timing jitter. Ideally the measurements should be performed on a higher harmonic where the jitter noise dominates. However, our spectrum analyzer had a 3 dB bandwidth of 26.5 GHz only allowing access to the fundamental and its first harmonic.

Characterizing the jitter using the harmonic at 20.6 GHz gives us rms jitters of 523 fs and 423 fs. The discrepancy between the two is most likely due to a slightly flawed value for the amplitude fluctuations or the combined filtering responses of the spectrum analyzer and the high-speed detector used.

One crucial thing that we have not yet commented on is the spectrum analyzer's finite noise floor. This can be done in a simple-minded fashion by interrogating the MSA's response to its local oscillator and viewing this spectrum superimposed with the spectrum due to one of the harmonics of the pulse train. Figure 3.12 shows that the fluctuations we are measuring are partially due to the MSA's own noise! This is particularly the case for the 10.3 GHz mode. In fact, these plots show us that our measurement at 20 GHz is actually more accurate since it is not as influenced by the fluctuations

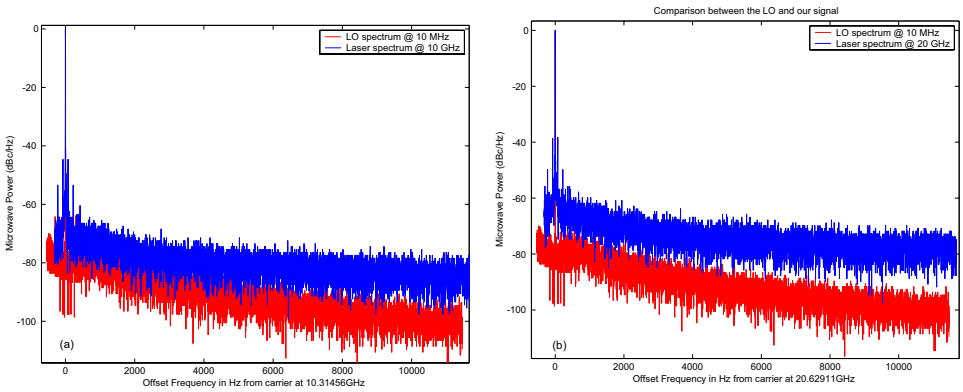

Figure 3.12: Comparison between the noise floor of the spectrum analyzer and our pulse train centered on (a) 10.3GHz and (b) 20.6GHz.

inherent in the spectrum analyzer. This provides a third, and likely more realistic, reason for the discrepancy between the rms jitter values (523 and 423 fs) found at the two frequencies above.

Finally, we should also characterize the noise of the driving electronics since it will provide a lower limit for the pulse train. This was done by using the output of our microwave frequency synthesizer as the input into the MSA. Figure 3.13 shows the spectrum synthesized signal generator used to drive the FM modulator in the laser. Clearly the driving electronic signal is not ideal; strong signals at $\sim$ 75 Hz and $\sim$ 221 Hz are visible. By performing a jitter characterization on this signal, we find that it corresponds to 395 fs of rms jitter.

Synthesizing the above results, we find that the majority of the jitter in this case is due to the electronics and not the laser. We also find that the AM side bands (seen looking at our mode-locked pulse train, see Fig. 3.10) come from the electronics and not the laser. In order to estimate the laser's jitter we assume that the laser jitter and the electronics jitter are uncorrelated, and then subtract the two to find

$$\sigma_{\text{laser}} = \sqrt{\sigma^2_{\text{system}} - \sigma^2_{\text{Electronics}}} = \sqrt{(423)^2 - (397)^2} = 146\text{fs}. \qquad (3.108)$$

Of course one should not place too much confidence in this result since we have seen that the spectrum analyzer is not operating ideally for the data we are acquiring. We

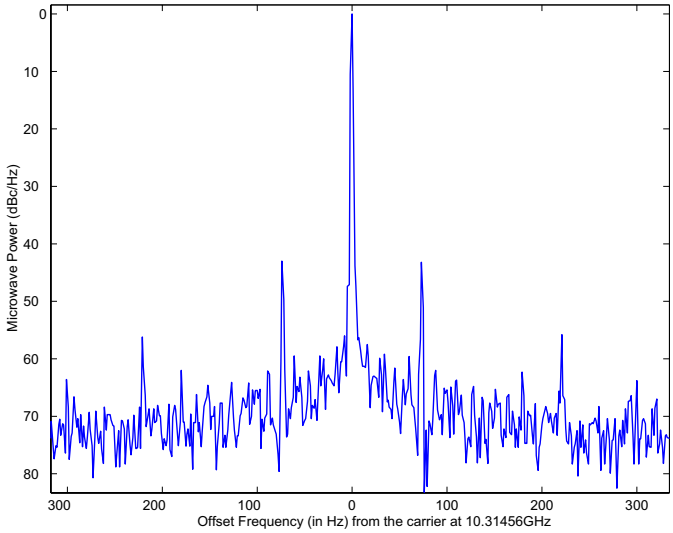

Figure 3.13: Spectrum of the synthesized signal generator used to drive the FM modulator in the laser.

can be confident, however, that we have found an upper limit on the jitter.

Finally, we point out that this technique is best suited for pulse trains with repetition rates < 5 GHz since they will provide access to multiple harmonics on the MSA and amplitude fluctuations and timing jitter can be separated accurately. Since our laser was mode locked at 10.3 GHz, we had access only to the fundamental peak and the first harmonic peak (located at 20.6 GHz). This did not affect the determination of the total RMS noise, but instead reduced the accuracy with which we could determine the constituent amplitude and jitter components.

3.5 Dispersion Measurements

In this section we describe the conventional techniques used for measuring dispersion in an optical fiber. Because mode-locked lasers generally have cavity lengths between 1–20 m, we will focus on characterizing fibers of similar lengths. We first point out that traditional time-of-flight characterization approaches, where an optical pulse source

has its carrier wavelength changed and a high-speed detector detects the pulses and the change in their arrival times, fail. For short pieces of fiber (glass, etc.), the delay between different wavelengths is on the order of a few femtoseconds or picoseconds, neither of which can be detected reliably using electronics. It is, however, possible to still perform a modified time-of-flight characterization by using a pulse source with an adjustable wavelength inside an autocorrelator.[110] By performing autocorrelation where one arm of the autocorrelator contains the material/fiber under test and the carrier wavelength of the source is changed, there will be a temporal shift in the autocorrelation. This can be directly used to determine the dispersion of the fiber.[110]

Still, a better approach is to use white-light interferometry.[111] In this scheme, a broadband source is used in conjunction with an interferometer and an OSA. One advantage of this approach is that it requires a broadband source as opposed to a pulse source (or modulated source) with an adjustable wavelength. Additionally, since white-light interferometry is very sensitive, it also allows for very accurate characterization, not to mention that it is easy to perform experimentally. Finally, by using a technique that relates time-of-flight to frequency shift inside a laser cavity, the dispersion of a mode-locked laser can be measured.[92] The advantage of this approach is that it is able to determine the dispersion in the laser as it is running; however, it is limited in that it only works in passively mode-locked lasers that incorporate grating- or prism-pairs.

3.5.1 In-Situ Technique

By inserting a razor blade into a passively mode-locked laser after a grating- or prism-pair, the operating wavelength of the laser may be tuned. However, because of dispersion, the laser cavity has different round-trip times at different wavelengths, and we expect to find slightly different repetition rates at different carrier frequencies. By noting the optical carrier frequency (using an OSA) and the repetition rate (using a spectrum analyzer), Knox was able to demonstrate that the cavity dispersion could be

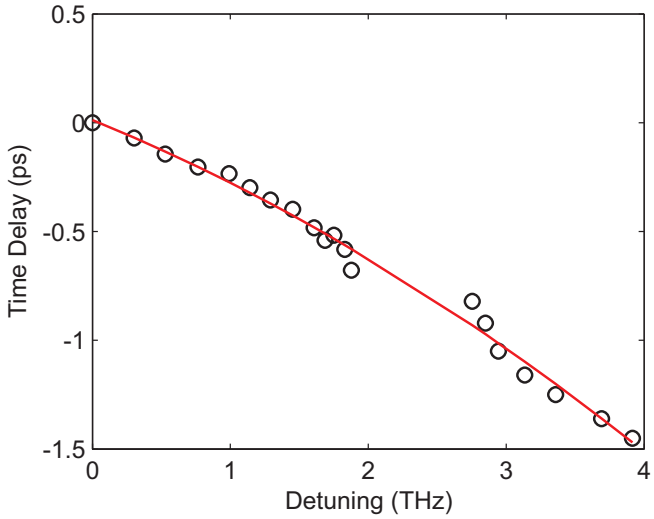

Figure 3.14: Time delay verses detuning $(\omega - \omega_0)$ for our FM mode-locked laser. The discrete markers represent the data points while the solid line is a fit.

found in a running laser.[92,93] By mode locking the laser of Section 2.1.2 with a SESAM and tuning the carrier frequency using a razor blade, the temporal delay versus detuning was plotted in Fig. 3.14.

Using the fit in Fig. 3.14, the dispersion of this cavity may be determined. Since the data exhibited a gap around the normal operating point, this measurement was repeated, and after averaging the results, we obtained the values used in our numerical and theoretical work of $\beta_2 = -6.3 \times 10^4$ fs^2 and $\beta_3 = 130.6 \times 10^4$ fs^3.

The mathematical explanation for this technique simply involves noting that the fundamental repetition rate of a Fabry–Perot mode-locked laser can be written as

$$\nu(\omega) = c\,[2(L-l) + 2ln(\omega)]^{-1}, \tag{3.109}$$

where the total (physical) cavity length is given by L and the length of the dispersive element with refractive index $n(\omega)$ is l.

We can write the round-trip group delay by taking the frequency derivative of the round-trip phase acquired by the pulse $[\omega/\nu(\omega)]$. This gives the result

$$T(\omega) = \frac{2(L-l)}{c} + 2l\frac{\partial}{\partial w}\left[\frac{n(\omega)\omega}{c}\right]. \tag{3.110}$$

Therefore, if we plot the changes in round-trip time with respect to the detuning between the carrier frequency and the frequency which we are expanding about we can determine the dispersion about a given frequency by fitting the curves with polynomials. This is facilitated by noting that we can write the changes in round-trip time by using the experimentally obtained repetition rate to write $\Delta T = \Delta\nu/\nu_0^2$. The phase acquired while propagating through a dispersive media may also be written as $\beta(\omega)l$ if we Taylor expand it about ω_0, which gives

$$l\beta(\omega) = l\sum_{n=0}^{\infty}\frac{\beta_n}{n!}(\omega-\omega_0)^n. \tag{3.111}$$

As a result, we can fit our data with its derivative, i.e.

$$l\sum_{n=0}^{\infty}\frac{\beta_{n+1}}{n!}(\omega-\omega_0)^n. \tag{3.112}$$

Using this approach, we can easily determine the dispersion in a passively mode-locked laser. In our example, we were only able to keep the laser mode locked (without adjusting cavity elements) within a small frequency range on either side of the normal carrier frequency. This limited the accuracy of this approach as can be seen by the fit in Fig. 3.14. This also limits the accuracy with which higher-order dispersion terms may be determined. For example, using this technique in our laser we found that our value of β_2 was fairly reproducible over multiple measurements whereas β_3 fluctuated considerably.

3.5.2 White-Light Interferometry

White-light interferometry provides another simple way to measure the dispersion of various cavity elements, albeit in their cold state; in other words, not while the laser is mode locked.[111–114] By constructing an interferometer, placing an element whose dispersion we wish to characterize in one of the arms, and exciting the device with a broad-

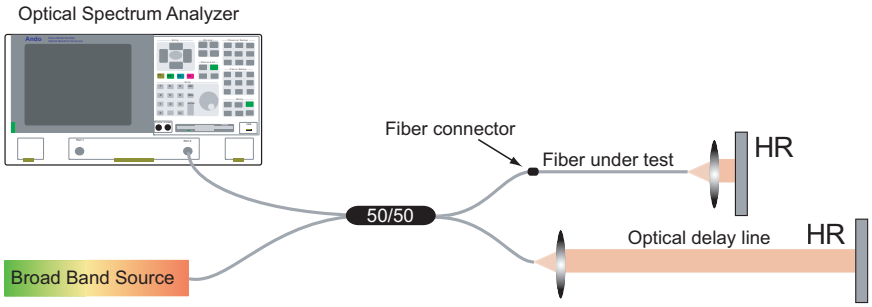

Figure 3.15: Experimental setup required to measure the dispersion of a fiber using white-light interferometry.

band optical source, the dispersion may be characterized accurately (See Fig. 3.15). Consider the effect in the frequency domain where we measure

$$I(\omega) = |a_{\text{ref}} A(\omega) e^{\beta_{\text{ref}}(\omega) d} + a_{\text{test}} A(\omega) e^{\beta_{\text{test}}(\omega) L}|^2. \tag{3.113}$$

In this equation, $\beta_{\text{ref}}(\omega)$ is the frequency-dependent propagation constant in the reference arm of length d, β_{test} is the frequency dependent propagation constant in the arm containing the element under test, and L is the physical length of the device under test.[‡‡] Assuming the power in the two arms has been equalized, an experimental requirement of this technique which may easily be achieved using a power meter, $a_0 = a_{\text{reference}} = a_{\text{test}}$, our result can be written as

$$I(\omega) = \alpha |A(\omega)|^2 \{1 - \cos[\phi(\omega)]\}, \tag{3.114}$$

where $\phi(\omega) = \beta_{\text{ref}}(\omega) d - \beta_{\text{test}}(\omega) L$, and α accounts for any loss in the device.

In order to determine the conventionally used dispersion parameters, we expand $\phi(\omega)$ in a Taylor series around the frequency of interest (in this case ω_0) to obtain

$$\phi(\omega) = L \sum_{n=0}^{\infty} \frac{\beta_n}{n!} (\omega - \omega_0)^n - \frac{d}{c}(\omega - \omega_0). \tag{3.115}$$

[‡‡]When using a Mach–Zehnder interferometer, the lengths d and L are the physical lengths of the two arms; however, when a Michelson interferometer is used, these lengths become twice the physical length of the elements due to the double-pass architecture of that interferometer.

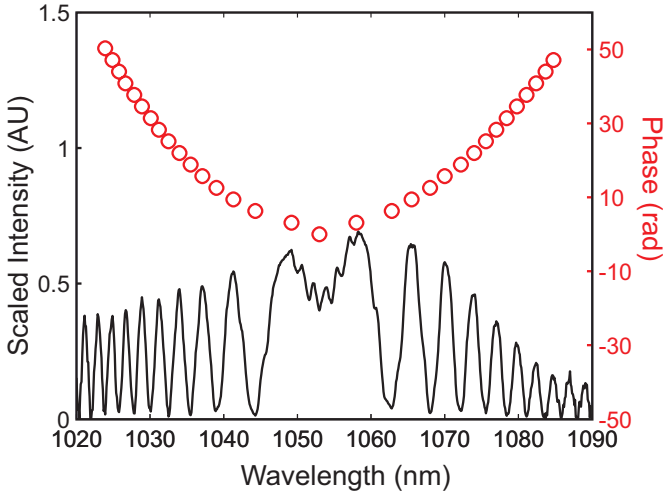

Figure 3.16: Normalized optical spectrum measured from the output of the interferometer when a superluminescent light emitting diode (SLED) was used as the white-light source.

Experimentally, the length of the reference arm can be adjusted until the zeroth-order fringe (or the "missing minimum" shown in Fig. 3.16 at λ = 1053 nm) is located at the wavelength we wish to expand about; this is depicted in Fig. 3.16. It is then easy to determine $\phi(\omega)$ by finding the spectral locations of the maxima and minima from the data, noting that the maxima occur when $\phi(\omega) = (2N+1)\pi$ and the minima occur when $\phi(\omega) = 2N\pi$. One can then fit $\phi(\omega)$ using a polynomial and Eq. (3.115) to obtain the dispersion coefficients. In this case, a ~ 0.5 m section of Lucent 980 fiber was found to have the following values: $\beta_2 = 3.8 \times 10^4$ fs^2/m, $\beta_3 = 11.3 \times 10^4$ fs^3/m, and $\beta_4 = 2.2 \times 10^6$ fs^4/m.

This technique, however, still warrants a few words on accuracy. By performing the characterization shown above, we are able to determine the values of the lower-order dispersion term (β_2) quite accurately. Of course, β_0 depends on the length of the two arms and is not of practical use, and β_1 is essentially cancelled out by centering the zeroth-order fringe at the frequency we have expanded about. In fact, by calibrating this device (using it without a test piece to determine any inherent dispersion in the device), the second-order dispersion coefficient of a fiber under test can be determined

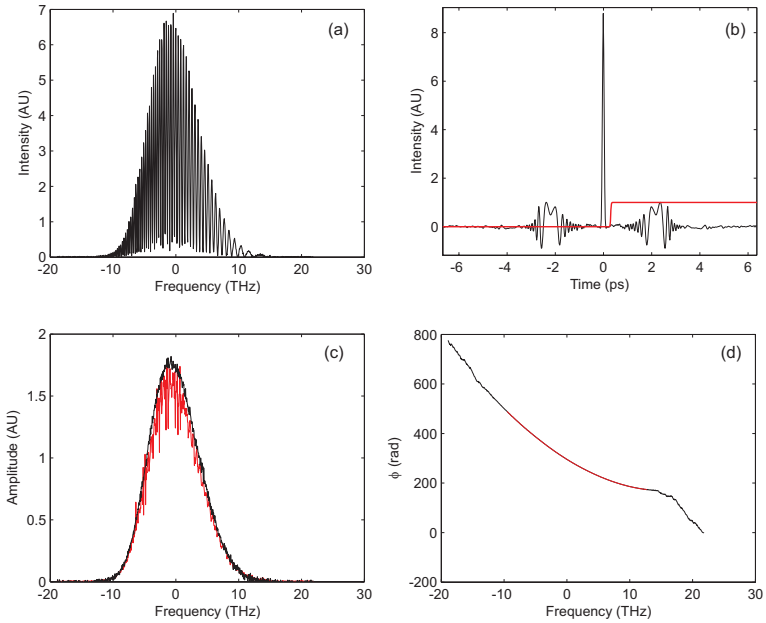

Figure 3.17: Normalized optical spectrum measured from the output of the interferometer where a superluminescent light emitting diode (SLED) was used as the white-light source.

to within a few fs^2/m.*

It should be noted that the accuracy with which we can determine the higher-order dispersion terms suffers if our source spectrum is not wide enough to allow these terms to adequately manifest themselves. Moreover, the determination of the maximum and minimum points is somewhat tedious and it discards the majority of the data points. In addition, unless a fitting method is used to locate the maxima/minima, the results can vary over different realizations even if the same data is used. A more sophisticated way to determine the spectral phase, which allows one to overcome some of these limitations, can be implemented by using Fourier-transform spectral interferometry.[115] This approach, which is also used in electric field reconstruction schemes,[116] involves Fourier transforming the spectrum, filtering it, and then transforming back to the frequency domain where the phase can easily be found by looking at the imaginary part

*The accuracy of this approach is ultimately limited by the bandwidth of the broad band source, the resolution of the OSA and how well it is calibrated, and how well the minima and maxima can be located.

of the result. Figure 3.17 demonstrates the application of this approach to the characterization of the same $\sim$0.5 m section of Lucent 980 fiber. To perform the filtering necessary, the information in the (pseudo) time domain needs to be separable from the dc term located at the origin. By changing the delay in the reference arm, the fringe period can be decreased in the spectral domain which avoids aliasing in the (pseudo) time domain. For example, Fig. 3.17(a) shows that the zeroth-order fringe has been shifted to the higher frequency (lower wavelength) side of the spectrum. This requirement has a deleterious effect which ultimately limits the utility of this method and will be discussed later in this section.

The real part of the time-domain signal is shown in Fig. 3.17(b) (black) along with the filter (red) used to select one side lobe. Fig. 3.17(c) shows the reconstructed spectrum (red) along with the experimental spectrum in one of the arms of the source (black). Although the numerical results display noise, the reconstructed spectrum agrees well with the input spectrum, especially when one notes that no scaling was used to obtain this fit; this gives us a degree of confidence in our results. Fig. 3.17(d) shows the reconstructed phase (black) as well as a region where the phase was fit to obtain the dispersion values $\beta_2 = (2.57 \pm 0.043) \times 10^4$ fs^2/m, $\beta_3 = (6.7 \pm 3.2) \times 10^4$ fs^3/m, and $\beta_4 = (0.85 \pm 20) \times 10^6$ fs^4/m. The fit was restricted to frequencies where the spectrum had non-negligible values to avoid computational artifacts. One of the advantages of this approach is that it is highly repeatable, yielding similar values (within $\sim$2%) for slightly different delays and data sets, whereas the manual approach is more susceptible to variation since the location of each fringe minimum and maximum needs to be determined. To quantify this claim, we were able to obtain β_2 with a standard deviation of $\leq$2% over the 10 spectra we recorded with different free-space lengths in the reference arm.

This approach is predicated on the assumption that aliasing does not occur in the time domain so that the filtering can be properly applied. Practically, this means that this approach cannot be used on data where the zeroth-order fringe exists, since it re-

sults in a large low-frequency term which causes aliasing; therefore, it limits the accuracy of our filtering. Additionally, by introducing a large delay into one arm (such that the zeroth-order fringe is pushed far away from the dc term), the spectrum will be modulated by a higher-frequency phase. Because of the limited resolution of the OSA, this will introduce error. Of course the best solution is a compromise in which the zeroth-order fringe is shifted to the wings of the spectrum where the power is low. It was found that good results could be achieved by placing the zero-order fringe $>$ 20-30 dBm below the peak value. This allows for acceptable filtering while not running into resolution issues. A convenient "rule of thumb," found to work well, is to satisfy the relation

$$\text{fringes}/\text{nm} = \frac{\text{Number of elements}}{12 * \text{window size } (\text{nm})}, \tag{3.116}$$

where fringes/nm refers to the number of fringe maxima or minima one finds within a nanometer window, number of elements is the number N of data points saved for a given measurement, and window size is the spectral width of the window on the OSA, i.e., $\lambda(N) - \lambda(1)$. Nevertheless, as the fringe period is decreased to avoid aliasing, not only do the resolution limitations of the OSA come into play, but we are also essentially shifting the minimum of our spectral phase away from the wavelength of interest. This has the unfortunate consequence that the phase term $\phi(\omega)$ gets dominated by β_1. Finally, when using either of these techniques, the length of the device under test needs to be long enough that an adequate number of fringes can be observed $\gtrsim 40$. When using the Fourier-transform spectral interferometry approach in conjunction with ultra broad-band sources ($>$ 200 nm), the limited resolution of the OSA requires that the fiber under test has a small value of $\beta_2 L$ such that when the zero-order fringe is moved out of the window the individual fringes can be accurately sampled by $\sim$ 10 points or more. Unfortunately, by decreasing the length of the device under test, the requirements on the characterization of the interferometer and the actual length of the device become more stringent to achieve results with comparable accuracy.

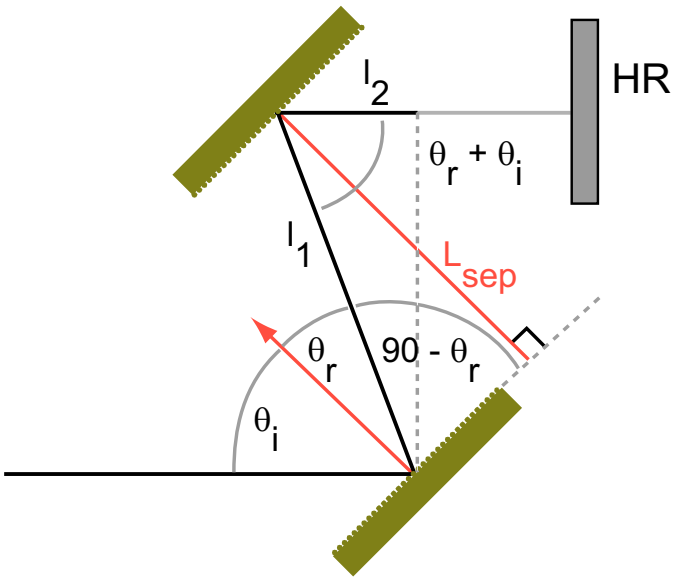

Figure 3.18: Geometrical layout for a dispersion-compensating, intra-cavity, grating pair. The angles defined in this figure are assumed to be in degrees. The red lines are defined as being normal to the respective grating surfaces.

3.5.3 Grating Pairs

In this work, we used an intra-cavity grating pair to compensate the second-order dispersion due to the optical fiber and the various bulk components in the FM mode-locked fiber laser of section 2.1.2. In order to determine the best grating-pair separation, one should have an idea for how much dispersion it will introduce into the cavity. Furthermore, grating pairs introduce additive third-order dispersion, which can limit pulse widths and create large pedestals in the time domain.[37]

In order to get an quantitative idea for how much dispersion a grating pair should introduce, we must draw the geometry of the double-pass grating pair used in our work in order to define some geometrical distances and angles.

Using Fig. 3.18 and basic geometry we obtain

$$\cos(\theta_r + \theta_i) = \frac{l_2}{l_1} \tag{3.117}$$

and

$$\sin(90-\theta_r)=\cos(\theta_r)=\frac{L_{\text{sep}}}{l_1}. \tag{3.118}$$

Using Eq. (3.117) we can write the total length travelled by a given frequency component

$$l(\omega)=l_1+l_2=l_1\left[1+\cos(\theta_r+\theta_i)\right], \tag{3.119}$$

which can be put in the more useful form

$$l(\omega)=\mathrm{L_{sep}}\mathrm{sech}(\theta_\mathrm{r})\left[1+\cos(\theta_\mathrm{r}+\theta_\mathrm{i})\right] \tag{3.120}$$

by using Eq. (3.118).

Since the optical path difference is given by $l(\omega)/c$, we find that

$$\phi_1 \triangleq \frac{d\phi}{d\omega}=\frac{\mathrm{L_{sep}}}{c}\mathrm{sech}(\theta_r)\left[1+\cos(\theta_r+\theta_i)\right]. \tag{3.121}$$

What we are really interested in are the coefficients of the higher-order terms, which we obtain by Taylor expanding the propagation constant

$$\phi(\omega)\approx\phi_0+\phi_1(\omega-\omega_0)+\frac{1}{2!}\phi_2(\omega-\omega_0)^2+\frac{1}{3!}\phi_3(\omega-\omega_0)^3+\cdots. \tag{3.122}$$

Therefore, to obtain the expected value for ϕ_2, we need only differentiate Eq. (3.122) once with respect to ω, i.e.

$$\phi_2=\left.\frac{d^2\phi}{d\omega^2}\right|_{\omega_0}=\left.\frac{d\phi_1}{d\omega}\right|_{\omega_0}=\frac{\mathrm{L_{sep}}}{c}\frac{d}{d\omega}\left\{\mathrm{sech}(\theta_r)\left[1+\cos(\theta_r+\theta_i)\right]\right\}_{\omega_0}. \tag{3.123}$$

However, in order to continue, we must remove all of the θ_r terms from our equation since θ_r is actually a function of ω. To do this, we now introduce the so-called grating equation

$$\sin(\theta_r)=\pm\left[\frac{2\pi c}{\omega\Lambda}-\sin(\theta_i)\right]. \tag{3.124}$$

This equation relates the angle light will diffract off of a grating to its carrier frequency ω, incident angle θ_i, and the grating period Λ (a quantity generally specified in mm^{-1}). Since this derivation is not as straightforward as one might expect, we carry it out explicitly

$$\phi_2 = \frac{\mathrm{L_{sep}}}{c}\left\{\left[\frac{d\cos(\theta_r)^{-1}}{d\omega}\right][1-\sin(\theta_r)\sin(\theta_i)] + \frac{d\cos(\theta_i)}{d\omega} - \frac{d\sin(\theta_r)}{d\omega}\left[\frac{\sin(\theta_i)}{\cos(\theta_r)}\right]\right\}_{\omega_0}. \tag{3.125}$$

Using the negative version of the grating equation, we find that

$$\frac{d\cos(\theta_i)}{d\omega} = 0, \tag{3.126}$$

and

$$\frac{d\sin(\theta_r)}{d\omega} = -\frac{d}{d\omega}\left[\frac{2\pi c}{\omega\Lambda} - \sin(\theta_i)\right]_{\omega} = \frac{2\pi c}{\omega\Lambda}. \tag{3.127}$$

Now we use the fact that

$$\cos(\theta_r) = \pm\sqrt{1-\sin^2(\theta_r)}. \tag{3.128}$$

Using the positive version of this relation, we find that

$$\frac{d}{d\omega}\frac{1}{\cos(\theta_r)} = \frac{d}{d\omega}\left[\sqrt{1-\left[\frac{2\pi c}{\omega\Lambda} - \sin(\theta_i)\right]}\right] = \frac{2\pi c}{\omega^2\Lambda}\frac{\sin(\theta_r)}{\cos^3(\theta_r)}. \tag{3.129}$$

Substituting our results into Eq. (3.125), we find

$$\phi_2 = \frac{2\pi \mathrm{L_{sep}}}{\omega_0^2\Lambda\cos^3(\theta_{r_0})}\left\{\sin(\theta_{r_0}) - \sin(\theta_i)\left[\sin^2(\theta_{r_0}) + \cos^2(\theta_{r_0})\right]\right\}, \tag{3.130}$$

where θ_{r_0} is just θ_r evaluated at the center frequency of our spectrum. Making the trigonometric simplification and using our grating equation, we find

$$\phi_2 = -\frac{4\pi^2 c\mathrm{L_{sep}}}{\omega_0^3\Lambda^2\cos^3(\theta_{r_0})}. \tag{3.131}$$

We now eliminate the θ_{r_0} angle from this result using the grating equation and write our result in terms of wavelength, since it is more commonly used in the laboratory environment:

$$\phi_2 = \frac{-\lambda_0^3 \mathrm{L_{sep}}}{\pi c^2 \Lambda^2} \left\{ 1 - \left[\frac{\lambda_0}{\Lambda} - \sin(\theta_i) \right]^2 \right\}^{-3/2}. \tag{3.132}$$

This result predicts the "dispersion" imparted on a pulse after the grating pair. To clarify our meaning, since this is often a point of confusion: the value given for the dispersion in Eq. (3.132) is valid after the pulse passes off of each grating twice, experiences a "double-pass" or exits the grating-pair. In going from Eq. (3.131) to Eq. (3.132), we multiplied by a factor of 2 to account for the double-pass, since our derivation up until that point assumed a single-pass.

The third-order dispersion can be found by taking a derivative of the second-order dispersion. It can then be written in terms of the second-order dispersion to give a more compact result. Since its derivation follows the same approach as that of ϕ_2, we simply write the result here:

$$\phi_3 = \frac{-3\lambda_0}{\pi c} \left\{ \frac{\cos^2(\theta_i) + \frac{\lambda_0}{\Lambda}\sin(\theta_i)}{1 - \left[\frac{\lambda_0}{\Lambda} - \sin(\theta_i) \right]^2} \right\} \phi_2, \tag{3.133}$$

where we have once again multiplied the single-pass dispersion by 2 to get the result for the grating pair

Before parting, we point out that the dispersion terms found in this section are, strictly speaking, not dispersion terms since their units are s^2 and s^3. That is, we could write $\beta_{2_{\mathrm{grating}}} = \phi_2 / \mathrm{L_{grating}}$ where $\mathrm{L_{grating}}$ is the characteristic length of the grating pair. However, such a result is not as physical as just using the ϕ_n values and so such a treatment is altogether avoided in this work.

3.6 Chapter Summary

This chapter introduced a few of the necessary experimental techniques required to accurately characterize mode-locked (fiber) lasers. Although some of these techniques should be well-known by those who work in the field of short-pulse mode-locked fiber lasers, they cannot, to the best of my knowledge, be found in any single source. Therefore, this chapter should be of use to other students who work in this field in the future. Moreover, some of these techniques were used in Chapter 2 to characterize the lasers discussed their, while those that have not already been used allow us to obtain the parameters required for modeling these lasers (see Chapter 5).

4 Theoretical Framework

This chapter provides the theoretical framework necessary to describe mode-locked (fiber) lasers. We begin by deriving one of the most general equations governing nonlinear short-pulse propagation in an optical waveguide. This equation reduces to the well-known nonlinear Schrödinger equation (NLSE) for pulses > 100 fs, at least in standard fibers.* The effect of gain on an optical field is then introduced in a simple manner and the Ginzburg–Landau equation is derived. The equations governing fiber amplifiers are listed and numerically solved for one of the doped fibers used in this work. An introduction to lasers is then provided before mode locking is theoretically addressed. The chapter concludes with derivations of the expected mode-locked pulse shapes and their associated parameters for AM, FM, and saturable-absorption-based mode locking based on Siegman's time-domain approach.[2]

*Strictly speaking, the validity of the NLSE depends on the nonlinearity of the waveguide and the pulse width and peak power being modeled.

4.1 Overview of Nonlinear Fiber Optics

4.1.1 Generalized Nonlinear Schrödinger Equation

Our theoretical work starts with Maxwell's equations:[117]

$$\nabla \times \mathbf{E} = -\frac{\partial \mathbf{B}}{\partial t} \qquad \text{Faraday's law} \tag{4.1}$$

$$\nabla \times \mathbf{H} = \mathbf{J} + \frac{\partial \mathbf{D}}{\partial t} \qquad \text{Ampère's circuital law} \tag{4.2}$$

$$\nabla \bullet \mathbf{D} = \rho_v \qquad \text{Gauss's law} \tag{4.3}$$

$$\nabla \bullet \mathbf{B} = 0 \qquad \text{No magnetic monopole} \tag{4.4}$$

which govern the propagation of the electric **E** and magnetic **H** fields. In these equations **J** represents the density of free currents (both convection and conduction) and ρ_v is the volume density of any free charges. Furthermore, the electric and magnetic flux densities **D** and **B**, respectfully, may be related to the electric and magnetic fields via:

$$\mathbf{D} = \varepsilon_0 \mathbf{E} + \mathbf{P}, \tag{4.5}$$

and

$$\mathbf{B} = \mu_0 \mathbf{H} + \mathbf{M}, \tag{4.6}$$

where ε_0 is the permittivity of free space, μ_0 is the permeability of free space, and **P** and **M** are the induced electric and magnetic polarizations.

Electromagnetic fields propagate under the influence of Eqs. (4.1)–(4.4), therefore, we must take the effects of all of these equations into account to describe the propagation of an optical pulse. Since optical media, such as fiber, are free from electric sources and are also nonmagnetic

$$\mathbf{J} = \mathbf{M} = 0. \tag{4.7}$$

By taking the curl of Eq. (4.1) and using Eqs. (4.6) and (4.7) we obtain:

$$\nabla \times \nabla \times \mathbf{E} = -\mu_0 \nabla \times \frac{\partial \mathbf{H}}{\partial t}. \tag{4.8}$$

Exchanging the order in which the spatial and temporal operators act on the magnetic field (**H**) allows us to substitute Eq. (4.2) into Eq. (4.8) yielding the generic wave equation that is used as the starting point for nonlinear optics:

$$\nabla \times \nabla \times \mathbf{E} = -\frac{1}{c^2}\frac{\partial^2 \mathbf{E}}{\partial t^2} - \mu_0 \frac{\partial^2 \mathbf{P}}{\partial t^2}, \tag{4.9}$$

where c is the speed of light in the vacuum and is given by $\varepsilon_0 \mu_0 = 1/c^2$.

Using the vector Identity $\nabla \times \nabla \times \mathbf{E} = \nabla(\nabla \bullet \mathbf{E}) - \nabla^2 \mathbf{E}$ and Eq. (4.3), we obtain the wave equation

$$\nabla^2 \mathbf{E} - \nabla(\nabla \bullet \mathbf{E}) - \frac{1}{c^2}\frac{\partial^2 \mathbf{E}}{\partial t^2} = \mu_0 \frac{\partial^2 \mathbf{P}}{\partial t^2}. \tag{4.10}$$

The induced polarization is then split into its constituent linear and nonlinear contributions via

$$\mathbf{P}(\vec{r},t) = \mathbf{P}_L(\vec{r},t) + \mathbf{P}_{NL}(\vec{r},t), \tag{4.11}$$

which may be related to the electric field through the optical susceptibility χ, a time dependent causal function. In the case of optical fibers, which possess inversion symmetry (they are centrosymmetric), the second-order susceptibility vanishes ($\chi^{(2)} = 0$) and we consider only the first- and third-order susceptibilities $\chi^{(1)}$ and $\chi^{(3)}$ respectively[45, 118–120]

$$\mathbf{P}_L(\vec{r},t) = \varepsilon_0 \int_{-\infty}^{\infty} \chi^{(1)}(t-t_1) \cdot \mathbf{E}(\vec{r},t_1) dt_1 \tag{4.12}$$

$$\mathbf{P}_{NL}(\vec{r},t) = \varepsilon_0 \int\int\int_{-\infty}^{\infty} \chi^{(3)}(t-t_1, t-t_2, t-t_3) \vdots \mathbf{E}(\vec{r},t_1)\mathbf{E}(\vec{r},t_2)\mathbf{E}(\vec{r},t_3) dt_1 dt_2 dt_3. \tag{4.13}$$

In these equations, $\cdot$ denotes the second-rank tensor multiplication and $\vdots$ denotes the fourth-rank tensor multiplication with the electric field. Before continuing, the Fourier transform $\mathscr{F}$ and its inverse $\mathscr{F}^{-1}$ are introduced:

$$\mathscr{F}[A(t)] \equiv \tilde{A}(\omega) = \int_{-\infty}^{\infty} A(t) e^{i\omega t} dt, \tag{4.14}$$

$$\mathscr{F}^{-1}\left[\tilde{A}(\omega)\right] \equiv A(t) = \frac{1}{2\pi}\int_{-\infty}^{\infty} \tilde{A}(\omega) e^{-i\omega t} d\omega. \tag{4.15}$$

Equations (4.12) and (4.13) are substituted into Eq. (4.11) which is subsequently substituted into our wave equation (4.10). We then make use of the inverse Fourier transform [Eq. (4.15)] and the relation $\mu_0\varepsilon_0 = 1/c^2$ to obtain

$$\begin{aligned}
&\frac{1}{2\pi}\nabla^2\int_{-\infty}^{\infty}\tilde{\mathbf{E}}(\vec{r},\omega)e^{-i\omega t}d\omega - \frac{1}{2\pi}\nabla\left[\nabla\bullet\int_{-\infty}^{\infty}\tilde{\mathbf{E}}(\vec{r},\omega)e^{-i\omega t}d\omega\right]\\
&-\frac{1}{2\pi c^2}\frac{\partial^2}{\partial t^2}\int_{-\infty}^{\infty}\tilde{\mathbf{E}}(\vec{r},\omega)e^{-i\omega t}d\omega\\
&=\frac{1}{2\pi c^2}\frac{\partial^2}{\partial t^2}\int_{-\infty}^{\infty}\left[\int_{-\infty}^{\infty}\chi^{(1)}(t-t_1)e^{-i\omega t_1}dt_1\right]\cdot\tilde{\mathbf{E}}(\vec{r},\omega)d\omega\\
&+\frac{1}{(2\pi)^3c^2}\frac{\partial^2}{\partial t^2}\int\int\int_{-\infty}^{\infty}\left[\int\int\int_{-\infty}^{\infty}\chi^{(3)}(t-t_1,t-t_2,t-t_3)\right.\\
&\left.\times e^{-i(\omega_1t_1+\omega_2t_2+\omega_3t_3)}dt_1dt_2dt_3\right]\vdots\tilde{\mathbf{E}}(\vec{r},\omega_1)\tilde{\mathbf{E}}(\vec{r},\omega_2)\tilde{\mathbf{E}}(\vec{r},\omega_3)d\omega_1d\omega_2d\omega_3. \quad (4.16)
\end{aligned}$$

Using Eq. (4.14) and multiplying both sides of the equation by 2π, this can be written as

$$\begin{aligned}
&\nabla^2\int_{-\infty}^{\infty}\tilde{\mathbf{E}}(\vec{r},\omega)e^{-i\omega t}d\omega - \nabla\left[\nabla\bullet\int_{-\infty}^{\infty}\tilde{\mathbf{E}}(\vec{r},\omega)e^{-i\omega t}d\omega\right] - \frac{1}{c^2}\frac{\partial^2}{\partial t^2}\int_{-\infty}^{\infty}\tilde{\mathbf{E}}(\vec{r},\omega)e^{-i\omega t}d\omega\\
&=\frac{1}{c^2}\frac{\partial^2}{\partial t^2}\int_{-\infty}^{\infty}\chi^{(1)}(\omega)\cdot\tilde{\mathbf{E}}(\vec{r},\omega)e^{-i\omega t}d\omega\\
&+\frac{1}{(2\pi c)^2}\frac{\partial^2}{\partial t^2}\int\int\int_{-\infty}^{\infty}\chi^{(3)}(\omega_1,\omega_2,\omega_3)e^{-i(\omega_1+\omega_2+\omega_3)t}\\
&\vdots\tilde{\mathbf{E}}(\vec{r},\omega_1)\tilde{\mathbf{E}}(\vec{r},\omega_2)\tilde{\mathbf{E}}(\vec{r},\omega_3)d\omega_1d\omega_2d\omega_3, \quad (4.17)
\end{aligned}$$

where we have defined the nonlinear optical susceptibilities in the frequency domain through their Fourier transforms

$$\int_{-\infty}^{\infty}\chi^{(1)}(t-t_1)e^{-i\omega t_1}dt_1 \triangleq \chi^{(1)}(\omega)e^{-i\omega t} \quad (4.18)$$

and

$$\begin{aligned}
&\int\int\int_{-\infty}^{\infty}\chi^{(3)}(t-t_1,t-t_2,t-t_3)e^{-i(\omega t_1+\omega_2t_2+\omega_3t_3)}dt_1dt_2dt_3\\
&\triangleq\chi^{(3)}(\omega_1,\omega_2,\omega_3)e^{-i(\omega_1+\omega_2+\omega_3)t}. \quad (4.19)
\end{aligned}$$

Next we interchange the order of operations for the integrals and the derivatives

$$\int_{-\infty}^{\infty}\nabla^2\tilde{\mathbf{E}}(\vec{r},\omega)e^{-i\omega t}d\omega-\int_{-\infty}^{\infty}\nabla\left[\nabla\bullet\tilde{\mathbf{E}}(\vec{r},\omega)\right]e^{-i\omega t}d\omega+\frac{1}{c^2}\int_{-\infty}^{\infty}\omega^2\tilde{\mathbf{E}}(\vec{r},\omega)e^{-i\omega t}d\omega$$
$$=-\frac{1}{c^2}\int_{-\infty}^{\infty}\omega^2\chi^{(1)}(\omega)\cdot\tilde{\mathbf{E}}(\vec{r},\omega)e^{-i\omega t}d\omega$$
$$-\frac{1}{(2\pi c)^2}\int\int\int_{-\infty}^{\infty}(\omega_1+\omega_2+\omega_3)^2\chi^{(3)}(\omega_1,\omega_2,\omega_3)e^{-i(\omega_1+\omega_2+\omega_3)t}$$
$$\vdots\tilde{\mathbf{E}}(\vec{r},\omega_1)\tilde{\mathbf{E}}(\vec{r},\omega_2)\tilde{\mathbf{E}}(\vec{r},\omega_3)d\omega_1d\omega_2d\omega_3, \tag{4.20}$$

then the Fourier transform of the entire equation is taken

$$\int\int_{-\infty}^{\infty}\nabla^2\tilde{\mathbf{E}}(\vec{r},\omega)e^{-i\omega t}d\omega e^{i\omega' t}dt-\int_{-\infty}^{\infty}\int_{-\infty}^{\infty}\nabla\left[\nabla\bullet\tilde{\mathbf{E}}(\vec{r},\omega)\right]e^{-i\omega t}d\omega e^{-i\omega' t}dt$$
$$+\frac{1}{c^2}\int\int_{-\infty}^{\infty}\omega^2\tilde{\mathbf{E}}(\vec{r},\omega)e^{-i\omega t}d\omega e^{i\omega' t}dt$$
$$=-\frac{1}{c^2}\int\int_{-\infty}^{\infty}\omega^2\chi^{(1)}(\omega)\cdot\tilde{\mathbf{E}}(\vec{r},\omega)e^{-i\omega t}d\omega e^{i\omega' t}dt$$
$$-\frac{1}{(2\pi c)^2}\int\int\int\int_{-\infty}^{\infty}(\omega_1+\omega_2+\omega_3)^2\chi^{(3)}(\omega_1,\omega_2,\omega_3)e^{-i(\omega_1+\omega_2+\omega_3)t}$$
$$\vdots\tilde{\mathbf{E}}(\vec{r},\omega_1)\tilde{\mathbf{E}}(\vec{r},\omega_2)\tilde{\mathbf{E}}(\vec{r},\omega_3)d\omega_1d\omega_2d\omega_3e^{i\omega' t}dt. \tag{4.21}$$

By introducing the Dirac delta function

$$\int_{-\infty}^{\infty}e^{i\omega t}dt=2\pi\delta(w), \tag{4.22}$$

we find

$$2\pi\int_{-\infty}^{\infty}\nabla^2\delta(\omega'-\omega)\tilde{\mathbf{E}}(\vec{r},\omega)d\omega-2\pi\int_{-\infty}^{\infty}\nabla\left[\nabla\bullet\tilde{\mathbf{E}}(\vec{r},\omega)\right]\delta(\omega'-\omega)d\omega$$
$$+\frac{2\pi}{c^2}\int_{-\infty}^{\infty}\delta(\omega'-\omega)\omega^2\tilde{\mathbf{E}}(\vec{r},\omega)d\omega$$
$$=-\frac{2\pi}{c^2}\int_{-\infty}^{\infty}\delta(\omega'-\omega)\omega^2\chi^{(1)}(\omega)\cdot\tilde{\mathbf{E}}(\vec{r},\omega)d\omega$$
$$-\frac{1}{2\pi c^2}\int\int\int_{-\infty}^{\infty}\delta(\omega'-\omega_1-\omega_2-\omega_3)(\omega_1+\omega_2+\omega_3)^2\chi^{(3)}(\omega_1,\omega_2,\omega_3)$$
$$\vdots\tilde{\mathbf{E}}(\vec{r},\omega_1)\tilde{\mathbf{E}}(\vec{r},\omega_2)\tilde{\mathbf{E}}(\vec{r},\omega_3)d\omega_1d\omega_2d\omega_3. \tag{4.23}$$

Dividing through by $1/2\pi$ and performing the integrals over ω and ω_3 gives us

$$\begin{aligned}\nabla^2\tilde{\mathbf{E}}(\vec{r},\omega') - \nabla\left[\nabla\bullet\tilde{\mathbf{E}}(\vec{r},\omega')\right] &= -\frac{\omega'^2}{c^2}\tilde{\mathbf{E}}(\vec{r},\omega') - \frac{\omega'^2}{c^2}\chi^{(1)}(\omega')\cdot\tilde{\mathbf{E}}(\vec{r},\omega') \\ &\quad -\frac{\omega'^2}{(2\pi c)^2}\int\int_{-\infty}^{\infty}\chi^{(3)}(\omega_1,\omega_2,\omega'-\omega_1-\omega_2) \\ &\quad \vdots\tilde{\mathbf{E}}(\vec{r},\omega_1)\tilde{\mathbf{E}}(\vec{r},\omega_2)\tilde{\mathbf{E}}(\vec{r},\omega'-\omega_1-\omega_2)d\omega_1 d\omega_2. \quad (4.24)\end{aligned}$$

Replacing ω' with ω, ω_2 with $-\omega_2$, and using the relation $\tilde{A}^*(\omega)=\tilde{A}(-\omega)$, we obtain a nonhomogeneous Helmhotz wave equation in the frequency domain:

$$\begin{aligned}\nabla^2\tilde{\mathbf{E}}(\vec{r},\omega)\ -\nabla\left[\nabla\bullet\tilde{\mathbf{E}}(\vec{r},\omega)\right] + \frac{\omega^2}{c^2}\varepsilon^{(1)}(\omega)\cdot\tilde{\mathbf{E}}(\vec{r},\omega) = \\ -\frac{\omega^2}{(2\pi c)^2}\int\int_{-\infty}^{\infty}\chi^{(3)}(\omega_1,-\omega_2,\omega-\omega_1+\omega_2) \\ \vdots\tilde{\mathbf{E}}(\vec{r},\omega_1)\tilde{\mathbf{E}}^*(\vec{r},\omega_2)\tilde{\mathbf{E}}(\vec{r},\omega-\omega_1+\omega_2)d\omega_1 d\omega_2, \quad (4.25)\end{aligned}$$

where we introduced the tensor $\varepsilon^{(1)}(\omega)=[1+\chi^{(1)}(\omega)]$. This is just the anisotropic Helmhotz equation driven by a nonlinear term.

We now restrict our focus to isotropic optical fiber. Moreover, by ignoring any fiber birefringence, we note that

$$\varepsilon^{(1)}(\omega) = \begin{bmatrix} \varepsilon_x(\omega), & 0, & 0 \\ 0, & \varepsilon_y(\omega), & 0 \\ 0, & 0, & \varepsilon_z(\omega) \end{bmatrix} = \varepsilon(\omega)\hat{I}, \quad (4.26)$$

where $\hat{I}$ is just the identity matrix and $\varepsilon(\omega)$ is scalar. Because we have ignored birefringence, we find that $\nabla\bullet\tilde{\mathbf{E}}(\vec{r},\omega)=0$ in all of our equations. In general, $\varepsilon(\omega)$ is complex, since $\chi^{(1)}$ can be complex; this motivates us to separate it into real and imaginary parts[45]

$$\varepsilon(\omega) = \left[n(\omega)+i\frac{\alpha(\omega)c}{2\omega}\right]^2 = n^2(\omega)+i\frac{n(\omega)\alpha(\omega)c}{\omega}-\frac{\alpha^2(\omega)c^2}{4\omega^2}, \quad (4.27)$$

where $n(\omega)$ is the wavelength dependent refractive index of the material and $\alpha(\omega)$ accounts for the material's wavelength dependent loss. At optical frequencies, where $\omega\sim 1.5\times 10^{15}$, the final term is negligible and

$$\varepsilon(\omega)\approx n^2(\omega)+i\frac{n(\omega)\alpha(\omega)c}{\omega}. \quad (4.28)$$

Using these simplifications and multiplying out the $\varepsilon^{(1)}(\omega)$ tensor, we find a simplified equation suitable for describing pulse propagation in optical fiber

$$\begin{aligned}\nabla^2\tilde{\mathbf{E}}(\vec{r},\omega) \; + \; & n(\omega)^2k^2(\omega)\tilde{\mathbf{E}}(\vec{r},\omega) + in(\omega)k(\omega)\alpha(\omega)\tilde{\mathbf{E}}(\vec{r},\omega) \\ & = -\frac{k^2(\omega)}{(2\pi)^2}\int\int_{-\infty}^{\infty}\chi^{(3)}(\omega_1,-\omega_2,\omega-\omega_1+\omega_2) \\ & \quad \vdots\tilde{\mathbf{E}}(\vec{r},\omega_1)\tilde{\mathbf{E}}^*(\vec{r},\omega_2)\tilde{\mathbf{E}}(\vec{r},\omega-\omega_1+\omega_2)d\omega_1 d\omega_2, \end{aligned} \tag{4.29}$$

where we have introduced the dispersion relation $k(\omega) = \omega/c$. In order to proceed analytically, we must make several simplifying assumptions starting with the approximation that the spatial and temporal effects are independent from one another. Strictly speaking, this limits the generality of all the work that follows to low-power (< 1 MW) guided-wave applications, since spatial-temporal effects are ignored. The motivation behind this assumption is that it allows us to apply separation-of-variables to Eq. (4.29) by postulating that the electric field takes the general form:

$$\begin{aligned}\tilde{\mathbf{E}}(\vec{r},\omega) \; = \; & \tilde{A}_x(z,\omega)\tilde{F}_x(\vec{r}_\perp,\omega)e^{i\beta_x(\omega)z}\hat{x} + \tilde{A}_y(z,\omega)\tilde{F}_y(\vec{r}_\perp,\omega)e^{i\beta_y(\omega)z}\hat{y} \\ & + \tilde{A}_z(z,\omega)\tilde{F}_z(\vec{r}_\perp,\omega)e^{i\beta_z(\omega)z}\hat{z}. \end{aligned} \tag{4.30}$$

This ansatz is then substituted into Eq. (4.29), where $\beta_j(\omega)$ is the propagation constant of the j^{th} component that can also be written as $n_{eff}(\omega)\omega/c$, $\tilde{F}_j(\vec{r}_\perp,\omega)$ is the spatial variation of our field, and $\tilde{A}_j(z,\omega)$ is the temporal variation of our field. However, because we have chosen to ignore birefringence, all of the propagation constants in Eq. (4.30) are identical; therefore, we introduce $\beta = \beta_j$. This allows one to obtain three coupled nonlinear partial differential equations which govern the propagation of the electric field. Following convention, we choose to work with the E_z (and H_z) fields at the moment. Substituting E_z from Eq. (4.30) into Eq. (4.29), after multiplying through

by $e^{-i\beta(w)z}$, this results in:

$$\tilde{F}_j(\vec{r}_\perp,\omega)\left[\frac{\partial^2\tilde{A}_j(z,\omega)}{\partial z^2}+2i\beta(\omega)\frac{\partial\tilde{A}_j(z,\omega)}{\partial z}\right]+\tilde{A}_j(z,\omega)\left\{\nabla_\perp^2\tilde{F}_j(\vec{r}_\perp,\omega)\right.$$
$$\left.+\left[n^2(\omega)k^2(\omega)+in(\omega)\alpha(\omega)k(\omega)\right]\tilde{F}_j(\vec{r}_\perp,\omega)-\beta^2(\omega)\tilde{F}_j(\vec{r}_\perp,\omega)\right\}$$
$$=-\frac{k^2(\omega)}{(2\pi)^2}\int\int_{-\infty}^{\infty}\chi^{(3)}(\omega_1,-\omega_2,\omega-\omega_1+\omega_2)\vdots\tilde{A}(z,\omega_1)\tilde{F}(\vec{r}_\perp,\omega_1)\tilde{A}^*(z,\omega_2)\tilde{F}^*(\vec{r}_\perp,\omega_2)$$
$$\times\tilde{A}(z,\omega-\omega_1+\omega_2)\tilde{F}(\vec{r}_\perp,\omega-\omega_1+\omega_2)e^{i\Delta\beta z}d\omega_1 d\omega_2, \tag{4.31}$$

where we have introduced $\Delta\beta=\beta(\omega_1)-\beta(\omega_2)+\beta(\omega-\omega_1+\omega_2)-\beta(\omega)$. In the above expressions, $j=z$; however, we can obtain identical equations for the other field components if we set $j=x,y$. Also note that in Eq. (4.31) we did not multiply out the third-order susceptibility tensor. Although this could be done if one wished to, it would constitute a very messy and ultimately unnecessary step in our treatment.

Since we have assumed that spatial and temporal functions are independent, we can proceed with the basic separation-of-variables approach by splitting Eq. (4.31) into two separate equations: a spatial one

$$\tilde{A}_j(z,\omega)\left[\nabla_\perp^2\tilde{F}_j(\vec{r}_\perp,\omega)+n^2(\omega)k^2(\omega)\tilde{F}_j(\vec{r}_\perp,\omega)-\beta^2(\omega)\tilde{F}_j(\vec{r}_\perp,\omega)\right]=0 \tag{4.32}$$

and a temporal one

$$\tilde{F}_j(\vec{r}_\perp,\omega)\left[\frac{\partial^2\tilde{A}_j(z,\omega)}{\partial z^2}+in(\omega)\alpha(\omega)k(\omega)\tilde{A}_j(z,\omega)+2i\beta(\omega)\frac{\partial\tilde{A}_j(z,\omega)}{\partial z}\right]$$
$$=-\frac{k^2(\omega)}{(2\pi)^2}\int\int_{-\infty}^{\infty}\chi^{(3)}(\omega_1,-\omega_2,\omega-\omega_1+\omega_2)\vdots\tilde{A}(z,\omega_1)\tilde{F}(\vec{r}_\perp,\omega_1)\tilde{A}^*(z,\omega_2)$$
$$\times\tilde{F}^*(\vec{r}_\perp,\omega_2)\tilde{A}(z,\omega-\omega_1+\omega_2)\tilde{F}(\vec{r}_\perp,\omega-\omega_1+\omega_2)e^{i\Delta\beta z}d\omega_1 d\omega_2, \tag{4.33}$$

where $j=z$ in this case. Under such conditions, we must satisfy Eq. (4.32) for the expected spatial distribution of our field subject to the boundary conditions of a given waveguide. Moreover, Eq. (4.33) must be satisfied by a temporal-field distribution. However, since the solution to Eq. (4.33) includes the spatial distribution, which must be obtained from Eq. (4.32), we must proceed by solving Eq. (4.32) first.

Fortunately, in order to fully describe our spatial field, it is only necessary for us

to describe two of the six field components[†] (here we are focusing on E_z and H_z); the other four components can easily be found through Maxwell's equations. We now further restrict our focus to the investigation of a cylindrical beam propagating in our waveguide. In order to do, so we define our spatial distribution and the $\nabla_\perp$ operator in cylindrical coordinates:

$$\nabla_\perp^2 = \frac{1}{r}\frac{\partial}{\partial r}\left(r\frac{\partial}{\partial r}\right) + \frac{1}{r^2}\frac{\partial^2}{\partial \phi^2} \tag{4.34}$$

and change the coordinate system of our spatial distribution

$$\Psi(r,\phi) = \tilde{F}_z(\vec{r}_\perp,\omega)e^{-im\phi}, \tag{4.35}$$

where we have dropped the frequency dependence of the field for simplicity and have introduced the integer constant m, which insures that the field is periodic in 2π. Equation (4.32) may now be written as

$$\frac{\partial^2\Psi(r,\phi)}{\partial r^2} + \frac{1}{r}\frac{\partial\Psi(r,\phi)}{\partial r} + \left[n^2(\omega)k(\omega)^2 - \beta^2(\omega) - \frac{m^2}{r^2}\right]\Psi(r,\phi) = 0, \tag{4.36}$$

which is just Bessel's differential equation. If $n^2(\omega)k^2(\omega) - \beta^2(\omega) > 0$, it has the following solution:

$$\Psi(r,\phi) = C_1 J_m(q_1 r) + C_2 Y_m(q_1 r). \tag{4.37}$$

In Eq. (4.37) $q_1 = \sqrt{n^2(\omega)k^2(\omega) - \beta^2(\omega)}$, J_m and Y_m are the Bessel functions of the first and second kind of order m, and constants C_1 and C_2 are determined by the boundary conditions. However, if $n^2(\omega)k^2(\omega) - \beta^2(\omega) < 0$, Eq. (4.36) is solved by

$$\Psi(r,\phi) = C_3 I_m(q_2 r) + C_4 K_m(q_2 r), \tag{4.38}$$

where $q_2 = -i\sqrt{n^2(\omega)k^2(\omega) - \beta^2(\omega)}$, I_m and K_m are the modified Bessel functions of the first and second kind of order m, and constants C_3 and C_4 are determined by

[†]Had birefringence been included, our spatial distribution would be more difficult to determine and this simplification would not be applicable.

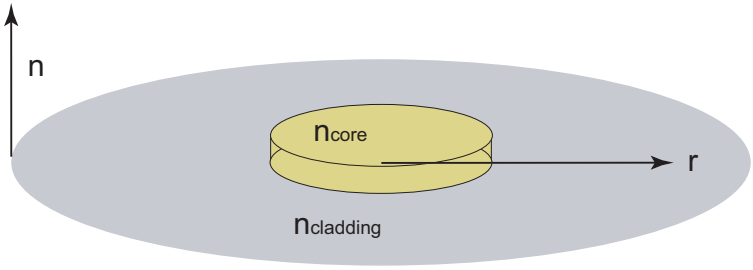

Figure 4.1: Cartoon depicting the refractive index variation of step-index fiber.

the boundary conditions. To continue from here, it is necessary to choose a specific waveguide. Let us now investigate the optical field's spatial distribution in an optical fiber by applying the appropriate boundary conditions. Assuming we are considering a step-index fiber ($n = n_1$ for $r < a$ and $n = n_2$ for $r > a$ where a is the radius of the core and $n_1 > n_2$ see Fig. 4.1), $C_2 = C_3 = 0$ and the spatial profile is given by $E_z(r,\phi) = C_1 J_m(q_1 r)e^{im\phi}$ and $H_z(r,\phi) = C_5 J_m(q_1 r)e^{im\phi}$ in the core and $E_z(r,\phi) = C_4 K_m(q_2 r)e^{im\phi}$ and $H_z(r,\phi) = C_8 K_m(q_2 r)e^{im\phi}$ in the cladding.

From Eq. (4.1) we can find the other 4 components of the electric and magnetic fields, assuming E_z and H_z are known, via

$$E_r = \frac{i}{q_p^2}\left(\beta\frac{\partial E_z}{\partial r} + \frac{\mu_0\omega}{r}\frac{\partial H_z}{\partial \phi}\right) \tag{4.39}$$

$$E_\phi = \frac{i}{q_p^2}\left(\frac{\beta}{r}\frac{\partial E_z}{\partial \phi} - \mu_0\omega\frac{\partial H_z}{\partial r}\right) \tag{4.40}$$

$$H_r = \frac{i}{q_p^2}\left(\beta\frac{\partial H_z}{\partial r} - \frac{\varepsilon_0 n_p^2\omega}{r}\frac{\partial E_z}{\partial \phi}\right) \tag{4.41}$$

$$H_\phi = \frac{i}{q_p^2}\left(\frac{\beta}{r}\frac{\partial H_z}{\partial \phi} + \varepsilon_0 n_p^2\omega\frac{\partial E_z}{\partial r}\right), \tag{4.42}$$

where $p = 1,2$ here. By substituting our field ansatz into Eqs. (4.39)–(4.42) in both regions and matching the boundary conditions (${}^1E_z = {}^2E_z$, ${}^1H_z = {}^2H_z$, ${}^1E_\phi = {}^2E_\phi$, and ${}^1H_\phi = {}^2H_\phi$), where the superscripts denote the fields in either the core ^{1} or the cladding ^{2}, we obtain a set of four equations that must be satisfied. In order to satisfy

Eq. (4.32), we find

$$\begin{bmatrix} J_m(q_1a), & 0, & -K_m(q_2a), & 0 \\ 0, & J_m(q_1a), & 0, & -K_m(q_2a) \\ \frac{\beta m}{aq_1^2}J_m(q_1a), & \frac{-i\omega\mu_0}{q_1}J'_m(q_1a), & \frac{\beta m}{aq_2^2}K_m(q_2a), & \frac{-i\omega\mu_0}{q_2}K'_m(q_2a) \\ \frac{i\omega n_1^2}{q_1}J'_m(q_1a), & \frac{\beta m}{aq_1^2}J_m(q_1a), & \frac{i\omega n_2^2}{q_2}K'_m(q_2a), & \frac{\beta m}{aq_2^2}K_m(q_2a) \end{bmatrix} \begin{bmatrix} C_1 \\ C_5 \\ C_4 \\ C_8 \end{bmatrix} = 0. \quad (4.43)$$

We have introduced the following shorthand notation:

$$K'_m(q_jr) = \frac{dK_m(q_jr)}{d(q_jr)} \quad (4.44)$$

$$J'_m(q_jr) = \frac{dJ_m(q_jr)}{d(q_jr)}. \quad (4.45)$$

Nontrivial solutions are found only when the determinant of the matrix in Eq. (4.43) equals zero. Although some simplifications may be introduced in order to streamline the mode treatment,[‡] no simple solution exists and one must use a computer in order to determine the propagation constant β even in the presence of these simplifications. After a solution is obtained for β, one can determine the coefficients necessary to construct the fields using the following relations:

$$C_4 = \frac{J_m(q_1r)}{K_m(q_2a)}C_1 \quad (4.46)$$

$$C_8 = \frac{J_m(q_1r)}{K_m(q_2a)}C_5 \quad (4.47)$$

$$C_5 = \frac{-i\beta m}{\omega\mu_0 a}\left[\frac{1}{q_1^2}+\frac{1}{q_2^2}\right]\left[\frac{J'_m(q_1a)}{J_m(q_1a)}+\frac{K'_m(q_2a)}{K_m(q_2a)}\right]^{-1}C_1. \quad (4.48)$$

Since it is straightforward to solve Eq. (4.43) for propagation constants that satisfy it, we do so for a waveguide with a core radius of 4.5 μm, $n_{core} = 1.452$ and

[‡]The interested reader is referred to Refs. [121], [122], [123], [124], and/or [45], which investigate these issues (in decreasing degrees of detail). Moreover, these books present some of the simplifications commonly made including the LP mode treatment.

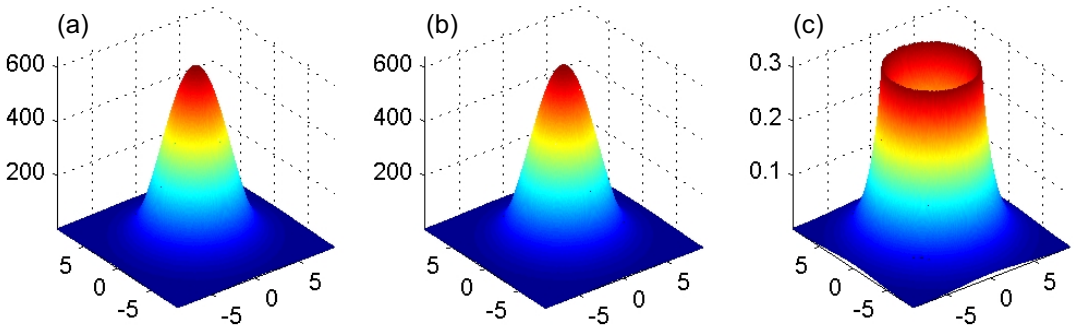

Figure 4.2: Components of the electric field predicted for the fundamental mode in this example. (a) depicts $|E_r|^2$, (b) depicts $|E_\phi|^2$, (c) shows $|E_z|^2$. The transverse units in the figures are in μm.

$n_{clad} = 1.450$. Investigating the mode structure of this waveguide for light with a carrier wavelength of 1050 nm, we find only one solution: $\beta = 8.682\ (\mu\text{m})^{-1}$, where $m = 1$. Since only one solution exists, in this case the HE_{11} mode, this would be referred to as a single-mode fiber. In the rest of this thesis we only consider single-mode fibers; issues relating to mode coupling, which can exist in multi-mode fibers, are ignored. Another important discovery is that when comparing the relative strengths of the various terms in Fig. 4.2, we find $\tilde{F}_z(\vec{r}_\perp,\omega) \ll \tilde{F}_j(\vec{r}_\perp,\omega)$, where $j = r,\phi$ or if one changes back to cartesian coordinates $j = x,y$. It is also noted that Eq. (4.32) will be satisfied for the other field components [$\tilde{E}_x(\vec{r},\omega)$ and $\tilde{E}_y(\vec{r},\omega)$]. Therefore, as long as we can assume the light propagating in a fiber takes on one of these spatial modes,[§] we can be confident that Eq. (4.32) is satisfied and we can shift our attention to searching for a solution to Eq. (4.33).

Equation (4.32) must still be solved. However, since we found that $\tilde{F}_z(\vec{r}_\perp,\omega) \ll \tilde{F}_j(\vec{r}_\perp,\omega)$, we can, to a good approximation, ignore E_z completely by setting it to zero.

[§]This assumption is almost always made in practice. However, situations can arise when this assumption becomes questionable or false; for example, the introduction of long-period gratings, fiber deformities, or stresses can couple the fiber modes to cladding/radiative modes. In these cases, care must be taken to asses the validity of the assumptions made in this derivation.

This approximation now leaves us with two coupled equations that govern E_x and E_y (or r and ϕ). Further investigation reveals that, although the mode structure changes with the polarization in a birefringent fiber, that is $\tilde{F}_x(\vec{r}_\perp,\omega)$ will differ from $\tilde{F}_y(\vec{r}_\perp,\omega)$, such effects are small in standard single-mode fiber and can be ignored in practice.[¶] Therefore, we assume $\tilde{F}_x(\vec{r}_\perp,\omega) \simeq \tilde{F}_y(\vec{r}_\perp,\omega)$. This reduces the problem of nonlinear pulse propagation in an optical fiber to the system of coupled equations given by Eq. (4.33) where $j = x,y$. In this treatment, the two fields can be assumed to share the same spatial mode profile; polarization is now accounted for by the terms $\tilde{A}_x(z,\omega)$ and $\tilde{A}_y(z,\omega)$ which couple to each other through the nonlinear term. This can be seen by expanding the tensor in Eq. (4.33) subject to all of the simplifications listed above.

Although one could continue with the derivation for the propagation of an arbitrarily polarized pulse, it increases the complexity of our treatment due to the susceptibility tensor. Since we did not investigate vector-based pulse propagation in this work, we now further restrict our focus to the propagation of scalar pulses. Focusing on scalar pulses, we finally evaluate the susceptibility tensor, noting that although Eq. (4.33) does not admit a general analytic solution, we can simplify it a bit.

If we neglect all resonant electronic nonlinearities we can use Kleinman symmetry to simplify the third-order susceptibility by noting that it only depends on the frequency differences within the wave.[119,125] Therefore, we introduce $g(\omega)$, where for our scalar field,[‖] $\chi^{(3)}(\omega_1,-\omega_2,\omega-\omega_1+\omega_2) = (2\pi)^2\chi^{(3)}_{xxxx}g(\omega_1-\omega_2)$, $\chi^{(3)}_{xxxx}$ is now a wavelength

[¶]Standard single-mode fiber does possess weak birefringence which leads to effects such as polarization-mode dispersion. Nevertheless, these effects are weak and do not strongly influence the mode structure. In strongly birefringent fiber, however, this issue warrants further investigation.

[‖]Note that we are now working with a scalar field only, A_x. If one has a field that is not linearly polarized, this treatment would have to be applied to two coupled governing equations of this form by noting that the nonlinear susceptibility would take a different form since the tensor will couple the two polarizations through the last term; see the chapter entitled “Cross-Phase Modulation” in Ref. [45] for such a treatment. Also note that $g(\omega)$ includes the nonlinear response due to Raman scattering. This effect has strong polarization dependence and therefore the functional shape of $g(\omega)$ will change depending on the exiting field.

independent scalar nonlinear coefficient, and $g(\omega)$ represents the causal response of the medium or the frequency dependence of the tensor.[125] This gives us

$$\begin{aligned}
&\tilde{F}(\vec{r}_\perp,\omega)\left[\frac{\partial^2\tilde{A}(z,\omega)}{\partial z^2}+in(\omega)\alpha(\omega)k(\omega)\tilde{A}(z,\omega)+2i\beta(\omega)\frac{\partial\tilde{A}(z,\omega)}{\partial z}\right]\\
&=-k^2(\omega)\chi^{(3)}_{xxxx}\int\int_{-\infty}^{\infty}g(\omega_1-\omega_2)\tilde{A}(z,\omega_1)\tilde{F}(\vec{r}_\perp,\omega_1)\tilde{A}^*(z,\omega_2)\\
&\times\tilde{F}^*(\vec{r}_\perp,\omega_2)\tilde{A}(z,\omega-\omega_1+\omega_2)\tilde{F}(\vec{r}_\perp,\omega-\omega_1+\omega_2)e^{i\Delta\beta z}d\omega_1 d\omega_2, \qquad (4.49)
\end{aligned}$$

where we have dropped the subscripts since our field is now assumed to be scalar.

By multiplying this equation by $\tilde{F}^*(\vec{r}_\perp,\omega)$ and then integrating over the spatial coordinates $\vec{r}_\perp$, we obtain

$$\begin{aligned}
\frac{\partial^2\tilde{A}(z,\omega)}{\partial z^2}\;&+\;in(\omega)\alpha(\omega)k(\omega)\tilde{A}(z,\omega)+2i\beta(\omega)\frac{\partial\tilde{A}(z,\omega)}{\partial z}\\
&=-\chi^{(3)}_{xxxx}k^2(\omega)\int\int_{-\infty}^{\infty}H(\omega,\omega_1,\omega_2)g(\omega_1-\omega_2)\\
&\times\;\tilde{A}(z,\omega_1)\tilde{A}^*(z,\omega_2)\tilde{A}(z,\omega-\omega_1+\omega_2)e^{i\Delta\beta z}d\omega_1 d\omega_2, \qquad (4.50)
\end{aligned}$$

where we introduced

$$H(\omega,\omega_1,\omega_2)=\frac{\int_{-\infty}^{\infty}\tilde{F}(\vec{r}_\perp,\omega_1)\tilde{F}^*(\vec{r}_\perp,\omega_2)\tilde{F}(\vec{r}_\perp,\omega-\omega_1+\omega_2)\tilde{F}^*(\vec{r}_\perp,\omega)d^2\vec{r}_\perp}{\int_{-\infty}^{\infty}|\tilde{F}(\vec{r}_\perp,\omega)|^2d^2\vec{r}_\perp}. \qquad (4.51)$$

We now argue that our field changes slowly such that $\partial^2\tilde{A}(z,\Omega)/\partial z^2\approx 0$. This simplification, known as the slowly varying envelop approximation (SVEA), is valid for pulses >20 fs and is thus valid for the work in this thesis which mainly focuses on picosecond pulses.

At this point, there are two directions in which we can proceed. We will follow the more rigorous of the two and then present the results of the other approach at the end, since it more closely mirrors the commonly used approach.

In order to continue, we re-define our temporal field in such a way that the spatial variation due to $H(\omega,\omega_1,\omega_2)$ can be brought outside of the integral. Following the

derivation in Ref. (120),** we introduce

$$H(\omega,\omega_1,\omega_2) \approx 1/2\sqrt[4]{S(\omega_1)S^*(\omega_2)S(\omega_1+\omega_2-\omega)S^*(\omega)}, \tag{4.52}$$

where $S(\omega)$ can be written in terms of the effective area of the fiber through

$$S(\omega) = \frac{A_{\text{eff}}(\omega)}{A_{\text{eff}}(\omega_0)} \tag{4.53}$$

and the effective area is defined by

$$A_{\text{eff}}(\omega) = \frac{\left[\int_{-\infty}^{\infty}\left|\tilde{F}(\vec{r}_\perp,\omega)\right|^2 d^2\vec{r}_\perp\right]^2}{\int_{-\infty}^{\infty}\left|\tilde{F}(\vec{r}_\perp,\omega)\right|^4 d^2\vec{r}_\perp}. \tag{4.54}$$

We also introduce a slowly varying envelope such that out field can be written as

$$\tilde{\phi}(\Omega,z) = \frac{1}{\sqrt{2}}\sqrt[4]{S(\omega)}\tilde{A}(z,\omega)e^{i[\beta(\omega)-\beta_0]z}, \tag{4.55}$$

where we have introduced a frequency detuning from the optical carrier via $\Omega = \omega - \omega_0$ and $\Omega_n = \omega_n - \omega_0$.

By dividing Eq. (4.50) by $\beta(\omega)$†† and substituting Eq. (4.55) into the result, subject to all the simplifications above, we arrive at

$$\begin{aligned}
&\frac{\sqrt{2}}{\sqrt[4]{S(\omega)}}\left\{\frac{\partial\tilde{\phi}(z,\Omega)}{\partial z} - i\left[\beta(\omega)-\beta_0\right]\tilde{\phi}(z,\Omega)\right\}e^{-i[\beta(\omega)-\beta_0]z} \\
&+\frac{n(\omega)\alpha(\omega)}{2n_{\text{eff}}(\omega)}\frac{\sqrt{2}}{\sqrt[4]{S(\omega)}}\tilde{\phi}(z,\Omega)e^{-i[\beta(\omega)-\beta_0]z} \\
&= \frac{i\chi^{(3)}_{xxxx}k(\omega)}{2n_{\text{eff}}(\omega)}\int_{-\infty}^{\infty}\int_{-\infty}^{\infty} g(\Omega_1-\Omega_2)\sqrt{2}\sqrt[4]{S(\omega)}\tilde{\phi}(z,\Omega_1) \\
&\times\tilde{\phi}^*(z,\Omega_2)\tilde{\phi}(z,\Omega-\Omega_1+\Omega_2)e^{-i[\beta(\omega)-\beta_0]z}d\Omega_1 d\Omega_2.
\end{aligned} \tag{4.56}$$

By multiplying through by the common elements, we find

$$\begin{aligned}
&\frac{\partial\tilde{\phi}(z,\Omega)}{\partial z} - i\left[\beta(\omega)-\beta_0\right]\tilde{\phi}(z,\Omega) + \frac{n(\omega)\alpha(\omega)}{2n_{\text{eff}}(\omega)}\tilde{\phi}(z,\Omega) \\
&= \frac{i\chi^{(3)}_{xxxx}\omega_0}{2c\ n_{\text{eff}}(\omega)}\sqrt{S(\omega)}\left(1+\frac{\Omega}{\omega_0}\right)\int_{-\infty}^{\infty}\int_{-\infty}^{\infty} g(\Omega_1-\Omega_2)\tilde{\phi}(z,\Omega_1) \\
&\times\tilde{\phi}^*(\Omega_2,z)\tilde{\phi}(z,\Omega-\Omega_1+\Omega_2)d\Omega_1 d\Omega_2.
\end{aligned} \tag{4.57}$$

**The rest of the derivation presented here follows directly from Ref. (120).

††recall that $\beta(\omega)$ can also be written as $n_{eff}(\omega)\omega/c$

Finally by introducing a nonlinear coefficient,

$$\sigma(\omega) = \frac{\chi^{(3)}_{xxxx}\omega_0\sqrt{S(\omega)}}{2c\, n_{eff}(\omega)}, \tag{4.58}$$

we obtain the generalized nonlinear Schrödinger equation in the frequency domain

$$\frac{\partial\tilde{\phi}(z,\Omega)}{\partial z} - i[\beta(\omega)-\beta_0]\,\tilde{\phi}(z,\Omega) + \frac{\alpha_{\text{eff}}(\omega)}{2}\tilde{\phi}(z,\Omega) = i\sigma(\omega)\left(1+\frac{\Omega}{\omega_0}\right) \times \int\int_{-\infty}^{\infty} g(\Omega_1-\Omega_2)\tilde{\phi}(z,\Omega_1)\tilde{\phi}^*(z,\Omega_2)\tilde{\phi}(z,\Omega-\Omega_1+\Omega_2)d\Omega_1 d\Omega_2, \tag{4.59}$$

where $\alpha_{\text{eff}}(\omega)$ is the total loss due to the intrinsic material loss as well as any waveguide induced losses. However, our field $\tilde{\phi}(z,\Omega)$ now depends on the mode structure. This physically intuitive result is both analytically and computationally difficult to work with. Moreover, any minimal increase in accuracy provided by this treatment is mitigated by the increased difficulty in working with this approach. As a result, we now repeat the derivation of the previous two pages under a more general assumption.

The other approach we could have taken makes the more questionable assumption that our mode profile is approximately constant with respect to the integral and that it can be removed from the integral. More specifically, it assumes

$$H(\omega,\omega_1,\omega_2) \approx \frac{\int_{-\infty}^{\infty}\left|\tilde{F}(\vec{r}_\perp,\omega)\right|^2 d^2\vec{r}_\perp}{A_{eff}(\omega)}. \tag{4.60}$$

By using this assumption and introducing a slowly-varying field, we redefine our field A through

$$\tilde{A}(z,\Omega) = \tilde{A}(z,\omega)e^{i[\beta(\omega)-\beta_0]z}\sqrt{\int_{-\infty}^{\infty}\left|\tilde{F}(\vec{r}_\perp,\omega)\right|^2 d^2\vec{r}_\perp} \tag{4.61}$$

and use this result in Eq. (4.50) to arrive at

$$\frac{\partial\tilde{A}(z,\Omega)}{\partial z} - i[\beta(\omega)-\beta_0]\tilde{A}(z,\Omega) + \frac{\alpha_{\text{eff}}(\omega)}{2}\tilde{\phi}(z,\Omega) = i\gamma(\omega)\left(1+\frac{\Omega}{\omega_0}\right) \times \int\int_{-\infty}^{\infty} g(\Omega_1-\Omega_2)\tilde{A}(z,\Omega_1)\tilde{A}^*(z,\Omega_2)\tilde{A}(z,\Omega-\Omega_1+\Omega_2)d\Omega_1 d\Omega_2, \tag{4.62}$$

where $\gamma(\omega)$ is defined via

$$\gamma(\omega) = \frac{\chi^{(3)}_{xxxx}\omega_0}{2c\, n_{eff}(\omega)A_{eff}(\omega)}. \tag{4.63}$$

Strictly speaking, the above equation is completely general; however, it is difficult to solve in practice because the parameters it requires are not well documented. Fortunately, if we concentrate our focus on the propagation of fields centered on ω_0, we can Taylor expand the effects of the propagation constant β, the loss α, and the nonlinear term γ around ω_0 using the following relations:

$$\beta(\omega) = \sum_{n=0}^{\infty} \frac{\beta_n}{n!}\Omega^n, \tag{4.64}$$

$$\alpha_{\text{eff}}(\omega) = \sum_{n=0}^{\infty} \frac{\alpha_n}{n!}\Omega^n, \tag{4.65}$$

$$\gamma(\omega) = \sum_{n=0}^{\infty} \frac{\gamma_n}{n!}\Omega^n. \tag{4.66}$$

Using the above Taylor expansions we can still obtain a high degree of accuracy. Moreover the lower order terms used in the expansions can be experimentally or computationally determined. Using these expansions in Eq. (4.62), we arrive at

$$\frac{\partial \tilde{A}(z,\Omega)}{\partial z} - i\sum_{n=1}^{\infty} \frac{\beta_n \Omega^n}{n!}\tilde{A}(z,\Omega) + \frac{1}{2}\sum_{n=0}^{\infty} \frac{\alpha_n \Omega^n}{n!}\tilde{\phi}(z,\Omega) = i\sum_{n=0}^{\infty} \frac{\gamma_n \Omega^n}{n!}\left(1+\frac{\Omega}{\omega_0}\right) \times \int\int_{-\infty}^{\infty} g(\Omega_1-\Omega_2)\tilde{A}(z,\Omega_1)\tilde{A}^*(z,\Omega_2)\tilde{A}(z,\Omega-\Omega_1+\Omega_2)d\Omega_1 d\Omega_2. \tag{4.67}$$

We can also write this equation in the time domain. Because we Taylor expanded the frequency dependent terms, this can be done without the need to include any extra convolution integrals. Therefore, by using the Fourier transform, we obtain

$$\frac{\partial A(z,t)}{\partial z} + \frac{1}{2}\sum_{n=0}^{\infty} \frac{i^n \alpha_n}{n!}\frac{\partial^n}{\partial t^n}A(z,t) - i\sum_{n=1}^{\infty} \frac{i^n \beta_n}{n!}\frac{\partial^n}{\partial t^n}A(z,t) = i\sum_{n=0}^{\infty} \frac{i^n \gamma_n}{n!}\frac{\partial^n}{\partial t^n}\left(1+\frac{i}{\omega_0}\frac{\partial}{\partial t}\right)A(z,t)\int_{-\infty}^{\infty} g(t')|A(z,t-t')|^2 dt'. \tag{4.68}$$

Conventionally, it is assumed that the pulse spectra are narrow enough such that $\gamma(\omega)$ and $\alpha(\omega)$ are essentially constant over the pulse spectrum. On the other hand,

since β is a phase term, a small change in β can still lead to a large change in our field; therefore, we use the Taylor-expanded version of this term. Nevertheless, we truncate the Taylor-series expansions for γ and α after the first term. To the best of my knowledge, this is always done in practice. To adhere to convention, we define $\alpha \triangleq \alpha_0$ and $\gamma \triangleq \gamma_0$ which enables us to arrive at[‡‡]

$$\frac{\partial A(z,t)}{\partial z} + \frac{\alpha}{2}A(z,t) - i\sum_{n=1}^{\infty}\frac{i^n\beta_n}{n!}\frac{\partial^n}{\partial t^n}A(z,t) = i\gamma\left(1+\frac{i}{\omega_0}\frac{\partial}{\partial t}\right) \times A(z,t)\int_{-\infty}^{\infty} g(t')|A(z,t-t')|^2 dt', \tag{4.69}$$

where the term $g(t)$ is given by[125]

$$g(t) = b\delta(t) + (1-b)g_R(t). \tag{4.70}$$

Equation (4.70) describes the medium's response, where $\delta(t)$ represents the instantaneous response, known as self-phase modulation (SPM), and $g_R(t)$ describes the delayed response due to stimulated Raman scattering (SRS), which can be modeled by two Lorentzian's in the frequency domain although it is highly polarization dependent.[125] In Eq. (4.70),

$$g_R(t) = \frac{\tau_1^2+\tau_2^2}{\tau_1\tau_2^2}\exp(-t/\tau_2)\sin(t/\tau_1)h(t), \tag{4.71}$$

where τ_1^{-1} gives the phonon frequency, τ_2^{-1} determines the bandwidth of the Lorentzian line, and $h(t)$ is the heavy side step function which insures causality. The constant b determines the relative strengths of the Kerr and Raman processes. In optical fiber, these parameters take the values of $b = 0.18$, $\tau_1 = 12.2$ fs, and $\tau_2 = 32$ fs.[125]

[‡‡]Although the spectral dependent loss most likely plays a small role and can be ignored, people modeling supercontinuum generation or intense pulses with broad spectra may wish to take some of the higher-order (with respect to the frequency dependence) nonlinear terms into account. I suspect that this will happen in the near future.

4.1.2 Nonlinear Schrödinger Equation

The nonlinear Schrödinger equation is, without question, the most well-known equation in nonlinear optics. Although it can be derived in a manner similar to the GNLSE, since we have already derived the more general of the two equations, we need only restrict its applicability.

If we investigate pulses with widths > 100, fs we can approximate the electronic response in Eq. (4.70) as being instantaneous ($g_R(t) \approx \delta(t)$). As with the $\chi^{(1)}$ susceptibility, $\chi^{(3)}$ is, in general, complex and can be split into real and imaginary parts. Therefore, one obtains a term $\propto (n_2 + i\alpha_2)|A|^2$ where n_2 is the nonlinear contribution to the refractive index and α_2 is an intensity dependent loss which can be attributed to two-photon absorption. In what follows, we assume that two-photon absorption is negligible. Furthermore, we limit our investigations to pulse propagation in the presence of finite dispersion. In such cases, pulses cannot develop shocks; that is, they do not acquire infinite slopes, and it is valid to ignore the self-steepening term given by $\partial/\partial t$ in Eq. (4.69) by setting it to zero. If one also assumes that higher-order dispersive effects ($n \geq 3$) do not play a strong role in the pulse shaping, we obtain:

$$\frac{\partial A(z,t)}{\partial z} + \beta_1 \frac{\partial A(z,t)}{\partial t} + \frac{\alpha}{2} A(z,t) + i\frac{\beta_2}{2}\frac{\partial^2 A(z,t)}{\partial t^2} = i\gamma A(z,t)|A(z,t)|^2. \qquad (4.72)$$

By performing the so-called Galelian transformation, changing to a time frame local to the pulse ($z = \xi$ and $T = t - \beta_1 z$), we obtain a modified NLSE which includes the effect of loss:

$$\frac{\partial A(\xi,T)}{\partial \xi} + i\frac{\beta_2}{2}\frac{\partial^2 A(\xi,T)}{\partial T^2} = i\gamma|A(\xi,T)|^2 A(\xi,T) - \frac{\alpha}{2}A(\xi,T). \qquad (4.73)$$

By introducing $\Psi(\xi,T) = A(\xi,T)\exp(-\alpha\xi/2)$ and $\gamma' = \gamma\exp(-\alpha\xi)$, we obtain the traditional NLSE

$$\frac{\partial \Psi(\xi,T)}{\partial \xi} + i\frac{\beta_2}{2}\frac{\partial^2 \Psi(\xi,T)}{\partial T^2} = i\gamma'|\Psi(\xi,T)|^2\Psi(\xi,T). \qquad (4.74)$$

Of course this equation is also obtained for lossless propagation since $\alpha = 0$ in Eq. (4.73).

4.1.3 Ginzburg–Landau Equation (GLE)

If we assume a gain media may be approximated as a pumped two-level system, then the effects on the field should be obtained by solving the Maxwell-Bloch equations for the specific dopant. Unfortunately, by using the Maxwell-Bloch equations, we restrict our treatment to a two-level system which is not consistent with a doped fiber. Due to the amorphous nature of silica glass and the manifolds which participate in the gain process, the emission and absorption spectrum for doped fibers are not simple functions. For this reason in addition to brevity, we omit such a detailed derivation and simply point out that in the most simplistic sense every gain media must saturate. Since it cannot provide more power than it is pumped with, energy must be conserved. In general, propagation through such a gain media, ignoring dispersion, nonlinearity, etc., is governed by

$$\frac{\partial A(t,z)}{\partial z} = \frac{1}{2}\int_{-\infty}^{\infty} g(t-t')A(t',z)dt' + N(t), \tag{4.75}$$

where we have introduced a noise term $N(t)$ due to amplified spontaneous emission (ASE). In the case of rare-earth doped fibers, where the upper state lifetime is ~ 1 ms, the saturation is based on the average power traveling through the gain media and may be written as

$$g(t,z) = \frac{g_0(z)}{1+P_{ave}(z)/P_{sat}}\int_{-\infty}^{\infty} \tilde{g}_s(\omega)e^{-i\omega t}d\omega. \tag{4.76}$$

In Eq. (4.76), $g_0(z)$ is the maximum small signal gain available at any location in the gain media (this allows one to take pump absorption into effect) and $\tilde{g}_s(\omega)$ is an arbitrary function which describes the normalized wavelength dependence of the gain. By introducing our gain term in this manner, we alow ourselves the ability to account for the shape of the emission cross spectrum if we wish. In this equation,

$$P_{ave}(z) = \frac{1}{T_m}\int_{T_m/2}^{T_m/2} |A(t,z)|^2 dt \tag{4.77}$$

is the average power passing through the gain medium (assuming a mode-locked laser), where T_m is the spacing between adjacent pulses and is inversely related to the repetition

rate of the system.

For an ideal two-level homogenously-broadened system, the spectral shape takes a Lorentzian profile[126]

$$g_s(\omega) = \frac{1}{1+(\omega-\omega_g)^2 T_2^2} \tag{4.78}$$

where we have introduced the dipole relaxation time T_2. In general, the gain in fiber lasers and amplifiers is inhomogeneously broadened due to the amorphous nature of silica glass. Such a gain spectrum is usually more consistent with a Gaussian shape, yet the Lorentzian approximation is commonly used as it allows one to develop an analytic treatment and produces good results. Regardless of the shape chosen, the gain spectrum can always be approximated as

$$g_s(\omega) \approx 1-(\omega-\omega_g)^2 T_2^2, \tag{4.79}$$

by Taylor expanding it; however, we caution that this shape is only valid around ω_g.

To continue, we assume that the carrier wavelength of the light to be amplified is close to ω_g ($\omega_g \approx \omega_0$) and substitute Eq. (4.79) into Eq. (4.76) which, using the Fourier transform, gives us the effect of the gain medium on the optical field:

$$\frac{\partial A(t,z)}{\partial z} = \frac{g_0(z)/2}{1+P_{ave}(z)/P_{sat}}\left[A(t,z)+T_2^2\frac{\partial^2 A(t,z)}{\partial t^2}\right]. \tag{4.80}$$

Next we assume that the gain and the optical intensity of our field are constant throughout the length of our gain medium which simplifies our result to

$$\frac{\partial A(t,z)}{\partial z} \approx \frac{g_{sat}}{2}\left[A(t,z)+T_2^2\frac{\partial^2 A(t,z)}{\partial t^2}\right], \tag{4.81}$$

where $g_{sat} = g_0(1+P_{ave}/P_{sat})^{-1}$. This assumption is only valid for lasers where the losses are small and evenly distributed. Therefore, Eq. (4.80) must be used to model lasers with large losses. In order to develop an analytic treatment in what follows, however, we assume that Eq. (4.81) is valid.

So far this derivation has ignored the effects due to propagation in an optical material as previously derived in this work. We may include these terms by noting that

although the parameter values may have a complicated dependence when the material is pumped (or excited), but their values should be fixed for a given set of parameters. Thus, we simply add the effect of gain, as shown in Eq. (4.81) to the NLSE [Eq. (4.73)] where we choose to retain the effects of dispersion up to third order:

$$\frac{\partial A(\xi,T)}{\partial \xi} + \frac{i}{2}\left(\beta_2 + i g_{sat} T_2^2\right)\frac{\partial^2 A(\xi,T)}{\partial T^2} - \frac{1}{6}\frac{\partial^3 A(\xi,T)}{\partial T^3} = i\gamma|A(\xi,T)|^2 A(\xi,T) + \frac{1}{2}\left(g_{sat} - \alpha\right)A(\xi,T) + N(t). \tag{4.82}$$

Although Eq. (4.82) has no known analytic solution, if the effects of the noise term and third-order dispersion (TOD) are both ignored, this equation reduces to the well-known Ginzburg–Landau equation, which has the following shape-preserving solution[127] known as an autosoliton[128] or a dissipative soliton:[129]

$$A(\xi,T) = a\left[\operatorname{sech}(T/\tau)\right]^{1+iq}\exp(i\kappa\xi), \tag{4.83}$$

In Eq. (4.83) the various terms we introduced are related to those of the system through the relations

$$\tau^2 = \frac{g_{sat}T_2^2 + \beta_2 q}{g_{sat} - \alpha}, \tag{4.84}$$

$$a^2 = \frac{1}{2\gamma\tau^2}\left[\left(q^2-2\right)\beta_2 + 3g_{sat}T_2^2 q\right], \tag{4.85}$$

$$\kappa = -\frac{1}{2\tau^2}\left[\left(1-q^2\right)\beta_2 - 2g_{sat}T_2^2 q\right], \tag{4.86}$$

$$q = \frac{3\beta_2}{2g_{sat}T_2^2} \pm \sqrt{\left(\frac{3\beta_2}{2g_{sat}T_2^2}\right)^2 + 2}\,. \tag{4.87}$$

The implications of such a solution will be discussed later in this thesis as they apply to mode-locked lasers.

4.2 Introduction to Fiber Amplifiers

The GLE incorporates optical amplification in a simple-minded fashion. Although the GLE can predict pulse propagation in a fiber amplifier accurately, it assumes fixed parameters for the gain and the gain saturation; they are therefore assumed to be known quantities. Moreover, the GLE ignores the effects of emission cross section and can only treat amplifier noise [commonly referred to as amplified spontaneous emission (ASE)] simplistically. If low power light is to be amplified, the background noise can grow to be large and ASE may play a significant role by causing deleterious effects such as energy fluctuations, timing jitter, and/or carrier frequency fluctuations. Its effect may be included in the GLE in an approximate fashion by assuming a noise photon is added to each mode through $N(t)$. Yet, when one is dealing with input signals of larger powers, those which saturate the gain media, the characteristics of the amplifier change because the signal can cause the ASE spectrum to shift as exited electrons are quickly converted to stimulated emission at such a high rate that the spontaneous emission, responsible for seeding the ASE, can be reduced.

As a consequence, one can develop accurate models for systems using the GLE for specific values of small-signal gain, gain saturation, and gain filtering. As the power of the pump used to invert the gain media is increased, however, these parameters change in a complex way. Experimentally, the gain media may be re-characterized for different pump powers, but it is difficult and time consuming to do so. Because of these facts, it can be both useful and insightful to treat a gain media by using a more thorough model. In this section, we do so by using the rate-equation approach. Focusing on ytterbium, which has a simple energy level structure accessible to optical frequencies that consists of two manifolds (see Fig. 4.3), we could derive the rate equations that govern the various signal powers in the gain media. However, in an effort to be pragmatic, the following rate-equations were cited from the work of Kelson and Amos:[130]

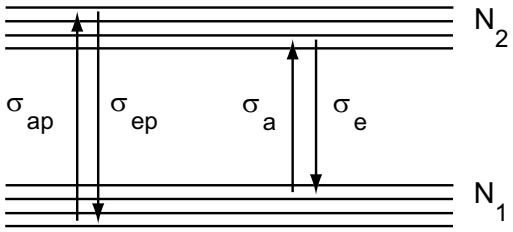

Figure 4.3: The energy level diagram for ytterbium showing the ${}^2F_{7/2}$ ground-state and ${}^2F_{5/2}$ excited-state manifolds, which are optically accessible for wavelengths ranging from $\sim$ 800-1100 nm. σ_{ap} represents pump absorption, σ_{ep} spontaneous emission due to the pump, and σ_a and σ_e are the cross-sectional absorption and emission coefficients.

$$\frac{N_2(z)}{N} = \frac{\frac{P_p(z)\sigma_{ap}\Gamma_p}{h\nu_p A} + \frac{\Gamma_s}{hcA}\int \sigma_a(\lambda)P(z,\lambda)\lambda\, d\lambda}{\frac{P_p(z)(\sigma_{ap}+\sigma_{ep})\Gamma_p}{h\nu_p A} + \frac{1}{\tau} + \frac{\Gamma_s}{hcA}\int [\sigma_e(\lambda)+\sigma_a(\lambda)]P(z,\lambda)\lambda\, d\lambda}, \quad (4.88)$$

$$\pm\frac{dP_p^{\pm}(z)}{dz} = -\Gamma_p\left\{\sigma_{ap}N + (\sigma_{ap}+\sigma_{ep})N_2(z)\right\}P_p^{\pm}(z) - \alpha(z,\lambda_p)P_p^{\pm}(z), \quad (4.89)$$

$$\begin{aligned}\pm\frac{dP^{\pm}(z,\lambda)}{dz} &= -\Gamma_s\left\{[\sigma_e(\lambda)+\sigma_a(\lambda)]N_2(z) - \sigma_a(\lambda)N\right\}P^{\pm}(z,\lambda) \\ &\quad + \Gamma_s\sigma_e(\lambda)N_2(z)P_0(\lambda) - \alpha(z,\lambda)P^{\pm}(z,\lambda), \end{aligned} \quad (4.90)$$

where $P_p(z) = P_p^+(z) + P_p^-(z)$ and $P(z,\lambda) = P^+(z,\lambda) + P^-(z,\lambda)$.

The derivation of Eqs. (4.88)–(4.90) is fairly straightforward as it simply considers the effect of a pump on a gain media where $N = N_1(z) + N_2(z)$ is used to eliminate $N_1(z)$. In this equation, N_j represents the number of electrons in level j, A is the effective area of the spatial mode, τ is the lifetime of the gain media, and Γ_j is a coefficient that describes the mode overlap between the pump and the signal. Moreover, the functions $\sigma_{ap} = \sigma_a(\lambda_p)$ and $\sigma_{ep} = \sigma_e(\lambda_p)$, where λ_p is the pump wavelength and $\sigma_e(\lambda)$ and $\sigma_a(\lambda)$ represent the emission and absorption cross sections respectively. $P_p(z)$ represents the pump power and is given in watts whereas $P(z,\lambda)$ represents the signal and ASE power and is given in units of watts/meter; both signals may be bi-directional as the fiber may be pumped from either or both ends and the ASE is always bi-directional.

These equations are easy to solve using a finite-element approach and the cross-sections for ytterbium shown in Fig. 4.4(a). Figure 4.4(b) shows the variation in ASE

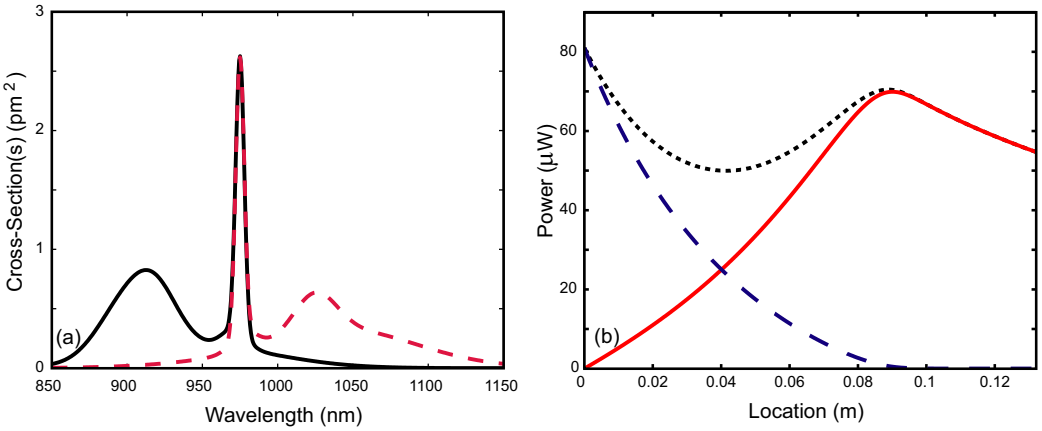

Figure 4.4: (a) The absorption (solid) and emission (dashed) cross-sections for a ytterbium-doped fiber (after Ref. [1]). (b) The forward ASE (solid), backward ASE (dashed), and total ASE (dotted) obtained by solving Eqs. (4.88)–(4.90).

powers for the forward and backward propagating ASE as well as the total ASE power along the fiber length. It was created using parameter values for a 5.2 inch piece of heavily-doped (α_p = 1170 dB/m) ytterbium fiber used to build a short-cavity laser. Figure 4.4(b) reveals that the fiber is not heavily pumped, as we can see the forward ASE rolls off since the pump has been heavily absorbed by the gain media. This fact was confirmed both computationally and experimentally by plotting the spontaneous emission as a function of fiber length in Fig. 4.5(a). Figure 4.5(b) shows the backward ASE spectrum predicted by this model. It is worth noting that Figs. 4.5(a) and (b) show good agreement between experiment and theory. The jagged features in Fig. 4.5(a) are due to scattering off of small defects in the cladding or variations in the dopant concentration with fiber length. For example, the small peak seen at $\sim$ 0.12 m is due to a splice between the doped fiber and a standard single-mode fiber. The discrepancy between the calculated ASE spectrum and that measured may be attributed to a difference between the actual absorption and emission cross-sections for this fiber and those used from Ref. [1].

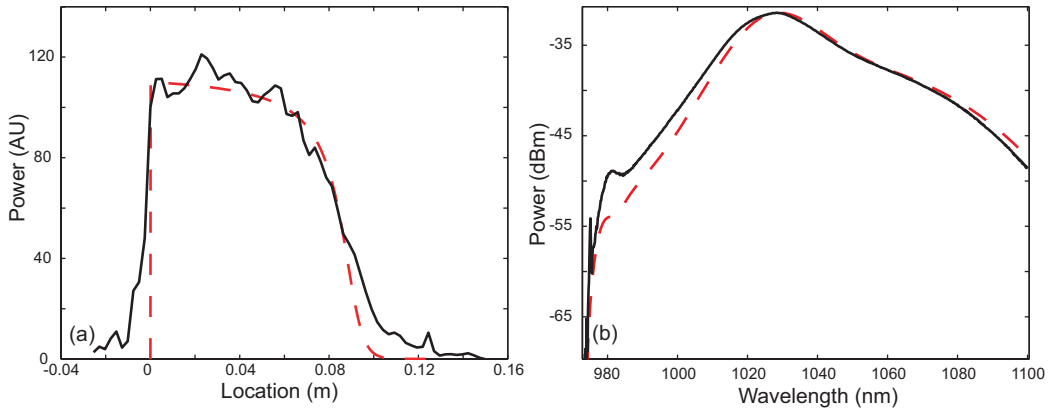

Figure 4.5: (a) Experimentally collected spontaneous emission (collected by scanning the side of the fiber with a power meter) as a function of fiber length (solid) and the numerically predicted spontaneous emission (dashed). (b) Experimentally obtained ASE spectrum (solid) and the numerically predicted ASE spectrum (dashed).

4.3 Elementary Laser Theory

A laser is simply an optical feedback loop; that is, an optical field passes through the same amplifier multiple times, thus feeding back on itself. It stands apart from its passive cousins — Fabry–Perot interferometers and ring cavities — in that it provides amplification to the field which exists within it. In this sense, a simple analogy to a laser would be when one places a microphone directly in front of its associated audio speaker. As discussed above, there is always some ASE in an amplifier system; in this analogy the speaker always emits some "static." This sound will be detected by the microphone, converted to an electronic signal, amplified by the system, and the output amplitude, i.e. the volume of the speaker, will increase. Everyone has experienced this at a concert or other venue and it represents a well-known active feedback system; in general, it results in an intense shrill sound being emitted by the speaker (as the system's gain saturates) and is only eliminated when the microphone is moved away from the speaker, certain electronic filters are applied to the signal, or the sensitivity/gain is reduced. This is also the operating principle behind a simple cw laser. We now investigate the

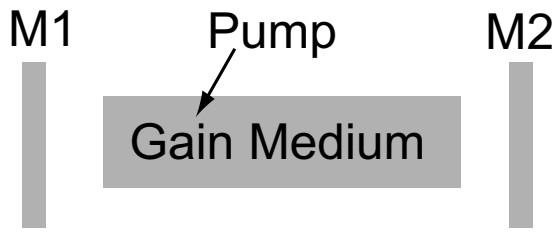

Figure 4.6: A simple Fabry–Perot laser cavity. M1 and M2 are highly reflective mirrors, and we assume that a small percentage of laser light "leaks" out the back of at least one mirror.

effects of propagation in such a system by starting from Eq. (4.82). Since we do not expect pulses in such a laser (in this simple-minded treatment), we ignore the effect of dispersion and a finite gain bandwidth. Moreover, if we focus on low power levels, we can ignore the nonlinear terms as well. Ignoring noise, we then obtain

$$\frac{\partial A(\xi)}{\partial \xi} = \frac{1}{2}\left(\frac{g_0}{1+P_{ave}/P_{sat}} - \alpha\right) A(\xi). \tag{4.91}$$

In this case, α takes into account material losses in the cavity, scattering losses, and the "loss" due to the output from the output coupler(s) or mirror(s). When $g_0(1+P_{ave}/P_{sat})^{-1} = \alpha$, we say that our laser has reached threshold since the field inside the cavity is constant: $\partial A(\xi)/\partial \xi = 0$. At this point, the gain becomes clamped, i.e. $g_{sat} = \alpha$. Otherwise our field would gain power without bound: an un-physical situation. If we pump harder, we expect that the output power will increase; however, with this simple model, we are unable to accurately factor the pump power into the expression since we do not know how g_0 or P_{sat} depend on pump power. It is possible to derive simple relations which predict this dependence, but, they are only valid in limiting regimes. For example, one such result predicts that P_{sat} is fixed and only g_0 varies; this is only valid for weakly pumped systems as P_{sat} also depends on the pump power.

To circumvent such issues, consider placing mirrors on either end of an amplifier (described by the equations in the previous section). Using this approach, we are able to accurately predict the role pump power plays. The result is that the output power grows from nothing until a transition region is entered. In the transition region, the output power grows exponentially with respect to input power until the laser reaches

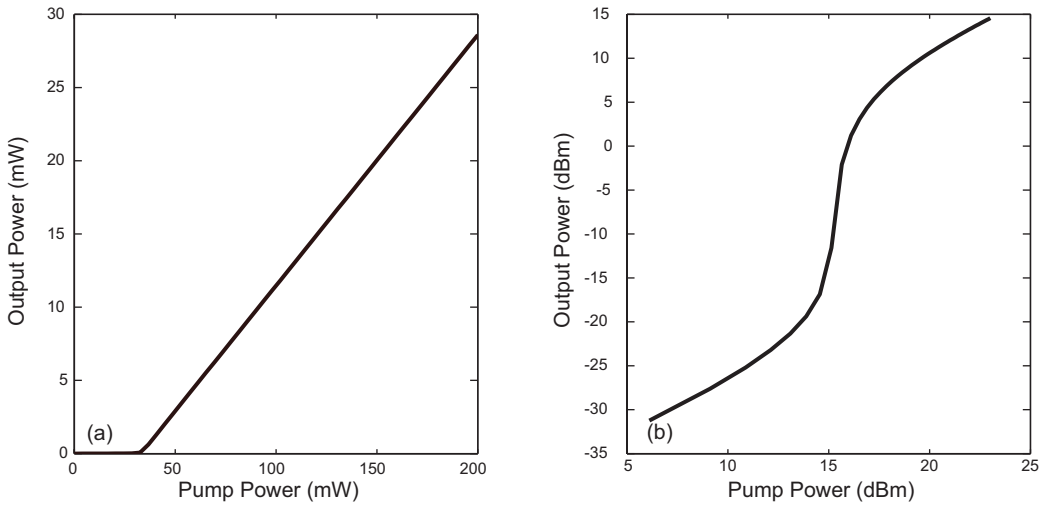

Figure 4.7: (a) Output power as a function of input power. (b) A log-log plot reveals the below-threshold (pump <34 mW for this laser) dynamics including the phase transition, which cannot be resolved in (a).

threshold,* after which point the laser output power maintains a linear relationship with the pump power until the gain medium is no longer able to supply gain or thermal or nonlinear effects become important. This behavior can be seen in Figs. 4.7(a) and 4.7(b). Figure 4.7(a) shows the conventional picture of laser behavior where a sharp transition region exists ∼34 mW. From this point on the output power is linear with respect to the pump power; this is one reason that slope efficiency is a valuable figure of merit for lasers. By plotting the same data on a log-log plot in Fig. 4.7(b), we clearly see the phase transition that occurs around 15 dBm.

4.4 Overview of Mode Locking

Mode locking is a technique that can be applied to a laser to coax/force it into producing pulses as opposed to cw light. Although mode locking may be described in either

*Note that the threshold predicted by this model will deviate from that predicted in Eq. (4.91) above due to the presence of ASE in this treatment.

the time domain or the frequency domain, as discussed in the introduction, this thesis focuses on the time-domain picture since it has led to more analytical results and allows one to easily develop an innate physical picture for the mode-locking process. Of course the time domain and frequency domain are inherently linked and the two pictures are complementary. In the time-domain picture, one either thinks of a mode-locked pulse as a ball bouncing around in a resonator or one thinks of the pulse as a particle that gets trapped by a potential formed by the mode locker. In either picture, the pulse develops a specific shape, width, chirp, etc. based on the parameters of the laser and the mode locker. The frequency-domain picture of mode locking consists of viewing the different cavity modes and noting that they maintain a constant phase relationship with one another; in essence, they are locked. One then recalls from the theory of discrete Fourier transforms that a truncated sum of exponentials looks like a pulse in the other domain. Since dispersion alters the spacing of the modes in the spectral domain, nonlinearity plays a less obvious role, and since keeping track of a large number of modes is intractable, we will use the time-domain treatment exclusively.

4.4.1 Master Equation of Mode Locking

The effect of mode locking a laser with pulses > 100 fs may be described by Eq. (4.82) if we add the effect of a mode-locking mechanism M to the field. Since we are using this approach, we have cast aside our ability to describe the effect of changes in pump power on the mode-locked pulse; still this is the most well-known treatment and it provides good results for given values of T_2, g_0, and P_{sat}. Before proceeding, it is customary to make a change of variables by setting $t = T$ and introducing $T = \xi / v_g$ where v_g is the group velocity of the optical field A(T,t). Doing so gives us Haus' so-called master

equation of mode locking:[3]

$$T_R\frac{\partial A}{\partial T} + \frac{i}{2}\left(\bar{\beta}_2 + i\bar{g}T_2^2\right)L_R\frac{\partial^2 A}{\partial t^2} - \frac{1}{6}\bar{\beta}_3 L_R\frac{\partial^3 A}{\partial t^3} = i\bar{\gamma}L_R|A|^2A + \frac{1}{2}(\bar{g}-\bar{\alpha})L_R A + M(A,t,T) + N(t). \quad (4.92)$$

It is important to note there are two time scales in this equation: the time t measured in the frame of the moving pulse and the propagation time T, often called the coarse-grained time.[39] Since we averaged over a single round trip, T is measured in terms of the round-trip time $T_R = L_R/v_g$. It is assumed that the time scale associated with the pulse is sufficiently smaller than T_R; therefore, the two times are essentially decoupled. This treatment is valid for most mode-locked lasers for which T_R exceeds 1 ns and pulse widths are typically less than 100 ps. However, the effect of the mode locker $M(A,t,T)$ has been written to allow for the possibility that it can change on the round-trip time scale. This type of behavior leads to effects such as Q-switching, FM oscillation, and modulator detuning.

The overbar in Eq. (4.92) denotes the averaged value of the corresponding parameter; for example, $\bar{\beta}_2$, $\bar{\beta}_3$, $\bar{\alpha}$ and $\bar{\gamma}$ represent the second-order dispersion, TOD, loss, and nonlinearity, respectively, averaged over the cavity length. The gain medium's finite bandwidth is assumed to have a parabolic filtering effect with a spectral full width at half maximum (FWHM) given by $\Delta_\omega = 2/T_2$. $T_m = F_{rep}^{-1} = m^{-1}T_R$ is the pulse slot, where F_{rep} is the frequency at which our laser is mode locked, and m is an integer ≥ 1 representing the harmonic the laser is mode locked at.

4.4.2 Saturable Absorption Mode Locking

In mode locking by use of a saturable absorber, the optical field experiences a time dependent loss. In this type of mode locking the field is gated by itself. Since no electronics are required, it is referred to as a type of "passive" mode locking. Common devices that act as saturable absorbers are saturable Bragg reflectors (SBRs),[131,132] semi-

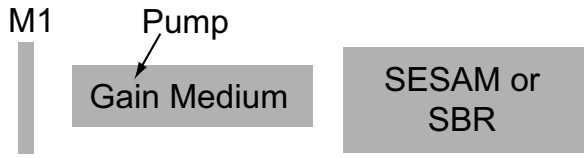

Figure 4.8: A simple saturable absorption mode-locked Fabry–Perot laser cavity. M1 and M2 are highly reflective mirrors; we assume that a small percentage of laser light "leaks" out the back of at least one mirror. In this laser, SA is assumed to be either a SBR or a SESAM.

conductor saturable absorber mirrors (SESAMs),[91] nonlinear optical loop mirrors,[32–34] nonlinear polarization rotation (NLPR) within a section of fiber in conjunction with a polarizing beam splitter,[35] APM, and various (carcinogenic) dyes which possess saturable absorption and were mainly investigated in the 1970's and 1980's.

Despite the device used, all saturable absorption mode lockers work on the principle that their loss decreases when they are probed with more intense powers. This effect naturally leads to pulse formation in a laser cavity where, for a fixed average power, cw light encounters more loss than a pulse. This can be seen in Fig. 4.9(a) where the attenuation experienced by light in a saturable absorber decreases with increasing power. The fact that this favors pulsed operation over cw operation is demonstrated in Fig. 4.9(b) by noting that, for a given energy, a pulse will experience less loss if it can temporally compress since its peak power will increase. Figure 4.9(c) clearly demonstrates that a saturable absorber temporally compresses pulses.

The effect of saturable absorption is mathematically formulated in a manner similar to the way in which gain saturation was taken into account (except the response time is assumed to be instantaneous here) and the intensity-dependent loss is written as

$$\alpha[A(t,T)] = \frac{\delta_{SA}}{1+\frac{|A(t,T)|^2}{I_{sat}}}. \tag{4.93}$$

Therefore, pulse propagation in a laser mode locked with a saturable absorber is mod-

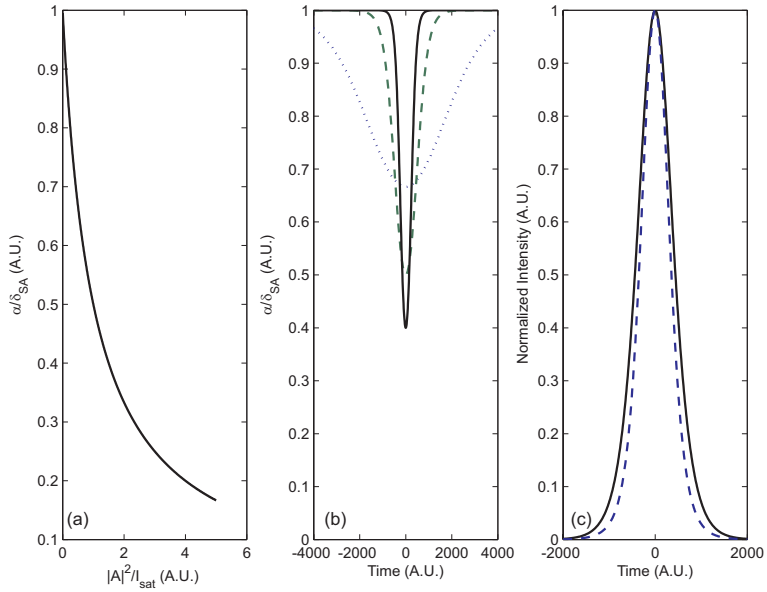

Figure 4.9: (a) Saturable absorption loss experienced by a cw field. (b) Time-dependent loss coefficient for a hyperbolic-secant pulse with a constant energy and peak intensities 0.5 (dotted), 1 (dashed), and 1.5 (solid) (in units of I_{sat}) demonstrates the losses experienced by different pulse widths due to a fast saturable absorber. (c) The input pulse [with a peak intensity of 1 from (b)] (solid) and the normalized output pulse after passing through a saturable absorber of length 1 (dashed).

eled by

$$T_R\frac{\partial A}{\partial T} + \frac{i}{2}\left(\bar{\beta}_2 + i\bar{g}\bar{T}_2^2\right)L_R\frac{\partial^2 A}{\partial t^2} - \frac{1}{6}\bar{\beta}_3 L_R\frac{\partial^3 A}{\partial t^3}$$
$$= i\bar{\gamma}L_R|A|^2A + \frac{1}{2}(\bar{g}-\bar{\alpha})L_R A - \frac{\delta_{SA}}{2}\left(1+\frac{|A|^2}{I_{sat}}\right)^{-1}A + N(t). \qquad (4.94)$$

Alas, Eq. (4.94) has no analytic solution. However, we can obtain an approximate analytic solution if we neglect the effects of noise, third-order dispersion, and also assume $|A|^2 \ll I_{sat}$. Under this approximation, we Taylor expand the effect of the saturable absorber. This gives us a differential equation describing the simplified laser

described above:

$$T_R\frac{\partial A}{\partial T} = -\frac{i}{2}\left(\bar{\beta}_2 + i\bar{g}T_2^2\right)L_R\frac{\partial^2 A}{\partial t^2} + i\bar{\gamma}L_R|A|^2A + \frac{1}{2}\left(\bar{g}-\bar{\alpha}\right)L_RA - \frac{\delta_{SA}}{2}\left(1-\frac{|A|^2}{I_{sat}}\right)A. \tag{4.95}$$

Once again we seek the existence of a field A that satisfies this equation. In this case, we note that Eq. (4.95) is similar to Eq. (4.82) and use Eq. (4.83) as an ansatz:

$$A(T,t) = a_0\left[\mathrm{sech}(t/\tau_0)\right]^{1+iq}\exp(i\kappa T). \tag{4.96}$$

Substituting Eq. (4.96) into Eq. (4.95) gives us the following pulse parameters:

$$a_0^2 = \frac{1}{2\bar{\gamma}\tau^2}\left[(q^2-2)\bar{\beta}_2 + 3\bar{g}T_2^2q\right], \tag{4.97}$$

$$\kappa = -\frac{L_R}{2T_R\tau^2}\left[(1-q^2)\bar{\beta}_2 - 2\bar{g}T_2^2q\right], \tag{4.98}$$

$$q = \frac{3\bar{\beta}_2}{2\bar{g}T_2^2} \pm \sqrt{\left(\frac{3\bar{\beta}_2}{2\bar{g}T_2^2}\right)^2 + 2 - \frac{\tau^2\delta_{SA}}{L_RI_{sat}\bar{g}T_2^2}}, \tag{4.99}$$

$$\tau^2 = -\frac{2\bar{\beta}_2q + \bar{g}T_2^2(1-q^2)}{\bar{g}-\bar{\alpha}-\delta_{SA}/(2L_R)}. \tag{4.100}$$

Compared with active mode locking, which will be discussed next, saturable absorption based mode locking allows one to generate femtosecond pulses, since saturable absorbers saturate on a femtosecond time scale and recover on a picosecond time scale; $\sim$ 200 fs pulses at repetition rates $\sim$ 10 MHz are routinely produced. Indeed, SESAM's have even been used to produce 10-GHz fundamentally mode-locked solid-state lasers.[47]

For all of its advantages, saturable absorption mode locking does have two disadvantages: the absence of pulse synchronization and the fact that these devices depend on the intracavity power. To synchronize such a laser, a phase-locked loop is often used to generate an error signal, which is in turn used to drive a piezo-electric device that adjusts the cavity length, although other techniques have also been demonstrated.[133]

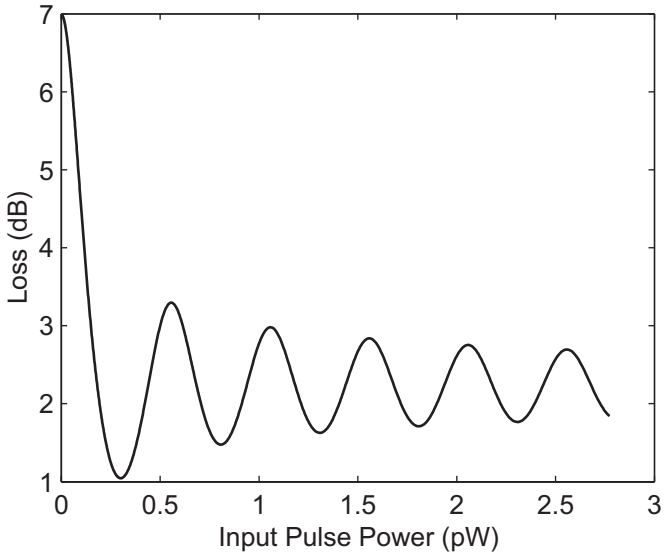

Figure 4.10: Effect Eq. (4.101) on a 220 fs FWHM hyperbolic-secant pulse as the power of the pulse is increased. In this figure, $\xi = 0.8$ and $I_{sat} = 1$ W.

Because saturable absorbers depend on the intracavity power, they also have a certain range of peak powers where they operate best. This issue manifests itself in a few ways. Specifically it means that if we change the power of the mode-locked pulse it becomes susceptible to splitting,[45, 76–78] where a single pulse may split into multiple pulses with an increase in power. Although this is related to dispersion and nonlinearity, whose combined effect can cause short intense pulses to split, it can also arise as a consequence of the mode locker. To illuminate the origin of this effect, consider a simplified model of a variant of passive mode locking; NLPR mode locking[87]

$$A_{\text{out}}(t,T) = A_{\text{in}}(t,T)\sqrt{(1-\xi)+\xi\sin^2\left(\pi|A_{\text{in}}(t,T)|^2/2I_{sat}\right)}, \tag{4.101}$$

where ξ is the modulation depth and I_{sat} is the saturation intensity. Figure 4.10 demonstrates the claim that there is an optimal power for a NLPR mode-locked laser to operate at by plotting the loss induced by this mechanism as a function of input pulse power; in this case, a 220 fs FWHM hyperbolic-secant pulse experiences its minimal loss at a power of 0.3 pW. This figure also shows the incentive for multiple pulses to form; a single pulse operating with a power ≥ 0.4 pW can experience a loss greater than

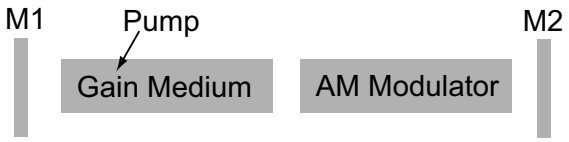

Figure 4.11: A simple AM mode-locked Fabry–Perot laser cavity. M1 and M2 are highly reflective mirrors; we assume that a small percentage of laser light "leaks" out the back of at least one mirror. AM modulator is an amplitude modulator.

the cumulative loss experienced by multiple pulses whose individual power is ~ 0.3 pW. This mode-locking mechanism was already leveraged experimentally in chapter 2, where we used this effect to induce pulse spitting and increase the repetition rate of an erbium-doped fiber laser.

4.4.3 AM Mode Locking

Mode locking through amplitude modulation, commonly known as AM mode locking, is conceptually the easiest of all mode-locking techniques to understand — in the time domain at least. It is achieved by placing an AM modulator inside a laser cavity and matching the frequency with which it is driven to a harmonic of the cavities fundamental frequency. The setup for such a laser is depicted in Fig. 4.11.

The effect of an AM modulator on the optical field is given by

$$M(A,t,T) = -\Delta_{AM}\left[1-\cos\left[\omega_m(t-T_s(T))\right]\right]A, \tag{4.102}$$

and so pulse propagation in such a laser is modeled by

$$\begin{aligned} T_R\frac{\partial A}{\partial T} &+ \frac{i}{2}\left(\bar{\beta}_2 + i\bar{g}T_2^2\right)L_R\frac{\partial^2 A}{\partial t^2} - \frac{1}{6}\bar{\beta}_3 L_R\frac{\partial^3 A}{\partial t^3} \\ &= i\bar{\gamma}L_R\left|A\right|^2 A + \frac{1}{2}\left(\bar{g}-\bar{\alpha}\right)L_R A + N(t) \\ &- \Delta_{AM}\left\{1-\cos\left[\omega_m(t-T_s(T))\right]\right\}A. \end{aligned} \tag{4.103}$$

The AM modulator has introduced a time-dependent loss into this equation. As a consequence, specific temporal locations, those that experience the lowest loss, become

more advantageous for light to align itself under. In this equation, T_s accounts for any detuning between the modulator and a harmonic of the cavity's repetition rate and is given by:[67]

$$T_s(T) = \left(\frac{T_h - T_m}{T_R}\right) T - \Delta t(T), \tag{4.104}$$

where T_m is the modulator period, T_h is the period of the cavity harmonic, and $\Delta t(T)$ can be used to include the time shift resulting from any shift in the carrier frequency. To clarify our treatment: $\Delta t(T)$, introduced by Haus in Ref. 67, simply allows us to maintain propagation in the frame of the pulse. On the other hand, if Δt is set to zero and $T_s(T) \neq 0$, a mode-locked pulse (subject to a slight detuning) would continuously drift through the simulation window.

It is interesting to note that if the effects of noise, nonlinearity, TOD, and pulse-modulator detuning are neglected one can obtain an analytic solution to this equation. By definition, a mode-locked pulse maintains all of its attributes (except for a phase ambiguity) from one round trip to the next. Therefore, we seek the existence of a field A which satisfies the governing equation

$$\begin{aligned} T_R\frac{\partial A}{\partial T} \; + \; & \frac{i}{2}\left(\bar{\beta}_2 + i\bar{g}T_2^2\right) L_R \frac{\partial^2 A}{\partial t^2} \\ & = \frac{1}{2}\left(\bar{g} - \bar{\alpha}\right) L_R A - \Delta_{AM}\left[1 - \cos\left(\omega_m t\right)\right] A. \end{aligned} \tag{4.105}$$

Unfortunately, Eq. (4.105) does not have an exact solution; however, if we assume a pulse is located at the minimum loss location of the AM modulator, we can Taylor-expand the modulator's effect and obtain the following result

$$\begin{aligned} T_R\frac{\partial A}{\partial T} \; + \; & \frac{i}{2}\left(\bar{\beta}_2 + i\bar{g}T_2^2\right) L_R \frac{\partial^2 A}{\partial t^2} \\ & = \frac{1}{2}\left(\bar{g} - \bar{\alpha}\right) L_R A - \frac{\Delta_{AM}}{L_R}\omega_m^2 t^2 A. \end{aligned} \tag{4.106}$$

Equation (4.106) is just Hermite's Differential Equation. It can be shown that only the lowest-order Hermite polynomial is stable[18] and thus one expects a solution of the form

$$A = a_0 \exp\left[-\frac{t^2(1+iq)}{2\tau_0^2}\right] \exp(i\kappa T). \tag{4.107}$$

By substituting Eq. (4.107) into Eq. (4.106), we find the pulse chirp, propagation constant, and width are given by

$$q = -\frac{\bar{g}T_2^2}{\bar{\beta}_2} \pm \sqrt{\left(\frac{\bar{g}T_2^2}{\bar{\beta}_2}\right)^2 + 1}, \tag{4.108}$$

$$\kappa = -\frac{L_R}{\tau^2 T_R}(\bar{g}T_2^2 q - \bar{\beta}_2), \tag{4.109}$$

$$\tau = \left\{\frac{L_R[\bar{g}T_2^2(1-q^2) + 2q\bar{\beta}_2]}{\Delta_{AM}\omega_m^2}\right\}^{1/4} \tag{4.110}$$

respectively. This result indicates that, in the presence of second-order dispersion, the pulses are chirped. However, if $\bar{\beta}_2 = 0$, we find that $q_+ = 0$ and $q_- = -\infty$. Clearly the $q_- = -\infty$ solution can be disregarded on physical rounds, resulting in $q = 0$ and $\kappa = 0$. Although this result also indicates that the mode-locked pulse parameters do not depend on the pulse power, our treatment ignored nonlinearity and so this is an oversimplification.

4.4.4 FM Mode Locking

Of the three mode-locking methods presented in this section, mode locking by frequency modulation (commonly termed FM mode locking) is the most conceptually difficult to understand in the time domain. In order to explain it, we will start with its effect on a field such that $M(A,t,T) = i\Delta_{FM}\cos[\omega_m(t+T_s(T))]A$, where T_s once again accounts for any detuning between the modulator and a harmonic of the cavity's repetition rate and is given by Eq. (4.104).

Using our expression for an FM mode locker, we note that the phase of the pulse is altered depending on when it passes through the modulator. It is perhaps useful to note that light passing through the modulator obtains a slight frequency shift unless it passes through the modulator at one of its extrema. This can be understood by Taylor-expanding the cosine term (where we have ignored the detuning effects for simplicity)

$$A_{out} = A_{in}e^{i\Delta_{FM}cos(\omega t)} \approx A_{in}e^{i\Delta_{FM}}e^{i\Delta_{FM}\omega t}e^{i/2\Delta_{FM}\omega^2 t^2}\ldots \tag{4.111}$$

The frequency shift imposed on the light that passes through the modulator far from an extrema will increase upon successive round trips through the cavity. Since the gain medium is assumed to exhibit a finite bandwidth, this light will eventually experience net loss as it walks out of the gain window and will die out. Only the light that passes through the modulator at one of its two extrema can exist over multiple round trips since that light does not experience a shift in its carrier frequency. In the presence of dispersion, the frequency shift will also manifest itself by causing the light to travel through the laser cavity at a different velocity then it initially had. This can lead to faster convergence times, increased stability, and even the possibility that limit cycle operation could be obtained. The effect of FM mode locking may be described by

$$\begin{aligned} T_R\frac{\partial A}{\partial T} &= -\frac{i}{2}\left(\bar{\beta}_2 + i\bar{g}T_2^2\right)L_R\frac{\partial^2 A}{\partial t^2} + \frac{1}{6}\bar{\beta}_3 L_R\frac{\partial^3 A}{\partial t^3} + i\bar{\gamma}L_R|A|^2A \\ &+ \frac{1}{2}(\bar{g}-\bar{\alpha})L_R A + i\Delta_{FM}\cos\left[\omega_m(t-T_s(T))\right]A + N(t). \end{aligned} \tag{4.112}$$

To obtain an analytic solution to this equation we must ignore noise, TOD, SPM, and detuning. Moreover we must also assume that our pulse is always located at one of the modulator's extrema. We can then Taylor-expand the cosine term to obtain

$$\begin{aligned} \frac{T_R}{L_R}\frac{\partial A}{\partial T} &+ \frac{i}{2}\left(\bar{\beta}_2 + i\bar{g}T_2^2\right)\frac{\partial^2 A}{\partial t^2} \\ &= \frac{1}{2}(\bar{g}-\bar{\alpha})A + i\frac{\Delta_{FM}}{L_R}\left(1-\frac{\omega_m^2 t^2}{2}\right)A. \end{aligned} \tag{4.113}$$

This equation is similar to Eq. (4.106) and therefore we once again seek a solution of the form

$$A = a_0\exp\left[-\frac{t^2(1+iq)}{2\tau_0^2}\right]\exp(i\kappa T). \tag{4.114}$$

By substituting Eq. (4.114) into Eq. (4.113), we find the pulse chirp, propagation constant, and width are given by

$$q = \frac{\bar{\beta}_2}{\bar{g}T_2^2} \pm \sqrt{\left(\frac{\bar{\beta}_2}{\bar{g}T_2^2}\right)^2 + 1}, \tag{4.115}$$

$$\kappa = \frac{L_R}{2T_R\tau^2}(\bar{\beta}_2 + \bar{g}T_2^2 q) + \frac{\Delta_{FM}}{T_R}, \tag{4.116}$$

$$\tau = \left\{\frac{L_R[2q\bar{g}T_2^2 - \bar{\beta}_2(1-q^2)]}{\Delta_{FM}\omega_m^2}\right\}^{1/4}, \tag{4.117}$$

respectively. This result indicates that, in the absence of second-order dispersion, FM mode-locked pulses are always chirped. However, if $\bar{\beta}_2 = 0$ and $q_\pm = \pm 1$ this result indicates that the mode-locked pulse parameters do not depend on the pulse power. This simplistic result is a consequence of our omission of any nonlinear effects and similar to the finding in our treatment of AM mode locking.

4.5 Conclusion

In conclusion, this chapter provided a brief but detailed introduction to pulse propagation in optical fibers starting from Maxwell's equations. By providing such a derivation, all of the simplifying assumptions used to obtain the traditional equations governing pulse propagation in optical fibers are clearly seen. The equations which govern optical amplifiers, cw lasers, and mode-locked lasers were also introduced. This chapter could be thought of as the physical and theoretical foundation on which all of the analytical and numerical work reported in later chapters of this thesis is based.

5 Numerical Simulations

Although experimental results were the intended focus of this work, without a good physical understanding of what is going on within a laser cavity, one limits the results he or she can achieve. This opinion is best demonstrated by the recent work of Ilday *et al*. who relied heavily on numerical simulations to help them build their "similariton" fiber laser.[40] It is worthy to note that a different and better-funded group had unsuccessfully tried to build such a laser before Ilday and co-workers started their work. Moreover, the similariton laser has the same cavity design as that of the original stretched-pulse fiber laser,[38] and so it is highly likely that this regime of operation had been experimentally discovered in the past and ignored (due to researchers either focusing only on generating short pulses or not understanding what they discovered).

Since mode-locked lasers are governed by nonlinear partial differential equations, which generally do not posses analytic solutions, the ability to model the pulses which they should produce is important. In this chapter we describe the modeling process and use it to explore the possibility of autosoliton pulses existing in the FM mode-locked fiber laser of chapter 2.

5.1 Introduction

It is well known that the propagation of ultrashort pulses in optical fiber is governed by the nonlinear Schrödinger equation (NLSE).[45] In the anomalous-dispersion regime, this equation allows for the fundamental-soliton solution that represents an optical pulse whose shape and width are invariant under propagation. In the context of fiber lasers, the NLSE must be modified to account for loss, gain, gain filtering, and a mode-locking element. Although the resulting equation has no closed form solution, it is well known that passive mode-locking mechanisms, such as nonlinear polarization rotation, nonlinear fiber-loop mirrors, and saturable absorbers, produce "soliton-like" pulses.[134]

Contemporary investigations into actively mode-locked lasers in the presence of dispersion and nonlinearity have not attracted as much attention as the above-mentioned passive techniques. This is most likely due to the shorter pulse durations that the passive approaches produce. Of course, there is still a demand for actively mode locking lasers since doing so provides a simple means by which one can ensure self-starting, increase the laser's repetition rate (through harmonic mode locking), and synchronize the laser pulses to a master clock.[35] In a laser devoid of dispersion and nonlinearity, both amplitude modulation (AM) and frequency modulation (FM) mode-locking techniques produce Gaussian pulses.[2] However, the existence of an FM mode-locked "soliton" laser in the presence of dispersion gain filtering and nonlinearity has not yet been fully investigated.

Haus and Silberberg were the first to address the effects of dispersion and nonlinearity on actively mode-locked lasers in 1986.[3] They found that the pulse width in an AM mode-locked laser can be reduced inside the cavity by introducing a nonlinear medium. This effect, known as soliton pulse compression, was first experimentally demonstrated in an AM mode-locked fiber laser by Kafka *et al*. in 1989.[31] Later, Kärtner *et al*. applied soliton perturbation theory to show that a stable soliton can exist in an AM mode-locked laser which incorporates dispersive and nonlinear elements.[39] Other relevant work nu-

merically compared both AM and FM mode-locked lasers to show that, in the presence of a Kerr medium, both pulse profiles become increasingly "sech-like" as either the gain is increased[135] or the modulation depth is decreased (AM only).[136] More recent efforts have addressed soliton stability in AM mode-locked, inhomogeneously broadened, lasers.[137]

Given the body of literature addressing actively mode-locked lasers, it is surprising to note that no concentrated effort has been directed toward FM mode-locked "soliton" lasers. Since such a venture may seem to be a logical extension of the prior AM efforts we point out that AM and FM mode-locking schemes differ in key areas. FM mode lockers interact with self-phase modulation (SPM) in a direct manner, whereas AM mode lockers affect the cavity loss and literally carve pulses out of cw light. As a consequence, FM mode lockers do not require biasing while their AM counterparts do.[66] Although it is well known that FM mode-locked lasers can jump between two degenerate operating states,[16] a dispersive laser cavity breaks this degeneracy and suppresses the laser's tendency to switch states.[4,66] Experimental work with FM mode-locked fiber lasers has also produced quasi-transform-limited pulses with time-bandwidth products as low as 0.30,[30] indicating "soliton" formation.[30,66,138,139] Still, the lack of an analytic theory capable of explaining FM mode locking in fiber lasers is not surprising in view of the difficulty in solving the governing nonlinear equation with the inclusion of an active mode-locking element.

We already investigated the operation of a high-repetition-rate, harmonically FM-mode-locked, ytterbium fiber laser experimentally[73] in chapter 2. We now investigate this laser numerically and semi-analytically. The approach used to model the laser is discussed below where the numerically obtained results are found to agree well with the experimental data, which verifies the accuracy of the model and the characterization of the laser.

5.2 Experimental Results

The FM technique has been used to mode lock erbium fiber lasers with time-bandwidth products as low as 0.30.[30] Although it has been suspected that this type of laser can produce hyperbolic-secant pulses,[4,30,66,67,135] neither the shape of the output pulses nor their spectra were experimentally investigated further than the fitting of autocorrelation traces. Most ytterbium fiber lasers reported to-date have used a passive mode-locking mechanism to take advantage of ytterbium's broad gain bandwidth and generate short pulses at relatively low repetition rates ($\leq$ 100 MHz). For example, a ytterbium fiber laser produced 36 fs mode-locked pulses,[140] the shortest to-date from any fiber laser, however, the repetition rate was below 50 MHz.

Ytterbium's large saturation fluence has also been exploited in the pursuit of high-power amplifiers and lasers. This feature also makes it an ideal gain medium for mode locking at higher harmonics where the laser's power must be split among a large number of circulating pulses. In chapter 2, we used the FM technique in a ytterbium fiber laser to produce mode-locked pulses at a high repetition rate exceeding 10 GHz.[73] The laser configuration is shown again in Fig. 5.1(a), where the combination of a half-wave plate ($\lambda/2$) and polarizing beam splitter (PBS2) not only provides variable output coupling, but also sets a linear polarization for the FM modulator and the grating pair. The measured average power at each of the three output ports is also indicated in Fig. 5.1(a).

A 30-mW mode-locking threshold was measured, but the 976-nm pump laser was operated at 150 mW to maximize the output power. All of the experimental results were obtained at this pump power using the output from port 1. The cavity also incorporates a grating pair to compensate the normal dispersion introduced by 1 m of ytterbium-doped fiber and 1.2 m of fiber associated with the 976/1050-nm WDM coupler. The net second- and third-order cavity dispersions, $d_2 = \int_0^L \beta_2(z)dz$ and $d_3 = \int_0^L \beta_3(z)dz$ (where L is the distance during one round trip within the cavity and β_2 and β_3 are the second- and third-order dispersion parameters), were measured to be $d_2 = -6.3 \times 10^4$ fs^2 and

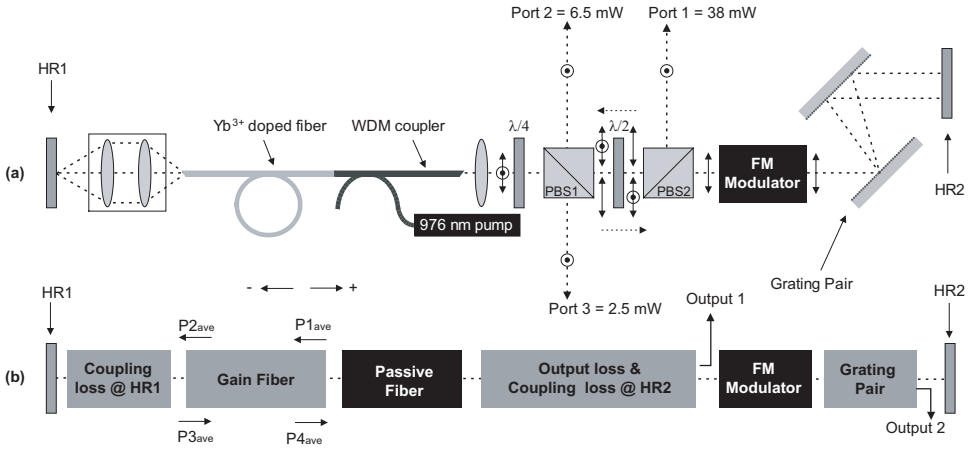

Figure 5.1: (a) Experimental laser configuration: HR, high-reflectivity mirrors; PBS, polarizing beam splitters; WDM, wavelength division multiplexer. The double sided arrows and the dots surrounded by circles represent the horizontal and vertical polarizations respectfully. (b) Numerically modeled laser configuration: the coupling losses take into account all cavity losses at the respective cavity ends, including the laser outputs.

$d_3 = 130.6 \times 10^4$ fs^3, respectively. This measurement, performed using a SESAM in place of HR1 and an *in-situ* technique (see Section 3.5 for more detail),[92] shows that this laser operates in the anomalous-dispersion regime.

All intracavity losses at the grating-pair side of the cavity (including the laser outputs) were measured individually and combined for a total power loss of 96% as the pulses pass through the grating pair, FM modulator, and the PBSs. Power losses at the HR1 cavity end were estimated to be approximately 20%. The small signal gain of the ytterbium-doped fiber was measured to be 4.3 ± 0.4 m^{-1} by using a narrowband CW laser (Koheras Y10-PM) operating at 1053 nm (see also Section 3.3). The gain-bandwidth was approximated by the 25-nm full width at half maximum (FWHM) of the amplified spontaneous emission (ASE) spectrum.

The optical spectrum of the mode-locked pulses is shown in Fig. 5.2 and has a FWHM of 0.8 nm. This spectrum is best fit by a function of the form $S(w) = S_0 \mathrm{sech}^2[(\omega - \omega_0)/\Delta\omega]$, as shown by the dotted curve in Fig. 5.2 (almost indistinguishable from the numerically obtained result which is discussed in Section 5.3), where $\Delta\omega/2\pi =$

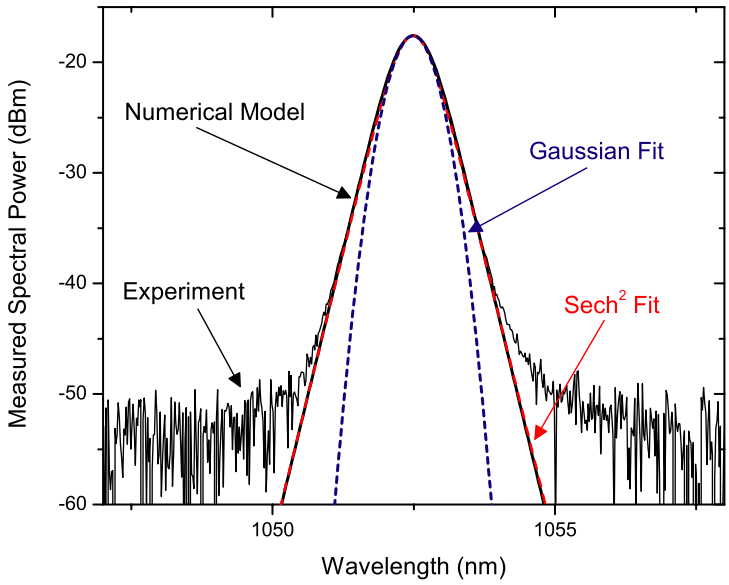

Figure 5.2: Experimentally measured pulse spectrum (solid curve with -55 dBm noise background), a hyperbolic secant fit (dashed red), a Gaussian fit (dotted blue), and the numerically simulated spectrum (solid black).

118.729 GHz. For comparison, the dashed curve shows the poor agreement obtained when a Gaussian fit is used. Assuming a transform-limited $\mathrm{sech}^2(t/\Delta t)$ pulse shape, this corresponds to a temporal pulse width of $\Delta t = 0.85$ ps (FWHM = 1.5 ps). Interferometric autocorrelation measurements, performed using two-photon absorption inside a photomultiplier tube,[94] yield a temporal FWHM of 2.0 ± 0.5 ps. This measurement indicates that our pulses are close to their transform limit.

In our actively mode-locked fiber laser the characteristic dispersion and nonlinear lengths are much longer than the 2.2 meters of fiber in the cavity. The dispersion length, $L_D = T_0^2/|\beta_2|$, for the 2-ps pulses is 45 m using the fiber's dispersion parameter $\beta_2 = 2.81 \times 10^4$ fs^2/m, or 90 m when using the cavity's average dispersion of $\bar{\beta}_2 = -1.43 \times 10^4$ fs^2/m. The nonlinear length, $L_{NL} = (\gamma P_0)^{-1}$ = 73.5 m, is calculated using a 1.13 W peak power (derived using an estimated average power of 26.5 mW in the fiber and 2-ps hyperbolic secant pulses) and the nonlinear parameter $\gamma \approx 0.012$ W^{-1}/m (mode field diameter ≈ 4.1 μm, n_2 = 2.6 $\times 10^{-20}$ m^2/W). Nonlinear

Table 5.1: Parameter Values Used in Numerical Simulations

$\beta_2 = 2.81\times10^4$ fs^2/m	$\beta_3 = 22\times10^4$ fs^3/m	$\alpha = 0.0$ m^{-1}	$\gamma = 0.012$ W^{-1}/m
$d_2^g = -9.34\times10^4$ fs^2	$d_3^g = 17.0\times10^4$ fs^3	$L_{gain} = 1.0$ m	$L_{WDM} = 1.2$ m
$g_0 = 4.3$ m^{-1}	$\Delta w_g/2\pi = 6.77$ THz	$P_{sat} = 24$ mW	$\lambda_0 = 1052.53$ nm
$F_{rep} = 10.3$ GHz	$\Delta = 0.45$	$\phi = 0$ rad	HR1 Power Loss = 20 %
HR2 Power Loss = 96 %			

polarization rotation of the intracavity field inside the 2.2 meters of fiber is negligible during a single round trip; moreover the polarizing beam splitter, PBS1, does not allow this effect to accumulate over multiple round trips. This viewpoint was experimentally confirmed by noting that rotating the quarter waveplate ($\lambda/4$) does not significantly affect the mode locking ability of the laser, although it does affect the spectral bandwidth due to the amount of loss introduced by PBS1. As a result, the pulse is not strongly affected by the dispersive and nonlinear effects during a single round trip, although these effects are certainly important over multiple round trips. We stress that this is in sharp contrast with passively mode-locked fiber lasers where polarization can change considerably during a single round trip, due to nonlinear effects, and the nonlinear and dispersion lengths can be comparable with the cavity length.

5.3 Numerical Simulations

A vector NLSE is generally required to describe pulse propagation in optical fiber, fiber amplifiers, or fiber lasers,[45] however, we have already experimentally shown that nonlinear polarization rotation in our fiber laser is negligible. Assuming dynamic polarization effects can be neglected, the vector equation can be reduced to the following scalar equation,

$$\frac{\partial A}{\partial z} + i\frac{\beta_2}{2}\frac{\partial^2 A}{\partial t^2} - \frac{\beta_3}{6}\frac{\partial^3 A}{\partial t^3} = i\gamma|A|^2 A - \frac{1}{2}\alpha A + \frac{1}{2}\int_{-\infty}^{\infty} g(t-t',z)A(t',z)dt', \quad (5.1)$$

where

$$g(t,z) = \frac{g_0(z)}{1+P_{ave}(z)/P_{sat}} \int_{-\infty}^{\infty} \tilde{g}_s(\omega) e^{-i\omega t} d\omega. \tag{5.2}$$

In this equation, A represents the slowly varying envelope of the optical field, β_2 and β_3 account for the second- and third-order fiber dispersion, and γ is the nonlinear parameter of the fiber. The fiber loss is given by α and the gain, whose time dependence results from a finite gain bandwidth, is given by $g(t,z)$. Since the gain bandwidth of our ytterbium fiber was estimated to be 25 nm ($\Delta w_g/2\pi = 6.759$ THz) and the laser produced pulses with less than 1-nm of bandwidth, the spectral filtering is not expected to strongly influence the pulse shape and the gain spectrum is approximated by a parabola $\tilde{g}_s(\omega) = (1 - 4\omega^2/\Delta\omega_g^2)$. We also assumed that the small signal gain over the 1-m of doped fiber is approximately constant, setting $g_0(z) = g_0$. Since the temporal separation between adjacent pulses in this laser ($\sim$ 100 ps) is much shorter than the relaxation time of ytterbium ($\sim$ 1.5 ms), the gain is saturated by the location-dependent average power of the pulses as shown in Eq. (5.2). The location dependent average power was determined using

$$P_{ave}^{\pm}(z) = \frac{1}{T_m} \int_{-T_m/2}^{T_m/2} \left| A^{\pm}(t,z) \right|^2 dt, \tag{5.3}$$

where $T_m = F_{rep}^{-1}$ is the duration of a single modulation cycle and F_{rep} is the frequency with which our modulator is driven. The $+$ and $-$ superscripts denote the direction in which the field propagates as defined in Fig. 5.1(b). In Eq. (5.2) $P_{ave}(z)$ was computed by summing the average powers of the counter propagating pulses for each spatial step using $P_{ave}(z) = P_{ave}^{+}(z) + P_{ave}^{-}(z)$. The gain saturation power, $P_{sat} = 24$ mW, was estimated by requiring that the model produce the measured average output power of $P4_{ave}$ = 62 mW [see Fig. 5.1(b)].

Our model uses Eq. (5.1) to propagate the pulses within the laser's active $[g_0(z) = g_0]$ and passive $[g_0(z) = 0]$ fiber sections. It then considers the influence of the other cavity elements individually, as depicted in Fig. 5.1(b). For example, we assume that the 600-grooves/mm grating pair acts as a dispersive element introducing single-pass second-

($d_2^g = -9.34 \times 10^4$ fs^2) and third-order dispersions ($d_3^g = 17.0 \times 10^4$ fs^3) into the cavity based on its configuration (30^0 incident angle, 12 cm separation) (see section 3.5 for a more detailed discussion).[128] The losses associated with the grating pair were lumped into a combined loss at the end mirror HR2, as previously noted in section 5.2.

The FM modulator was treated as if it modified an incident field, A_{in}, according to[2,67]

$$A_{out}(t,T) = e^{i\Delta\cos\{\omega_m[t+T_s(T)]\}}A_{in}(t,T), \tag{5.4}$$

where $\omega_m = 2\pi F_{rep}$ is the modulation frequency, assumed throughout this work to be a harmonic of the laser's fundamental repetition rate. Any time delay between the modulator and the pulse reference frame including the effect of driving the modulator at a frequency other than a harmonic of the laser cavity is accounted for by $T_s(T)$ in Eq. (5.4), which is defined in Eq. (4.104) and is set to zero unless otherwise noted. Using a high-resolution optical spectrum analyzer and a continuous-wave semiconductor laser (Sacher Lasertechnik TEC 500) operating at 1.05 μm, a modulation depth, $\Delta = 0.45$, was measured when driving the modulator with the same frequency (10.3 GHz) and power (10 W) used to mode lock the laser.* All of the parameter values used in our simulations are summarized in Table I for convenience.

The model considers a laser mode locked at its 281$^{\text{st}}$ harmonic by using a 97 picosecond temporal simulation window together with periodic boundary conditions. This simplification is commonly used and justified, in this case, through the experimental observation of low pulse-pulse amplitude and timing jitter. Furthermore, a side-mode suppression measured to be > 70 dB in Fig. 2.12 indicates that neighboring pulses exhibit a high degree of similarity.[73]

Figure 5.1(b) shows the block diagram used to model the laser shown in Fig. 5.1(a). The model "unfolds" the laser cavity, passing the slowly varying field, A, through each cavity component twice during a single round trip. The numerical results, taken at

*See section 3.2 for the results of this characterization and a more thorough discussion.

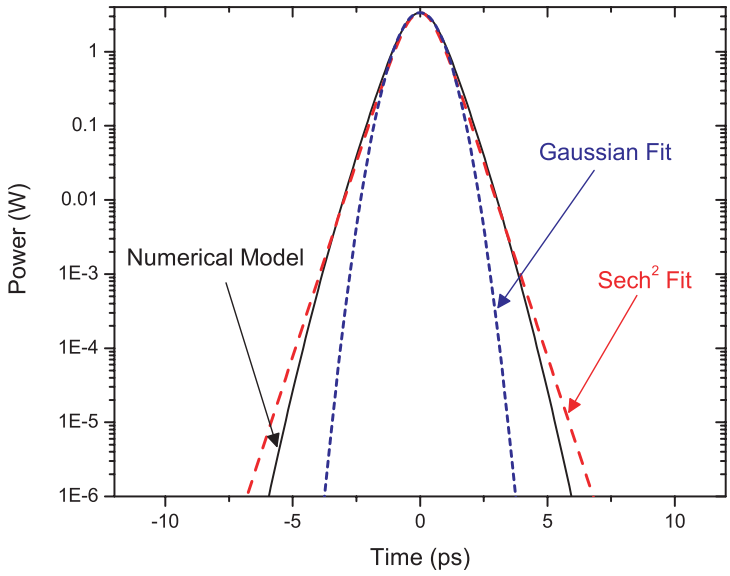

Figure 5.3: Numerically predicted temporal profile of mode-locked pulses (solid black), hyperbolic secant fit (dashed red), and a Gaussian fit (dotted blue).

"output 1" [specified in Fig. 5.1(b)] and shown by the solid curve in Fig. 5.2 (the experimental results were also extracted from the same location), were obtained by solving this problem using the symmetric split-step method[†] on a 1024-point temporal grid with 200 spatial steps per round trip. The simulated spectrum matches the $S(w) = S_0 \mathrm{sech}^2[(w - w_0)/\Delta w]$ fit to the experimental results, shown by the dotted curve (see Fig. 5.2), revealing excellent agreement.

Figure 5.3 shows the corresponding pulse in the time domain. A Gaussian fit to the numerical data is once again quite poor, whereas a hyperbolic secant fit is found to agree well. The model predicts 1.57-ps hyperbolic secant pulses, which is consistent with the experimental measurements of section 2. Figure 5.4 shows a simulated mode-locked pulse building up from noise (using a 1 photon/mode strength, complex, Gaussian-distributed, noise seed) over the first 2500 round trips, while Fig. 5.5 shows the convergence of the pulse width to its steady state value. The large number of round trips necessary before the mode-locked pulse converges is expected since the nonlinear

[†]Appendix C contains a detailed explanation of this technique.

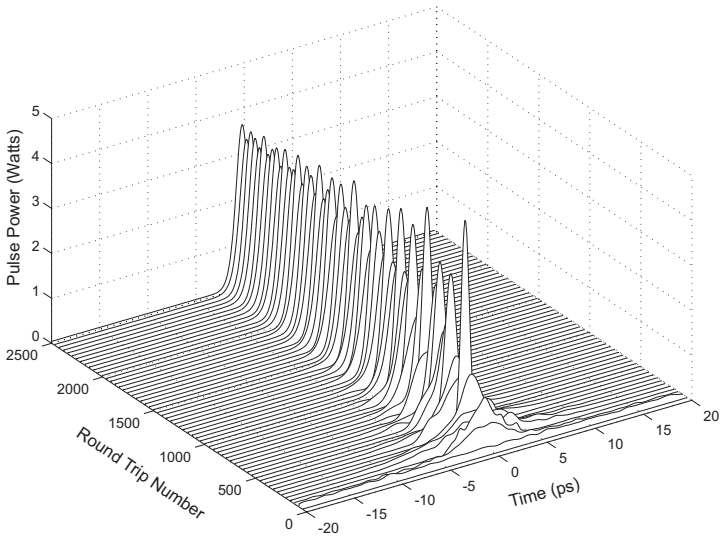

Figure 5.4: Numerically simulated pulse formation from noise. Note that the laser has not converged to a steady state even after 2500 round trips.

and dispersive effects are weak over a single round trip. As a consequence, many round trips are required before the effects of nonlinearity and dispersion balance. Finally, the FWHM as a function of location within the cavity (after the model converged) varied by < 2 % revealing that the pulse does not experience any large changes in width during a single round trip.

5.4 Effects of Pulse-Modulator Detuning

Experimentally it is difficult to insure that the modulator is always driven synchronously with the cavities fundamental repetition rate, unless regenerative mode locking is used. This occurs because any mechanical variations or thermal changes will alter the optical path length of the cavity — thereby changing its repetition rate. To be thorough, one should investigate how such changes effect the mode locking of the laser. In order to do this, we assume that the cavity length has drifted such that the driving frequency and the fundamental cavity frequency no longer coincide. As a result of the modulator's

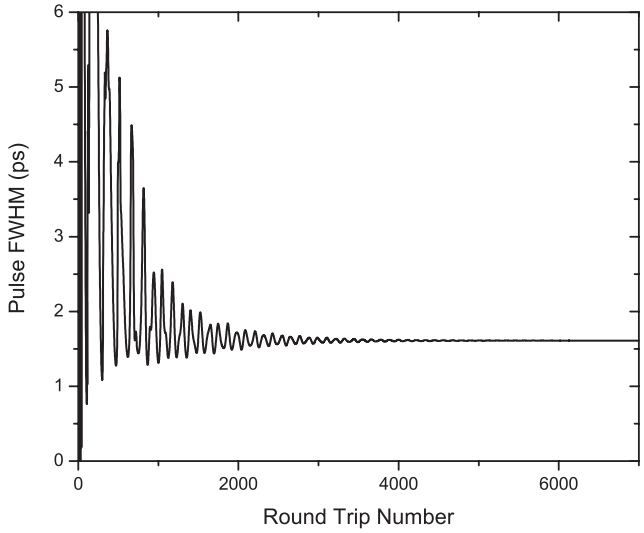

Figure 5.5: Pulse temporal FWHM as a function of round trip showing the numerical model converges to a steady state solution only after 5000 round trips.

driving frequency and the cavity's repetition rate no longer coinciding, the pulse will essentially pass through the modulator at a different temporal location each round trip and we will not obtain traditional cw mode locking. By passing through the modulator at locations other than its extremum, the pulse will experience a change in its carrier frequency. During propagation through the cavity it will adjust its temporal location through second-order dispersion. If the value of dispersion is large, the laser should remain operational even in the presence of large detunings since it should function as overdamped system. As the cavity dispersion is decreased the system will transition to an underdamped one and the temporal/spectral locations of the pulse will wander. Eventually, if the dispersion is reduced enough or the detuning is increased enough, the laser will no longer be able to form well-defined pulses and will enter into the so-called FM oscillation regime.

Therefore, for small detunings, we expect that the laser will remain mode locked, but will exhibit some time-varying properties. Figure 5.6 confirms this behavior by showing that the temporal pulse location varies on a round trip basis. Physically, this is expected. When the pulse passes through the modulator slightly detuned from the

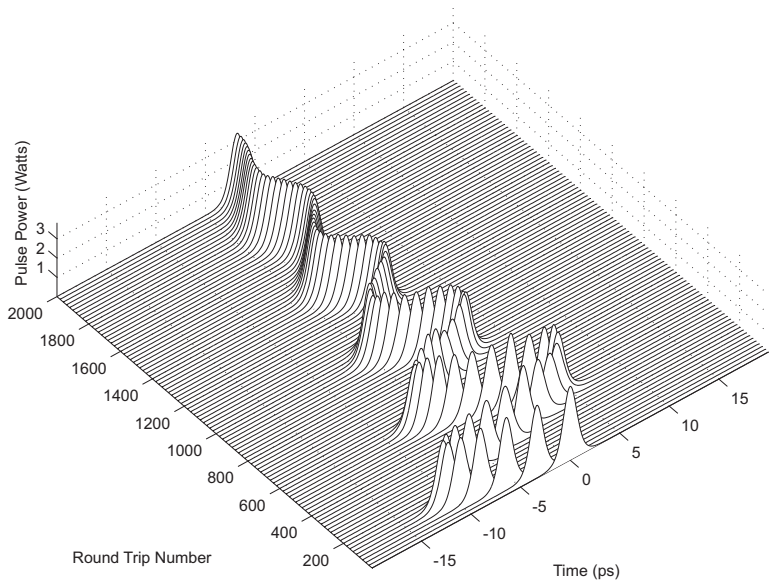

Figure 5.6: Time-domain behavior of a pulse driven by a phase modulator detuned from the cavity repetition rate by -40 kHz.

center it acquires a carrier-frequency shift. This is in turn converted to a timing shift by propagation through dispersive cavity or due to loss from spectral filtering. In the figure above, the pulse eventually stabilizes; however, it acquires a constant shift in its carrier frequency due to the detuning and does not pass through the modulator at either of its extrema, as is usually the case.

When subject to large detunings, we do not expect to achieve mode locking. Clearly there must exist a maximum detuning, at which the pulses can no longer keep up with the modulator's varying timing. By increasing the value of detuning, this regime may also be probed; to do so, however, requires a fine spectral resolution. Figure 5.7 demonstrates the results obtained from such a simulation using a 2^{17}-point temporal grid with 200 spatial steps per round trip. In order to increase the spectral resolution, the width of the temporal window was increased by a factor of 124 to allow the simulation region to extend over a 21.028 ns window. Figure 5.7(c) shows limited part of the time-domain pulse train; clearly no stable solution is present. Moreover, by allowing the computer simulation to continue, we find that this complicated structure changes from one round

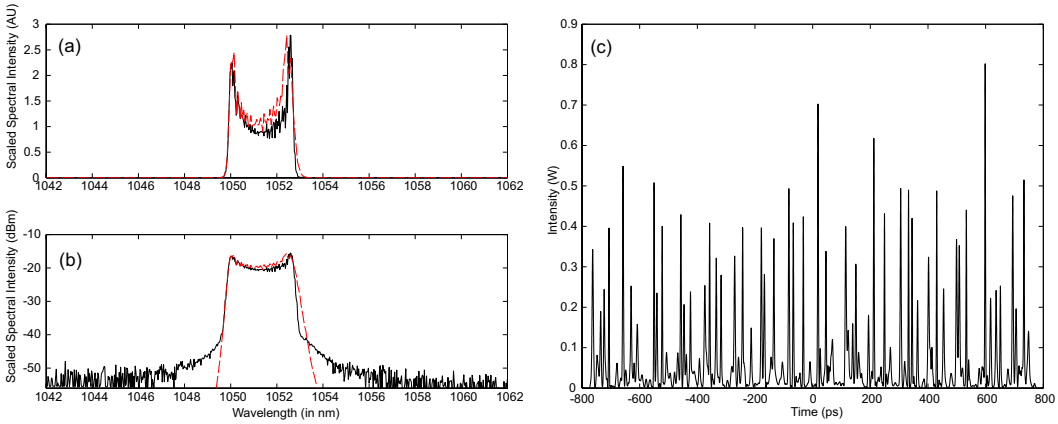

Figure 5.7: Optical spectrum of the FM mode-locked laser of Chapter 2 when the driving frequency of the FM modulator is detuned by -94 kHz from where mode-locked operation is achieved. In order to compare the computer simulations (dashed) with experimental results obtained using an OSA (solid), temporal averaging and spectral downsampling were both employed (See Appendix B for a detailed explanation of this issue and the procedure used). (a) shows the spectrum on a linear scale whereas (b) shows the spectrum on a log scale. (c) shows the corresponding pulse-train behavior in the time domain. We caution, however, that this pulse train does not coverage to a steady-state in this case.

trip to the next.

5.5 Stability of Steady-State Solutions

In the absence of dispersion and nonlinearity, an FM mode-locked laser will form pulses at either extreme $\{\omega_m[t+T_s(T)]=0$ or π in Eq. (5.4)$\}$ of the modulation cycle. This behavior has been experimentally observed in lasers where the mode-locked pulse train shifts between these two temporal locations in a random fashion.[16] In their pioneering work,[2] Kuizenga and Siegman noted that the degeneracy between these two states is broken when the modulation frequency is detuned from the laser's longitudinal mode spacing. This enables the gain medium to exhibit a dispersive effect. However, they were unable to suppress this switching experimentally.[16] Later, Tamura and Nakazawa showed that the switching between the two states is suppressed in lasers with "large"

intracavity dispersion, resulting in stable laser operation.[4] Depending on the sign of the cavity dispersion, the pulse at one of the two extremum will be spectrally broadened with respect to the other; this occurs as a consequence of modulator-induced chirp. The broader spectrum will experience more attenuation due to spectral filtering and the laser will operate in the other state to minimize loss.[4,66] Consequently, mode-locked pulses pass through the modulator acquiring a positive chirp $\{\omega_m[t+T_s(T)]=0\}$ in an anomalously dispersive cavity, while the modulator-induced chirp will be negative $\{\omega_m[t+T_s(T)]=\pi\}$ in a normally dispersive cavity.[4,66]

In this section we verify that our numerical model agrees with the findings of Tamura and Nakazawa[4,66] by subjecting a mode-locked pulse to an abrupt phase jump in the modulator's driving electronics. This allows us, for what we believe to be the first time, to investigate the pulse-switching mechanism in action, as well as the dynamical switching behavior. Two completely different pulse-switching mechanisms are also identified for the first time in the context of these lasers.

To verify that the numerical model predicts both the stable and unstable temporal operating locations, the modulator's phase is abruptly changed after a mode-locked pulse is first formed. The theory, mentioned above, predicts that stable mode-locked pulses only form under the positive cycle of the FM modulator (in our anomalously dispersive cavity) and so the pulse is expected to temporally shift. In order to keep the pulses located within the central region of our simulation window, all the simulations in this section use $\phi = T_s(T) = \pi/2$ [see Eq. (5.4)] which locates the extremum of the modulator at $\pm$ 24.25 ps. Figure 5.8 shows the effect of a half-cycle clock phase shift (48.5 ps at 10.3 GHz or $\phi \rightarrow \phi + \pi$) on a mode-locked pulse. When the clock phase is shifted, at the 2000^{th} round trip, the pulse temporally broadens and eventually its power is redistributed amongst the two nearest stable modulator extremum. Although the pulse switches as expected, it only does so after first switching to what appears to be an unstable state, as shown by the constant pulse shape in Fig. 5.8 between round trips 2500–6000.

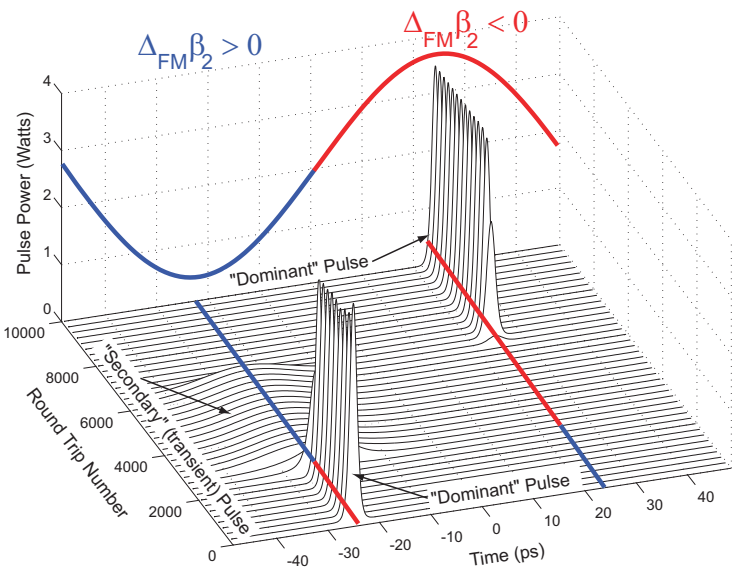

Figure 5.8: Demonstration of pulse switching. The phase of the FM modulator was changed by π at the 2000^{th} round trip, shifting the location of the stable operating points, which have been identified by the solid lines to provide a convenient visual reference.

To examine the switching mechanism in more detail, the temporal and spectral FWHM of the pulse were plotted as functions of round trip and are shown in Fig. 5.9. After shifting the modulator's phase by π, the pulse experiences a short period of spectral compression whereas the pulse temporally broadens immediately; both are followed by a constant period of broader bandwidth. To verify that this behavior is not related to a numerical anomaly, a noise term was added to Eq. (5.1) and the simulations were repeated. These results, labeled "including noise" in Fig. 5.9, reveal that even in the presence of noise there is a region after 2500 round trips where the pulse spectrum and width stabilize. To explain this switching behavior, we note that the reduced spectral width found in the first transition region, between 2000 and 2500 round trips, ensures that the effect of spectral filtering on the temporally broadening pulse is weaker than its effect on either the original pulse or the (newly shifted) stable pulse. This enables the pulse to continue broadening unabated. Since the pulse passes through the modulator extremum associated with an unstable state, it starts acquiring

an unbalanced modulator-induced chirp. This chirp results in a drastic increase in the pulse spectrum after 2500 round trips. Instead of this broadening continuing until the pulse switches states, the pulse becomes trapped in a local (globally unstable) potential due to an equalization between second-order dispersion and modulator-induced chirp. The pulse remains in this unstable/secondary state, without changing shape, until it is destabilized by the formation of the stable/dominant pulse. The stable pulse has less bandwidth (0.8 nm compared to 2.26 nm see Fig. 5.9) than its unstable counterpart. As a consequence of spectral filtering, the stable/dominant pulse will experience less loss than the unstable/secondary pulse thus providing the laser the incentive necessary to switch states. The only remaining question is how the laser actually switches between these two temporally displaced states. In our simulations we find that the stable pulses are seeded by the wings of the unstable pulse and by noise. As a consequence, when the noise was ignored many round trips were required to reach a new equilibrium, whereas faster switching was observed in the presence of noise, since it provided a stronger seed (see Fig. 5.9).

It was previously found that the inclusion of SPM, whose sign is always positive, can prohibit mode locking in the normal dispersion regime. This occurs because the modulator-induced chirp reduces the SPM-induced chirp. As a consequence both pulse formation and soliton pulse compression mechanisms are weakened.[66] In an effort to investigate the role nonlinear effects play on pulse switching in this laser, the saturation power was artificially doubled while all other parameters were held constant. Figure 5.10, which plots contours of constant intensity, examines this increased energy scenario using the same phase shift as before. This figure reveals a different switching mechanism where the pulse remains intact, shifting to the right side of the temporal window and settling down after about 2000 round trips, but only after following a zig-zag path indicative of relaxation oscillations.

The pulse shift to the right side of the window in Fig. 5.10 is not incidental; it is governed by the sign of the cavity's net third-order dispersion. When the signs of

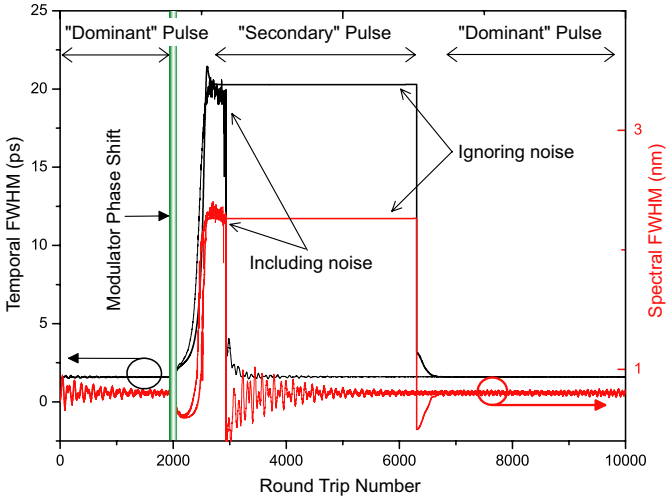

Figure 5.9: Temporal and Spectral FWHM as a function of round trip, corresponding to the data plotted in Fig. 5.8. The location where the modulator's phase was shifted is identified as well as the stable and unstable operating regimes for case where noise was ignored. The same data is also plotted when noise was included in the numerical simulations and is labeled "including noise."

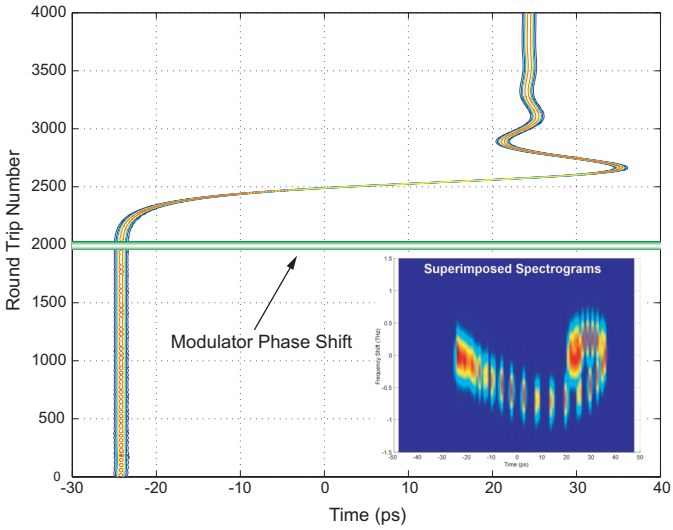

Figure 5.10: Effect of TOD on pulse switching when the cavity's TOD > 0. The pulse remains intact while temporally shifting to sync up with the (new) stable cycle of the modulator where it is once again stable.

the third-order dispersion (TOD) for both fibers and the grating pair are flipped, the pulse moves to the left side of the temporal window while exhibiting identical dynamic

features. These results, which constitute a temporal analog of a mirror image, can be understood by noting that the group velocity of a pulse is affected by finite values of TOD.

Although TOD was included in the model used to generate Fig. 5.8, the effect of SPM on the pulse was not strong enough to keep it intact when the modulator's phase was shifted; instead the pulse broadened, remaining centered on $t = 0$. Figure 5.11 summarizes our results using a cartoon (not a simulation) to focus on the effects of an abrupt phase change on two pulses in a harmonically mode-locked pulse train. Figure 5.11(a) diagrammatically shows the effect of this switching mechanism on pulse energy when the switching is governed by the growth of a new pulse from the wings of the initial pulse and/or from noise. Figure 5.11(b) examines the behavior found with increased power and positive TOD; the pulses shift in the opposite direction when TOD is negative. With their increased peak powers, the pulses seen in Figs. 5.10 and 5.11(b) can be viewed as "solitons," which are able to maintain their shape through the interplay between second-order dispersion and SPM, despite the perturbation from the FM modulator. They avoid dispersing long enough to experience the temporal kick of TOD, which sends these pulses to the stable operating points. In the absence of SPM, the pulses immediately broaden, as depicted in Fig. 5.11(a), and the effects of TOD are weakened. Larger values of TOD will encourage even these pulses to remain intact by "pushing" them towards a new equilibrium with increasing strength. However, a single pulse's energy will still be distributed between the two nearest final pulses. In this case the energy splitting will become asymmetric (from the perspective of a single pulse), favoring one operating point over the other depending on the sign of the TOD. It is also noted that arbitrarily increasing the TOD will eventually disrupt the modulator's ability to synchronize the pulses, thus disabling the mode-locking mechanism altogether.

When the modulator's phase was abruptly changed, it was found that the (shifted) stable operating states were reached more quickly with an increase in either the modulation depth or the anomalous dispersion value. The stable operating states were also

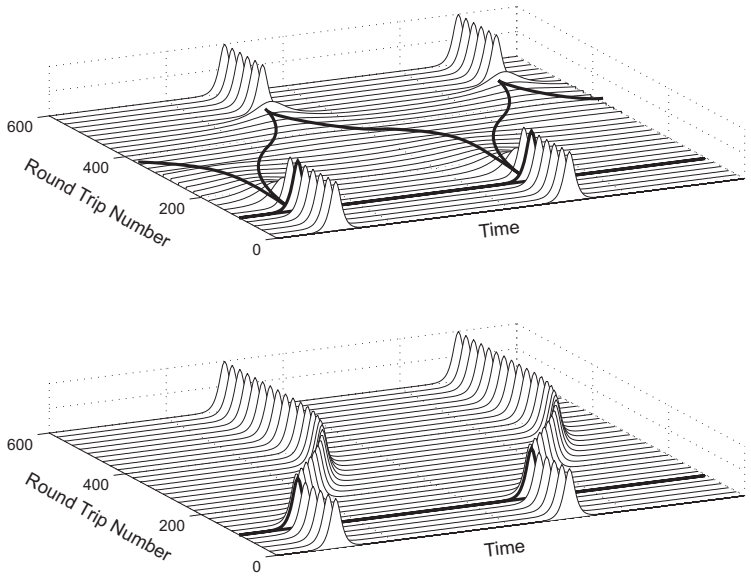

Figure 5.11: A depiction of the energy transfer between modulation cycle locations when the driving frequency is abruptly changed by a half-clock cycle for the case where: (a) SPM effects are weak and (b) SPM effects are important and TOD > 0. The darkened trace in both plots, at the 100^{th} round trip, represents the location where the modulator's phase is shifted. The solid lines in (a) show how the energy from each pulse is redistributed.

reached more quickly when a spectral filter was used or the gain bandwidth was otherwise decreased. We also find that the repetition rate becomes important since it governs the temporal separation between the stable/dominant and unstable/secondary states. At lower repetition rates, the pulses are more prone to decay since they must shift between modulator extremum temporally separated by larger amounts. We also note that the effect of TOD on the picosecond pulses simulated is weak, and so switching should occur more quickly for femtosecond pulses. The large phase jump, used in this section for demonstration purposes, is impractical in a mode-locked laser under normal operating conditions. However, the different switching mechanisms identified in this section will still occur for smaller phase jumps (due to electronic noise, thermal effects, etc.) although it may become more difficult to differentiate between them.

5.6 Implications of the Ginzberg–Landau Equation

Although passive optical fibers support solitons in the anomalous-dispersion regime, Eq. (5.1) does not have a standard soliton solution because of the presence of gain and loss. In addition to this, none of the parameters $\beta_2,\ \beta_3,\ \gamma,\ \alpha,$ or g are constants, rather they all vary over the cavity length. This situation is analogous to long-haul lightwave systems in which fibers of two or more types are used to form a periodic dispersion map.[141] In such systems new types of solitons, known as dispersion-managed solitons, exist in the form of chirped Gaussian pulses.[142] We can, however, rule this possibility out in our fiber laser because the nonlinear and dispersive effects are relatively weak, and because the pulse width barely changes during a single round trip. This is in sharp contrast to dispersion-managed lightwave systems where pulse width changes considerably. Of course the presence of a hyperbolic secant spectrum also clearly indicates that a Gaussian solution is not appropriate.

Another class of solitons exists in optical systems in which pulses experience gain and loss as they propagate. Such solitons are known as autosolitons[128] or dissipative solitons.[143] Since simulations show the pulse width does not change much during a single round trip, and our output spectrum has a hyperbolic secant profile, the pulses emitted by our laser are more consistent with autosolitons than with dispersion-managed solitons. Recent investigations into fiber lasers mode locked with multiple pulses also support this conclusion through the study of pulse interactions.[81,82] To justify this claim, we average all the parameters used in Section 3 over one round trip and write the resulting equation in the form[128,144]

$$\frac{\partial A}{\partial z}+\frac{i}{2}\left(\bar{\beta}_2+i\bar{g}T_2^2\right)\frac{\partial^2 A}{\partial t^2}-\frac{1}{6}\bar{\beta}_3\frac{\partial^3 A}{\partial t^3}=i\bar{\gamma}|A|^2A \\ +\frac{1}{2}\left(\bar{g}-\bar{\alpha}\right)A+\frac{i2\Delta}{L}\cos(\omega_m t+\phi)A, \tag{5.5}$$

where the overbar denotes the averaged value of the corresponding parameter, i.e., $\bar{\beta}_2 = \frac{1}{L}\int_0^L \beta_2(z)dz$ and so on. Finite gain bandwidth is again assumed to have a parabolic filtering effect with a spectral width given by $T_2 = 2/\Delta w_g = 47$ fs/rad. The averaged saturated gain is given by $\bar{g} = \bar{g_0}\left(1+\bar{P}_{ave}/P_{sat}\right)^{-1}$ where $\bar{P}_{ave}$, the average intracavity power, is now a constant and therefore location independent.

The strength of the modulation term in Eq. (5.5) was computationally found to have only a weak effect on the final pulse shape and width, so by assuming that we already have a pulse the modulator's effect can be neglected in this equation. We also note that actively mode-locked lasers rarely produce pulses in the femtosecond regime. One can use this as an argument to ignore the effects of TOD. Under such conditions, this equation reduces to the well known Ginzburg–Landau equation which has the shape-preserving autosoliton[128] solution:

$$A(z,t) = N_s \mathrm{sech}(t/\tau)^{1+iq}\exp(ikz), \tag{5.6}$$

where

$$\tau^2 = \frac{\bar{g}T_2^2 + \bar{\beta}_2 q}{\bar{g}-\bar{\alpha}}, \tag{5.7}$$

$$N_s^2 = \frac{1}{2\gamma\tau^2}\left[\left(q^2-2\right)\bar{\beta}_2 + 3\bar{g}T_2^2 q\right], \tag{5.8}$$

$$k = -\frac{1}{2\tau^2}\left[\left(1-q^2\right)\bar{\beta}_2 - 2\bar{g}T_2^2 q\right], \tag{5.9}$$

and

$$q = \frac{3\bar{\beta}_2}{2\bar{g}T_2^2} \pm \sqrt{\left(\frac{3\bar{\beta}_2}{2\bar{g}T_2^2}\right)^2 + 2}\,. \tag{5.10}$$

Equations (5.7)-(5.10) require the value of $\bar{g}$ which depends on $\bar{P}_{ave}$, itself a function of τ [Eq. (5.7)] and N_s [Eq. (5.8)], and so we have an underdetermined system. In order to circumvent this problem without introducing error, the value of $\bar{g}$ was obtained by numerically solving Eq. (5.5). The resulting value was then used in Eqs. (5.7)-(5.10) to

determine the parameters for the shape of the temporal field.

This analytic solution should be compared with the numerical results obtained in Section 3 before one can claim that our mode-locked laser emits autosolitons. To facilitate such a comparison, we note that the chirp parameter, q, may be computationally determined for an autosoliton by using:

$$q = \frac{i}{E}\int_{-\infty}^{\infty} t\left[A^*\frac{\partial A}{\partial t} - A\frac{\partial A^*}{\partial t}\right]. \tag{5.11}$$

Using the values $\bar{\beta_2} = -1.43545\times10^4$ fs^2/m, $\bar{\beta_3} = 29.7273\times10^4$ fs^3/m, $\bar{\gamma} = 0.012$ W^{-1}/m, $\bar{\alpha} = 0.7822771$ m^{-1}, and $\bar{g} = 0.7827525$ m^{-1}, the autosoliton approach predicts $\tau = 1.1058$ ps, and $q = 0.0802$. To compare these values with the numerical model we extract the field at "output 2" [See Fig. 5.1(b)] where it is expected to have the minimal (map-induced) chirp and therefore be consistent with an autosoliton. The numerical model predicts pulses with $\tau = 0.8912$ ps and $q = 0.0117$, yielding less than ideal agreement with the autosoliton theory.

Although we have been advocating the idea that the mode-locked pulses are autosolitons, based on the governing equation and recent work,[81,82] the merits of treating the pulses as fundamental solitons may also be investigated. By substituting ($A^{\pm}(z,t) = A_0\mathrm{sech}(t/\tau)e^{\pm ikz}$) into Eq. (5.3), using both $P_{ave} = P^+_{ave}(z) + P^-_{ave}(z) = 2P^+_{ave}$ (since the power is constant in the average model) and the fundamental soliton condition ($L_D = L_{NL}$), we arrive at the pulse width predicted by conventional soliton theory (assuming the cavity dispersion is anomalous):

$$\tau = \frac{4F_{rep}|\bar{\beta_2}|}{\bar{\gamma}P_{ave}}. \tag{5.12}$$

Using our numerically obtained average power, $P_{ave} = 35.928$ mW, and assuming a standard soliton we find that $\tau = 1.372$ ps and of course $q = 0$ by definition. Although neither prediction is accurate, the autosoliton theory is 30% closer to the numerically obtained width than the soliton theory. This indicates that there is certainly a distinction to be made between these two types of solitons in fiber lasers.

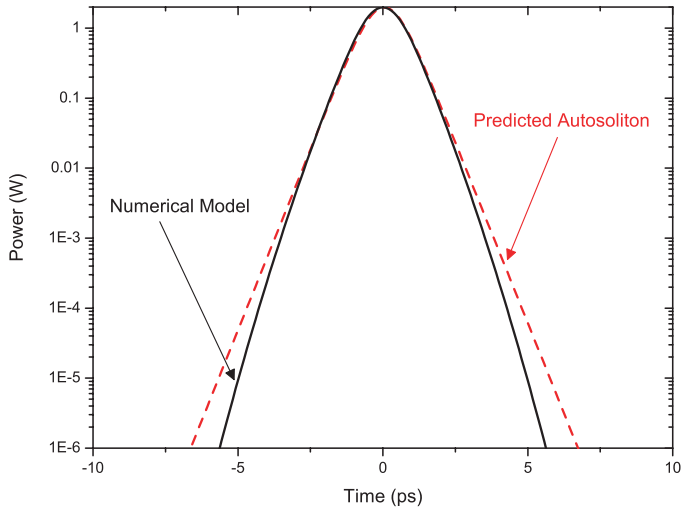

Figure 5.12: Temporal profile of the numerically simulated pulse (solid black) and the predicted autosoliton (dotted red).

Further investigation shows that the poor agreement between autosoliton theory and numerical modeling can be attributed to the high intracavity losses in our laser, which makes the use of the average model questionable. To model a laser with lower intracavity losses, the fraction of the power re-entering the fiber in the HR2 arm was increased from 4% to 60% and the gain was decreased to $g_0 = 1.2$ m^{-1}, in order to maintain the same power level. Using these parameters the full model gives a temporal pulse width of $\tau = 0.8578$ ps and a chirp parameter $q = 0.0027$, whereas the autosoliton theory predicts a pulse width of $\tau = 0.8412$ ps, and a pulse chirp parameter $q = 0.0172$. Figure 5.12 compares the pulse shape obtained from the full model to the pulse predicted by autosoliton theory using these values. Although excellent agreement is obtained for the pulse width and temporal shape (as seen in Fig. 5.12), the chirp parameters are once again in poor agreement.

Our results suggest that the existence of a dispersion map is at the root of the poor agreement for the chirp parameter q; after all the dispersion map causes q to vary within the cavity. We verified this statement by eliminating the grating pair and adjusting the dispersion such that it is constant inside the laser in the numerical model of section 5.3.

Under such conditions, the predictions of autosoliton theory agree with the numerical model within a few percent. Although perfect agreement is not expected due to the effects of third-order dispersion (which is primarily responsible for the deviation between pulse shapes seen in Fig. 5.12) and the mode locker, which were both ignored in assuming the autosoliton pulse shape, we conclude that the mode-locked pulses emitted by our laser are essentially in the form of autosolitons. Despite the autosoliton solution, a laser will not form mode-locked pulses on its own; a mode-locking element is always required. However, the active fiber will always try to impose the autosoliton shape on any pulse circulating within the cavity. Therefore, if the effect of the mode-locking element on the field is weaker than this active fiber shaping mechanism, as is frequently the case in FM mode locking, this shaping mechanism will dominate and we will essentially end up with autosolitons.

5.7 Simplified Model of our Passively Mode-Locked Laser

In this section, we provide the results of a simplified model of NLPR based mode locking. This treatment uses Eq. (4.101) to model the effect of the fast saturable absorption experienced by the pulses in NLPR. Although the coupled differential equations that govern the evolution of the two polarizations may be numerically solved for this laser [see Ref. 80 and the references therein], such a model requires many extra parameters and should yield similar results in many cases. Moreover, since we did not fully characterize this laser, it does not make sense to use such an involved model that would only present us with a larger parameter space.

In order to model the laser depicted in Fig. 2.1, we used the parameter values listed in table 5.2 supplemented by the associated repetition rate, either 12.7 MHz or 8.4 MHz. The length of the passive fiber in the cavity was given by $L_{\text{SMF}} = c/(1.5F_{rep}) - L_{\text{erbium}}$, where F_{rep} is the repetition rate of the laser and we have assumed that the refractive in-

Table 5.2: Parameter Values Used in our Passive Mode Locking Simulations

SMF:	$\beta_2 = -2.13 \times 10^4$ fs^2/m	$\beta_3 = 0$ fs^3/m	$\alpha = 92 \times 10^{-6}$ m^{-1}	$\gamma = 0.0013$ W^{-1}/m
erbium:	$\beta_2 = 3.23 \times 10^4$ fs^2/m	$\beta_3 = 0$ fs^3/m	$\alpha = 92 \times 10^{-6}$ m^{-1}	$\gamma = 0.0013$ W^{-1}/m
$\xi = 0.9$	$I_{sat} = 1500$ W	$\lambda_0 = 1560$ nm	$L_{(\text{erbium})} = 6.5$ m	Power Loss = 15 %
$g_0 = 1.52$ m^{-1}	$\Delta w_g/2\pi = 3.08$ THz	$P_{sat} = 1.0$ mW		

dex of the fiber is 1.5. The modeling of the fiber in this laser cavity was accomplished in the same manner described in section 5.3 and in appendix C. After propagating through the gain fiber, a lumped loss, identified as Power Loss in table 5.2, was introduced to represent the loss experienced due to the output port and any splice losses in the cavity. Upon propagation through the passive fiber the effect of the polarization rotation and the large polarization-dependent loss of the isolator was approximated by using Eq. (4.101). As a consequence of the long cavity length and the parameters chosen for the various effects,[‡] we find that the mechanism for pulse splitting in this cavity is the interplay between dispersion and nonlinearity. Such a conclusion may be reached by noting that the peak powers of the pulses never surpass the saturation intensity in Eq. (4.101). Therefore, the exact form we choose to model the NLPR mechanism will have only a small effect on the actual pulse shape obtained.

The time-domain results of this model are shown in Fig. 5.13 where the mode-locked pulse if formed rapidly. In this case the peak power is such that the noise included in this model is not even visible in the figure. The main point of these results is to demonstrate that when one changes the length of the passive fiber, as done experimentally, and repeats the computer simulation many pulses are obtained; albeit with a change of the polarization controller. This result is found in Fig. 5.14, where a contour-

[‡]Since this laser was not fully characterized, these parameters certainly depart from the actual values and so we do not expect a 1:1 correspondence between our numerical results and the experimental results. Moreover, it is more than likely that the pump was completely absorbed in the erbium-doped fiber, essentially reducing the effect of the gain by introducing reabsorption at the signal wavelength. This computer simulation was only included to give an idea for the types of results one would expect to obtain in this mode-locking regime it is by no way extensive.

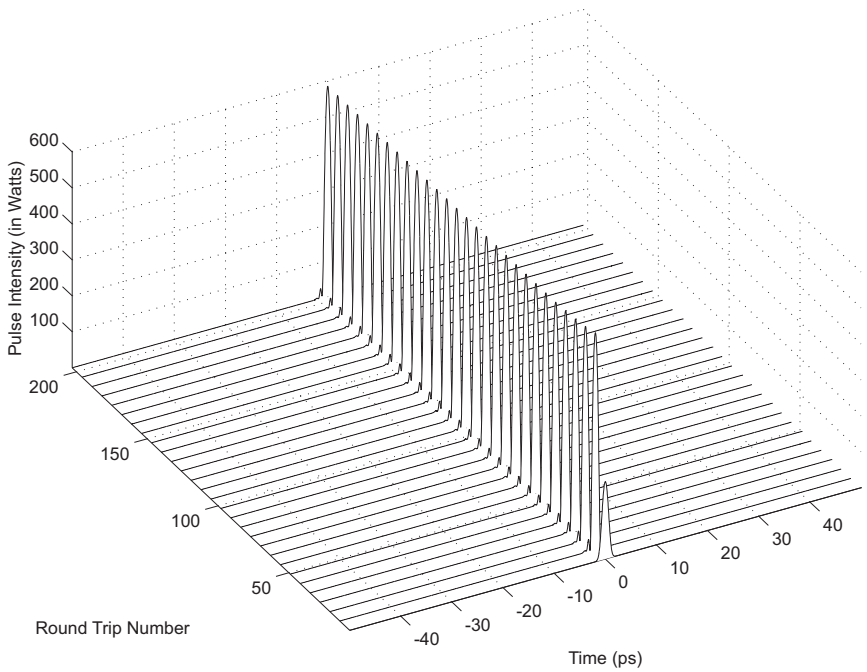

Figure 5.13: Pulse buildup from noise in the NLPR mode-locked laser with the 12.7 MHz repetition rate.

type plot verifies the formation of multiple pulses and indicates in this case that they are subject to large fluctuations and collisions. This behavior is to be expected in all but the most optimized systems due to the lack of any temporal gating from an active mode locker.

One thing immediately revealed using this simplified model is that the mode-locked pulse is subject to an extreme amount of breathing. During a single round trip a pulse experiences large fluctuations in width and peak power. These large changes in pulse parameters cause the pulse to shed energy in the form of dispersive waves and are responsible for the large Kelly sidebands visible in Fig. 2.5 when the extra section of fiber was placed in the cavity.

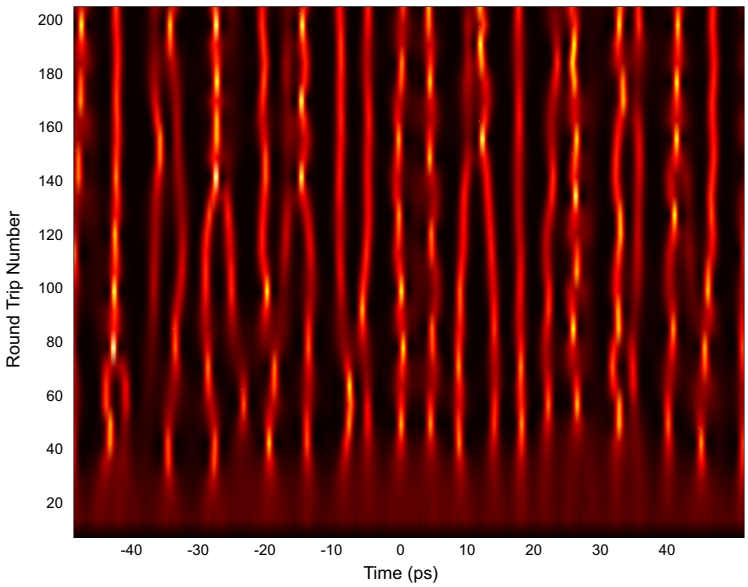

Figure 5.14: Pulse buildup from noise in the NLPR mode-locked laser with the 8.4 MHz repetition rate. Here we find the formation of multiple pulses in the cavity.

5.8 Conclusion

In conclusion, this chapter examined a high-repetition-rate, harmonically, FM-mode-locked, ytterbium fiber laser experimentally, numerically, and analytically. Pulse stability was investigated and the role of third-order dispersion and the unstable modulator extremum on abrupt phase jumps in an FM mode-locked laser was investigated for what we believe to be the first time. The short cavity length and low peak powers allowed us to approximate the pulse dynamics with an average model given by a modified Ginzberg–Landau equation. The averaged equation was then analytically investigated assuming the laser is mode locked with an autosoliton. The results of this analytic theory were compared to the numerical results and found to be in good agreement in a lower-loss laser cavity. Such a treatment of the laser also shows that the effect of the FM modulator on the field is much weaker than the active fiber and thus appears only as a small perturbation. This fact reveals that active-fiber based pulse shaping is the

overriding pulse shaping mechanism in this laser.

Strictly speaking, this type of laser is expected to have a pulse consistent with an autosoliton, as opposed to a standard soliton. In fact any deviation from the autosoliton shape may be attributed to the fact that this laser does, in reality, have a dispersion map with finite third-order dispersion, an FM modulator, and discreet losses. Although the distinction between these two types of solitons is subtle for actively mode-locked lasers producing picosecond pulses, we believe that it should be more pronounced at higher modulation frequencies which are able to produce shorter pulses that will experience stronger spectral filtering, resulting in a larger gain/loss imbalance, and hence an increased chirp.

6 Rate Equations for Mode-Locked Lasers

Although we have already used the long-standing theory's of Siegman[2] and Haus[19] in chapter 4 to obtain analytic solutions for the expected pulses in active and passive mode-locked lasers, we wish to extend their results if at all possible. For example, in the theory developed for saturable absorption based mode locking it was possible to incorporate most of the important effects, yet, TOD had to be ignored. Moreover, the theory is only valid if the pulse power is much less than the saturation power of the device and the Taylor expansion of the saturable absorber's effect is valid. Additionally, the theory developed for the active mode locking ignores the effects of both TOD and SPM.

6.1 The Moment Method

In an effort to obtain more accurate results, we have applied the moment method[145] to the equations governing pulse propagation in all three types of mode-locked lasers. The moment method allows us to develop ordinary differential equations that govern the evolution of the pulse parameters rather than the electric field. Moreover, this approach can take into account all of the terms in Eq. (4.92), thereby lifting the restriction on the

parameter space.

If we ignore the phase $kT+\phi_0$ in Eqs. (5.6) and (4.107), a mode-locked pulse is fully quantified by five parameters: energy E, temporal shift ξ, frequency shift Ω, chirp q, and width τ. Following the moment method, these parameters are defined in terms of integrals over the temporal pulse profile via[146,147]

$$E(T) = \int_{-\infty}^{\infty} |A(T,t)|^2\, dt, \tag{6.1}$$

$$\xi(T) = \frac{1}{E}\int_{-\infty}^{\infty} t\,|A(T,t)|^2\, dt, \tag{6.2}$$

$$\Omega(T) = \frac{i}{2E}\int_{-\infty}^{\infty}\left[A^*\frac{\partial A}{\partial t} - A\frac{\partial A^*}{\partial t}\right] dt, \tag{6.3}$$

$$q(T) = \frac{i}{E}\int_{-\infty}^{\infty}(t-\xi)\left[A^*\frac{\partial A}{\partial t} - A\frac{\partial A^*}{\partial t}\right] dt, \tag{6.4}$$

$$\tau^2(T) = \frac{2C_3}{E}\int_{-\infty}^{\infty}(t-\xi)^2\,|A(T,t)|^2\, dt, \tag{6.5}$$

where the constant C_3, defined later in this section, converts the root-mean-square width into pulse width τ. In order to obtain analytic results, the pulse shape must be an analytic function which is differentiable everywhere as well as square integrable.* To investigate how the five pulse parameters evolve during propagation under the influence of a governing equation, we differentiate Eqs. (6.1)–(6.5) with respect to the course-grained time T and obtain[148]

$$\frac{dE}{dT} = \int_{-\infty}^{\infty}\left[A^*\frac{\partial A}{\partial T} + A\frac{\partial A^*}{\partial T}\right] dt, \tag{6.6}$$

$$\frac{d\xi}{dT} = -\frac{1}{E}\frac{dE}{dT}\xi + \frac{1}{E}\int_{-\infty}^{\infty} t\left[A^*\frac{\partial A}{\partial T} + A\frac{\partial A^*}{\partial T}\right] dt, \tag{6.7}$$

$$\frac{d\Omega}{dT} = -\frac{1}{E}\frac{dE}{dT}\Omega + \frac{i}{2E}\int_{-\infty}^{\infty}\left[\frac{\partial}{\partial T}\left(A^*\frac{\partial A}{\partial t}\right) - \frac{\partial}{\partial T}\left(A\frac{\partial A^*}{\partial t}\right)\right] dt, \tag{6.8}$$

$$\frac{dq}{dT} = -\frac{1}{E}\frac{dE}{dT}q + \frac{i}{E}\int_{-\infty}^{\infty}(t-\xi)\left[\frac{\partial}{\partial T}\left(A^*\frac{\partial A}{\partial t}\right) - \frac{\partial}{\partial T}\left(A\frac{\partial A^*}{\partial t}\right)\right] dt, \tag{6.9}$$

$$\tau\frac{d\tau}{dT} = -\frac{1}{2E}\frac{dE}{dT}\tau^2 + \frac{C_3}{E}\int_{-\infty}^{\infty}(t-\xi)^2\left[A^*\frac{\partial A}{\partial T} + A\frac{\partial A^*}{\partial T}\right] dt. \tag{6.10}$$

*This restricts the application of this technique to investigating similaritons since they posses a kink. Nevertheless, the possibility of removing the kink does exist although such an approach is likely to provide a complicated analytic result.

To continue from here, we must restrict our focus to a specific governing equation. In our case, we are interested in mode-locked lasers and wish to investigate the changes in the pulse parameters under the influence of the master equation of mode locking [Eq. (4.92)]. Unfortunately, we cannot develop a generic treatment for this problem since it depends on the mode-locking mechanism denoted by $M(A,t)$. However, we point out that the resulting equations we obtain will all contain certain core terms due to the common effects found in Eq. (4.82) regardless of the mode-locking mechanism.

In the rest of this chapter, we apply the moment method to the equation that all of our mode-locking processes have in common: the Ginzburg–Landau equation (GLE). The results obtained in this chapter will be appended to the results found in the following chapters for each specific mode-locking mechanism to obtain a complete rate-equation approach for the various mode-locking techniques.

6.2 Application to the GLE

In this section, we start by substituting the GLE into Eqs. (6.6)–(6.10) for one pulse parameter at a time. Integration-by-parts[†] is then used to simplify the integrals.

6.2.1 Evolution of Pulse Energy

To determine how the energy changes with propagation, we insert the GLE into Eq. (6.6). To simplify the appearance of the math we split our result into two pieces:

$$\begin{aligned} A^*\frac{\partial A}{\partial T} = &-\frac{i\beta_2}{2}\frac{L_R}{T_R}A^*\frac{\partial^2 A}{\partial t^2}+\frac{\bar{g}T_2^2}{2}\frac{L_R}{T_R}A^*\frac{\partial^2 A}{\partial t^2}+\frac{\beta_3}{6}\frac{L_R}{T_R}A^*\frac{\partial^3 A}{\partial t^3} \\ &+\frac{(\bar{g}-\bar{\alpha})}{2}\frac{L_R}{T_R}|A|^2+i\gamma|A|^4, \end{aligned} \tag{6.11}$$

[†]See appendix D.1 for a complete list of the simplifications provided by using integration by parts.

and

$$A\frac{\partial A^*}{\partial T} = \frac{i\beta_2}{2}\frac{L_R}{T_R}A\frac{\partial^2 A^*}{\partial t^2} + \frac{\bar{g}T_2^2}{2}\frac{L_R}{T_R}A\frac{\partial^2 A^*}{\partial t^2} + \frac{\beta_3}{6}\frac{L_R}{T_R}A\frac{\partial^3 A^*}{\partial t^3} + \frac{(\bar{g}-\bar{\alpha})}{2}\frac{L_R}{T_R}|A|^2 - i\gamma|A|^4. \tag{6.12}$$

Combining these results and using Eq. (6.6), we find

$$\frac{T_R}{L_R}\frac{dE}{dT} = -\frac{i\beta_2}{2}\int_{-\infty}^{\infty}\left[A^*\frac{\partial^2 A}{\partial t^2} - A\frac{\partial^2 A^*}{\partial t^2}\right]dt + \frac{\bar{g}T_2^2}{2}\int_{-\infty}^{\infty}\left[A^*\frac{\partial^2 A}{\partial t^2} + A\frac{\partial^2 A^*}{\partial t^2}\right]dt + \frac{\beta_3}{6}\int_{-\infty}^{\infty}\left[A^*\frac{\partial^3 A}{\partial t^3} + A\frac{\partial^3 A^*}{\partial t^3}\right]dt + (\bar{g}-\bar{\alpha})\int_{-\infty}^{\infty}|A|^2\,dt. \tag{6.13}$$

Now, by using our integration-by-parts relations, Eqs. (D.2), (D.11), and (D.14), this result is simplified to become

$$\frac{T_R}{L_R}\frac{dE}{dT} = (\bar{g}-\bar{\alpha})E - \bar{g}T_2^2\int_{-\infty}^{\infty}\left|\frac{\partial A}{\partial t}\right|^2 dt. \tag{6.14}$$

6.2.2 Evolution of Pulse Center

Following the same approach as above, we substitute Eq. (4.82) into Eq. (6.7). Since we already found the terms in the bracketed expression inside the integral, by adding Eqs. (6.11) and (6.12), we can immediately write

$$\frac{T_R}{L_R}\frac{d\xi}{dT} = -(\bar{g}-\bar{\alpha})\xi + \frac{\bar{g}T_2^2}{E}\xi\int_{-\infty}^{\infty}\left|\frac{\partial A}{\partial t}\right|^2 dt - \frac{i\beta_2}{2E}\int_{-\infty}^{\infty}t\left[A^*\frac{\partial^2 A}{\partial t^2} - A\frac{\partial^2 A^*}{\partial t^2}\right]dt + \frac{\bar{g}T_2^2}{2E}\int_{-\infty}^{\infty}t\left[A^*\frac{\partial^2 A}{\partial t^2} + A\frac{\partial^2 A^*}{\partial t^2}\right]dt + \frac{\beta_3}{6E}\int_{-\infty}^{\infty}t\left[A^*\frac{\partial^3 A}{\partial t^3} + A\frac{\partial^3 A^*}{\partial t^3}\right]dt + \frac{(\bar{g}-\bar{\alpha})}{E}\int_{-\infty}^{\infty}t\,|A|^2\,dt. \tag{6.15}$$

Next, Eq. (6.1) is used in conjunction with our integration-by-parts relations Eqs. (D.15)–(D.19) to obtain:

$$\frac{T_R}{L_R}\frac{d\xi}{dT} = \beta_2\Omega - \frac{\bar{g}T_2^2}{E}\left[\int_{-\infty}^{\infty}t\left|\frac{\partial A}{\partial t}\right|^2 dt - \xi\int_{-\infty}^{\infty}\left|\frac{\partial A}{\partial t}\right|^2 dt\right] + \frac{\beta_3}{2E}\int_{-\infty}^{\infty}\left|\frac{\partial A}{\partial t}\right|^2 dt. \tag{6.16}$$

6.2.3 Evolution of Spectral Shift

To find the change in carrier frequency, it is helpful to use the chain rule to obtain the following result:

$$\frac{\partial}{\partial T}\left(A^*\frac{\partial A}{\partial t}\right) = A^*\frac{\partial^2 A}{\partial T\,\partial t} + \frac{\partial A^*}{\partial T}\frac{\partial A}{\partial t}. \tag{6.17}$$

Then using Eq. (4.82) we can write

$$\begin{aligned} A^*\frac{\partial^2 A}{\partial T\,\partial t} &= -\frac{i\beta_2}{2}\frac{L_R}{T_R}A^*\frac{\partial^3 A}{\partial t^3} + \frac{\bar{g}T_2^2}{2}\frac{L_R}{T_R}A^*\frac{\partial^3 A}{\partial t^3} + \frac{\beta_3}{6}\frac{L_R}{T_R}A^*\frac{\partial^4 A}{\partial t^4} \\ &+ \frac{(\bar{g}-\bar{\alpha})}{2}\frac{L_R}{T_R}A^*\frac{\partial A}{\partial t} + i\gamma\frac{L_R}{T_R}|A|^2\frac{\partial |A|^2}{\partial t} + i\gamma\frac{L_R}{T_R}A^*|A|^2\frac{\partial A}{\partial t}. \end{aligned} \tag{6.18}$$

We also find

$$\begin{aligned} \frac{\partial A^*}{\partial T}\frac{\partial A}{\partial t} &= \frac{i\beta_2}{2}\frac{L_R}{T_R}\frac{\partial^2 A^*}{\partial t^2}\frac{\partial A}{\partial t} + \frac{\bar{g}T_2^2}{2}\frac{L_R}{T_R}\frac{\partial^2 A^*}{\partial t^2}\frac{\partial A}{\partial t} + \frac{\beta_3}{6}\frac{L_R}{T_R}\frac{\partial^3 A^*}{\partial t^3}\frac{\partial A}{\partial t} \\ &+ \frac{(\bar{g}-\bar{\alpha})}{2}\frac{L_R}{T_R}A^*\frac{\partial A}{\partial t} - i\gamma\frac{L_R}{T_R}A^*|A|^2\frac{\partial A}{\partial t}. \end{aligned} \tag{6.19}$$

Putting these two results together we obtain

$$\begin{aligned} \frac{\partial}{\partial T}\left(A^*\frac{\partial A}{\partial t}\right) &= -\frac{i\beta_2}{2}\frac{L_R}{T_R}\left[A^*\frac{\partial^3 A}{\partial t^3} - \frac{\partial^2 A^*}{\partial t^2}\frac{\partial A}{\partial t}\right] + \frac{\bar{g}T_2^2}{2}\frac{L_R}{T_R}\left[A^*\frac{\partial^3 A}{\partial t^3} + \frac{\partial^2 A^*}{\partial t^2}\frac{\partial A}{\partial t}\right] \\ &+ \frac{\beta_3}{6}\frac{L_R}{T_R}\left[A^*\frac{\partial^4 A}{\partial t^4} + \frac{\partial^3 A^*}{\partial t^3}\frac{\partial A}{\partial t}\right] + (\bar{g}-\bar{\alpha})\frac{L_R}{T_R}A^*\frac{\partial A}{\partial t} \\ &+ i\gamma\frac{L_R}{T_R}|A|^2\frac{\partial |A|^2}{\partial t}. \end{aligned} \tag{6.20}$$

By taking the complex conjugate of this, we find

$$\begin{aligned} \frac{\partial}{\partial T}\left(A\frac{\partial A^*}{\partial t}\right) &= \frac{i\beta_2}{2}\frac{L_R}{T_R}\left[A\frac{\partial^3 A^*}{\partial t^3} - \frac{\partial^2 A}{\partial t^2}\frac{\partial A^*}{\partial t}\right] + \frac{\bar{g}T_2^2}{2}\frac{L_R}{T_R}\left[A\frac{\partial^3 A^*}{\partial t^3} + \frac{\partial^2 A}{\partial t^2}\frac{\partial A^*}{\partial t}\right] \\ &+ \frac{\beta_3}{6}\frac{L_R}{T_R}\left[A\frac{\partial^4 A^*}{\partial t^4} + \frac{\partial^3 A}{\partial t^3}\frac{\partial A^*}{\partial t}\right] + (\bar{g}-\bar{\alpha})\frac{L_R}{T_R}A\frac{\partial A^*}{\partial t} \\ &- i\gamma\frac{L_R}{T_R}|A|^2\frac{\partial |A|^2}{\partial t}. \end{aligned} \tag{6.21}$$

Therefore,

$$\begin{aligned}\left[\frac{\partial}{\partial T}\left(A^*\frac{\partial A}{\partial t}\right)-\frac{\partial}{\partial T}\left(A\frac{\partial A^*}{\partial t}\right)\right] &= -\frac{i\beta_2}{2}\frac{L_R}{T_R}\left[A^*\frac{\partial^3 A}{\partial t^3}+A\frac{\partial^3 A^*}{\partial t^3}\right]\\ &+\frac{i\beta_2}{2}\frac{L_R}{T_R}\left[\frac{\partial A^*}{\partial t}\frac{\partial^2 A}{\partial t^2}+\frac{\partial A}{\partial t}\frac{\partial^2 A^*}{\partial t^2}\right]+\frac{\bar{g}T_2^2}{2}\frac{L_R}{T_R}\left[A^*\frac{\partial^3 A}{\partial t^3}-A\frac{\partial^3 A^*}{\partial t^3}\right]\\ &-\frac{\bar{g}T_2^2}{2}\frac{L_R}{T_R}\left[\frac{\partial A^*}{\partial t}\frac{\partial^2 A}{\partial t^2}-\frac{\partial A}{\partial t}\frac{\partial^2 A^*}{\partial t^2}\right]+\frac{\beta_3}{6}\frac{L_R}{T_R}\left[A^*\frac{\partial^4 A}{\partial t^4}-A\frac{\partial^4 A^*}{\partial t^4}\right]\\ &-\frac{\beta_3}{6}\frac{L_R}{T_R}\left[\frac{\partial A^*}{\partial t}\frac{\partial^3 A}{\partial t^3}-\frac{\partial A}{\partial t}\frac{\partial^3 A^*}{\partial t^3}\right]+(\bar{g}-\bar{\alpha})\frac{L_R}{T_R}\left[A^*\frac{\partial A}{\partial t}-A\frac{\partial A^*}{\partial t}\right]\\ &+2i\gamma\frac{L_R}{T_R}|A|^2\frac{\partial|A|^2}{\partial t}. \end{aligned} \tag{6.22}$$

Substituting the preceding term into Eq. (6.8) gives us

$$\begin{aligned}\frac{d\Omega}{dT} &= -(\bar{g}-\bar{\alpha})\frac{L_R}{T_R}\Omega+\frac{\bar{g}T_2^2}{E}\frac{L_R}{T_R}\Omega\int_{-\infty}^{\infty}\left|\frac{\partial A}{\partial t}\right|^2dt+\frac{\beta_2}{4E}\frac{L_R}{T_R}\int_{-\infty}^{\infty}\left[A^*\frac{\partial^3 A}{\partial t^3}+A\frac{\partial^3 A^*}{\partial t^3}\right]dt\\ &-\frac{\beta_2}{4E}\frac{L_R}{T_R}\int_{-\infty}^{\infty}\left[\frac{\partial A^*}{\partial t}\frac{\partial^2 A}{\partial t^2}+\frac{\partial A}{\partial t}\frac{\partial^2 A^*}{\partial t^2}\right]dt+\frac{i\bar{g}T_2^2}{4E}\frac{L_R}{T_R}\int_{-\infty}^{\infty}\left[A^*\frac{\partial^3 A}{\partial t^3}-A\frac{\partial^3 A^*}{\partial t^3}\right]dt\\ &-\frac{i\bar{g}T_2^2}{4E}\frac{L_R}{T_R}\int_{-\infty}^{\infty}\left[\frac{\partial A^*}{\partial t}\frac{\partial^2 A}{\partial t^2}-\frac{\partial A}{\partial t}\frac{\partial^2 A^*}{\partial t^2}\right]dt+\frac{i\beta_3}{12E}\frac{L_R}{T_R}\int_{-\infty}^{\infty}\left[A^*\frac{\partial^4 A}{\partial t^4}-A\frac{\partial^4 A^*}{\partial t^4}\right]\\ &-\frac{i\beta_3}{12E}\frac{L_R}{T_R}\int_{-\infty}^{\infty}\left[\frac{\partial A^*}{\partial t}\frac{\partial^3 A}{\partial t^3}-\frac{\partial A}{\partial t}\frac{\partial^3 A^*}{\partial t^3}\right]dt+(\bar{g}-\bar{\alpha})\frac{L_R}{T_R}\Omega\\ &-\frac{\gamma}{E}\frac{L_R}{T_R}\int_{-\infty}^{\infty}|A|^2\frac{\partial|A|^2}{\partial t}dt. \end{aligned} \tag{6.23}$$

Amazingly, this messy result may be overwhelmingly simplified by using Eqs. (D.20)–(D.27) to

$$\frac{T_R}{L_R}\frac{d\Omega}{dT}=-\frac{\bar{g}T_2^2}{E}\left[\frac{i}{2}\int_{-\infty}^{\infty}\left[\frac{\partial A^*}{\partial t}\frac{\partial^2 A}{\partial t^2}-\frac{\partial A}{\partial t}\frac{\partial^2 A^*}{\partial t^2}\right]dt-\Omega\int_{-\infty}^{\infty}\left|\frac{\partial A}{\partial t}\right|^2dt\right]. \tag{6.24}$$

6.2.4 Evolution of Chirp

The change in chirp, which is given by Eq. (6.9), may be simplified by noting that we already found the bracketed terms in the integral of Eq. (6.22). Therefore, we can

immediately write

$$\begin{aligned}\frac{T_R}{L_R}\frac{dq}{dT} &= -(\bar{g}-\bar{\alpha})\,q+\frac{\bar{g}T_2^2}{E}Q\int_{-\infty}^{\infty}\left|\frac{\partial A}{\partial t}\right|^2 dt\\ &+\frac{\beta_2}{2E}\int_{-\infty}^{\infty}(t-\xi)\left[A^*\frac{\partial^3 A}{\partial t^3}+A\frac{\partial^3 A^*}{\partial t^3}\right]dt\\ &-\frac{\beta_2}{2E}\int_{-\infty}^{\infty}(t-\xi)\left[\frac{\partial A^*}{\partial t}\frac{\partial^2 A}{\partial t^2}+\frac{\partial A}{\partial t}\frac{\partial^2 A^*}{\partial t^2}\right]dt\\ &+\frac{i\bar{g}T_2^2}{2E}\int_{-\infty}^{\infty}(t-\xi)\left[A^*\frac{\partial^3 A}{\partial t^3}-A\frac{\partial^3 A^*}{\partial t^3}\right]dt\\ &-\frac{i\bar{g}T_2^2}{2E}\int_{-\infty}^{\infty}(t-\xi)\left[\frac{\partial A^*}{\partial t}\frac{\partial^2 A}{\partial t^2}-\frac{\partial A}{\partial t}\frac{\partial^2 A^*}{\partial t^2}\right]dt\\ &+\frac{i\beta_3}{6E}\int_{-\infty}^{\infty}(t-\xi)\left[A^*\frac{\partial^4 A}{\partial t^4}-A\frac{\partial^4 A^*}{\partial t^4}\right]\\ &-\frac{i\beta_3}{6E}\int_{-\infty}^{\infty}(t-\xi)\left[\frac{\partial A^*}{\partial t}\frac{\partial^3 A}{\partial t^3}-\frac{\partial A}{\partial t}\frac{\partial^3 A^*}{\partial t^3}\right]\\ &+(\bar{g}-\bar{\alpha})\frac{i}{E}\int_{-\infty}^{\infty}(t-\xi)\left[A^*\frac{\partial A}{\partial t}-A\frac{\partial A^*}{\partial t}\right]dt\\ &-\frac{2\gamma}{E}\int_{-\infty}^{\infty}(t-\xi)\,|A|^2\frac{\partial\,|A|^2}{\partial t}dt. \end{aligned}\tag{6.25}$$

By this point, the reader will not be surprised to learn that this result may also be simplified by using Eqs. (D.28)–(D.38) to

$$\begin{aligned}\frac{T_R}{L_R}\frac{dq}{dT} &= \frac{2\beta_2}{E}\int_{-\infty}^{\infty}\left|\frac{\partial A}{\partial t}\right|^2 dt+\frac{i\beta_3}{2E}\int_{-\infty}^{\infty}\left[\frac{\partial A^*}{\partial t}\frac{\partial^2 A}{\partial t^2}-\frac{\partial A}{\partial t}\frac{\partial^2 A^*}{\partial t^2}\right]dt+\frac{\gamma}{E}\int_{-\infty}^{\infty}|A|^4 dt\\ &+\frac{\bar{g}T_2^2}{E}\left[q\int_{-\infty}^{\infty}\left|\frac{\partial A}{\partial t}\right|^2 dt-i\int_{-\infty}^{\infty}(t-\xi)\left[\frac{\partial A^*}{\partial t}\frac{\partial^2 A}{\partial t^2}-\frac{\partial A}{\partial t}\frac{\partial^2 A^*}{\partial t^2}\right]dt\right].\end{aligned}\tag{6.26}$$

6.2.5 Evolution of Pulse Width

Finally, the change in the pulse width may be found by starting with Eq. (6.10)

$$\tau\frac{d\tau}{dT}=-\frac{1}{2E}\frac{\partial E}{\partial T}\tau^2+\frac{C_3}{E}\int_{-\infty}^{\infty}(t-\xi)^2\left[A^*\frac{\partial A}{\partial T}+A\frac{\partial A^*}{\partial T}\right]dt\tag{6.27}$$

and then using Eqs. (6.11) and (6.12) to obtain the following result:

$$\begin{aligned}\frac{T_R}{L_R}\tau\frac{d\tau}{dT} &= -\frac{(\bar{g}-\bar{\alpha})}{2}\tau^2+\frac{\bar{g}T_2^2}{2E}\tau^2\int_{-\infty}^{\infty}\left|\frac{\partial A}{\partial t}\right|^2 dt\\ &- \frac{i\beta_2 C_3}{2E}\int_{-\infty}^{\infty}(t-\xi)^2\left[A^*\frac{\partial^2 A}{\partial t^2}-A\frac{\partial^2 A^*}{\partial t^2}\right]dt\\ &+ \frac{\bar{g}T_2^2 C_3}{2E}\int_{-\infty}^{\infty}(t-\xi)^2\left[A^*\frac{\partial^2 A}{\partial t^2}+A\frac{\partial^2 A^*}{\partial t^2}\right]dt\\ &+ \frac{\beta_3 C_3}{6E}\int_{-\infty}^{\infty}(t-\xi)^2\left[A^*\frac{\partial^3 A}{\partial t^3}+A\frac{\partial^3 A^*}{\partial t^3}\right]dt\\ &+ \frac{(\bar{g}-\bar{\alpha})}{2}\tau^2. \end{aligned} \tag{6.28}$$

Once again, by using Eq. (6.5) and Eqs. (D.39)–(D.44), this result may be simplified to

$$\begin{aligned}\frac{T_R}{L_R}\frac{d\tau}{dT} &= \frac{\beta_2 q C_3}{\tau}+\frac{\beta_3 C_3}{\tau E}\int_{-\infty}^{\infty}(t-\xi)\left|\frac{\partial A}{\partial t}\right|^2 dt\\ &+ \frac{\bar{g}T_2^2}{2E}\left[\tau\int_{-\infty}^{\infty}\left|\frac{\partial A}{\partial t}\right|^2 dt+\frac{2EC_3}{\tau}-\frac{2C_3}{\tau}\int_{-\infty}^{\infty}(t-\xi)^2\left|\frac{\partial A}{\partial t}\right|^2 dt\right]. \end{aligned} \tag{6.29}$$

6.2.6 Analytic Results

The results obtained above all include integrals that can only be done if one assumes a specific shape for the mode-locked pulses. The fact that a pulse shape must be assumed, which may depart from the actual pulse shape, is one of the drawbacks of this approach. Nevertheless, the results predicted from this method are in excellent agreement with full numerical simulations. Thus we assume that the pulse shape can take one of the following two commonly-assumed forms: either a perturbed Gaussian

$$A = a_0\left\{\exp\left[-(t-\xi)^2/(2\tau^2)\right]\right\}^{1+iq}\times\exp\left[-i\Omega(t-\xi)+i\kappa T+i\phi_0\right], \tag{6.30}$$

or a perturbed autosoliton

$$A(T,t) = a_0\left\{\operatorname{sech}\left[(t-\xi)/\tau\right]\right\}^{1+iq}\times\exp\left[-i\Omega(t-\xi)+i\kappa T+i\phi_0\right]. \tag{6.31}$$

We now substitute these two shapes into Eqs. (6.14), (6.16), (6.26), (6.24), and (6.29). By using the derivatives and integrals found in Appendices D.2 and D.3, we are able to get the following ordinary differential equations for the various pulse parameters:

$$\frac{T_R}{L_R}\frac{dE}{dT} = (\bar{g}-\bar{\alpha})E - \frac{\bar{g}T_2^2}{2\tau^2}\left[C_0\left(1+q^2\right)+2\Omega^2\tau^2\right]E, \tag{6.32}$$

$$\frac{T_R}{L_R}\frac{d\xi}{dT} = \bar{\beta}_2\Omega - \bar{g}T_2^2 q\Omega + \frac{\bar{\beta}_3}{4\tau^2}\left[C_0\left(1+q^2\right)+2\Omega^2\tau^2\right], \tag{6.33}$$

$$\frac{T_R}{L_R}\frac{d\Omega}{dT} = -C_0\frac{\bar{g}T_2^2}{\tau^2}\left(1+q^2\right)\Omega, \tag{6.34}$$

$$\begin{aligned}\frac{T_R}{L_R}\frac{dq}{dT} = {} & \frac{\bar{\beta}_2}{\tau^2}\left[C_0\left(1+q^2\right)+2\Omega^2\tau^2\right] \\ & - \frac{\bar{g}T_2^2}{\tau^2}q\left[C_1\left(1+q^2\right)+2\Omega^2\tau^2\right] \\ & + C_2\frac{\bar{\gamma}E}{\sqrt{2\pi}\tau} + \frac{\bar{\beta}_3\Omega}{\tau^2}\left[\frac{3}{2C_0}\left(1+q^2\right)+\Omega^2\tau^2\right],\end{aligned} \tag{6.35}$$

$$\frac{T_R}{L_R}\frac{d\tau}{dT} = C_3\frac{\bar{\beta}_2}{\tau}q + C_3\frac{\bar{\beta}_3}{\tau}q\Omega + C_0C_3\frac{\bar{g}T_2^2}{2\tau}\left(C_4-q^2\right), \tag{6.36}$$

where the constants C_n ($n = 0$ to 4) are introduced such that they all equal 1 for a Gaussian pulse. In the case of an autosoliton, $C_0 = 2/3$, $C_1 = 1/3$, $C_2 = \sqrt{2\pi}/3$, $C_3 = 6/\pi^2$, and $C_4 = 2$.

To demonstrate the utility of our results, we solve Eqs. (6.32)–(6.36) using the fourth-order Runge–Kutta scheme. It is important to point out that although we have ignored the presence of both noise and the mode locker, we can still investigate these equations numerically since the GLE does admit the so-called autosoliton solution in the anomalous dispersion regime. Therefore, using the parameters found in Table 5.1[‡], we obtain the results shown in Fig. 6.1 where we seeded our code with the values $E = 0.5$ pW, $q = 0.0$, $\tau = 0.5$ ps, $\Omega = 0.0$ Hz, and $\xi = 0.0$ s. The fact that this system converges to a steady state is due to the presence of the autosoliton solution. However, the autosoliton potential was found to be weak when compared with that of the mode-locking mechanisms investigated in later chapters. To qualify this claim, we point out

[‡]NOTE: in determining the saturated gain, we have multiplied the average power by a factor of 2 in order to model a Fabry–Perot laser cavity.

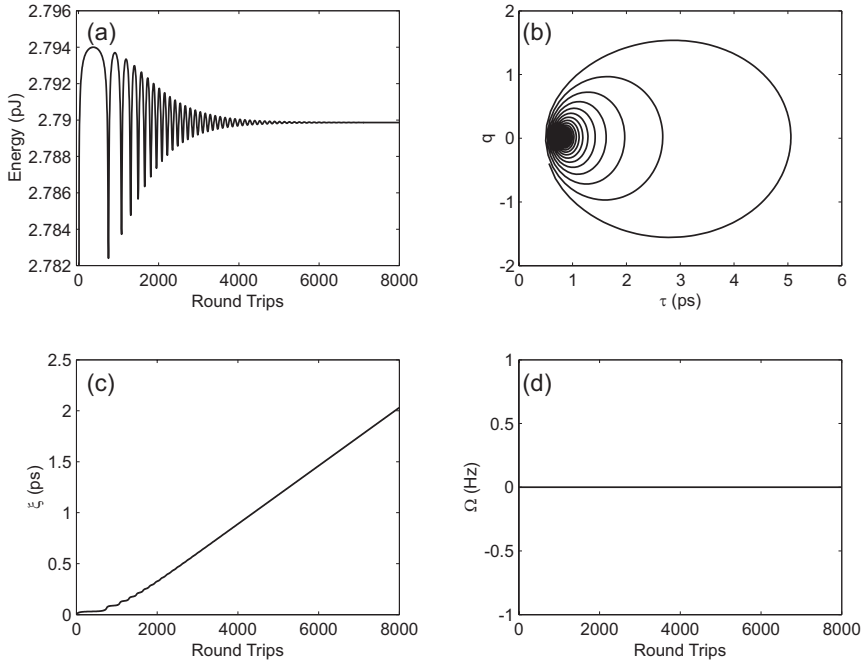

Figure 6.1: Convergence of Eqs. (6.32)–(6.36) to their steady-state values: (a) demonstrates the convergence of the pulse energy, (b) is a phase plot of q with respect to τ which corkscrews down to a single point revealing a single steady state, and (c) shows the non-convergence of ξ on a steady state. This initially counterintuitive result is not alarming since it converges to a linear function with a fixed slope. It is a physical ramification of the presence of third-order dispersion, which temporally shifts the pulse arrival time [see Eq. (6.33) where $\Omega = 0$]. Finally, plot (d) reveals that the pulse experiences no spectral shift.

that the convergence of our solution strongly depends on the initial values chosen. This indicates that this regime is not likely to exist by itself. For example, in later chapters where the effect of a mode locker is added to the equations obtained here, we find a more robust region of convergence where a steady state is found for a much wider range of initial parameters and will form from noise.

In this case our method predicts the following steady state pulse parameters: $\bar{g} = 0.17018\ \mathrm{m}^{-1}$, $E = 2.7899$ pJ, $q = 0.018048$, $\tau = 0.83683$ ps, and $\Omega = 0$ Hz. However, ξ does not approach a single value; rather it approaches a constant value of 0.28562 fs for the delay experienced by the pulse per round trip — this effect accrues over multiple

round trips.

6.3 Comparison with Theory

Since we are in essence solving Eq. (4.82), which has an analytic solution, it is important that we compare our result to the result predicted by theory. In fact, if we use our perturbed autosoliton ansatz, we should obtain complete agreement between our perturbation approach and the analytic result. Using the value obtained for the saturated gain[§] in Eqs. (5.7)–(5.10), we find the errors between the method presented in this chapter and the analytically predicted results: $E_{\text{error}} = 0.122$ %, $\xi_{\text{error}} = 100$ %, $\Omega_{\text{error}} = 0.00$ %, $q_{\text{error}} = 0.830$ %, and $\tau_{\text{error}} = 0.001$ %. The small discrepancy between these different values is due to how long we allow the numerical simulation to continue[¶] and the presence of third-order dispersion in our approach. Also, recall that third-order dispersion is not included in the analytic theory. This is why we found an error of 100 % for the pulse location.

6.4 Comparison with Numerical Simulations

Of course a full numerical simulation of Eq. (4.82) must also produce the same results if our approach is accurate. The pulse formed as a result of this simulation had the following values: $\bar{g} = 0.17018$ m^{-1}, $E = 2.7899$ pJ, $\tau = 0.8406$ ps, $q = 0.0175$, and $\Omega = -5.967$ GHz. These parameters agree with the results obtained above within a few percent except for a shift in the carrier frequency. The carrier frequency shift originates

[§]All analytic solutions require a priori knowledge of the saturated gain, a value which may only be obtained by solving the full problem. In our treatment here, however, this value is accurately obtained.

[¶]Note: the simulation approaches the steady-state values with an accuracy related to how long the simulations are allowed to continue.

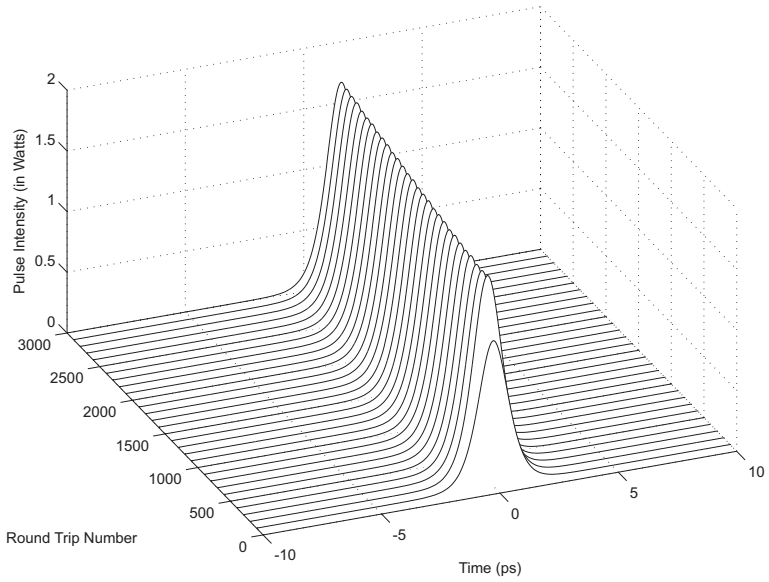

Figure 6.2: Numerical solution of Eq. (4.82) in the anomalous-dispersion regime in the absence of noise. Although seeded by a pulse, a distinct solution is found — the so-called autosoliton.

from pulse asymmetry due to third-order dispersion. Unfortunately, it would not be practical to incorporate pulse asymmetry into our model. However, the overall agreement validates our numerical simulations used throughout this work.

Before parting, we point out that in order to obtain the autosoliton shown in Fig. 6.2, we had to seed our simulation with a pulse with parameters close to those of the autosoliton. Since the autosoliton solution is not robust, seeding from a similar pulse is required. Moreover, the autosoliton will not persist indefinitely in the presence of noise without an external cleanup mechanism. To demonstrate this point, we allow the simulation performed above to continue over more round trips and plot both the spectral evolution [in Fig. 6.3(a)] and the temporal evolution [in Fig. 6.3(b)]. In this case, what appears to be noise on the spectrum is due to a growing cw background that creeps into the simulation due to numerical error. This is why lasers, which have noise due to spontaneous emission, require a mode-locking mechanism to form trains of stable pulses. Moreover, this figure demonstrates that the autosoliton is not a robust solution. However, despite the noise clearly visible on the spectrum, the time-domain pulse

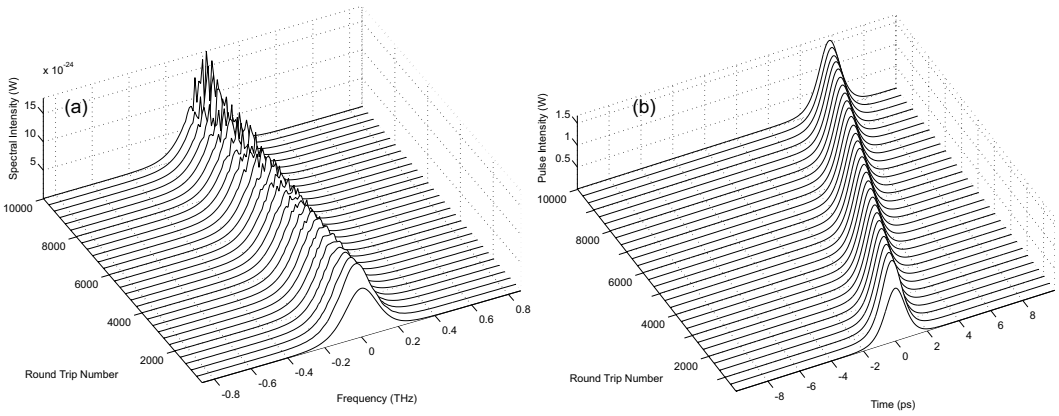

Figure 6.3: Spectrum of the pulse solution found by solving Eq. (4.82) in the anomalous-dispersion regime in the absence of noise. Figure (a) shows that the pulse starts to develop a cw background despite the fact that figure (b) appears to have converged to a specific solution.

shown in Fig. 6.3(b) still appears to maintain its shape over the simulation range; it will eventually disperse.

6.5 Application to Mode-Locked Lasers

Equations (6.32)–(6.36) describe the propagation of a Gaussian pulse or an autosoliton under the influence of the GLE. Since this equation is common to the master equation of mode locking, which can be used to describe all of the mode-locking mechanisms studied as part of this thesis work, the terms in Eqs. (6.32)–(6.36) are common to the rate-equation approach we develop for mode locking in the subsequent chapters. By concatenating the results obtained in the following chapters with the results found here, we will arrive at our so-called mode-locking rate equations. Of course, if we focus on steady-state mode locking, we can simplify the system of five coupled differential equations into a system of five algebraic equations by noting that the derivative terms must vanish (or equal a constant for ξ under passive mode locking). This is required if a steady-state exists, since the pulse properties should remain fixed from one round trip

to the next. Under active mode locking, all of the derivatives vanish, but in the presence of third-order dispersion, ξ will change from one round trip to the next.

6.6 Conclusion

In this short chapter, the moment method was applied to a modified Ginzberg–Landau equation, which included third-order dispersion, for two well-known pulse shapes. Good agreement was found when the results of our approach were compared with the analytic results expected in the anomalous-dispersion regime in the absence of third-order dispersion. The agreement between the two results verifies the accuracy of our approach and indicates that by including the effects of the various mode-locking mechanisms in our treatment we should be able to incorporate the effect the mode locker has on the steady-state pulse parameters. The next three chapters use this approach to explore saturable absorption based mode locking, AM mode locking, and FM mode locking respectively. The use of this approach results in the development of a more comprehensive analytic theory than was previously available.

7 Saturable Absorption Rate Equations

In Chapter 6, we applied the moment method to the GLE; in this chapter, we focus on lasers mode locked by a saturable absorber. By concatenating the results obtained in this chapter, for the effect a thin-sheet saturable absorber has on an electric field, with those of chapter 6 for the effect of the GLE on an electric field, we arrive at our so-called saturable-absorption mode-locking rate equations.

7.1 Saturable-Absorption based Mode Locking

Recall from chapter 4 that the effect of a fast saturable absorber on an optical field can be represented by

$$\frac{T_R}{L_R}\frac{\partial A}{\partial T} = -\frac{\delta_{SA}}{2L_R}\left(\frac{A(T,t)}{1+|A(T,t)|^2/I_{sat}}\right), \tag{7.1}$$

where δ_{SA} is the modulation depth and I_{sat} is the saturation of the device. Aside from assuming a pulse shape, when one may not even exist, we now encounter another limitation of the moment method: spatial averaging. The moment method, as applied in this work, assumes that all of the effects within the laser cavity are spatially averaged

over the cavity length which includes the effect of the mode locker.*

7.1.1 Evolution of Pulse Energy

To determine how the energy changes with propagation, we use Eq. 6.6 to operate on this term. To keep things simple, we do this by splitting it into pieces:

$$A^* \frac{\partial A}{\partial T} = -\frac{\delta_{SA}}{2T_R}\left(\frac{|A|^2}{1+|A|^2/I_{sat}}\right) \tag{7.2}$$

and

$$A \frac{\partial A^*}{\partial T} = -\frac{\delta_{SA}}{2T_R}\left(\frac{|A|^2}{1+|A|^2/I_{sat}}\right). \tag{7.3}$$

Combining these results and using Eq. 6.6, we find

$$\frac{T_R}{L_R}\frac{dE}{dT} = -\frac{\delta_{SA}}{L_R}\int_{-\infty}^{\infty}\left(\frac{|A|^2}{1+|A|^2/I_{sat}}\right). \tag{7.4}$$

Since saturable absorption is an intensity gating effect, we expect it to play a direct role in setting the cavity energy and this term must be non-zero.

7.1.2 Evolution of Pulse Center

The change in pulse location is done in the same fashion by substituting Eqs. (7.2) and (7.3) into Eq. (6.7) which gives us

$$\frac{T_R}{L_R}\frac{d\xi}{dT} = \frac{\delta_{SA}}{L_R E}\left[\xi\int_{-\infty}^{\infty}\left(\frac{|A|^2}{1+|A|^2/I_{sat}}\right)dt - \int_{-\infty}^{\infty}\left(\frac{t\,|A|^2}{1+|A|^2/I_{sat}}\right)dt\right]. \tag{7.5}$$

Since saturable absorbers have no internal clock,† we expect that this term should equal zero, in the absence of TOD.

*It is possible to extend the application of the moment method to (partially) get past this limitation; however, it results in a set of ≥ 10 equations and was not the focus of our work.

†The relaxation time of the saturable absorber is assumed to be instantaneous in this work.

7.1.3 Evolution of Spectral Shift

To find the change in carrier frequency, we use the relation from chapter Eq. (6)

$$\frac{\partial}{\partial T}\left(A^*\frac{\partial A}{\partial t}\right) = A^*\frac{\partial^2 A}{\partial T\partial t} + \frac{\partial A^*}{\partial T}\frac{\partial A}{\partial t}. \tag{7.6}$$

Then, using 4.82, we can write

$$\begin{aligned} A^*\frac{\partial^2 A}{\partial T\partial t} = &-\frac{\delta_{SA}}{2T_R}\left(\frac{1}{1+|A|^2/I_{sat}}\right)\left(A^*\frac{\partial A}{\partial t} - \frac{|A|^2}{1+|A|^2/I_{sat}}\frac{A^*}{I_{sat}}\frac{\partial A}{\partial t}\right. \\ &\left. - \frac{|A|^2}{1+|A|^2/I_{sat}}\frac{A}{I_{sat}}\frac{\partial A^*}{\partial t}\right). \end{aligned} \tag{7.7}$$

We also find that

$$\frac{\partial A^*}{\partial T}\frac{\partial A}{\partial t} = -\frac{\delta_{SA}}{2T_R}\frac{|A|^2}{1+|A|^2/I_{sat}}A^*\frac{\partial A}{\partial t}. \tag{7.8}$$

Putting these two results together we obtain

$$\begin{aligned} \frac{\partial}{\partial T}\left(A^*\frac{\partial A}{\partial t}\right) = &-\frac{\delta_{SA}}{2T_R}\left(\frac{1}{1+|A|^2/I_{sat}}\right)\left(2A^*\frac{\partial A}{\partial t} - \frac{|A|^2}{1+|A|^2/I_{sat}}\frac{A^*}{I_{sat}}\frac{\partial A}{\partial t}\right. \\ &\left. - \frac{|A|^2}{1+|A|^2/I_{sat}}\frac{A}{I_{sat}}\frac{\partial A^*}{\partial t}\right). \end{aligned} \tag{7.9}$$

By taking the complex conjugate of this, we skip a lot of redundant math and get the following result:

$$\begin{aligned} \frac{\partial}{\partial T}\left(A\frac{\partial A^*}{\partial t}\right) = &-\frac{\delta_{SA}}{2T_R}\left(\frac{1}{1+|A|^2/I_{sat}}\right)\left(2A\frac{\partial A^*}{\partial t} - \frac{|A|^2}{1+|A|^2/I_{sat}}\frac{A}{I_{sat}}\frac{\partial A^*}{\partial t}\right. \\ &\left. - \frac{|A|^2}{1+|A|^2/I_{sat}}\frac{A^*}{I_{sat}}\frac{\partial A}{\partial t}\right). \end{aligned} \tag{7.10}$$

Therefore,

$$\begin{aligned} \left[\frac{\partial}{\partial T}\left(A^*\frac{\partial A}{\partial t}\right) - \frac{\partial}{\partial T}\left(A\frac{\partial A^*}{\partial t}\right)\right] = &-\frac{\delta_{SA}}{T_R}\left(\frac{1}{1+|A|^2/I_{sat}}\right) \\ &\times \left(A^*\frac{\partial A}{\partial t} - A\frac{\partial A^*}{\partial t}\right). \end{aligned} \tag{7.11}$$

By substituting this result into Eq. (6.8) we find

$$\frac{T_R}{L_R}\frac{d\Omega}{dT} = \frac{\delta_{SA}}{L_R E}\Omega\int_{-\infty}^{\infty}\left(\frac{|A|^2}{1+|A|^2/I_{sat}}\right)dt - \frac{i\delta_{SA}}{2L_R E}\int_{-\infty}^{\infty}\left(\frac{|A|^2}{1+|A|^2/I_{sat}}\right)\left(A^*\frac{\partial A}{\partial t} - A\frac{\partial A^*}{\partial t}\right)dt. \tag{7.12}$$

7.1.4 Evolution of Chirp

The change in chirp, which is given by Eq. (6.9) can be found quickly by using Eq. 7.11:

$$\frac{T_R}{L_R}\frac{dq}{dT} = \frac{\delta_{SA}}{L_R E}q\int_{-\infty}^{\infty}\left(\frac{|A|^2}{1+|A|^2/I_{sat}}\right)dt - \frac{i\delta_{SA}}{2L_R E}\int_{-\infty}^{\infty}(t-\xi)\left(\frac{|A|^2}{1+|A|^2/I_{sat}}\right)\left(A^*\frac{\partial A}{\partial t} - A\frac{\partial A^*}{\partial t}\right)dt. \tag{7.13}$$

7.1.5 Evolution of Pulse Width

Finally, the change in the pulse width may be found by starting with Eq. (6.10):

$$\frac{T_R}{L_R}\frac{d\tau}{dT} = \frac{\delta_{SA}}{L_R E}\left[\frac{\tau}{2}\int_{-\infty}^{\infty}\left(\frac{|A|^2}{1+|A|^2/I_{sat}}\right)dt - \frac{1}{\tau C_1}\int_{-\infty}^{\infty}(t-\xi)^2\left(\frac{|A|^2}{1+|A|^2/I_{sat}}\right)dt\right]. \tag{7.14}$$

7.2 Analytic Results

Since saturable absorption mode-locked lasers almost universally produce “solition” pulses,[‡] we use our autosoliton ansatz in Eqs. (7.4)–(7.14). This allows us to predict the

[‡]Note that stretched-pulse mode locking produces either chirped Gaussian or hyperbolic-secant pulses or parabolic pulses depending on the spectral filtering and the sign and strength of the disper-

pulse parameters of a saturable-absorption mode-locked laser by solving the following five rate equations:

$$\frac{T_R}{L_R}\frac{dE}{dT} = (\bar{g}-\bar{\alpha})E - \frac{\bar{g}T_2^2}{2\tau^2}\left[C_0\left(1+q^2\right)+2\Omega^2\tau^2\right]E - \frac{\delta_{SA}}{L_R}\frac{2\tau I_{sat}}{\sqrt{1+\frac{2\tau I_{sat}}{E}}}\coth^{-1}\left(\sqrt{1+\frac{2\tau I_{sat}}{E}}\right), \tag{7.15}$$

$$\frac{T_R}{L_R}\frac{d\xi}{dT} = \bar{\beta}_2\Omega - \bar{g}T_2^2 q\Omega + \frac{\bar{\beta}_3}{4\tau^2}\left[C_0\left(1+q^2\right)+2\Omega^2\tau^2\right], \tag{7.16}$$

$$\frac{T_R}{L_R}\frac{d\Omega}{dT} = -C_0\frac{\bar{g}T_2^2}{\tau^2}\left(1+q^2\right)\Omega, \tag{7.17}$$

$$\begin{aligned}\frac{T_R}{L_R}\frac{dq}{dT} = {} & \frac{\bar{\beta}_2}{\tau^2}\left[C_0\left(1+q^2\right)+2\Omega^2\tau^2\right] - \frac{\bar{g}T_2^2}{\tau^2}q\left[C_1\left(1+q^2\right)+2\Omega^2\tau^2\right] \\ & + C_2\frac{\bar{\gamma}E}{\sqrt{2\pi}\tau} + \frac{\bar{\beta}_3\Omega}{\tau^2}\left[\frac{3}{2C_0}\left(1+q^2\right)+\Omega^2\tau^2\right] \\ & + \frac{\delta_{SA}}{L_R E}\frac{2\tau I_{sat}}{\sqrt{1+\frac{2\tau I_{sat}}{E}}}q\cosh^{-1}\left(\sqrt{1+\frac{2\tau I_{sat}}{E}}\right) \\ & - \frac{\delta_{SA}\tau I_{sat}}{4L_R E}q\left\{\ln^2\left[1+\frac{E}{\tau I_{sat}}\left(1-\sqrt{1+\frac{2\tau I_{sat}}{E}}\right)\right]\right. \\ & \left. + \ln^2\left[1+\frac{E}{\tau I_{sat}}\left(1+\sqrt{1+\frac{2\tau I_{sat}}{E}}\right)\right]\right\},\end{aligned} \tag{7.18}$$

$$\begin{aligned}\frac{T_R}{L_R}\frac{d\tau}{dT} = {} & C_3\frac{\bar{\beta}_2}{\tau}q + C_3\frac{\bar{\beta}_3}{\tau}q\Omega + C_0C_3\frac{\bar{g}T_2^2}{2\tau}\left(C_4-q^2\right) \\ & - \frac{3\delta_{SA}\tau^2 I_{sat}}{L_R E}\frac{1}{\sqrt{1+\frac{2\tau I_{sat}}{E}}}\coth^{-1}\left(\sqrt{1+\frac{2\tau I_{sat}}{E}}\right) \\ & - \frac{\delta_{SA}\tau^2 I_{sat}}{4\pi^2 L_R E}\frac{1}{\sqrt{1+\frac{2\tau I_{sat}}{E}}}\times\left\{\ln^3\left[-\left(\frac{E}{\tau I_{sat}}+1\right)-\frac{E}{\tau I_{sat}}\sqrt{1+\frac{2\tau I_{sat}}{E}}\right]\right. \\ & \left. - \ln^3\left[-\left(\frac{E}{\tau I_{sat}}+1\right)+\frac{E}{\tau I_{sat}}\sqrt{1+\frac{2\tau I_{sat}}{E}}\right]\right\},\end{aligned} \tag{7.19}$$

sion map. However, stretched-pulse mode locking involves a large dispersion map within the cavity and results in mode-locked pulses which breathe heavily. Therefore, the formulation of our method presented here limits the accuracy of our results to weak dispersion maps only since our approach averages the effect of all of the elements over the cavity length.

where the constants $C_0 = 2/3$, $C_1 = 1/3$, $C_2 = \sqrt{2\pi}/3$, $C_3 = 6/\pi^2$, and $C_4 = 2$ are identical to those defined in chapter 6 for the autosoliton.

7.3 Conclusion

This chapter analytically investigated the effect of a simple saturable absorber on pulse formation in a mode-locked laser. Although the equations obtained here could be applied to a passively mode-locked laser, the accuracy of the results would depend on the extent to which the pulse breathes in the laser cavity and the applicability of the saturable absorber model used. In an effort to extend this treatment, one could reformulate these results for a more generic saturable absorber which possesses a finite recovery time etc.. However, this would result in extra equations and since this work did not focus on saturable absorption based mode locking, we did not develop such a treatment.

8 AM Rate Equations

In Chapter 7 we applied the moment method to a saturable-absorption-based mode-locked laser. In this chapter, we follow the same approach, but consider an AM mode-locked laser. Once again, we concatenate the results obtained in this chapter, for the effect an AM mode locker has on a pulse, with those of chapter 6. This approach gives us our so-called AM mode-locking rate equations.

8.1 Application to AM Mode Locking

The effect of a sinusoidally driven AM modulator on an optical field may be represented by

$$T_R \frac{\partial A}{\partial T} = -\Delta_{AM} \{B - \cos[\omega_m (t - t_s)]\} A(T,t), \tag{8.1}$$

where $B \geq 1$ accounts for biasing and device losses, Δ_{AM} is the modulation depth, ω_m is the modulation frequency (assumed to be identical to that of the mode-locked pulse train in this work,* i.e. $\omega_m = 2\pi F_{rep}$), and $t_s = T_s(T)$ accounts for any delay between the center of the modulation cycle and the temporal window in which the pulses are

*If the driving frequency is not a harmonic of the cavity's fundamental repetition rate, the moment method begins to break down since no pulse may even exist. This is another, perhaps more subtle,

viewed.

By re-defining the averaged cavity loss as $\bar{\alpha}' = \bar{\alpha} + 2\Delta_{AM}B/L_R$, we can simplify our treatment. Thus, by comparing Eqs. (4.92) and (8.1), we note that for AM mode locking we can identify $M(A,t) = \Delta_{AM}\cos[\omega_m(t-t_m)]A(T,t)$.

8.1.1 Evolution of Pulse Energy

To determine how the energy changes with propagation, we use Eq. (6.6) in conjunction with Eq. (8.1). Once again, we split the terms into

$$A^*\frac{\partial A}{\partial T} = \frac{\Delta_{AM}}{T_R}\cos[\omega_m(t-t_s)]\,|A|^2 \tag{8.2}$$

and

$$A\frac{\partial A^*}{\partial T} = \frac{\Delta_{AM}}{T_R}\cos[\omega_m(t-t_s)]\,|A|^2. \tag{8.3}$$

By combining these results and using Eq. (6.6), we find

$$\frac{T_R}{L_R}\frac{dE}{dT} = \frac{2\Delta_{AM}}{L_R}\int_{-\infty}^{\infty}\cos[\omega_m(t-t_s)]\,|A|^2 dt. \tag{8.4}$$

Obviously, an AM modulator directly changes the energy of the field which passes through it, after all that is what the device is designed to do. As already noted, there is a bias component to the modulator that must also be included. In this work, we included the bias term by re-defining the loss $\bar{\alpha}$ in Eq. (6.32).

---

limitation of the moment method. However, for detunings where pulses are still formed, the moment method will still predict their behavior albeit with a decreasing accuracy.

8.1.2 Evolution of Pulse Center

The change in pulse location is found in the same fashion by substituting Eqs. (8.2) and (8.3) into Eq. (6.7), which results in:

$$\frac{T_R}{L_R}\frac{d\xi}{dT} = -\frac{2\Delta_{AM}}{L_R E}\left\{\xi\int_{-\infty}^{\infty}\cos\left[\omega_m\left(t-t_s\right)\right]|A|^2\,dt - \int_{-\infty}^{\infty}t\cos\left[\omega_m\left(t-t_s\right)\right]|A|^2\,dt\right\}. \tag{8.5}$$

We have also shown that an AM modulator changes the central location (with respect to time) of a pulse. We point out that this occurs because of the device's time-dependent loss carves out a temporal window that permits pulse formation.

8.1.3 Evolution of Spectral Shift

To find the change in carrier frequency, we once again use the relation

$$\frac{\partial}{\partial T}\left(A^*\frac{\partial A}{\partial t}\right) = A^*\frac{\partial^2 A}{\partial T\,\partial t} + \frac{\partial A^*}{\partial T}\frac{\partial A}{\partial t}. \tag{8.6}$$

Then using Eq. (4.82), we can write

$$A^*\frac{\partial^2 A}{\partial T\,\partial t} = \frac{\Delta_{AM}}{T_R}\cos\left[\omega_m\left(t-t_s\right)\right]A^*\frac{\partial A}{\partial t} - \frac{\Delta_{AM}\omega_m}{T_R}\sin\left[\omega_m\left(t-t_s\right)\right]|A|^2. \tag{8.7}$$

We also find that

$$\frac{\partial A^*}{\partial T}\frac{\partial A}{\partial t} = \frac{\Delta_{AM}}{T_R}\cos\left[\omega_m\left(t-t_s\right)\right]A^*\frac{\partial A}{\partial t}. \tag{8.8}$$

Putting the previous two results together through Eq. (8.6) we obtain

$$\frac{\partial}{\partial T}\left(A^*\frac{\partial A}{\partial t}\right) = \frac{2\Delta_{AM}}{T_R}\cos\left[\omega_m\left(t-t_s\right)\right]A^*\frac{\partial A}{\partial t} - \frac{\Delta_{AM}\omega_m}{T_R}\sin\left[\omega_m\left(t-t_s\right)\right]|A|^2. \tag{8.9}$$

By taking the complex conjugate of this, we skip a lot of redundant math and find

$$\begin{aligned}\frac{\partial}{\partial T}\left(A\frac{\partial A^*}{\partial t}\right) &= \frac{2\Delta_{AM}}{T_R}\cos\left[\omega_m\left(t-t_s\right)\right]A\frac{\partial A^*}{\partial t}\\ &- \frac{\Delta_{AM}\omega_m}{T_R}\sin\left[\omega_m\left(t-t_s\right)\right]|A|^2.\end{aligned} \tag{8.10}$$

Therefore,

$$\left[\frac{\partial}{\partial T}\left(A^*\frac{\partial A}{\partial t}\right)-\frac{\partial}{\partial T}\left(A\frac{\partial A^*}{\partial t}\right)\right]=\frac{2\Delta_{AM}}{T_R}\cos\left[\omega_m\left(t-t_s\right)\right]\left[A^*\frac{\partial A}{\partial t}-A\frac{\partial A^*}{\partial t}\right]. \tag{8.11}$$

Substituting this result into Eq. (6.8) gives us

$$\begin{aligned}\frac{T_R}{L_R}\frac{d\Omega}{dT} &= -\frac{\Delta_{AM}}{L_R E}\left\{2\Omega\int_{-\infty}^{\infty}\cos\left[\omega_m(t-t_s)\right]|A|^2\,dt\right.\\ &\left.- i\int_{-\infty}^{\infty}\cos\left[\omega_m\left(t-t_s\right)\right]\left[A^*\frac{\partial A}{\partial t}-A\frac{\partial A^*}{\partial t}\right]dt\right\}.\end{aligned} \tag{8.12}$$

This result reveals that an AM modulator will place a time varying shift in the carrier frequency of the field passing through it if it is not aligned with the minimum loss location.

8.1.4 Evolution of Chirp

The change in chirp, which is given by Eq. (6.9), may be simplified by using Eq. (8.11) to

$$\begin{aligned}\frac{T_R}{L_R}\frac{dq}{dT} &= -\frac{2\Delta_{AM}}{L_R E}\left\{q\int_{-\infty}^{\infty}\cos\left[\omega_m\left(t-t_s\right)\right]|A|^2\,dt\right.\\ &\left.- i\int_{-\infty}^{\infty}(t-\xi)\cos(\omega_m\left[t-t_s\right])\left[A^*\frac{\partial A}{\partial t}-A\frac{\partial A^*}{\partial t}\right]dt\right\}.\end{aligned} \tag{8.13}$$

The AM modulator can also change the pulse chirp if the pulse is not aligned with the minimum loss location.

8.1.5 Evolution of Pulse Width

Finally, the change in the pulse width may be found by starting with Eq. (6.10); it is given by

$$\frac{T_R}{L_R}\frac{d\tau}{dT} = -\frac{\Delta_{AM}}{L_R E}\left\{\tau\int_{-\infty}^{\infty}\cos\left[\omega_m(t-t_s)\right]|A|^2\,dt - \frac{2C_3}{\tau}\int_{-\infty}^{\infty}(t-\xi)^2\cos\left[\omega_m(t-t_s)\right]|A|^2\,dt\right\}. \tag{8.14}$$

Although the results were obtained in this section via the moment method, one can confirm them by operating on a pulse with a given analytic shape and then asking how the various pulse parameters change as it passes through such a device. An intermediate treatment similar to this approach is provided in Ref. 149 for an AM mode-locked laser using the moment method. If the results of both approaches are Taylor-expanded and detuning is ignored, we obtain full agrement between the two approaches. This verifies our approach and the applicability of the moment method in this application.

8.2 Analytic Results

If our two pulse ansatz [Eqs. (6.30) and (6.31)] are used in Eqs. (8.4), (8.5), (8.12), (8.13), and (8.14), we end up with the effect an AM mode locker has on the field inside

a laser cavity:

$$\frac{T_R}{L_R}\frac{dE}{dT} = \left(\bar{g}-\bar{\alpha}'\right)E - \frac{\bar{g}T_2^2}{2\tau^2}\left[C_0\left(1+q^2\right)+2\Omega^2\tau^2\right]E + \frac{2\Delta_{AM}}{L_R}\Psi_0\cos\left[\omega_m(\xi-t_s)\right]E, \tag{8.15}$$

$$\frac{T_R}{L_R}\frac{d\xi}{dT} = \bar{\beta}_2\Omega - \bar{g}T_2^2 q\Omega + \frac{\bar{\beta}_3}{4\tau^2}\left[C_0\left(1+q^2\right)+2\Omega^2\tau^2\right] - \frac{\Delta_{AM}\tau}{L_R}\Psi_1\sin\left[\omega_m(\xi-t_s)\right], \tag{8.16}$$

$$\frac{T_R}{L_R}\frac{d\Omega}{dT} = -C_0\frac{\bar{g}T_2^2}{\tau^2}\left(1+q^2\right)\Omega - \frac{\Delta_{AM}\omega_m}{L_R}q\Psi_0\sin\left[\omega_m(\xi-t_s)\right], \tag{8.17}$$

$$\frac{T_R}{L_R}\frac{dq}{dT} = \frac{\bar{\beta}_2}{\tau^2}\left[C_0\left(1+q^2\right)+2\Omega^2\tau^2\right] - \frac{\bar{g}T_2^2}{\tau^2}q\left[C_1\left(1+q^2\right)+2\Omega^2\tau^2\right] + C_2\frac{\bar{\gamma}E}{\sqrt{2\pi}\tau} + \frac{\bar{\beta}_3\Omega}{\tau^2}\left[\frac{3}{2C_0}\left(1+q^2\right)+\Omega^2\tau^2\right] - \frac{\Delta_{AM}\tau}{L_R}\Psi_1\left\{q\kappa\cos\left[\omega_m(\xi-t_s)\right]+2\Omega\sin\left[\omega_m(\xi-t_s)\right]\right\}, \tag{8.18}$$

$$\frac{T_R}{L_R}\frac{d\tau}{dT} = C_3\frac{\bar{\beta}_2}{\tau}q + C_3\frac{\bar{\beta}_3}{\tau}q\Omega + C_0C_3\frac{\bar{g}T_2^2}{2\tau}\left(C_4-q^2\right) - \frac{\Delta_{AM}\tau}{2L_R}\Psi_2\cos\left[\omega_m\left(\xi-t_s\right)\right], \tag{8.19}$$

where the constants C_n ($n = 0$ to 4) are identical to those defined in chapter 6. In these equations, we have also introduced

$$\Psi_0 = \exp\left(-\omega_m^2\tau^2/4\right), \tag{8.20}$$

$$\Psi_1 = \omega_m\tau\Psi_0, \tag{8.21}$$

$$\Psi_2 = \omega_m^2\tau^2\Psi_0, \tag{8.22}$$

for the Gaussian pulse and

$$\Psi_0 = \left(\pi\omega_m\tau/2\right)\operatorname{csch}\left(\pi\omega_m\tau/2\right), \tag{8.23}$$

$$\Psi_1 = \left[\pi\coth\left(\pi\omega_m\tau/2\right)-2/(\omega_m\tau)\right]\Psi_0, \tag{8.24}$$

$$\Psi_2 = \left\{2+3\operatorname{csch}^2\left(\pi\omega_m\tau/2\right)\left[3+\cosh(\pi\omega_m\tau) - 4/(\pi\omega_m\tau)\sinh(\pi\omega_m\tau)\right]\right\}\Psi_0, \tag{8.25}$$

for the autosoliton.

Equations (8.15)–(8.19) are analogous to the traditional rate equations used for cw lasers and we refer to them as the AM mode-locking rate equations. They were numerically solved in a fraction of the time required to solve the original equation [Eq. (4.92) with M given by Eq. (8.1)] by using the fourth-order Runge–Kutta method and the parameters found in Table 5.1.[†] Figure 8.1 displays how pulse energy E, width τ, and chirp q change from one round trip to the next when seeded with the initial values $E(0) = 1$ fJ, $\xi(0) = 0$ fs, $\Omega(0) = 0$ GHz, $\tau(0) = 0.5$ ps, and $q(0) = 0$. The plots for $\tau(T)$ and $q(T)$ were combined into one phase-space plot by plotting q as a function of τ. As seen in part (a) of Fig. 8.1, pulse energy increases from 1 fJ to ≈ 2.74 pJ in less than 200 round trips and converges rapidly to its steady-state value. Only ~ 2000 round trips are necessary before the pulse parameters converge to their steady-state values.

Equations (8.15)–(8.19) are analogous to the rate equations used for continuous-wave lasers in the sense that they describe how the pulse parameters E, ξ, Ω, q, and τ change from one round trip to the next. For example, Eq. (8.15) shows that the energy is enhanced by the gain (first term) but reduced by both the gain filtering (second term) and the AM mode locker (third term). Similarly, Eq. (8.19) shows that the modulator shortens optical pulses as they pass through it (last term).

To illustrate pulse dynamics, we solve Eqs. (8.15)–(8.19) for a Fabry–Perot fiber laser using realistic parameter values. More specifically, we use $\bar{\beta}_2 = \pm 0.014$ ps^2/m, $\bar{\gamma} = 0.012$ W^{-1}/m, $\bar{g}_0 = 0.55$ m^{-1}, $\bar{\alpha} = 0.17$ m^{-1}, $T_2 = 47$ fs/rad, $P_{\text{sat}} = 12.5$ mW, $F_{\text{rep}} = 10$ GHz, $L_R = 4$ m, $T_R = 40$ ns, and $\Delta_{AM} = 0.3$. Figure 8.1 shows the approach

[†]Our solution assumes a Fabry–Perot laser cavity. Therefore, the mode-locked pulse passes through the gain media twice during a single round trip and so the power, which saturates the gain media, must be determined by taking the counter-propagating pulses into account. In the averaged cavities we are considering in these sections, a steady-state mode-locked pulse will have the same power everywhere in the cavity. This allows us to simply divide the saturation power by 2 in these sections. In a through model, the counter-propagating pulses should be taken into account; see chapter 5 for a discussion of such an approach.

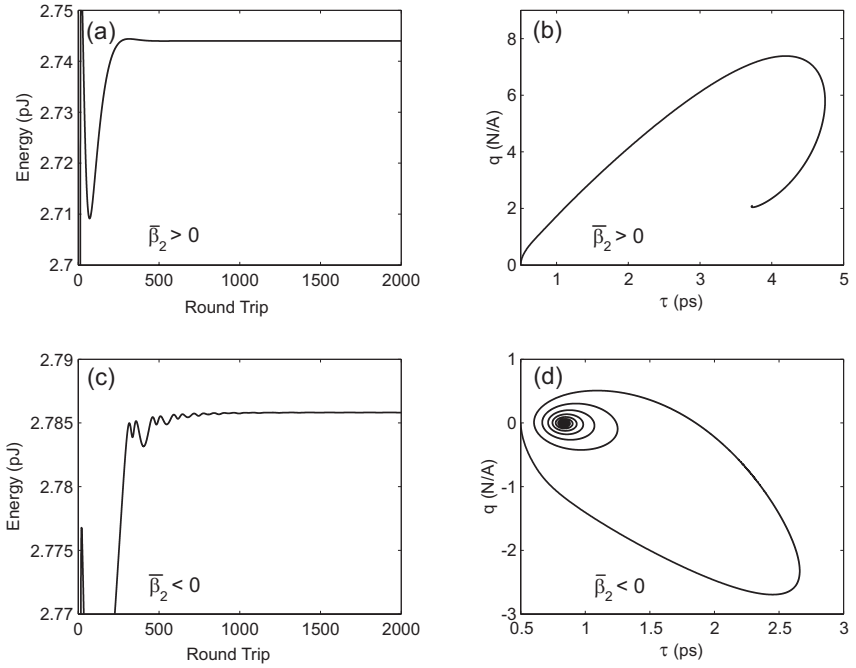

Figure 8.1: Evolution of pulse energy E, width τ, and chirp q over multiple round trips in the case of anomalous (bottom row) and normal (top row) dispersion.

to steady state in both the normal- and anomalous-dispersion regimes. It reveals that the pulse converges quickly in the normal-dispersion region but takes > 1000 round trips before converging in the anomalous-dispersion region. Although the rate of convergence depends on the initial conditions used ($E = 1$ fJ, $q = 0$, and $\tau = 0.5$ ps), this type of behavior is expected since the nonlinear effects are weaker in the normal-dispersion region. In the normal-dispersion regime, the nonlinear effects add to the effect of dispersion and broaden the pulse to $\tau = 3.73$ ps, thus reducing its peak power and the role played by nonlinearity. In the anomalous-dispersion regime, the interplay between dispersion and nonlinearity prolongs the convergence. We also point out the robustness of our approach since the initial energy used is more than 2500 times smaller than the steady-state value obtained.

To quantify the accuracy of our rate-equation model, we solved Eq. (4.92) numerically with the above parameter values and a 1 photon/mode strength, complex,

Gaussian-distributed noise seed. We found that the approach to steady state follows a pattern that is quite close to that seen in Fig. 8.1. The final steady-state value of pulse width agrees within 2.5% in the case of anomalous dispersion. The agreement is not as good in the case of normal dispersion although it is within 9%. This is a consequence of the pulse shape, which deviates from the Gaussian shape assumed due to nonlinearity, especially for small modulation depths Δ_{AM}.

Figure 8.1 also reveals the mode-locked pulse in the normal-dispersion regime is chirped ($q \simeq 2$), whereas the chirp is nearly zero ($q \approx 0$) in the anomalous-dispersion regime. This behavior is a consequence of the interplay between dispersion and nonlinearity. In the anomalous regime, the two effects produce chirps with opposite signs, which partially cancel one another, whereas, the chirps add in the normal-dispersion regime.[128]

8.3 Comparison with Numerical Simulations

As seen in Fig. 8.1, all pulse parameters converge toward a constant value after a sufficiently large number of round trips. Under steady-state conditions, the derivatives in Eqs. (8.15)–(8.19) can be set to zero. If a steady-state has been reached and we assume the effects of third-order dispersion are small, we can ignore the ξ and Ω equations by setting those two terms to zero. This allows us to obtain the following set of coupled algebraic equations for the saturated gain, pulse width, and chirp:

$$\bar{g}_{ss} = \left(\bar{\alpha} + \frac{\Delta_{AM}\omega^2\tau_{ss}^2}{2C_5L_R}\right)\left[1 - \frac{T_2^2}{2\tau_{ss}^2}\left(1+q_{ss}^2\right)\right]^{-1}, \tag{8.26}$$

$$\tau_{ss} = \left(C_4\Delta_{AM}\omega_m^2/L_R\right)^{-1/4}\left[\left(2\bar{\beta}_2/C_1\right)q_{ss} + C_2\bar{g}_{ss}T_2^2\left(C_3 - q_{ss}^2\right)\right]^{1/4}, \tag{8.27}$$

$$q_{ss} = -d \pm \left[d^2 + C_3 + C_6\bar{\gamma}E\,\tau_{ss}/\left(C_5\bar{\beta}_2\sqrt{2\pi}\right)\right]^{1/2}, \tag{8.28}$$

where the dimensionless parameter d is defined as

$$d = \frac{1}{2\beta_2}\left[\left(1+C_3\right)\bar{g}_{ss}T_2^2 + \left(\frac{C_1}{C_5} - \frac{C_4}{C_2}\right)\frac{\Delta_{AM}\omega_m^2\tau_{ss}^4}{L_R}\right]. \tag{8.29}$$

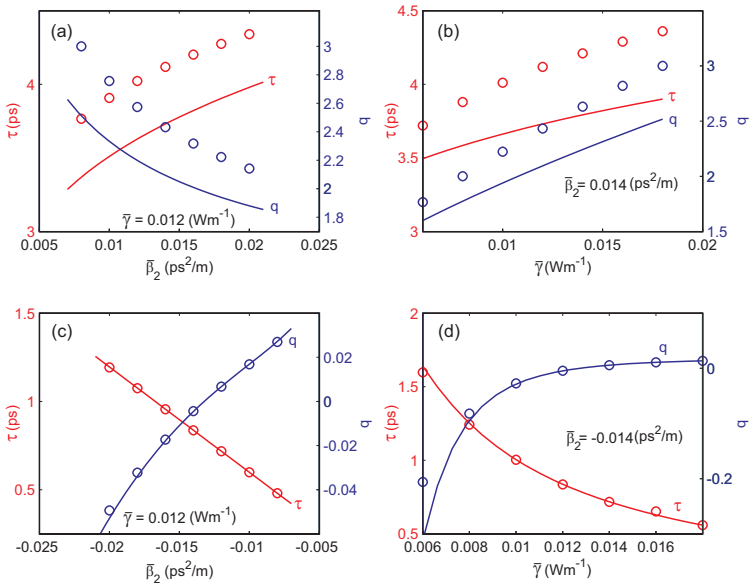

Figure 8.2: Steady-state pulse width and chirp as functions of $\bar{\beta}_2$ (left column) and nonlinear parameter $\bar{\gamma}$ (right column). Dispersion is normal for the top row and anomalous for the bottom row. The discrete markers come from solving Eq. (4.92) while the solid lines come from solving Eqs. (8.26)–(8.28).

Equation (8.26) reveals that the saturated gain is determined by the cavity losses, the modulator, and the mode-locked pulse spectrum. Equations (8.28) and (8.29) show how the chirp is affected by changing the cavity losses, nonlinearity, or the modulation depth. For example, if the nonlinear parameter is set to zero, pulses remain chirped; however, if dispersion is also set to zero, $d \to \infty$ and $q_{ss} = 0$ is the only physically valid solution. Of course, we should use the Gaussian pulse shape under such conditions following Refs. 2 and 4. Setting $C_n = 1$ in Eq. (8.27), we find that the steady state pulse width in the absence of dispersive and nonlinear effects is given by

$$\tau_{ss} = \left(\frac{\bar{g}L_R}{\Delta_{AM}}\right)^{1/4} \sqrt{\frac{T_2}{\omega_m}}. \tag{8.30}$$

This equation is identical to the result first found by Kuizenga and Siegman as it should be.[2]

The most powerful feature of Eqs. (8.26)–(8.28) is that they can be used to instantly[‡]

[‡]Our theoretical results shown in Fig. 8.2 took < 0.1 second to generate

predict the impact of fiber dispersion and nonlinearity as well as modulation depth and frequency on the mode-locked pulses. Figure 8.2 shows the results obtained as $\bar{\beta}_2$ and $\bar{\gamma}$ are varied. Plots (a) and (b) investigate the case where dispersion is normal ($\bar{\beta}_2 > 0$); they also reveal a discrepancy between our theory and the full model [i.e. the solution to Eq. (4.92)]. This error, which is $<$15%, is again due to the pulse shape which deviates from the assumed Gaussian shape. Plots (c) and (d), both made assuming anomalous dispersion, exhibit excellent agreement between our theory and the full model. The agrement persists even over the large parameter space explored demonstrating the robustness of our theory in this case. By comparing Figs. 8.2(a) and (c), it is found that as the magnitude of dispersion is decreased, pulse width is reduced but chirp increases. Qualitatively, this behavior is the same in both regions. Comparing Figs. 8.2(b) and (d), however, we observe an interesting feature. Increasing the nonlinearity in the normal-dispersion region results in a large increase in both pulse width and chirp. However, in the anomalous-dispersion regime, an increase in nonlinearity reduces the pulse width while the chirp increases only slightly. For example, pulse width τ_{ss} is reduced below 1 ps for $\bar{\gamma} > 0.012$ W^{-1}/m while chirp is nearly zero. If the nonlinearity is increased to $\bar{\gamma} = 0.028$ W^{-1}/m, the theory predicts pulses with $\tau_{ss} = 0.36$ ps indicating a pulse 3 times smaller than those predicted by the Kuizenga–Siegman limit.[2] This result was also verified by the full model.

This demonstrates that femtosecond pulses can be realized in actively mode-locked lasers by incorporating elements with large values of $\bar{\gamma}$ into the cavity. Photonic-crystal fibers or tapered fibers can be used for this purpose. Since chirp can be nearly eliminated in the anomalous-dispersion regime, optimized actively mode-locked fiber lasers should produce near transform-limited femtosecond pulses.

8.4 Conclusion

In this chapter, we investigated AM mode locking via our rate-equation approach. This allowed us to incorporate the effect of the modulator depth as well as second- and third-order dispersion. We find that in the presence of second-order dispersion the pulses become chirped while third-order dispersion pushes the pulses away from the extrema of the modulation cycle where they would otherwise form.

9 FM Rate Equations

In this chapter we apply the moment method to mode locking via frequency modulation or FM mode locking. By concatenating the results obtained in this chapter with those of chapter 6 we arrive at our so-called FM rate-equations for mode locking. Before proceeding we point out that FM mode locking is essentially an indirect mode-locking mechanism. The differential loss required to suppress cw lasing and initiate pulse formation is obtained as a consequence of spectral filtering which becomes important because the FM modulator chirps the light in the cavity to such an extent that the cw light acquires a large bandwidth.

9.1 Application to FM Mode Locking

The effect of a sinusoidally driven FM modulator on an optical field may be represented by

$$T_R \frac{\partial A}{\partial T} = i\Delta_{FM} \cos\left[\omega_m (t + t_s)\right] A, \tag{9.1}$$

where Δ_{FM} is the modulation depth, ω_m is the modulation frequency (assumed to be identical to that of the mode-locked pulse train in this work,* i.e. $\omega_m = 2\pi F_{rep}$), and t_s accounts for any delay between the center of the modulation cycle and the temporal window in which the pulses are viewed. By comparing Eqs. (4.92) and (9.1) we note that for FM mode locking $M(A,t) = i\Delta_{FM}\cos[\omega_m(t+t_s)]A$.

9.1.1 Evolution of Pulse Energy

To determine how the energy changes with propagation we use Eq. (6.6) to operate on this term. To keep things simple we do this by splitting it into pieces:

$$A^*\frac{\partial A}{\partial T} = -\frac{i\Delta_{FM}}{T_R}\cos[\omega_m(t-t_s)]\,|A|^2 \tag{9.2}$$

and

$$A\frac{\partial A^*}{\partial T} = \frac{i\Delta_{FM}}{T_R}\cos[\omega_m(t-t_s)]\,|A|^2. \tag{9.3}$$

Combining these results and using Eq. (6.6) we find

$$\frac{T_R}{L_R}\frac{dE}{dT} = 0. \tag{9.4}$$

Therefore, an FM modulator does not directly change the energy of a pulse, however, it should be noted that passive losses associated with the device have been ignored here. The loss associated with a practical device, which can not be ignored, is simply factored into the determination of the averaged passive losses, $\bar{\alpha}$, appearing in Eq. (4.92).

*If the driving frequency is not a harmonic of the cavity's fundamental repetition rate the moment method breaks down since the existence of a pulse is not expected; this is the other, perhaps more subtle, limitation of the moment method. See the comments in chapter 8.

9.1.2 Evolution of Pulse Center

The change in pulse location is found in the same fashion by substituting Eqs. (9.2) and (9.3) into Eq. (6.7) which gives us:

$$\frac{T_R}{L_R}\frac{d\xi}{dT} = 0. \tag{9.5}$$

This tells us that FM modulators do not directly change pulse location.

9.1.3 Evolution of Spectral Shift

To find the change in carrier frequency imparted on a field due to an FM modulator we once again start with the relation

$$\frac{\partial}{\partial T}\left(A^*\frac{\partial A}{\partial t}\right) = A^*\frac{\partial^2 A}{\partial T\partial t} + \frac{\partial A^*}{\partial T}\frac{\partial A}{\partial t}. \tag{9.6}$$

Then using Eq. (4.82) we can write

$$\begin{aligned} A^*\frac{\partial^2 A}{\partial T\partial t} &= -i\Delta_{FM}\omega_m\frac{1}{T_R}\sin\left[\omega_m\left(t-t_s\right)\right]|A|^2 \\ &\quad + i\Delta_{FM}\frac{1}{T_R}\cos\left[\omega_m\left(t-t_s\right)\right]A^*\frac{\partial A}{\partial t}. \end{aligned} \tag{9.7}$$

We also find

$$\frac{\partial A^*}{\partial T}\frac{\partial A}{\partial t} = -i\Delta_{FM}\frac{1}{T_R}\cos\left[\omega_m\left(t-t_s\right)\right]A^*\frac{\partial A}{\partial t}. \tag{9.8}$$

Putting these two results together we obtain

$$\frac{\partial}{\partial T}\left(A^*\frac{\partial A}{\partial t}\right) = -i\Delta_{FM}\omega_m\frac{1}{T_R}\sin\left[\omega_m\left(t-t_s\right)\right]|A|^2. \tag{9.9}$$

By taking the complex conjugate of this we skip a lot of redundant math to get

$$\frac{\partial}{\partial T}\left(A\frac{\partial A^*}{\partial t}\right) = i\Delta_{FM}\omega_m\frac{1}{T_R}\sin\left[\omega_m\left(t-t_s\right)\right]|A|^2. \tag{9.10}$$

Therefore,

$$\left[\frac{\partial}{\partial T}\left(A^{*}\frac{\partial A}{\partial t}\right)-\frac{\partial}{\partial T}\left(A\frac{\partial A^{*}}{\partial t}\right)\right]=-2i\Delta_{FM}\omega_{m}\frac{1}{T_{R}}\sin\left[\omega_{m}\left(t-t_{s}\right)\right]\left|A\right|^{2}. \tag{9.11}$$

Substituting this result into Eq. (6.8) gives us

$$\frac{T_{R}}{L_{R}}\frac{d\Omega}{dT}=\frac{\Delta_{FM}\omega_{m}}{L_{R}E}\int_{-\infty}^{\infty}\sin\left[\omega_{m}\left(t-t_{s}\right)\right]\left|A\right|^{2}dt. \tag{9.12}$$

This result reveals perhaps the most important effect of an FM modulator: an FM modulator places a time-varying shift in the carrier frequency of the field passing through it. By changing the carrier frequency of light in the presence of filtering (or a gain media with a finite bandwidth) FM mode locking acquires the loss mechanism necessary for pulse formation and background suppression. Moreover, we should point out that because an FM modulator can change the carrier frequency of the light propagating through it FM modulators indirectly change the arrival time of light propagating in a dispersive media. This fact has been exploited by groups making adjustable optical delay lines, most notably by van Howe and co-workers.[150–152]

9.1.4 Evolution of Chirp

The change in chirp, which is given by Eq. (6.9), may be immediately written by using Eq. (9.11)

$$\frac{T_{R}}{L_{R}}\frac{dq}{dT}=\frac{2\Delta_{FM}\omega_{m}}{L_{R}E}\int_{-\infty}^{\infty}\left(t-\xi\right)\sin\left[\omega_{m}\left(t-t_{s}\right)\right]\left|A\right|^{2}dt \tag{9.13}$$

This result indicates that the FM modulator also changes the pulse chirp as one might expect.

9.1.5 Evolution of Pulse Width

Finally, the change in the pulse width may be found by starting with Eq. (6.10)

$$\frac{T_{R}}{L_{R}}\frac{d\tau}{dT}=0 \tag{9.14}$$

Although the results were obtained in this section via the moment method they can also be confirmed by operating on a pulse with a given analytic shape and then asking how the various pulse parameters change. If the results are Taylor expanded we get full agrement. This acts as a sanity check.

9.2 Analytic Results

If our two pulse ansatz are used in Eqs. (9.4)–(9.14) we end up with the effect a synchronously driven FM mode locker has on the field inside a laser cavity:

$$\frac{T_R}{L_R}\frac{dE}{dT} = (\bar{g}-\bar{\alpha})E - \frac{\bar{g}T_2^2}{2\tau^2}\left[C_0\left(1+q^2\right)+2\Omega^2\tau^2\right]E, \tag{9.15}$$

$$\frac{T_R}{L_R}\frac{d\xi}{dT} = \bar{\beta}_2\Omega - \bar{g}T_2^2 q\Omega + \frac{\bar{\beta}_3}{4\tau^2}\left[C_0\left(1+q^2\right)+2\Omega^2\tau^2\right], \tag{9.16}$$

$$\frac{T_R}{L_R}\frac{d\Omega}{dT} = -C_0\frac{\bar{g}T_2^2}{\tau^2}\left(1+q^2\right)\Omega + \frac{\Delta_{FM}\omega_m}{L_R}\Psi_0\sin\left[\omega_m\left(\xi-t_s\right)\right], \tag{9.17}$$

$$\begin{aligned}\frac{T_R}{L_R}\frac{dq}{dT} = {} & \frac{\bar{\beta}_2}{\tau^2}\left[C_0\left(1+q^2\right)+2\Omega^2\tau^2\right] - \frac{\bar{g}T_2^2}{\tau^2}q\left[C_1\left(1+q^2\right)+2\Omega^2\tau^2\right] \\ & + C_2\frac{\bar{\gamma}E}{\sqrt{2\pi}\tau} + \frac{\bar{\beta}_3\Omega}{\tau^2}\left[\frac{3}{2C_0}\left(1+q^2\right)+\Omega^2\tau^2\right] \\ & + \frac{\Delta_{FM}\omega_m\tau}{L_R}\Psi_1\cos\left[\omega_m\left(\xi-t_s\right)\right],\end{aligned} \tag{9.18}$$

$$\frac{T_R}{L_R}\frac{d\tau}{dT} = C_3\frac{\bar{\beta}_2}{\tau}q + C_3\frac{\bar{\beta}_3}{\tau}q\Omega + C_0C_3\frac{\bar{g}T_2^2}{2\tau}\left(C_4-q^2\right), \tag{9.19}$$

where the constants C_n ($n=0$ to 4) are identical to those defined in chapter 6, however,

$$\Psi_0 = \exp\left(-\omega_m^2\tau^2/4\right) \tag{9.20}$$

$$\Psi_1 = \omega_m\tau\Psi_0 \tag{9.21}$$

for the Gaussian pulse. For the autosoliton,

$$\Psi_0 = (\pi\omega_m\tau/2)\,\mathrm{csch}\left(\pi\omega_m\tau/2\right), \tag{9.22}$$

$$\Psi_1 = \left[\pi\coth\left(\pi\omega_m\tau/2\right)-2/(\omega_m\tau)\right]\Psi_0. \tag{9.23}$$

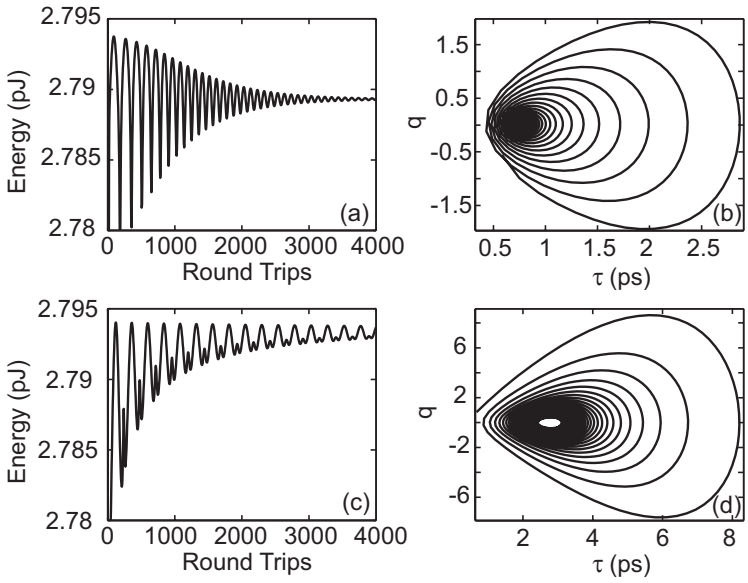

Figure 9.1: Evolution of pulse energy E, width τ, and chirp q over multiple round trips in the case of anomalous (top row) and normal (bottom row) dispersion.

Equations (9.15)–(9.19) are analogous to the traditional rate equations used for cw lasers and we refer to them as the FM mode-locking rate equations. They were numerically solved in a fraction of the time required to solve the original equation [Eq. (4.92)] by using the fourth-order Runge–Kutta method and the parameters found in Table 5.1.[†] Figure 9.1 displays how pulse energy E, width τ, and chirp q change from one round trip to the next when seeded with the initial values $E(0) = 1$ fJ, $\xi(0) = 0$ fs, $\Omega(0) = 0$ GHz, $\tau(0) = 0.5$ ps, and $q(0) = 0$. The plots for $\tau(T)$ and $q(T)$ were combined into one phase-space plot by plotting q as a function of τ. As seen in the first column of Fig. 9.1, pulse energy increases from 1 fJ to ≈ 2.8 pJ in less than 100 round trips but then exhibits damped oscillations as it evolves over thousands of round trips. In fact, more than 4000 round trips are necessary before the pulse parameters converge to their steady-state values (a situation similar to that found when performing the numerical

[†]As in chapters 6–8, our solution once again assumes a Fabry–Perot laser cavity. Therefore, the mode-locked pulse passes through the gain media twice during a single round trip and the saturation term must be doubled.

simulations to create Figs. 5.4 and 5.5 in the chapter 5). Note that in the case of normal dispersion [Fig. 9.1(d)] the pulse has not reached a final steady state even after 4000 round trips. In general, the approach to steady state takes longer when the residual cavity dispersion is normal since the modulator's compression effect must balance both dispersive and nonlinear broadening. In fact, it has even been reported that a train of well-separated mode-locked pulses could not be experimentally realized at a high repetition rate in this regime.[4,66] Of course, this result depends on the laser parameters: in the presence of nonlinearity, it indicates that stronger modulation depths are required to obtain mode locking in the normal-dispersion regime.

9.3 Comparison with Numerical Simulations

In the preceding section, the evolution of pulse parameters toward their steady-state values was studied by solving the mode-locking rate equations numerically. Although good agreement was obtained, the true strength of our approach lies in predicting the steady-state values for mode-locked pulses. Assuming that the mode-locked laser has reached a steady state, the pulse parameters may be determined quasi-analytically by setting the derivatives to zero in Eqs. (9.15)–(9.19). The resulting system of nonlinear algebraic equations is easily solved using the Newton–Raphson technique.[‡] Since this scheme converges quickly, given a reasonable initial guess, parametric studies may be performed effortlessly.

Figure 9.2 demonstrates the strength of our approach by studying the effect of modulation depth on pulse width. To put this work in perspective, our results are presented, along with those based on previous theories, in both anomalous and normal dispersion regimes. In both cases, we consider a linear nondispersive cavity (squares), a linear dispersive cavity (triangles), and a cavity with both nonlinearity and dispersion (cir-

[‡]See Appendix E for an introduction to this technique.

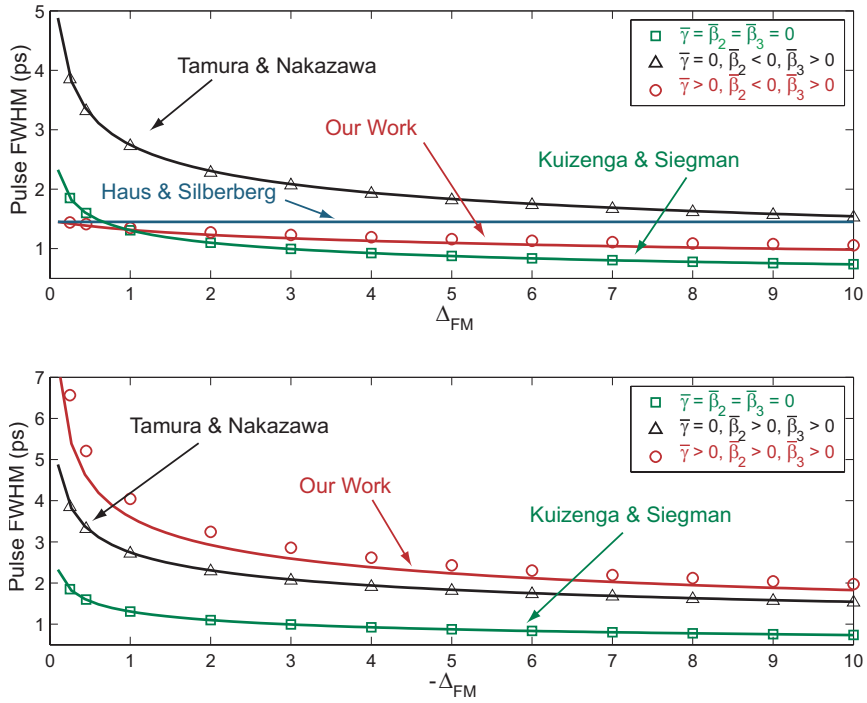

Figure 9.2: Pulse width predicted by our theory as a function of modulation depth in the anomalous (a) and normal (b) dispersion regimes. In each case, we compare our predictions with numerical simulations and with the theories given in Refs. 2 and 3 (when $\bar{\beta}_2 < 0$), and 4.

cles). Data points marked with symbols were obtained using the full numerical model [Eq. (4.92)] whereas the solid lines were generated using the corresponding analytic treatment in each case. The theory developed by Kuizenga and Siegman[2] predicts the pulse width when dispersion and nonlinearity are neglected. With the inclusion of dispersion, an extended version of this theory used by Tamura and Nakazawa[2,4] predicts the pulse width. Haus and Silberberg's theory predicts the pulse parameters when both nonlinearity and anomalous dispersion are included; yet, fails to include TOD or modulation depth and is invalid in the normal dispersion regime.[3] As a result, only the theory developed in this work is found to be in good agreement with the numerical results in the presence of both nonlinearity and dispersion. Moreover, our theory reproduces all of the prior results in the appropriate limits.

A noteworthy feature of Fig. 9.2(a) is that for modulation depths $\Delta_{FM} < 0.9$ the

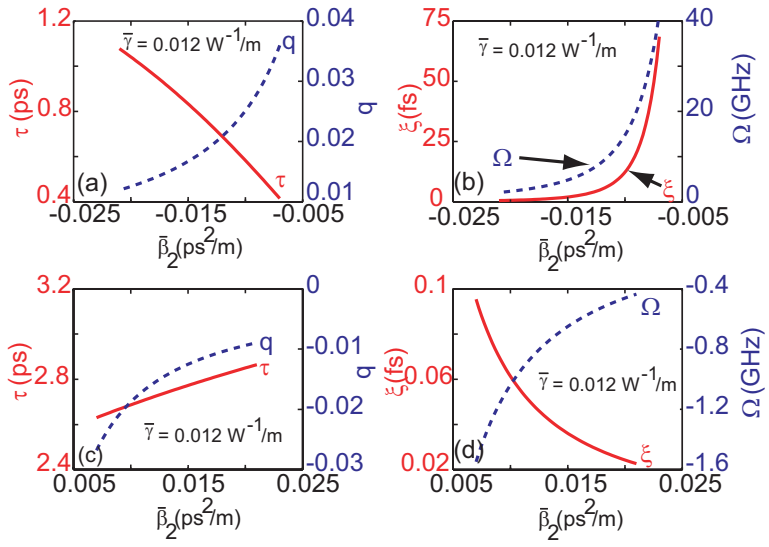

Figure 9.3: Steady-state pulse width τ, chirp q, (left column) temporal shift ξ, and frequency shift Ω (right column) in the anomalous (top row) and normal (bottom row) dispersion regimes.

mode-locked pulse experiences soliton pulse compression[3,30,31,39,153,154] since the pulse width becomes shorter than that predicted by the simplified theory of Ref. 2. For $\Delta_{FM} > 0.9$, the modulator plays an increasingly dominant role. Nevertheless, excellent agreement is obtained between the simulations and our theory even for large modulation depths (1.3% error for $\Delta_{FM} = 0.25$, 7% error for $\Delta_{FM} = 10$). Conversely, the agreement in Fig. 9.2(b) is seen to increase with the modulation depth (15% error for $\Delta_{FM} = -0.25$, 7% error for $\Delta_{FM} = -10$). This behavior can be understood by noting that the modulator's preferred shape is a Gaussian.[2,4] As a result, our accuracy improves with modulation depth in the normal dispersion regime but deteriorates in the anomalous dispersion regime.

An important question we can answer with our semi-analytic approach [Eqs. (9.15)–(9.19)] is how the residual cavity dispersion $\bar{\beta}_2$ and the nonlinear parameter $\bar{\gamma}$ affect the final steady-state pulses. Figure 9.3 shows how the pulse parameters τ, q, ξ, and Ω vary with $\bar{\beta}_2$ in the anomalous (top row) and normal (bottom row) dispersion regimes. The shortest pulses are obtained in the case of anomalous dispersion for small values of $|\bar{\beta}_2|$:

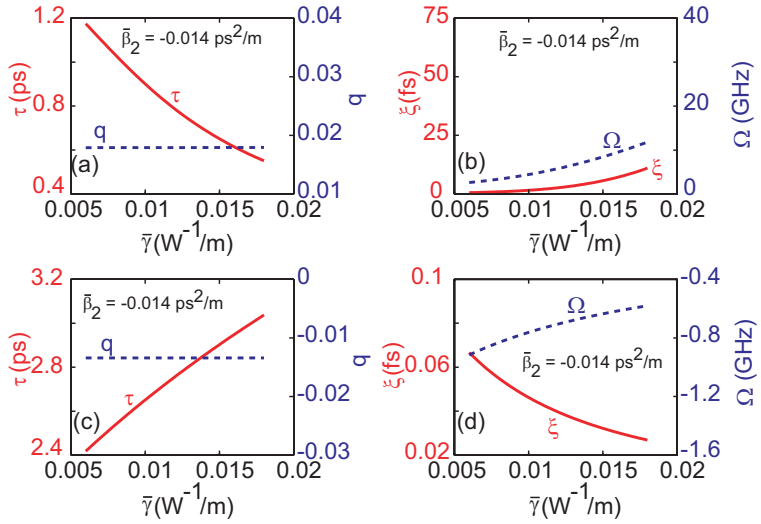

Figure 9.4: Same as Fig. 9.3 except the pulse parameters are plotted as a function of the nonlinear parameter.

pulse FWHM reduces to below 1 ps for $|\bar{\beta}_2| < 0.01$ ps^2/m. In contrast, pulse FWHM exceeds 4 ps in the normal dispersion case and increases as $\bar{\beta}_2$ increases. Notice that when $|\bar{\beta}_2| < 0.01$ ps^2/m, the pulse position shifts because TOD plays an increasing role in the laser (especially in the anomalous dispersion regime where the pulse spectrum is broader). Figure 9.4 shows the effect on the pulse parameters when the nonlinear parameter $\bar{\gamma}$ is varied for a fixed value of $\bar{\beta}_2$; dispersion is anomalous for the top row and normal for the bottom row. In the case of anomalous dispersion, the pulse becomes shorter for larger values of $\bar{\gamma}$. The situation is opposite in the case of normal dispersion. Figure 9.4 also reveals the interesting result that chirp, q, is essentially independent of $\bar{\gamma}$.

9.4 Steady-State Pulse Parameters

In an effort to obtain an “analytic” result, we turn our attention to the case where the effect of TOD is negligible, as is frequently the case for actively mode-locked lasers.

Under such conditions, both ξ and $\Omega = 0$ in the steady state, and Eqs. (9.15)–(9.19) reduce to a set of three equations for E, q, and τ. After a large number of round trips, we can set the derivatives to zero and obtain

$$\frac{T_R}{L_R}\frac{dE}{dT} = \bar{g}_{ss} - \bar{\alpha} - \frac{\bar{g}_{ss}T_2^2}{2\tau_{ss}^2}C_0\left(1+q_{ss}^2\right) = 0, \tag{9.24}$$

$$\frac{T_R}{L_R}\frac{dq}{dT} = \frac{\bar{\beta}_2}{\tau_{ss}^2}C_0\left(1+q_{ss}^2\right) - \frac{\bar{g}_{ss}T_2^2}{\tau_{ss}^2}q_{ss}C_1\left(1+q_{ss}^2\right) + C_2\frac{\bar{\gamma}E_{ss}}{\sqrt{2\pi}\tau_{ss}} + \frac{\Delta_{FM}\omega_m\tau_{ss}}{L_R}\Psi_1 = 0, \tag{9.25}$$

$$\frac{T_R}{L_R}\frac{d\tau}{dT} = C_3\bar{\beta}_2 q_{ss} + C_0C_3\frac{\bar{g}_{ss}T_2^2}{2}\left(C_4 - q_{ss}^2\right) = 0. \tag{9.26}$$

If we go one step further and assume that $\bar{g}_{ss}$ and E_{ss} are known quantities, as assumed in previous analytic studies,[2–4] we are able to obtain, for what we believe to be the first time, a fully analytic description of FM mode-locked lasers in the presence of dispersion, nonlinearity, and modulation depth. Equation (9.26) can be written as $q^2 - 2dq - C_4 = 0$, where $d = \bar{\beta}_2/(C_0\bar{g}_{ss}T_2^2)$ is a dimensionless dispersion parameter. The steady-state chirp parameter is then given by

$$q_{ss} = d \pm \sqrt{d^2 + C_4} \tag{9.27}$$

and the pulse width is found by solving Eq. (9.25) for τ_{ss}. It is imperative to point out that Eq. (9.25) predicts multiple solutions are possible, in principle, for a given set of laser parameters. The stability of these solutions is discussed in detail in the next section. Here we point out that only one solution dominates in practice, and we focus on it for the time being. Interestingly, Eq. (9.27) shows that chirp is independent of the nonlinear parameter $\bar{\gamma}$. It is also independent of the modulation parameters, a somewhat surprising feature for FM modulation, which affects the optical phase directly. Despite the fact that TOD was ignored, this finding agrees with Fig. 9.4 where all effects were included yet chirp was essentially independent of $\bar{\gamma}$.

Equation (9.24) predicts the extent to which the mode-locking threshold exceeds

the cw value $\bar{\alpha}$. More specifically,

$$\begin{aligned}\bar{g}_{ss} &= \bar{\alpha}\left[1-\frac{C_0T_2^2}{2\tau_{ss}^2}\left(1+q_{ss}^2\right)\right]^{-1} \\ &\approx \bar{\alpha}+\frac{C_0T_2^2\bar{\alpha}}{2\tau_{ss}^2}\left(1+q_{ss}^2\right). \end{aligned} \tag{9.28}$$

Since $\sqrt{1+q_{ss}^2}/\tau_{ss}$ is related to pulse spectral width, this equation has a simple interpretation: the threshold gain for an FM mode-locked laser exceeds the total cavity loss by an amount that depends on the fraction of the gain spectrum occupied by the mode-locked pulse spectrum. A similar result is obtained for AM mode locking, although modulator loss is important in that case.[149]

As noted in the previous section, our theory reproduces previously known results in the appropriate limits. If the effect of the modulator is ignored, by setting $\Delta_{FM}=0$, our results collapse to those of Ref. 3 in the anomalous dispersion regime. If nonlinearity is ignored, by setting $\bar{\gamma}=0$, we obtain the results of Ref. 4. If we go one step further and also neglect second-order dispersion and TOD, we should recover the results of Ref. 2. Under such conditions $d=0$ and $q_{ss}=\pm\sqrt{C_4}$. Of course, in the absence of nonlinearity, we expect a chirped Gaussian pulse and $C_4=1$, yielding $q_{ss}=\pm1$. The temporal FWHM (after Taylor expanding the Ψ_1 term) of the Gaussian pulse is then simply given by

$$\tau_{FWHM}=2\sqrt{\sqrt{2}\ln(2)}\left(\frac{\bar{g}_{ss}L_R}{\Delta_{FM}}\right)^{1/4}\left(\frac{T_2}{\omega_m}\right)^{1/2}. \tag{9.29}$$

This equation is identical to the result obtained in Ref. 2.

Equations (9.27) and (9.28) are coupled, however, in most practical cases $\bar{g}_{ss}$ exceeds $\bar{\alpha}$ by $<0.5\%$. Using the parameter values of Table 5.1 and solving Eqs. (9.25)–(9.27), we find that $\bar{g}_{ss}=\bar{\alpha}+2.02\times10^{-4}$ m^{-1} confirming that this is indeed true here. Therefore, to facilitate a fully analytic approach, we assume $\bar{g}_{ss}\approx\bar{\alpha}$ which only introduces a slight penalty in accuracy. Under this assumption, our rate-equation approach predicts a steady-state chirp of $q_{ss}=0.0179$ and a pulse width of $\tau_{ss}=0.787$ ps (FWHM = $1.76\tau_{ss}$). These values agree well with those found by directly solving

Eq. (4.92) ($\tau_{ss} = 0.798$ ps, $q_{ss} = 0.0174$). The good agreement found here justifies the $\bar{g}_{ss} \approx \bar{\alpha}$ approximation as well as the simplified approach of ignoring the ξ and Ω equations adopted in this section.

The mode-locking rate equations can also provide information on the approach to steady-state which frequently involves relaxation oscillations as seen in Figs. 5.5 and 9.1. We have performed a linear stability analysis on Eqs. (9.25) and (9.26) to obtain the following expression for the relaxation-oscillation frequency associated with small perturbations:

$$\omega_r = \frac{L_R}{\tau_0 T_R}\sqrt{BC - D^2}, \tag{9.30}$$

where

$$B = -\frac{C_3}{\tau_{ss}}\left[\bar{\beta}_2 - C_0 \bar{g} T_2^2 q_{ss}\right], \tag{9.31}$$

$$C = \frac{C_2 \bar{\gamma} E}{\sqrt{2\pi}} + \frac{4\Delta_{FM}\omega_m^2 \tau_{ss}^3}{C_3 L_R}, \tag{9.32}$$

$$D = \frac{1}{2\tau_{ss}}\left[2\bar{\beta}_2 C_0 q_{ss} - \bar{g} T_2^2 C_1 \left(1 + 3q_{ss}^2\right)\right]. \tag{9.33}$$

However, to obtain these results in a compact form it was necessary to Taylor-expand Ψ_1 to first order about $\tau = \tau_{ss}$. Equation (9.30) predicts an oscillation frequency of 230 kHz using the parameters of Table 1 and $\bar{g}_{ss} \approx \bar{\alpha}$. This result agrees well with the 235 kHz value obtained through numerically solving Eq. (4.92), again justifying the use of the approximations made. Figure shows these results on the same plot; clearly the computational result has more structure including other frequency components at 300 and 370 kHz. This figure also reveals that there appears to be some components at all of the frequencies present, however, this is related to the noise background and applying the fast Fourier transform to a finite number of data points.

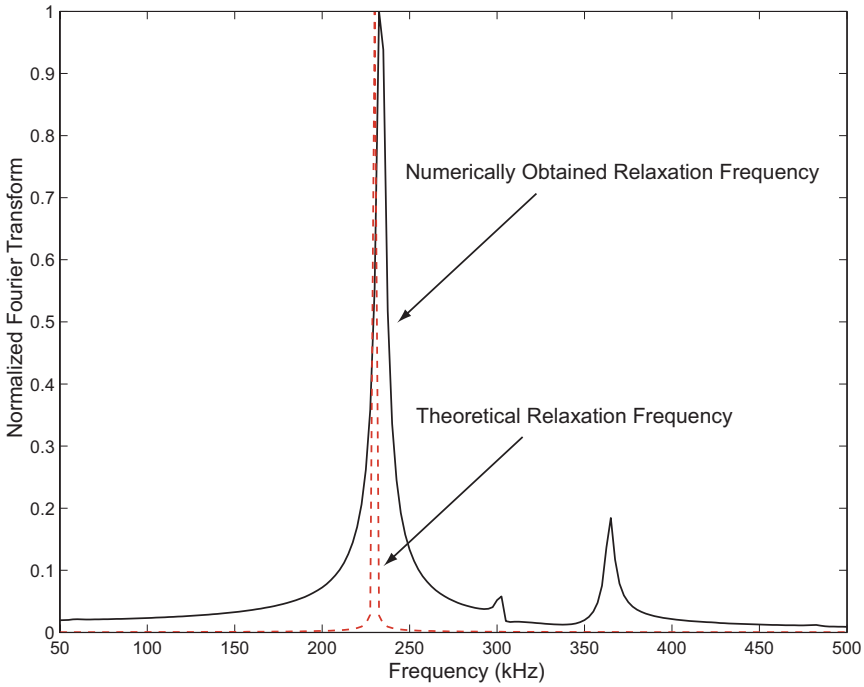

Figure 9.5: Numerically predicted relaxation oscillation frequency (solid) and that predicted by our theory (dashed).

9.5 Stability of Steady-State Solutions

It is well known that FM mode-locked lasers can operate with pulses at either modulator extremum.[2,16,30] These two possible operating states correspond to $\omega_m(t-t_s)=0$ and $\omega_m(t-t_s)=\pi$; they also make FM mode-locked lasers prone to a switching instability.[2,4,16,66] Our theory predicts pulse formation at both of these locations, as it should. For example, pulse chirp q in Eq. (9.27) has two possible steady-state values. In a linear nondispersive cavity, a single pulse width τ is associated with each value of chirp q.[2] However, the presence of dispersive and nonlinear terms in Eq. (9.25) allows multiple solutions for τ for each value of q.

Figure 9.6 shows how the two solutions for q vary with the residual cavity dispersion $\bar{\beta}_2$ [via Eq. (9.27)]. The curve labeled $\Delta_{FM}>0$ represents the chirp imposed on the pulse located at the $\omega_m(t-t_s)=0$ modulator extremum while the curve labeled

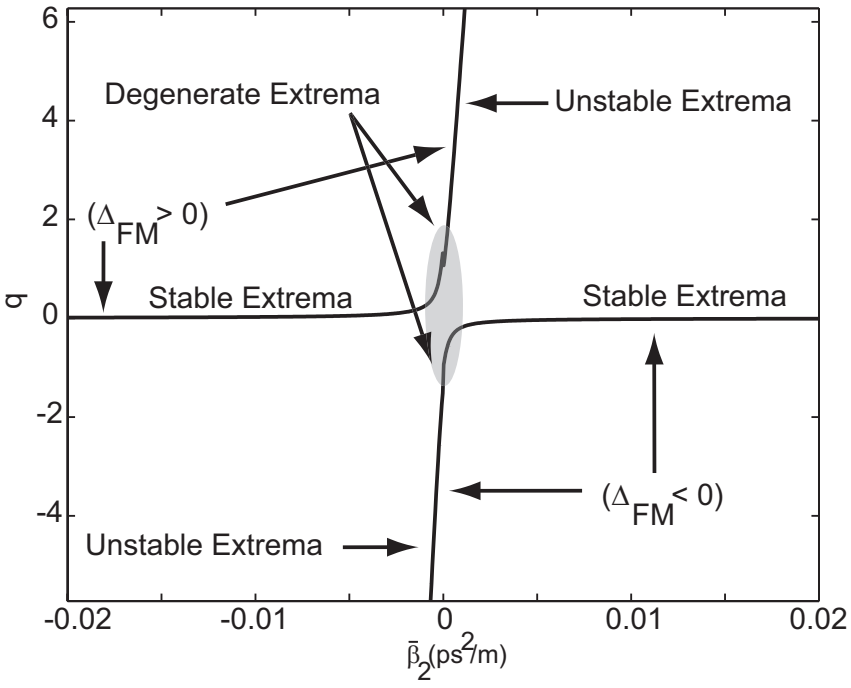

Figure 9.6: Chirp as a function of average dispersion $\bar{\beta}_2$ from Eq. (9.27).

$\Delta_{FM} < 0$ represents the chirp imposed on the pulse at the other extremum. In a linear nondispersive cavity $q = \pm 1$. However, Fig. 9.6 shows that by introducing residual second-order dispersion into the cavity the pulse chirp in FM mode-locked lasers can be reduced significantly to $q \approx 0$. This result, which could be inferred from Figs. 9.3 and 9.4, is also in agreement with the experimental findings of many groups.[4, 30, 31, 66, 139, 155] Another interesting feature to note is that the two states are temporally separated from one another: as cavity dispersion is increased from anomalous to normal, a pulse must temporally shift to align itself with the modulator's other extrema. Two shifting mechanisms have previously been identified through numerical simulations: shifting initiated through noise (or growth from pulse wings) and shifting initiated by TOD.[28]

In section 5, we focused on the $\Delta_{FM} > 0$ case in the anomalous dispersion regime (characterized by $\tau = 0.787$ ps and $q = 0.0179$). In this section, we start with the physical explanation as to why one state dominates in an FM mode-locked laser; we then

use the moment method to map out the stable/unstable points of operation in a visually intuitive fashion. Focusing again on the anomalous dispersion regime and the laser whose parameters are given in Table 1, we find that the chip parameter can be either very small ($q = 0.0179$) or very large ($q = -111.73$). When $\Delta_{FM} = 0.45$, we find a solution ($\tau = 0.787$ ps) only for the $q = 0.0179$ case. The situation is much more complicated for $\Delta_{FM} = -0.45$ [i.e. $\omega_m(t - t_s) = \pi$]. We now find five possible solutions; each with a different pulse width. For $q = 0.0179$, three solutions are found: $\tau = 0.94$, 1.5, and 149 ps. When $q = -111.73$ two solutions are found: $\tau = 16.2$ and 93.3 ps. Although these results were obtained using Eqs. (9.25) and (9.27), they were also verified by solving the full system of Eqs. (9.15)–(9.19) in the steady-state. Only one among these five potential solutions for $\Delta_{FM} = -0.45$ is likely to be stable. Indeed, a stability analysis reveals that all three states found for $q = 0.0179$ are unstable (A simple way to perform such an analysis is discussed later in this section). Among the remaining two states, the solution with $\tau = 93.3$ ps is not physical at our 10.3-GHz repetition rate since these pulses extend outside the pulse slot. Therefore, we are only left with one stable solution when $\Delta_{FM} = -0.45$: $\tau = 16.2$ ps and $q = -111.73$.

Having found a unique solution for positive and negative values of Δ_{FM}, we now investigate their relative stability. The pulse spectra are quite different for these two solutions. Indeed, the spectral FWHM is 0.23 THz when $\Delta_{FM} = 0.45$ but broadens to 2.17 THz when $\Delta_{FM} = -0.45$. Pulses with narrower spectra will clearly incur less loss due to the finite gain bandwidth [see Eq. (9.28)] and any other wavelength-dependent loss in the cavity; they are therefore favored by the laser. For this reason, we call this solution "dominant" and the other, higher loss, solution "secondary." The dominant mode-locked pulses always form under modulator cycles satisfying the condition $\Delta_{FM}\bar{\beta}_2 \leq 0$. This behavior, first alluded to by Kuizenga and Siegman,[2] was investigated in a series of papers by Nakazawa *et al.*[4, 66, 139, 155] in the mid 1990's. Furthermore, Tamura and Nakazawa's argument that the switching tendency is suppressed in the presence of strong dispersion[4] is verified by Fig. 9.6 if one recalls that the pulse

spectra is proportional to $\sqrt{1+q^2}/\tau$ and then applies the spectral filtering argument.

We now turn our attention to the effects of dispersion on pulse stability, as predicted by the moment method. Equations (9.15)–(9.19) reveal that changes in ξ and Ω do not have a strong effect on the other pulse parameters so long as $2\Omega\tau \ll C_0$. Figures 9.3 and 9.4 show that $\Omega\tau < 10^{-2}$ over a broad range of operating conditions. Since $C_0 \leq 1$ we can assume pulse energy, width, and chirp are approximately independent of Ω and ξ. Doing so allows us to solve Eq. (9.17) analytically and obtain

$$\begin{aligned}\Omega(T) &= \frac{\Delta_{FM}\omega_m\tau^2}{C_0 L_R \bar{g} T_2^2 (1+q^2)} \Psi_0 \sin\left[\omega_m(\xi - t_s)\right] \\ &\quad + C\exp\left[-\frac{C_0 L_R \bar{g} T_2^2 \left(1+q^2\right)}{\tau^2 T_R} T\right],\end{aligned} \tag{9.34}$$

where C is an integration constant. Noting the second term vanishes for $T \gg T_R$, Eq. (9.34) is substituted into Eq. (9.16) to give us the following equation for $T_R d\xi/dT$, a quantity we refer to as the temporal shift per round trip of the pulse relative to the modulation cycle:

$$\begin{aligned}T_R\frac{d\xi}{dT} &= L_R\left(\bar{\beta}_2 - \bar{g}T_2^2 q\right)\frac{\Delta_{FM}\omega_m\tau^2}{C_0 L_R \bar{g} T_2^2 (1+q^2)} \\ &\quad \times \Psi_0 \sin\left[\omega_m(\xi - t_s)\right] + L_R\frac{\bar{\beta}_3}{4\tau^2}\left[C_0\left(1+q^2\right)\right. \\ &\quad \left. + \frac{2\Delta_{FM}^2\omega_m^2\tau^6}{C_0^2 L_R^2 \bar{g}^2 T_2^4 \left(1+q^2\right)^2}\Psi_0^2 \sin^2\left[\omega_m(\xi - t_s)\right]\right].\end{aligned} \tag{9.35}$$

By varying the detuning between the pulse location and modulator extrema, $\xi - t_s$, the magnitude of this shift is mapped out, along with arrows indicating its direction, in Fig. 9.7, where four different regimes are shown for the dominant mode-locked solution ($\tau = 0.787$ ps and $q = 0.0179$). In Fig. 9.7, the stable and unstable locations are identified with a square and a circle, respectively, and they occur at pulse-modulator detunings where the pulse does not experience a temporal shift. The stable points occur at locations where a slight perturbation results in a temporal shift that restores the initial state. Unstable states, on the other hand, are identified where a slight perturbation sends the pulse to a different state. TOD manifests itself by making the magnitude of

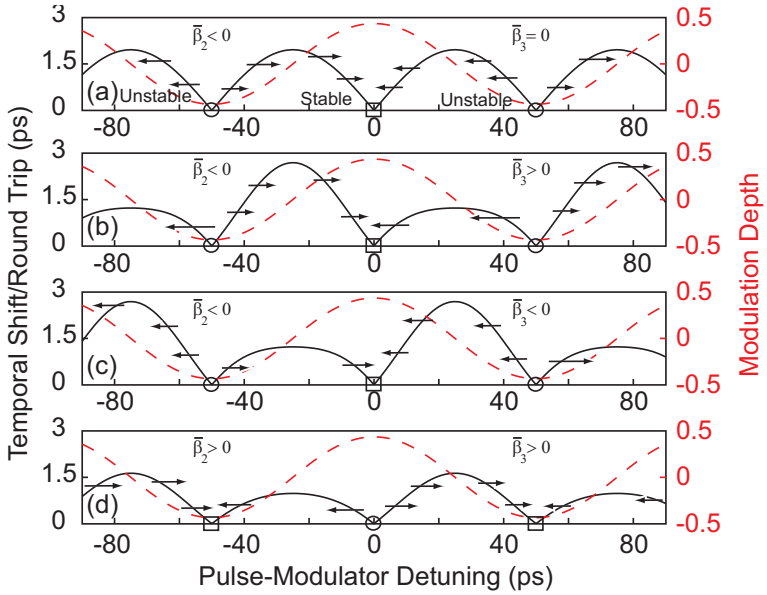

Figure 9.7: Temporal shift per round trip as a function of pulse-modulator detuning using the dominant pulse parameters ($\tau = 0.787$ ps, $q = 0.0179$). These figures identify the stable (square) and unstable (circle) operating locations as well as the strength and direction of the pulse velocity for the following cases: (a) $\bar{\beta}_2 < 0$ & $\bar{\beta}_3 = 0$, (b) $\bar{\beta}_2 < 0$ & $\bar{\beta}_3 > 0$, (c) $\bar{\beta}_2 < 0$ & $\bar{\beta}_3 < 0$, (d) $\bar{\beta}_2 > 0$ & $\bar{\beta}_3 > 0$. The imaginary part of the modulator's signal is plotted by the dashed line to aid in location identification for a fixed modulation depth of $\Delta_{FM} = 0.45$.

$d\xi/dT$ asymmetric about the stable/unstable points depending on its sign as seen by comparing Figs. 9.7(a)–(c). In Fig. 9.7(a), where $\bar{\beta}_3 = 0$, the magnitude of the temporal shift experienced by the pulse is symmetric about the stable/unstable operating points. In contrast, pulse shift becomes asymmetric in Figs. 9.7(b) and (c) where $\bar{\beta}_3 \neq 0$. Depending on the sign of $\bar{\beta}_3$, pulses temporally shift faster in one direction; this intuitive result was previously reported through numerical simulations.[28]

Equation (9.35) also provides a simple way to investigate the stability of the pulse solutions by using the values obtained for τ and q in this equation and plotting the results. These plots immediately reveal that the three $\Delta_{FM} < 0$ and $q = 0.0179$ solutions (previously noted) are unstable; full numerical simulations of Eq. (4.92) were also used to verify this claim.

To demonstrate what happens in the normal dispersion regime, Fig. 9.7(d) shows

the case $\bar{\beta}_2 > 0$. As seen in the figure, the $\Delta_{FM} < 0$ extremum of the modulation cycle represents the stable location for pulse formation. We point out that this result agrees with the simple rule $\Delta_{FM}\bar{\beta}_2 < 0$ and has been confirmed numerically.

Using the Gaussian ansatz, temporal shift per round trip can also be plotted for a nondispersive linear cavity, by setting $\bar{\beta}_2 = \bar{\beta}_3 = \bar{\gamma} = 0$ and using Eq. (9.35). In this case, pulse width and chirp are found to be $\tau = 0.7432$ ps and $q = \pm 1$ by using Eqs. (9.27) and (9.29). The absence of dispersion and nonlinearity has caused the dominant and secondary solutions to collapse into one solution differing only in the sign of the chirp. As a consequence, neither solution dominates and we expect pulses to simultaneously exist under both modulator extrema. Experimentally, however, the laser randomly switches through noise-induced perturbations between the two states; they have not been found to coexist.[16]

If the parameters of the secondary pulse ($\tau = 16.2$ ps and $q = -111.73$) are used instead of those of the dominant pulse, the results shown in Fig. 9.8 are obtained. Figures 9.8(a,b) show that the secondary pulses exist at the opposite modulator extrema as that of the dominant pulses, as expected. By comparing Figs. 9.8(a,b) to 9.7(a,b), we find the temporal shifts experienced by the pulses during a single round trip are much stronger for dominant pulses than those experienced by secondary pulses. That is, our theory shows dominant pulses are bound more tightly to their stable operating points than secondary pulses. This is expected on physical grounds and is a direct consequence of second-order dispersion and spectral filtering.

Once again we see that TOD has added an asymmetry to the strength of the pulse shift by comparing Figs. 9.8(a) and (b). Since the laser needs a finite amount of time to switch between states, it becomes possible to observe the secondary state, at least through numerical simulations. Despite the fact that this state is not dominant, numerical evidence for its transient existence has been confirmed by considering the effect of an abrupt half clock cycle phase shift in the driving electronics on the dominant pulse.[28] It was found that the pulse shifts under the influence of the TOD, re-synchronizing with

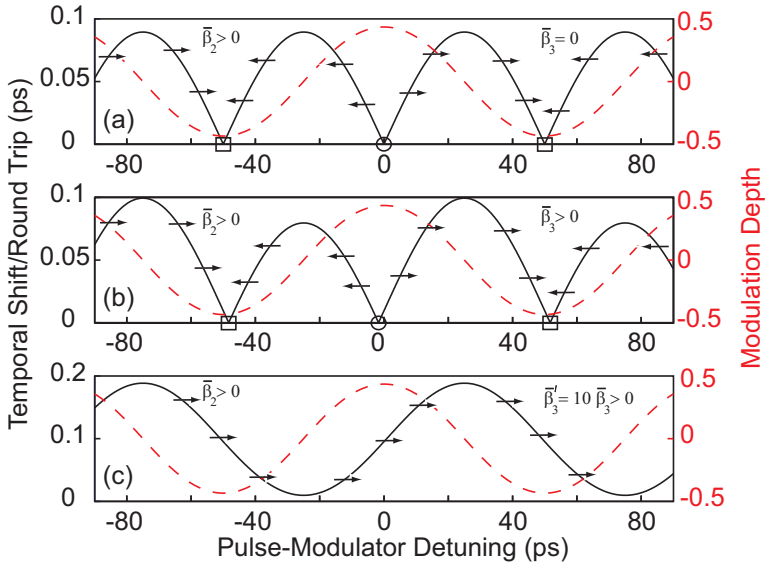

Figure 9.8: Temporal shift per round trip as a function of pulse-modulator detuning using the secondary pulse parameters ($\tau_0 = 16.2$ ps, $q_0 = -111.73$). These figures identify the stable (square) and unstable (circle) operating locations as well as the strength and direction of the pulse velocity for the following cases: (a) $\bar{\beta}_2 < 0$ & $\bar{\beta}_3 = 0$, (b) $\bar{\beta}_2 < 0$ & $\bar{\beta}_3 > 0$, (c) result of large TOD on stable pulses. The imaginary part of the modulator's signal is plotted by the dashed line to aid in location identification for a fixed modulation depth of $\Delta_{FM} = 0.45$.

the stable modulation extrema, while essentially retaining its shape. If the TOD is weak, or the pulse is unable to survive the perturbation intact, it broadens instead of shifting. In Ref. [28] the pulse broadened but then become trapped in a local potential until it was destabilized by the re-formation of the dominant pulse, which was seeded by the pulse wings and noise. The transient state found in that work is just what we have referred to as the secondary state here.

According to the current work, it follows from Fig. 9.7(b) that if the pulse survives the modulator-induced perturbation and retains its width and chirp, its center would be subject to the temporal shift identified in that figure. To clarify our meaning, consider what happens if a steady-state mode-locked pulse located at a $\xi - t_s = -48$ ps is subjected to a π phase shift through the driving electronics. According to Fig. 9.7(b),

the pulse would physically shift to relocate itself under the correct modulation cycle ($\xi - t_s = 0$ ps). If, however, the pulse can not survive the perturbation, it will broaden while remaining centered on $\xi - t_s = -48$ ps. Instead of broadening unabated, it will become trapped in a local potential associated with the secondary state [$\tau = 16.2$ ps and $q = -111.73$ see Fig. 9.8(b)]. At this point, the pulse is locally stable. The laser will only return to its dominant steady-state mode-locked pulse when the secondary state is destabilized by the laser's choice to operate in the lower loss state located at $\xi - t_s = 0$ ps (in this case, the stable pulse grows from noise). By increasing pulse energy the pulse may remain intact through solitonic shaping, despite the modulator-induced perturbation. Such a pulse would then switch out of the shallow secondary-state potential. Comparing Figs. 9.7(b) and (c) we further expect that the direction of pulse-center shift should depend on the sign of the TOD. All of these effects were numerically observed and explored in Ref. [28].

Finally Fig. 9.8(c) answers the question as to what happens when TOD is increased. In this case, TOD was increased by a factor of 10 to $\bar{\beta}_3 = 300 \times 10^4$ fs^3/m and we find that mode-locked operation is no longer possible since the shifting effect of the TOD is stronger than the modulator's ability to synchronize the pulses.

9.6 Conclusion

By applying our rate-equation approach to FM mode locking we obtained a system of five equations which govern the evolution of the important pulse parameters. This allowed us to incorporate the effect of the modulator depth as well as second- and third-order dispersion on the pulse parameters. By comparing the results predicted by our rate-equation approach with those of full numerical simulations we found that our approach provides more accurate results than those obtained by using other analytic approaches.

Our approach also allowed us to solve for all of the steady-state pulse solutions in an FM mode-locked laser. Using simple physical arguments we were able to identify the steady-state pulse parameters. The rate-equation approach also allowed us to predict the relaxation oscillation frequency expected for such a laser. Finally, an investigation of the effect pulse-modulator detuning has on the mode-locked pulses provided an analytic framework able to describe the pulse-pulse switching which was numerically investigated in section 5.5.

10 Conclusion

In this thesis, we presented a detailed study of mode-locked lasers. Experimental investigations provided a starting point for numerical simulations and explored high-repetition rate mode-locked fiber lasers. Our experimental investigations also supplemented and directed our analytic work and served as the source for all of the numerical values used in both numerical and analytic investigations.

A general analytic tool was developed which allowed us to recover the results of all prior theories in the appropriate limits. Additionally, this theory allowed us to go beyond prior results in certain cases, for example, in the mapping out of stability in FM mode-locked lasers.

A short list of future directions, related to the work presented in this thesis, that could be explored in the future include: an experimental verification of the FM mode-locking stability issue using an electronically controllable phase-delay line and an FM mode-locked laser or the application of the Moment Method to stretched-pulse fiber lasers (although the complexity of the results obtained will likely outdo their usefulness). An application of our rate-equation treatment to a similariton mode-locked fiber laser would also be interesting. Unfortunately, such an application would require a nontrivial pulse-shape stitching to insure the derivative of the similarition pulse was a continuous function. The demonstration of passive mode locking at a high harmonic

in this thesis, through pulse splitting, identifies the need for a technique able to stabilize large pulse trains in passively mode-locked lasers. Another obvious question that this work raises is whether noise can be included in our Moment Method treatment of a mode-locked laser. In this case, issues with cavity lifetime must now be artificially incorporated into the treatment to limit the extent to which noise can grow. It is because this limitation would have to be artificially introduced that these results were not presented in this thesis. Finally, our rate equation formalism could be applied to a laser mode locked with a SESAM using a more accurate model that incorporated its recovery time etc..

In conclusion, the field of mode-locked lasers still holds more undiscovered effects; however, while in graduate school, I believe I watched much of the field shift from a research area to an engineering area. In the near future, theoretical developments will continue to be made, but I expect more effort will be put into suppressing deleterious effects such as Q-switching while insuring reliable self-starting and reducing amplitude and timing jitter. Moreover, it is highly probable that the pursuit of the shortest pulses possible from all-fiber lasers, common in the 1990's, will be all but abandoned in the next ten years as scientists and laser companies set their sights on high-power applications. As the field shifts focus, new theoretical problems will be encountered ranging from heat dissipation issues to novel fiber structures which support multiple modes and/or include dispersion tailoring to the effects of gain media under intense pump powers. This will require more detailed gain modeling.

Finally, although passive schemes are the most highly valued for their simplicity, I expect a lot more to be done with opto-electronics and electronics, particularly phase-locked loops. Since electronic feedback systems can be built to regulate long-term drift issues and make lasers transition from laboratory devices to devices that are used as the building blocks for a broader and broader range of devices for the medical community, micro-machining, forensics, etc., such a transition will most likely require the miniaturization of these technologies and laser systems. Along with the integration

of electronics and feedback loops into laser systems, computer interfaces should also become commonplace among all commercial fiber lasers within the next five years.

Bibliography

[1] R. Paschotta, J. Nilsson, A. C. Tropper, and D. C. Hanna, “Ytterbium-doped fiber amplifiers,” IEEE J. Quantum Electron. **33**, 1049–1056 (1997).

[2] D. J. Kuizenga and A. E. Siegman, “FM and AM mode locking of the homogeneous laser–Part I: theory,” IEEE J. Quantum Electron. **QE-6**, 694–708 (1970).

[3] H. A. Haus and Y. Silberberg, “Laser mode locking with addition of nonliner index,” IEEE J. Quantum Electron. **QE-22**, 325–331 (1986).

[4] K. Tamura and M. Nakazawa, “Pulse energy equalization in harmonically FM mode-locked lasers with slow gain,” Opt. Lett. **21**, 1930–1932 (1996).

[5] B. R. Washburn, S. E. Ralph, and R. S. Windeler, “Ultrashort pulse propagation in air-silica microstructure fiber,” Opt. Express **10**, 575–580 (2002).

[6] K. Gürs and R. Müller, “Breitband-modulation durch Steuerung der emission eines optischen masers (Auskople-modulation),” Phys. Lett. **5**, 179–181 (1963).

[7] W. E. Lamb, Jr., “Theory of an optical maser,” Phys. Rev. **134**, A1429–A1450 (1964).

[8] M. DiDomenico, Jr., “Small-signal analysis of internal (coupling-type) modulation of lasers,” J. Appl. Phys. **35**, 2870–2876 (1964).

[9] L. E. Hargrove, R. L. Fork, and M. A. Pollack, “Locking of He-Ne laser modes induced by synchronous intracavity modulation,” Appl. Phys. Lett. **5**, 4–5 (1964).

[10] S. E. Harris and R. Targ, “FM oscillation of the He-Ne laser,” Appl. Phys. Lett. .

[11] S. E. Harris and O. P. McDuff, “Theory of FM laser oscillation,” IEEE J. Quantum Electron. .

[12] H. W. Mocker and R. J. Collins, “Mode competition and self-locking effects in a Q-switched Ruby laser,” Appl. Phys. Lett. **15**, 270–273 (1965).

[13] R. E. McClure, “Mode locking behavior of gas lasers in long cavities,” Appl. Phys. Lett. **15**, 148–150 (1965).

[14] J. Hirano and T. Kimura, “Generation of high-repetition-rate optical pulses by a He-Ne laser,” Appl. Phys. Lett. **12**, 186–198 (1968).

[15] E. P. Ippen, C. V. Shank, and A. Dienes, “Passive mode locking of the cw dye laser,” Appl. Phys. Lett. **21**, 348–350 (1972).

[16] D. J. Kuizenga and A. E. Siegman, “FM and AM mode locking of the homogeneous laser–Part II: experimental results in a Nd:YAG laser with internal FM modulation,” IEEE J. Quantum Electron. **QE-6**, 709–715 (1970).

[17] D. M. Kim, S. Marathe, and T. A. Rabson, “Eigenfunction analysis of mode-locking process,” J. Appl. Phys. **44**, 1673–1675 (1973).

[18] H. A. Haus, “A theory of forced mode locking,” IEEE J. Quantum Electron. **QE-11**, 323–330 (1975).

[19] H. A. Haus, “Therory of mode locking with a fast saturable absorber,” J. Appl. Phys. **46**, 3049–3058 (1975).

[20] D. E. Spence, P. N. Kean, and W. Sibbett, “60-fsec pulse generation from a self-mode-locked Ti:sapphire laser,” Opt. Lett. **16**, 42–44 (1991).

[21] U. Morgner, F. X. Kärtner, S. H. Cho, Y. Chen, H. A. Haus, J. G. Fujimoto, E. P. Ippen, V. Scheuer, G. Angelow, and T. Tschudi, “Sub-two-cycle pulses from a Kerr-lens mode-locked Ti:Sapphire laser,” Opt. Lett. **23**, 411–413 (1999).

[22] E. Snitzer, “Optical Maser action of a Nd^{+3} in a Barium crown glass,” Phys. Rev. Lett. **7**, 444–446 (1961).

[23] M. I. Dzhibladze, Z. G. Esiashvili, E. S. Teplitskii, S. K. Isaev, and V. R. Sagaradze, Kvantovaya Elektron. **10**, 432–434 (1983).

[24] L. F. Mollenauer and R. H. Stolen, “The Soliton Laser,” Opt. Lett. **9**, 13–15 (1984).

[25] K. J. Blow and D. Wood, “Mode-locked lasers with nonlinear external cavites,” J. Opt. Soc. Am B **5**, 629–632 (1988).

[26] J. Mark, L. Liu, K. Hall, H. Haus, and E. Ippen, “Femtosecond pulse generation in a laser with a nonlinear external resonator,” Opt. Lett. **14**, 48–50 (1989).

[27] E. Ippen, H. Haus, and L. Liu, “Additive pulse mode locking,” J. Opt. Soc. Am. B **6**, 1736–1745 (1989).

[28] N. G. Usechak, J. D. Zuegel, and G. P. Agrawal, “FM mode-locked fiber lasers operating in the autosoliton regime,” IEEE J. Quantum Electron. **41**, 753–761 (2005).

[29] G. Geister and R. Ulrich, “Neodymium-fibre laser with integrated-optic mode locker,” Opt. Commun. **68**, 187–189 (1988).

[30] M. W. Phillips, A. I. Ferguson, and D. C. Hanna, “Frequency-modulation mode locking of a Nd^{3+}-doped fiber laser,” Opt. Lett. **14**, 219–221 (1989).

[31] J. D. Kafka, T. Baer, and D. W. Hall, “Mode-locked erbium-doped fiber laser with soliton pulse shaping,” Opt. Lett. **15**, 1269–1271 (1989).

[32] I. N. Duling, “All-fiber modelocked figure eight laser,” Opt. Soc. Am 1990 Annual Meeting **5**, 306–310 (1990).

[33] I. N. Duling, “All-fiber ring soliton laser mode locked with a nonliear mirror,” Opt. Lett. **16**, 539–541 (1991).

[34] I. N. Duling, “Subpicosecond all-fibre erbium laser,” Electron. Lett. **27**, 544–545 (1991).

[35] M. Hofer, M. H. Ober, F. Haberl, and M. E. Fermann, “Characterization of ultrashort pulse formation in passively mode-locked fiber lasers,” IEEE J. Quantum Electron. **28**, 720–728 (1992).

[36] K. Tamura, H. A. Haus, and E. P. Ippen, “Self-starting additive pulse mode-locked erbium fibre ring laser,” Electron. Lett. **28**, 2226–2228 (1992).

[37] J. R. Buckley, S. W. Clark, and F. W. Wise, “Generation of ten-cycle pulses from an ytterbuim fiber laser with cubic phase compensation,” Opt. Lett. **31**, 1340–1342 (2006).

[38] K. Tamura, E. P. Ippen, H. A. Haus, and L. E. Nelson, “77-fs pulse generation from a streched-pulse mode-locked all-fiber ring laser,” Opt. Lett. **18**, 1080–1082 (1993).

[39] F. X. Kärtner, D. Kopf, and U. Keller, “Solitary-pulse stabilization and shortening in actively mode-locked lasers,” J. Opt. Soc. Am. B **12**, 486–496 (1995).

[40] F. O. Ilday, J. R. Buckley, W. G. Clark, and F. W. Wise, “Self-similar evolution of parabolic pulses in a laser,” Phys. Rev. Lett. (2004).

[41] M. E. Fermann, V. I. Kruglov, B. C. Thomsen, J. M. Dudley, and J. D. Harvey, Phys. Rev. Lett. **84**, 6010 (2000).

[42] B. C. Collings, K. Bergman, and W. H. Knox, "Stable multigigahertz pulse-train formation in a short-cavity passively harmonic mode-locked erbium/ytterbium fiber laser," Opt. Lett. **15**, 123–125 (1998).

[43] S. Gray, A. B. Grudinin, W. H. Loh, and D. N. Payne, "Femtosecond harmonically mode-locked fiber laser with time jitter below 1 ps," Opt. Lett. **20**, 189–191 (1995).

[44] A. B. Grudinin and S. Gray, "Passive harmonic mode locking in soliton fiber lasers," J. Opt. Soc. Am. B **14**, 144–154 (1997).

[45] G. P. Agrawal, *Nonlinear Fiber Optics* (Academic Press, New York, 1995), second edn.

[46] L. Krainer, R. Paschotta, S. Lecomte, M.Moser, K. Weingarten, and U. Keller, "Compact Nd:$GdVO_4$ lasers with pulse repetition rates up to 160 GHz," IEEE J. Quantum Electron. **38**, 1331–1338 (2002).

[47] L. Krainer, D. Nodop, G. Spühler, S. Lecomte, M. Golling, R. Paschotta, D. Ebling, T. Ohgoh, T. Hayakawa, K. Weingarten, and U. Keller, "Compact 10-GHz Nd:$GdVO_4$ laser with 0.5-W average output power and low timing jitter," Opt. Lett. **29**, 2629–2631 (2004).

[48] S. Longhi, P. Laporta, S. Taccheo, and O. Svelto, "Third-order-harmonic mode locking of a bulk erbium:ytterbium:glass laser at a 2.5-GHz repetition rate," Opt. Lett. **23**, 1985–1987 (1994).

[49] Z. Ahmed and N. Onodera, "High repetition rate optical pulse generation by frequency multiplication in activly modelocked fibre ring lasers," Electron. Lett. **32**, 455–457 (1996).

[50] E. Yoshida and M. Nakazawa, “80∼200 GHz erbium doped fibre laser using a rational harmonic mode-locking technique,” Electron. Lett. **32**, 1370–1372 (1996).

[51] G. Zhu and N. K. Dutta, “Eighth-order rational harmonic mode-locked fiber laser with amplutude-equalized output operatint at 80 Gbits/s,” Opt. Lett. **30**, 2212–2214 (2005).

[52] K. S. Abedin, N. Onodera, and M. Hyodo, “Repetion-rate multiplication in actively mode-locked fiber lasers by higher-order FM mode locking using a high-finesse Fabry–Perot filter,” Appl. Phys. Lett. **73**, 1311–1313 (1998).

[53] K. S. Abedin, N. Onodera, and M. Hyodo, “Higher order FM mode locking for pulse-repetition-rate enhancement in activly mode-locked lasers: theory and experiment,” IEEE J. Quantum Electron. **35**, 875–890 (1999).

[54] K. S. Abedin, N. Onodera, and M. Hyodo, “Generation of a 64-GHz, 3.3-ps transform-limited pulse train from a fiber laser employing higher-order frequency-modulated mode locking,” Opt. Lett. **22**, 1564–1566 (1999).

[55] K. S. Abedin, M. Hyodo, and N. Onodera, “Active stabilization of a higher-order mode-locked fiber laser opterating at a pule-repetition rate of 154 GHz,” Opt. Lett. **26**, 151–153 (2001).

[56] C. X. Yu, H. A. Haus, E. P. Ippen, W. S. Wong, and A. Sysoliatin, “Gigahertz-repetition-rate mode-locked fiber laser for continuum generation,” Opt. Lett. **25**, 1418–1420 (2000).

[57] S. Yang, E. A. Ponomarev, and X. Bao, “40-GHz transform limited pulse generation from FM oscillation fiber laser with external cavity chirp compensation,” IEEE Photon. Tech. Lett. **16**, 1631–1633 (2004).

[58] M. Nakazawa and E. Yoshida, “A 40-GHz 850-fs regenerativly FM mode-locked polarization-maintaining erbium fiber ring laser,” IEEE Photon. Tech. Lett. **12**, 1613–1615 (2000).

[59] R. P. Davey, K. Smith, and A. McGuire, “High-speed, mode-locked, tunable, integrated erbium fibre laser,” Electron. Lett. **28**, 482–484 (1992).

[60] H. Takara, S. Kawanishi, M. Saruwatari, and K. Noguchi, “Generation of highly stable 20GHz transofrm-limited optical pulses from activly mode-locked Er^{3+}-doped fibre lasers with an all-polarization mantaining ring cavity,” Electron. Lett. **28**, 2095–2096 (1992).

[61] T. F. Carruthers and I. N. D. III, “10-GHz, 1.3-ps erbium fiber laser employing soliton pulse shortening,” Opt. Lett. **21**, 1927–1929 (1996).

[62] T. F. Carruthers, I. N. D. III, M. Horowitz, and C. R. Menyuk, “Dispersion management in a harmonically mode-locked fiber soliton laser,” Opt. Lett. **25**, 153–155 (2000).

[63] B. Bakhshi and P. A. Andrekson, “40 GHz actively modelocked polarisation-maintaining erbium fibre ring laser,” Electron. Lett. **36**, 411–413 (2000).

[64] E. J. Greer and K. Smith, “All-optical FM mode-locking of fibre laser,” Electron. Lett. **28**, 17411 743 (1992).

[65] B. P. Nelson, K. Smith, and K. J. Blow, “Mode-locked erbium fibre laser using all-optical nonlinear loop modulator,” Electron. Lett. **28**, 656–658 (1992).

[66] M. Nakazawa, E. Yoshida, and K. Tamura, “10GHz, 2ps regeneratively and harmonically FM mode-locked erbium fibre ring laser,” Electron. Lett. .

[67] H. A. Haus, D. J. Jones, E. P. Ippen, and W. S. Wong, “Theory of soliton stablity in asynchronous modelocking,” IEEE J. Lightwave Tech. **14**, 622–627 (1996).

[68] S. Longhi and P. Laporta, “Time-domain analysis of frequency modulation laser oscillation,” A. Phys. Lett. **73**, 720–722 (1998).

[69] V. Cautaerts, D. J. Richardson, R. Paschotta, and D. C. Hanna, “Stretched pulse Yb^{3+}:silica fiber laser,” Opt. Lett. **22**, 316–318 (1997).

[70] L. Lefort, J. H. V. Price, D. J. Richardson, G. J. Spüler, R. Paschotta, U. Keller, A. R. Fry, and J. Weston, “Practical low-noise stretched-pulse Yb^{3+}-doped fiber laser,” Opt. Lett. **27**, 291–293 (2002).

[71] J. E. Rothenberg, “unknown,” Appl. Opt. **39**, 6931 (2000).

[72] S. Lecomte, L. Krainer, R. Paschotta, M. J. P. Dymott, K. J. Weingarten, and U. Keller, “Optical parametric oscilator with a 10-GHz repetiton rate and 100-mW average output power in the spectral region near 1.5nm,” Opt. Lett. **27**, 1714–1716 (2002).

[73] N. G. Usechak, G. P. Agrawal, and J. D. Zuegel, “Tunable, high-repetition-rate, harmonically mode-locked ytterbium fiber laser,” Opt. Lett. **29**, 1360–1362 (2004).

[74] Y. Deng and W. H. Knox, “Self-starting passive harmonic mode-locked femto-sectond Yb^{3+}-doped fiber laser at 1030 nm,” Opt. Lett. **29**, 2121–2123 (2004).

[75] B. Ortaç, A. Hideur, G. Martel, and M. Brunel, “2-GHz passive harmonically mode-locked Yb-doped double-cladd fiber laser,” Appl. Phys. B **81**, 507–509 (2005).

[76] T. Erneux, “Q-switching bifurication in a laser with a saturable absorber,” J. Opt. Soc. Am. B **5**, 1063–1069 (1988).

[77] N. Akhmediev, J. M. Soto-Crespo, and G. Town, “Pulsing solitons, chaotic solitions, periodic doubling, and pulse coexistance in mode-locked lasers:Complex Ginzburg–Landau equation approach,” Phys. Rev. E **63**, 056 602 (2001).

[78] J. M. Soto-Crespo, M. Grapinet, P. Grelu, and N. Akhmediev, “Bifurcations and multiple-period soliton pulsations in a passively mode-locked fiber laser,” Phys. Rev. E **70**, 066 612 (2004).

[79] R. Weill, B. Vodonos, A. Gordon, A. Bekker, V. Smulakovsky, O. Gat, and B. Fischer, “Noise dependent buildup of multiple pulses in mode-locked lasers along with a cascade of phase transitions,” Conference on Lasers and Electro-Optics (CLEO) **2** (2004).

[80] P. Grelu, F. Belhache, F. Gutty, and J. M. Soto-Crespo, “Relative phase locking of pulses in a passively mode-locked fiber laser,” J. Opt. Soc. Am B **20**, 863–870 (2003).

[81] M. Olivier, V. Roy, M. Pinché, and F. Bablin, “Pulse collisions in the streched-pulse fiber laser,” Opt. Lett. **29**, 1461–1463 (2004).

[82] P. Grelu and N. Akhmediev, “Group interactions of dissipative solitons in a laser cavity: the case of 2+1,” Opt. Express **12**, 3184–3189 (2004).

[83] Y. Deng, M. W. Koch, F. Lu, G. W. Wicks, and W. H. Knox, “Colliding-pulse passive harmonic mode-locking in a femtosecond Yb-doped fiber laser with a semiconductor saturable absorber,” Opt. Express **12**, 3872–3877 (2004).

[84] M. E. Grein, L. A. Jiang, H. A. Haus, E. P. Ippen, C. McNeilage, J. H. Searls, and R. S. Windeler, “Observation of quantum-limited timing jitter in an active, harmonically mode-locked fiber laser,” Opt. Lett. **27**, 957–959 (2002).

[85] M. E. Grein, H. A. Haus, Y. Chen, and E. P. Ippen, “Quantum-limited timing jitter in actively modelocked lasers,” IEEE J. Quantum Electron. **40**, 1458–1470 (2004).

[86] T. Yilmaz, C. M. DePriest, P. Delfyett, Jr., S. Etemad, A. Braun, and J. H. Abeles, “Supermode suppressino to below -130 dBc/Hz in a 10 GHz harmonically mode-

locked external sigma cavity semiconductor laser," Opt. Express **11**, 1090–1095 (2003).

[87] F. O. Ilday, J. R. Buckley, H. Lim, F. W. Wise, and W. G. Clark, "Generation of 50-fs, 5-nJ pulses at 1.03 μm from a wave-breaking-free fiber laser," Opt. Lett. **28**, 1365–1367 (2003).

[88] S. M. J. Kelly, "Characteristic sideband instability of periodically amplified average soltion," Electron. Lett. **28**, 806–807 (1992).

[89] J. P. Gordon, "Dispersive perturbations of solitons of the nonlinear Schroedinger equation," J. Opt. Soc. Am. B **9**, 91–97 (1992).

[90] J. D. Zuegel and D. W. Jacobs-Perkins, "An Efficient, High-Frequency Bulk Phase Modulator," App. Opt. **43**, 1946–1950 (2004).

[91] U. Keller, K. J. Weingarten, F. X. Kärtner, D. Kopf, B. Braun, I. D. Jung, R. Fluck, C. Hönninger, N. Matuschek, and J. A. der Au, "Semiconductor saturabe absorber mirrors (SESAM's) for femtosecond to nanosecond pulse generation in solid-state lasers," IEEE J. Sel. Top. Quantum Electron. **2**, 435–453 (1996).

[92] W. H. Knox, "In situ measurement of complete intracavity dispersion in an operationg Ti:sapphire femtosecond laser," Opt. Lett. **17**, 514–516 (1992).

[93] W. H. Knox and J. P. Gordon, "Frequency-domain dispersion measurements in tunable mode-locked lasers," J. Opt. Soc. Am. B **11**, 2071–2079 (1993).

[94] J. M. Roth, T. E. Murphy, , and C. Xu, "Ultrasensitive and high-dynamic-range two-photon absorption in a GaAs photomultiplier tube," Opt. Lett. **27**, 2076–2078 (2002).

[95] K. Mogi, K. Naganuma, and H. Yamada, “A Novel Real-Time Chirp Measurment Method for Ultrashort Optical Pulses,” Jpn. J. Appl. Phys. **27**, 2070–2081 (1988).

[96] F. Rana, H. Lee, R. Ram, M. Grein, L. Jiang, E. Ippen, and H. Haus, “Characterization of the noise and correlations in harmonically mode-locked lasers,” J. Opt. Soc. Am. B **19**, 2609–2621 (2002).

[97] D. von der Linde, “Characterization of the Noise in Continuously Operating Mode-Locked Lasers,” Appl. Phys. B **39**, 201–217 (1986).

[98] Y. Muramoto, Y. Hirota, K. Yoshino, H. Ito, and T. Ishibashi, “10GHz, 2ps regeneratively and harmonically FM mode-locked erbium fibre ring laser,” Electron. Lett. .

[99] D. J. Kane and R. Trebino, “Characterization of arbitrary femtosecond pulses using frequency-resolved optical gating,” IEEE J. Quantum Electron. **29**, 571–579 (1993).

[100] V. Wong and I. A. Walmsley, “Characterization of the electric field of ultrashort optical pulses,” J. Opt. Soc. Am. B **13**, 2453–2463 (1996).

[101] C. Iaconis and I. A. Walmsley, “Spectral phase interferometry for direct electric-field reconstruction of ultrashort optical pulses,” Opt. Lett. **23**, 792–794 (1998).

[102] D. N. Fittinghoff, J. L. Bowie, J. N. Sweetser, R. T. Jennings, M. A. Krumbügel, K. W. DeLong, R. Trebino, and I. A. Walmsley, “Measurement of the intensity and phase of ultraweak, ultrashort laser pulses,” Opt. Lett. **21**, 884–886 (1996).

[103] C. Dorrer and I. Kang, “Highly sensitive direct characterization of femtosecond pulses by electro-optics shearing interferometry,” Opt. Lett. **28**, 477–479 (2003).

[104] D. A. Bender, M. P. Hasselbeck, and M. Sheik-Bahae, “Sensitive ultrashort pulse chirp measurement,” Opt. Lett. **31**, 122–124 (2006).

[105] L.-P. Chen, Y. Wang, and J.-M. Liu, “Spectral measurement of the noise in continuous-wave mode-locked laser pulses,” IEEE J. Quantum Electron. **32**, 1817–1825 (1996).

[106] L. A. Jiang, S. T. Wong, M. E. Grein, E. P. Ippen, and H. A. Haus, “Measuring timing jitter with optical cross correlations,” IEEE J. Quantum Electron. **38**, 1047–1052 (2002).

[107] M. C. Gross, M. Hanna, K. M. Patel, and S. E. Ralph, “Spectral method for the simultaneous determination of uncorrelated and correlated amplitude and timing jitter,” Appl. Phys. Lett. **80**, 3694–3696 (2002).

[108] E. Wolf, “New theory of partial coherence in the space-frequency domain. Part I: spectra and cross spectra of steady-state sources,” J. Opt. Soc. Am. B **72**, 343351 (1982).

[109] A. V. Oppenheim, A. S. Willsky, and S. H. Nawab, *Signals & Systems* (Prentice Hall, New Jersey, 1997), second edn.

[110] D. Ouzounov, D. Homoelle, W. Zipfel, W. W. Webb, A. L. Gaeta, J. A. West, J. C. Fajardo, and K. W. Koch, “Dispersion measurements of microstructured fibers using femtosecond laser pulses,” Opt. Commun. **192**, 219–223 (2001).

[111] H. T. Shang, “Chromatic dispersion measurement by white-light interferometry on metre-length single-mode optical fibers,” Electron. Lett. **17**, 603–605 (1981).

[112] L. G. Cohen, “Comparison of single-mode fiber dispersion measurement techniques,” IEEE J. Lightwave Tech. **LT-3**, 958–966 (1985).

[113] S. Diddams and J.-C. Diels, “Dispersion measurements with white-light interferometry,” IEEE J. Quantum Electron. **13**, 1120–1129 (1996).

[114] B. C. Collings, K. Bergman, S. T. Cundiff, S. Tsuda, J. N. Kutz, J. E. Cunningham, W. Y. Jan, M. Koch, and W. H. Knox, “Short cavity erbium/ytterbium

fiber lasers mode-locked with a saturable bragg reflector," IEEE J. Sel. Top. in Quantum. Electron. **3**, 1065–1075 (1997).

[115] L. Lepetit, G. Chériaux, and M. Joffre, "Linear techniques of phase measurement by femtosecond spectral interferometry for applications in spectroscopy," J. Opt. Soc. Am. B **12**, 2467–2474 (1995).

[116] I. A. Walmsley, "Characterization of Ultrashort Optical Pulses in the Few-Cycle Regime UIsing Spectral Phase Interferometry for Direct Electric-Field Reconstruction," Topics Appl. Phys. **95**, 265–292 (2004).

[117] D. K. Cheng, *Fundamentals of Engineering Electromagnetics* (Addison-Wesley, New York, 1995).

[118] R. W. Boyd, *Nonlinear Optics* (Academic Press, Boston, 2002), second edn.

[119] R. W. Hellwarth, "Third-order optical susceptibilites of liquids and solids," Progress Quantum Electron. **5**, 1–68 (1977).

[120] P. V. Mamyshev and S. V. Chernikov, "Ultrashort-pulse propagation in optical fibers," Opt. Lett. **15**, 1076–1078 (1990).

[121] C. A. Balanis, *Advanced Engineering Electromagnetics* (John Wiley & Sons, New York, 1989).

[122] C. R. Pollock, *Fundamentals of Optoelectronics* (Richard D. Irwin, Inc., Boston, 1995).

[123] A. Yariv, *Optical Electronics in Modern Communications* (Oxford University Press, New York, 1997), fifth edn.

[124] G. Keiser, *Optical Fiber Communications* (McGraw-Hill, Inc., New York, 1991), second edn.

[125] K. J. Blow and D. Wood, “Theoretical description of transient stimulated Raman scattering in optical fibers,” IEEE J. Quantum Electron. **25**, 2665–2673 (1989).

[126] L. Allen and J. H. Eberly, *Optical Resoncance and Two-Level Atoms* (Dover Publications, New York, 1987).

[127] N. R. Pereira and L. Stenflo, “Nonlinear Schrödinger equation including growth and damping,” Phys. Fluids **20**, 1733–1734 (1977).

[128] G. P. Agrawal, *Applications of Nonlinear Fiber Optics* (Academic Press, New York, 2001).

[129] N. Akhmediev and E. A. Ankiewicz, *Dissipative Solitons* (Springer, New York, 2005).

[130] I. Kelson and A. A. Hardy, “Strongly pumped fiber lasers,” IEEE J. Quantum Electron. **34**, 1570–1577 (1998).

[131] S. Tsuda, W. H. Knox, S. T. Cunduff, W. Y. Jan, and J. E. Cunningham, “Low-loss intracavity AlAs/AlFaAs saturable Bragg reflectro for femtosecond mode locking in solid-state lasers,” Opt. Lett. **20**, 1406–1408 (1995).

[132] S. Tsuda, W. H. Knox, S. T. Cunduff, W. Y. Jan, and J. E. Cunningham, “Mode locking ultrafast solid-state lasers with saturabe Bragg reflectors,” IEEE J. Sel. Top. Quantum Electron. **2**, 454–464 (1996).

[133] N. H. Bonadeo, W. H. Knox, J. M. Roth, and K. Bergman, “Passive harmonic mode-locked soliton fiber laser stabilized by an optically pumped saturabe Bragg reflector,” Opt. Lett. **23**, 1421–1423 (2000).

[134] L. E. Nelson, D. J. Jones, K. Tamura, H. A. Haus, and E. P. Ippen, “Ultrashort-pulse fiber ring lasers,” Appl. Phys. B **65**, 277–294 (1997).

[135] A. M. Dunlop, W. J. Firth, and E. M. Wright, “Pulse shapes and stability in Kerr and active mode-locking (KAML),” Opt. Express **2**, 204–211 (1998).

[136] J. G. Caputo, C. B. Clausen, M. P. Sörensen, and S. Bischoff, “Amplitude-modulated fiber-ring laser,” J. Opt. Soc. Am. B **17**, 705–712 (2000).

[137] W. Lu, L. Yan, and C. R. Menyuk, “Soliton stability conditions in actively mode-locked inhomogeneously broadened lasers,” J. Opt. Soc. Am. B **20**, 1473–1478 (2003).

[138] M. Nakazawa and E. Yoshida, “A 40-GHz 850-fs regeneratively FM mode-locked polarization-maintaining erbium fiber ring laser,” IEEE Photon. Tech. Lett. .

[139] E. Yoshida, K. Tamura, and M. Nakazawa, “Intracavity Dispersion Effects of a Regeneratively and Harmonically FM Mode-Locked Erbium-Doped Fiber Laser,” IEICE Trans. Electron. **E81-C**, 189–194 (1998).

[140] F. O. Ilday, J. Buckley, L. Kuznetsova, and F. W. Wise, “Generation of 36-fs pulses from a ytterbuim fiber laser,” Opt. Exp. **11**, 3550–3554 (2003).

[141] R.-M. Mu, V. S. Grigoryan, and C. R. Menyuk, “Comparison of theory and experiment for dispersion-managed solitons in a recirculating fiber loop,” IEEE J. Sel. Top. Quantum Electron. **6**, 248–257 (2000).

[142] N. J. Smith, F. M. Knox, N. J. Doran, K. J. Blow, and I. Benion, “Enhanced power solitons in optical fibres with periodic dispersion management,” Electron. Lett. **32**, 54–55 (1996).

[143] N. N. Akhmediev, A. Ankiewicz, and J. M. Soto-Crespo, “Stable soliton pairs in optical transmission lines and fiber lasers,” J. Opt. Soc. Am. B **15**, 515–523 (1998).

[144] S. Wabnitz, "Suppression of soliton interactions by phase modulation," Electron. Lett. **19**, 1711–1713 (1993).

[145] S. N. Vlasov, V. A. Petrishchev, and V. I. Talanov, "Averaged description of wave beams in linear and nonlinear media (the method of moments)," Radiophys. Quantum Electron. **14**, 1062–1070 (1971).

[146] C. J. McKinstrie, "Effects of filtering on Gordon-Haus timing jitter in dispersion-managed systems," J. Opt. Soc. Am. B **19**, 1275–1285 (2002).

[147] J. Santhanam and G. P. Agrawal, "Raman-induced spectral shifts in optical fibers: general theory based on the moment method," Opt. Comm. **222**, 413–420 (2003).

[148] N. G. Usechak and G. P. Agrawal, "Rate-equation approach for frequency-modulation mode locking using the moment method," J. Opt. Soc. Am. B **22**, 2570–2580 (2005).

[149] N. G. Usechak and G. P. Agrawal, "Semi-analytic technique for analyzing mode-locked lasers," Opt. Express **13**, 2075–2081 (2005).

[150] J. van Howe and C. Xu, "Ultrafast optical delay line using soliton propagation between a time-prism pair," Opt. Express **13**, 1138–1143 (2005).

[151] J. van Howe and C. Xu, "Ultrafast optical delay line by use of a time-prism pair," Opt. Lett. **30**, 99–101 (2005).

[152] J. Sharping, Y. Okawachi, J. van Howe, C. Xu, Y. Wang, A. E. Willner, and A. L. Gaeta, "All-optical, wavelength and bandwidth preserving, pulse delay based on parametric wavelength conversion and dispersion," Opt. Express **13**, 7872–7877 (2005).

[153] T. Brabec, C. Spielmann, and F. Krausz, "Mode locking in solitary lasers," Opt. Lett. **16**, 1961–1963 (1991).

[154] D. Kopf, F. X. Kärtner, K. J. Weingarten, and U. Keller, “Pulse shortening in a Nd:glass alser by gain reshaping and soliton formation,” Opt. Lett. **19**, 2146–2148 (1994).

[155] K. Tamura, E. Yoshida, and M. Nakazawa, “Forced Phase Modulation and Self Phase Modulation Effects in Dispersion-Tuned Mode-Locked Fiber Lasers,” IE-ICE Trans. Electron. **E81-C**, 195–200 (1998).

[156] L. Mandel and E. Wolf, *Optical Coherence and Quantum Optics* (Cambridge University Press, New York, 1995).

[157] M. Bieler, M. Spitzer, G. Hein, U. Siegner, and E. O. Göbel, “Ultrafast optics estabilishes metrological standards in high-frequency electronics,” Appl. Phys. A **78**, 429–433 (2004).

[158] P. L. Francois, “Nonlinear propagation of ultrashort pulses in optical fibers: total field formulation in the frequency domain,” JOSA B. **8**, 276–293 (1991).

[159] G. Chang, T. B. Norris, and H. G. Winful, “Optimization of supercontinuum generation in photonic crystal fibers for pulse compression,” Opt. Lett. **28**, 546–548 (2003).

[160] T. Kremp and W. Freude, “Fast split-step wavelet collocation method for WDM system parameter optimization,” IEEE J. Lightwave Technol. **23**, 1491–1502 (2005).

[161] L. R. Watkins and Y. R. Zhou, “Modeling propagation in optical fibers using wavelets,” IEEE J. Lightwave Technol. **12**, 1536–1542 (1994).

[162] I. Pierce, P. Rees, and K. A. Shore, “Wavelet operators for nonlinear optical pulse propagation,” J. Opt. Soc. Am. A **17**, 2431–2439 (2000).

[163] T. Kremp, “High-order split-step finite difference metod for nonlinear optical pulse propagation,” CLEO conferene paper **JThE57** (2005).

A Pulse Properties

This appendix focuses on the time and frequency representations of hyperbolic secant and Gaussian pulses including their associated FWHM's and time-bandwidth products.

A.1 Hyperbolic Secant Pulses

Starting with a hyperbolic secant pulse in time, we have

$$\phi(t) = A_0 \operatorname{sech}\left(\frac{t}{T_0}\right). \tag{A.1}$$

The FWHM is trivially found by considering $|\phi(t = \frac{1}{2}T_{FWHM})|^2 = \frac{1}{2}|\phi(t = 0)|^2$ which gives:

$$T_{FWHM} = 2\ \ln(\sqrt{2}+1)T_0 \approx 1.763T_0. \tag{A.2}$$

Now we find the spectrum by simply Fourier transforming the field:

$$\tilde{\phi}(\Omega) = A\pi T_0 \operatorname{sech}\left(\frac{\pi\Omega T_0}{2}\right). \tag{A.3}$$

The FWHM of the spectrum is given by

$$\Omega_{FWHM} = \frac{4\ln(\sqrt{2}+1)}{\pi T_0} \approx \frac{1.122}{T_0}. \tag{A.4}$$

If we can assume that our pulse has a narrow spectrum, we find:

$$\left|\tilde{\phi}(\lambda)\right|^2 \approx |A|^2 \pi^2 T_0^2 \mathrm{Sech}^2\left(\frac{\pi^2 c T_0 \Delta\lambda}{\lambda_0^2}\right)\left(\frac{2\pi c}{\lambda_0^2}\right), \tag{A.5}$$

$$\lambda_{FWHM} \approx \frac{2\ln(\sqrt{2}+1)\lambda_0^2}{\pi^2 c T_0} = 5.958\times 10^{-10}\frac{\lambda_0^2}{T_0}, \tag{A.6}$$

where we introduced $\Delta\lambda = \lambda_{FWHM}/2$. On the other hand, if our pulse spectrum is not narrow, we should use

$$\left|\tilde{\phi}(\lambda)\right|^2 = |A|^2 \pi^2 T_0^2 \mathrm{sech}^2\left[\frac{\pi T_0}{2}\left(\frac{2\pi c}{\lambda} - \frac{2\pi c}{\lambda_0}\right)\right]\left(\frac{2\pi c}{\lambda^2}\right) \tag{A.7}$$

to describe the spectrum. In order to obtain the above relation for the spectral width, we used the fact that $\Omega = \omega - \omega_0 = \frac{2\pi c}{\lambda} - \frac{2\pi c}{\lambda_0}$ since we removed the carrier frequency from this measurement. As a consequence, $\lambda_\pm = \lambda_0 \pm \lambda_{FWHM}/2$, and we find that $\lambda_{FWHM} = 2\lambda_0 - 2\lambda_- = -2\lambda_0 + 2\lambda_+$. Therefore,

$$T_0 = \frac{\ln(\sqrt{2}+1)}{\pi^2 c}\frac{(2\lambda_0 - \lambda_{FWHM})\,\lambda_0}{\lambda_{FWHM}}. \tag{A.8}$$

Finally, the time-bandwidth product (TBP) for a hyperbolic secant pulse is given by:

$$\mathrm{TBP} = \frac{T_{FWHM}\cdot\Omega_{FWHM}}{2\pi} = \frac{8\left[\ln\left(\sqrt{2}+1\right)\right]^2}{2\pi^2} = 0.314833. \tag{A.9}$$

A.2 Gaussian Pulses

Starting with a Gaussian field in time,

$$\phi(t) = Ae^{-t^2/2T_0^2}. \tag{A.10}$$

The FWHM is trivially found by considering $|\phi(t = \frac{1}{2}T_{FWHM})|^2 = \frac{1}{2}|\phi(t=0)|^2$ which gives:

$$T_{FWHM} = 2\sqrt{\ln(2)}T_0 = 1.665T_0. \tag{A.11}$$

Now we find the spectrum by simply Fourier transforming the field:

$$\tilde{\phi}(\Omega) = A\sqrt{2\pi}T_0 e^{-\Omega^2 T_0^2/2}. \tag{A.12}$$

The FWHM of this spectrum is given by

$$\Omega_{FWHM} = \frac{2\sqrt{ln(2)}}{T_0}. \tag{A.13}$$

Under the assumption that our spectrum is narrow, we find:

$$\left|\tilde{\phi}(\lambda)\right|^2 \approx |A|^2 2\pi T_0^2 \exp\left[-\left(\frac{2\pi c}{\lambda_0^2}\Delta\lambda\right)^2 T_0^2\right]\left(\frac{2\pi c}{\lambda_0^2}\right). \tag{A.14}$$

This gives the FWHM as

$$\lambda_{FWHM} \approx \frac{\sqrt{\ln(2)}\lambda_0^2}{\pi c T_0}. \tag{A.15}$$

If we cannot assume a narrow spectrum, then

$$\left|\tilde{\phi}(\lambda)\right|^2 = |A|^2 2\pi T_0^2 \exp\left[-\left(\frac{2\pi c}{\lambda} - \frac{2\pi c}{\lambda_0}\right)^2 T_0^2\right]\left(\frac{2\pi c}{\lambda^2}\right). \tag{A.16}$$

Once again we used the fact that $\Omega = \omega - \omega_0 = \frac{2\pi c}{\lambda} - \frac{2\pi c}{\lambda_0}$. We also define $\lambda_\pm = \lambda_0 \pm \lambda_{FWHM}/2$, and then find that $\lambda_{FWHM} = 2\lambda_0 - 2\lambda_- = -2\lambda_0 + 2\lambda_+$. Therefore,

$$T_0 = \frac{\sqrt{\ln(2)}}{2\pi c}\frac{(2\lambda_0 - \lambda_{FWHM})\,\lambda_0}{\lambda_{FWHM}} \tag{A.17}$$

Finally, the time-bandwidth product for a Gaussian is given by:

$$\text{TBP} = \frac{T_{FWHM}\cdot\Omega_{FWHM}}{2\pi} = \frac{4\ln(2)}{2\pi} = 0.4412712. \tag{A.18}$$

B Measurement Limitations

A brief but important topic which is essential in any experiment is to have an understanding of what is really being measured. Of course, when using a computer or theoretical model to predict the experimental performance of a system, this topic also becomes important. In order to facilitate accurate comparisons between any model and experiment, the non-ideal performance of the experimental equipment must be accounted for. In this section, we simply note the performance limitations of the most common devices used to characterize mode-locked lasers.

B.1 Optical Spectrum Analyzers

In the field of mode-locked lasers, the Optical Spectrum Analyzer (OSA) is frequently used to observe the spectrum of a mode-locked pulse train. Naively, one would expect that this device provides the scientist with a spectrum of a mode-locked pulse. In actuality, these devices have both finite response times and finite spectral resolutions. The ramification of the finite spectral resolution is that low-frequency modulation (kHz - GHz) of the optical signal is not detectable. Among other things, this includes the fact that OSA's are unable to resolve the longitudinal modes of the laser cavity that man-

ifest themselves as δ-function like peaks in the optical spectrum of a pulse train. In effect the optical spectrum of a mode-locked laser has a sinusoidal modulation related to the repetition rate of the laser which cannot be seen on an OSA unless the laser is mode locked at a frequency in the GHz range (the actual value depends on the carrier frequency and the device resolution).

As a consequence of the finite response time, the OSA will also temporally average the spectrum so that only slow changes or trends (on a ms time scale) can be resolved using this device. When comparing computer simulations to experimental results obtained using an OSA, we may need to take these limitations into account as in the case of FM oscillation.

If we assume that the intensity spectrum to be measured by an OSA is given by $\Psi(\lambda, T)$, we can write the response of the OSA as:

$$\mathrm{OSA}(\Lambda) \approx \mathrm{r_{esp}} \sum_{\mathrm{n=1}}^{\mathrm{\#points}} \int_{\Lambda_\mathrm{n}}^{\Lambda_{\mathrm{n+1}}} \left[\frac{1}{\mathrm{T_{int}}} \int_0^{\mathrm{T_{int}}} \Psi(\lambda, \mathrm{T}) \mathrm{dT} \right] \mathrm{d}\lambda, \tag{B.1}$$

where r_{esp} is related to both the detector efficiency and any loss of the device. In addition, $\Lambda_{n+1} - \Lambda_n \geq \Delta\Lambda$, where $\Delta\Lambda$ is the finite resolution of the OSA (frequently 0.05nm). In writing this result, we have assumed we have a spectrum $\psi(\lambda)$ which can change on a slow time scale T. We have also assumed that λ represents a continuous frequency range whereas Λ represents a discrete number of points used by the device to reconstruct the actual spectrum. This result shows us that the device has a finite response time that is usually limited by the sweep rate of the OSA and usually $\sim$1 ms/nm. Physically, this result indicates that OSAs perform some time averaging over the spectrum since they require a finite amount of time to scan over the spectrum. As a consequence of the finite filtering, the OSA attributes all of the power within a specific frequency range (or bin) to a single point.

Before parting, we note that, although grating based spectrometers do not have the same sweep issue as OSAs, their detectors still have a response time associated with them. Additionally, their resolution is limited by the size of the detector's pixels and the

frequency range over which they are configured to operate. As a result, these devices may also be modeled by the above equation, although the values may be quite different.

B.2 Oscilloscopes

An Oscilloscope displays voltage verses time of an electrical signal. The basic limitation of these devices is that they have a finite bandwidth and thus low-pass filter high-frequency input signals. For example, the state of the art in sampling oscilloscopes* is currently around 100 GHz (LeCroy WaveExpert 9000 and SDA 100G); however, real-time oscilloscopes† can only operate at frequencies $\leq$ 10 GHz at the present time. In terms of optics, the optical field must first be detected and converted to a current (or voltage) using a photodiode (and transimpedance amplifier) before an oscilloscope can even be used; currently, the fastest this can be done is $\sim$ 80 GHz.[98] In what follows, we assume an ideal square-law detector‡ is directly connected to an oscilloscope. We can then write the output signal expected on the oscilloscope as:§

$$V(T) \approx r_{\text{esp}} \sum_{n-1}^{\#\text{ points}} \int_{T_n}^{T_{n+1}} \left[\int_{-\infty}^{\infty} |A(\tau)|^2 h(t-\tau) d\tau \right] dt, \tag{B.2}$$

where $h(T)$ incorporates the finite bandwidth of the detector and oscilloscope combination and r_{esp} accounts for the responsivity of the detector. Moreover, we have assumed

*Sampling oscilloscopes assume a waveform is constant. By repeatedly sampling a waveform at a lower repetition rate but at temporally shifted locations, a higher (apparent) bandwidth may be achieved than possible using a real-time oscilloscope by temporally interleaving all of the data collected over a few acquisitions.

†Real-time oscilloscopes acquire a wave form using a single trigger and are always preferred over sampling oscilloscopes if one can is working with frequencies where they are available.

‡An ideal square-law detector has a response that is directly proportional to the intensity of any optical field incident upon it.

§Strictly speaking, these devices should be modeled using the Wiener–Khintchine theorem,[156] but our interest is in band-limited signals from computer simulations. Therefore, we ignore this fact to keep the explanation in this section simple.

that the detector has a built in transimpedence amplifier and a 50Ω output resistance.

Both detectors and oscilloscopes are bandwidth-limited due to their finite response times, which makes them look like low-pass filters. In general, one of the two filters dominates and we can approximate the response of the system as that of the limiting low-pass filter, which can take the generic form

$$h(\omega) = \frac{1}{\prod_{p=0}^{n} a_p(-i\omega/\omega_0)^n}, \tag{B.3}$$

where ω_0 is related to the 3dB bandwidth by $\omega_0 = 2\pi f_{3dB}$ and a_p are the coefficients for a Butterworth filter of order n and $a_0 = a_n = 1$.[¶] By using Eq. (B.3) in Eq. (B.2), we obtain the response of the detector-oscilloscope combination to the optical field $A(T)$. Of course, it is also quite simple to incorporate the finite response time of both devices.

Because of the filtering, when we apply this treatment to a mode-locked pulse train, we lose information about the individual pulses. To make this fact visual, consider a noisy pulse train as depicted in Fig. B.1. In an actual oscilloscope, we frequently see ringing in response to short pulses whose rise time is faster than the oscilloscope can accurately measure. This is a consequence of the filtering and/or the $\sin(x)/x$ interpolation used by the oscilloscope to connect the various samples. In our treatment above, we have ignored the interpolation and assumed that the oscilloscope is dominated by a single-pole, low-pass filter and so our results do not include this feature.

Figure B.1 immediately reveals an interesting result that all experimentalists should be aware of; since the high-frequency components of the signal have been filtered, we

[¶]Older oscilloscopes use chains of amplifiers to drive their CRT displays; this results in a Gaussian filter response. Newer digital oscilloscopes have responses that seek to be maximally flat from DC to their 3dB frequency and look more like higher-order butterworth filters with their phase corrected to be linear. The responses of these oscilloscopes fall off more quickly after their 3dB frequency than their older analog counterparts, which leads to excessive ringing for signals that exceed the bandwidth of the oscilloscope. In our work, however, we assume the filtering is simply limited by a standard low-pass filter dominated by a single-pole as shown in Eq. (B.3) when $n = 1$. For critical applications, where the bandwidth of the signal is close to the bandwidth of the oscilloscope, the transfer function of the oscilloscope is required to deconvolve the reported oscilloscope trace.[157]

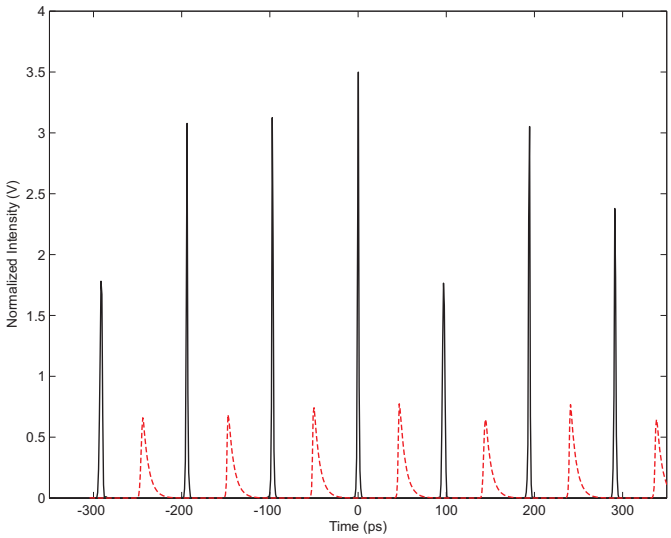

Figure B.1: A noisy pulse train (solid) containing 1.5-ps pulses at a 10.3 GHz repetition rate and the response expected from a 25-GHz bandwidth oscilloscope (dashed and shifted by 50 ps for easy visual inspection).

have lost most of the information about the pulse-pulse variation. To illustrate this, compare the relative magnitudes of the pulses located at 0 and 100 ps. Before filtering, a change from 3.6 to 1.8 V is observed, whereas after filtering the change has been suppressed such that it is now only 0.78 to 0.65 V. This demonstrates the reason oscilloscopes and electronics are unable to characterize high-frequency timing jitter and cross-correlation is required as noted in 3.4.

B.3 Microwave Spectrum Analyzers

A microwave spectrum analyzer (MSA) measures the microwave spectrum (from 100Hz to $\sim$80 GHz) of an electrical signal. The effect of this device on an optical pulse train

can approximately be written as[‖]

$$MSA(f) \approx \left| r_{\text{esp}} h(2\pi f) \int_{-\infty}^{\infty} |A(t)|^2 e^{i2\pi f} dt \right|^2, \tag{B.4}$$

where $h(2\pi f) = h(\omega)$ is the filter response. For a single-pole, passive, low-pass filter, the response is once again given by Eq. (B.3) above, where $n = 1$. It is important to note that microwave spectrum analyzer's have very good resolution bandwidths, usually as good a 1 Hz. Because of the number of points required to obtain such an accuracy numerically, the results from Eq. (B.4) will almost always be limited by the computational grid, and experimental results will have a better accuracy. Moreover, the resolution bandwidth must be taken into account when comparting experimental results to the computational ones. In the case of the OSA, the resolution obtained by the numerics exceeded that which can be provided by the OSA. In the case of a MSA however, the resolution is limited by the numerics. Therefore, to compare experimental results with computer simulations, the experimental data must be processed using an averaging similar to what was used for the OSA and oscilloscope.

$$Exp_{\text{low-res}}(n) \approx \sum_{n=1}^{\text{size}} \text{Data(m)}, \tag{B.5}$$

where "size" is given by the numerical resolution bandwidth (Δf) divided by the experimental resolution bandwidth after the quantity has been rounded down to the nearest integer.

For an ideal optical pulse train, the electrical spectrum is the Fourier transform of the optical pulse envelope multiplied by the filter response and a series of δ functions (spaced by the repetition rate of the laser). Non-ideal pulse trains were treated in greater detail in section 3.4.

[‖]Please see the discussion regarding the use of the Wiener–Khintchine theorem in 3.4 before using this. Since we are considering a signal of finite extent we do not have an infinite power issue and we have simplified our treatment by ignoring the Wiener–Khintchine theorem here. Strictly speaking this is mathematically flawed, however, for our purposes here it provides approximate results that were adequate for our work.

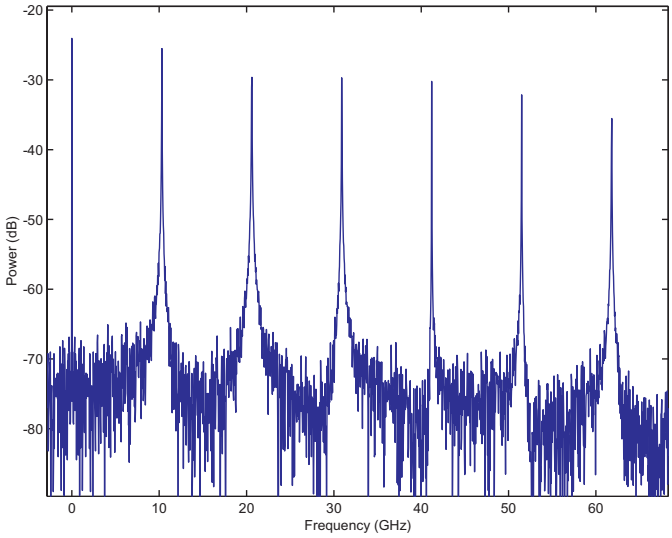

Figure B.2: The expected microwave spectrum from a 25-GHz spectrum analyzer in response to a noisy $\sim$ 1.5 picosecond pulse train consisting of 256 pulses.

The noise floor seen in Fig. B.2 is limited by the spectral resolution used to create the pulse train. In this case, our pulse train was obtained by modeling 256 pulses in an FM mode-locked laser over a thousand round trips (well before the laser cavity converged to a steady-state solution). Therefore, the pulse train has not yet converged and acts as a noisy signal. Because of the number of pulses simulated, we had to use 131,072 points to represent the pulse train and the simulation time increased such that it took $\sim$ 1 min to perform a single round trip on a 3 GHz pentium with 1 Gbyte of RAM. We point out that $\sim$ 4,000 round trips are usually required to achieve stable mode locking when only a single pulse is simulated.

Figure B.2 clearly shows that the laser is mode locked at 10.3 GHz and that the DC contribution to the spectrum is very δ-function like in agreement with our analytic work in 3.4. It is, however, important to note that this figure does not conform to the cartoon depicted in Fig. 3.9 since fluctuations among 256 neighboring pulses correspond to high-frequency variations and the treatment detailed in Section 3.4 was developed for low-frequency fluctuations. Finally, we point out that the resolution of this figure is 40 MHz, far worse than the 1-Hz resolution used to acquire the experimental results in

chapter 2.

C Numerical Modeling

Computer simulations play a pivotal role in the field of mode-locked lasers since the pulse shapes produced by these lasers generally cannot be described analytically. When performing studies or seeking to benchmark a new analytic treatment, the solutions to the full problem are required for comparison; these may only be obtained by solving the governing nonlinear partial differential equation(s). As a consequence, the ability to solve these equations is vital. In this section we introduce the most commonly used approach as well as a few of its variants. Two alternative approaches are subsequently presented since they posses some advantages and could increase in popularity in the future.

C.1 The Split-Step Method

The split-step method is readily identifiable as the workhorse of nonlinear fiber optics as it is used almost exclusively in the field. Not only does this method have an intuitive "derivation," but it is easy to implement and is not prone to diverging. To explain the basic idea behind this method, consider the master equation of mode locking, Eq. (4.92),

which we rewrite here for convenience:

$$\frac{T_R}{L_R}\frac{\partial A}{\partial T} + \frac{i}{2}\left(\bar{\beta}_2 + i\bar{g}T_2^2\right)\frac{\partial^2 A}{\partial t^2} - \frac{1}{6}\bar{\beta}_3\frac{\partial^3 A}{\partial t^3} = i\bar{\gamma}|A|^2 A + \frac{1}{2}(\bar{g} - \bar{\alpha})A + M(A,t) + N(t). \tag{C.1}$$

Before attempting to solve this equation, we point out that a numerical evaluation of the higher-order derivatives in the time domain has the tendency to become unwieldy; this is particularly the case for pulses with steep features. To circumvent this pitfall, the split-step method makes use of the following fundamental property of Fourier transforms:

$$\mathrm{FT}\left[\frac{d^n A(t,z)}{dt^n}\right] \rightarrow (-i\omega)^n \tilde{A}(\omega,z), \tag{C.2}$$

where FT denotes the Fourier transform as defined in chapter 4 and $\tilde{A}$ is the Fourier transformed field. The split-step technique takes advantage of this property by treating the terms involving derivatives in Fourier space while accounting for the nonlinear terms in the time domain. The use of both domains to achieve a solution to the equation is, in fact, how the technique got its name since a single step is split into two steps where the dispersive and nonlinear effects are treated separately. In other words, the step is split between two different types of effects, one treated in the time domain and the other treated in the frequency domain.

To solve the master equation using this technique, it is instructive to write it as

$$\frac{T_R}{L_R}\frac{\partial A}{\partial T} = (\hat{D} + \hat{N})A + \hat{PC} \tag{C.3}$$

where the dispersive terms are given by

$$\hat{D} = -\frac{i}{2}\left(\bar{\beta}_2 + i\bar{g}T_2^2\right)\frac{\partial^2}{\partial t^2} + \frac{1}{6}\bar{\beta}_3\frac{\partial^3}{\partial t^3} \tag{C.4}$$

and the nonlinear term is given by

$$\hat{N} = i\bar{\gamma}|A|^2. \tag{C.5}$$

The other terms are labeled $\hat{PC}$ (for Personal choice) since their effects may be included in either domain. For the master equation of mode locking they are given by

$$\hat{PC} = \frac{1}{2}(\bar{g} - \bar{\alpha})A + M(A,t) + N(t). \tag{C.6}$$

The effects of the $\hat{PC}$ terms were not included in either $\hat{D}$ or $\hat{N}$ since the choice of how to treat them is up to the scientist. Of course $\hat{PC}$ must be handled in at least one of the two domains, although these effects can also be split between both domains to potentially obtain better results. In the rest of this section, however, the $\hat{PC}$ terms are ignored since their treatment will coincide with that of either/both the $\hat{D}$ or $\hat{N}$ terms.

To solve the master equation, we note that the dispersive part of Eq. (C.3) may be written in the frequency domain by Fourier transforming the equation and using Eq. (C.2) to obtain

$$\frac{T_R}{L_R}\frac{\partial \tilde{A}}{\partial T} = i\left[\frac{1}{2}\left(\bar{\beta}_2 + i\bar{g}T_2^2\right)\omega^2 + \frac{1}{6}\bar{\beta}_3\omega^3\right]\tilde{A}. \tag{C.7}$$

This equation is then easily solved by

$$\tilde{A}' = \tilde{A}\exp\left\{i\frac{L_R}{T_R}\left[\frac{1}{2}\left(\bar{\beta}_2 + i\bar{g}T_2^2\right)\omega^2 + \frac{1}{6}\bar{\beta}_3\omega^3\right]\Delta\xi\right\}, \tag{C.8}$$

where $\tilde{A}'$ signifies the solution, in frequency space, advanced by one step of size $\Delta\xi$. After the field is advanced, under the effects of dispersion, it is inverse Fourier transformed back into the time domain to give A'.

The nonlinear term in Eq. (C.3) is approximately solved in an analogous fashion yielding

$$A'' \approx A'\exp\left[i\frac{L_R}{T_R}\bar{\gamma}|A'|^2\Delta\xi\right]. \tag{C.9}$$

In Eq. (C.9), we point out that it was assumed that the values of A'' and A' are similar enough that the approximate solution is essentially an exact solution. This is one location where error is introduced into the split-step scheme; however, variations on this simple-minded approximation exist, which increase its accuracy. One such variation uses a trapezoidal approximation to gain an increased accuracy. However, if an issue

with accuracy arises in practice, it is common to reduce the step size as opposed to searching for a more accurate technique.

The split-step method, as presented above, is only globally accurate to first-order due to the way in which its operators are applied in a single step ($\hat{N}\hat{D}$ or $\hat{D}\hat{N}$). To examine the accuracy of this technique, consider the question as to whether there is a difference between $\hat{N}\hat{D}$, $\hat{D}\hat{N}$, or some other variation in the order in which the operators are applied. Since the operators $\hat{N}$ and $\hat{D}$ do not commute, we must look at their commutation relation to gain insight on what our accuracy is and/or how to increase it if possible. Since these operators appear in the exponential function, their commutation relationship is given by the Campbell-Baker-Hausdorff (BCH) theorem:[156]

$$e^{\hat{D}}e^{\hat{N}} = \exp\left\{\hat{D}+\hat{N}+\frac{1}{2}[\hat{D},\hat{N}]+\frac{1}{12}\left([\hat{D},\hat{D},\hat{N}]+[\hat{N},\hat{N},\hat{D}]\right)+\cdots\right\}. \tag{C.10}$$

It is more instructive, however, to look at

$$\begin{aligned} e^{m\hat{D}}e^{\hat{N}}e^{n\hat{D}} = \exp\Bigg\{ & (n+m)\hat{D}+\hat{N}-\frac{1}{2}(m-n)[\hat{D},\hat{N}] \\ & + \left(\frac{1}{12}(m^2+n^2)-\frac{1}{4}m-\frac{1}{12}mn\right)[\hat{D},[\hat{D},\hat{N}]] \\ & + \frac{1}{12}(m+n)[\hat{N},[\hat{N},\hat{D}]]+\cdots\Bigg\} \end{aligned} \tag{C.11}$$

which can be derived from the basic BCH theorem. In Eq. (C.11) we have allowed for a more complex variation than the simple form of either $\hat{N}\hat{D}$ or $\hat{D}\hat{N}$. In this equation, we point out that m and n are free parameters that need only satisfy the condition $m+n=1$. To increase the accuracy of the split-step scheme, however, we note that by symmetrizing the way in which it is applied (i.e. by setting $m=n=1/2$) the global accuracy of the split-step is increased to second-order, since the limiting error term now goes as $\Delta\xi^3$ as opposed to the $\Delta\xi^2$ error term of the basic split-step (either $n=1,m=0$ or $n=0,m=1$). The resulting variation of the split-step is known as the symmetric split-step and is (supposedly) the most widely used form.

It is also worthy to note that other variants of the split-step have been used to further increase the accuracy beyond second order, most notably the so-called higher-

order split-step of Blow and Wood.[125] Their scheme increases the global accuracy of the split-step to fourth-order by taking four forward steps of size $\Delta\xi$ followed by one backward step of size $2\Delta\xi$ and ending with four more forward steps of size $\Delta\xi$. This prescription cancels the next higher-order term in the BCH expansion increasing the accuracy. However, nine steps are required to propagate the distance of only six and so it has an overhead cost associated with it. Due to the overhead and the increased complexity of implementing such higher-order schemes, they are rarely used in practice. As already noted, if a problem is encountered in a numerical simulation, researchers usually opt to reduce the step size as opposed to using a more sophisticated scheme. In parting, we note that the split-step relies heavily on the fast Fourier transform (FFT) to translate the field between the time and frequency domains. The FFT algorithm is well-known and requires $n\ln(n)$ operations and so, as its name implies, it is fast.

C.2 Finite Difference Methods

The master equation can also be solved using a direct integration technique,[158] such as forth-order Runge-Kutta or the more accurate Runge-Kutta-Felberg scheme.[159] When using such an approach, however, the split-step scheme is still used to alternate between the time domain (to handle the nonlinearity) and the frequency domain (to handle dispersion). Unfortunately, this approach is prone to diverging, whereas the standard split-step is not. Still there are applications where its use could be beneficial, such as in the study of supercontinuum generation since it allows one to easily incorporate the spectral dependence of the nonlinearities.[159]

The Runge-Kutta-Fehlberg method has been used in the past as it is a specific adaptation of the well known Runge-Kutta method which is accurate to fifth-order. It gives solutions to an equation of the form $y' = f(x,y)$ by finding intermediate values accord-

ing to:

$$F_1 = hf(x_n, y_n) \quad \text{where} \quad x_n = x_0 + nh, \quad x_{n+1} = x_0 + (n+1)h$$

$$F_2 = hf(x,y) \quad \text{where} \quad x = x_n + \tfrac{1}{4}h, \quad y = y_n + \tfrac{1}{4}F_1$$

$$F_3 = hf(x,y) \quad \text{where} \quad x = x_n + \tfrac{3}{8}h, \quad y = y_n + \tfrac{3}{32}F_1 + \tfrac{9}{32}F_2$$

$$F_4 = hf(x,y) \quad \text{where} \quad x = x_n + \tfrac{12}{13}h, \quad y = y_n + \tfrac{1932}{2197}F_1 - \tfrac{7200}{2197}F_2 + \tfrac{7296}{2197}F_3$$

$$F_5 = hf(x,y) \quad \text{where} \quad x = x_n + h, \quad y = y_n + \tfrac{439}{216}F_1 - 8F_2 + \tfrac{3680}{513}F_3 - \tfrac{845}{4104}F_4$$

$$F_6 = hf(x,y) \quad \text{where} \quad x = x_n + \tfrac{1}{2}h, \quad y = y_n - \tfrac{8}{27}F_1 + 2F_2 - \tfrac{3544}{2565}F_3 + \tfrac{1859}{4104}F_4 - \tfrac{11}{40}F_5.$$

By using all of the F_n intermediate values, the actual differential equation is solved to fourth-order by:

$$e_{n+1} = y_n + \left(\frac{25}{216}F_1 + \frac{1408}{2565}F_3 + \frac{2197}{4104}F_4 - \frac{1}{5}F_5\right) + O(h^4) \tag{C.12}$$

and to fifth-order by

$$y_{n+1} = y_n + \left(\frac{16}{135}F_1 + \frac{6656}{12825}F_3 + \frac{28561}{56430}F_4 - \frac{9}{50}F_5 + \frac{2}{55}F_6\right) + O(h^5).$$

One nice aspect of this technique is that it provides an error estimate by subtracting the fourth-order result from our fifth-order scheme; therefore, $\varepsilon \approx y_{n+1} - e_{n+1}$. This makes iterative stepping (where the step size is adjusted) simple to implement.

To show the utility of this approach, we have shown the result of propagating a fifth-order soliton over one soliton period in Fig. C.1. We have also used this technique to model supercontinuum generation by solving the generalized nonlinear schrödinger equation in the frequency domain [Eq. (4.67)]. The result of this simulation is shown in Fig. C.2, where we note that after a SPM induced compression the pulse breaks apart and then experiences the so-called soliton self-frequency shift as its spectrum red-shifts and is temporally delayed. In this case, the results obtained by using Runge-Kutta-Felberg were identical to those found by using the split-step; however, a small step size was required to insure that divergence was not a problem. Because of the increased

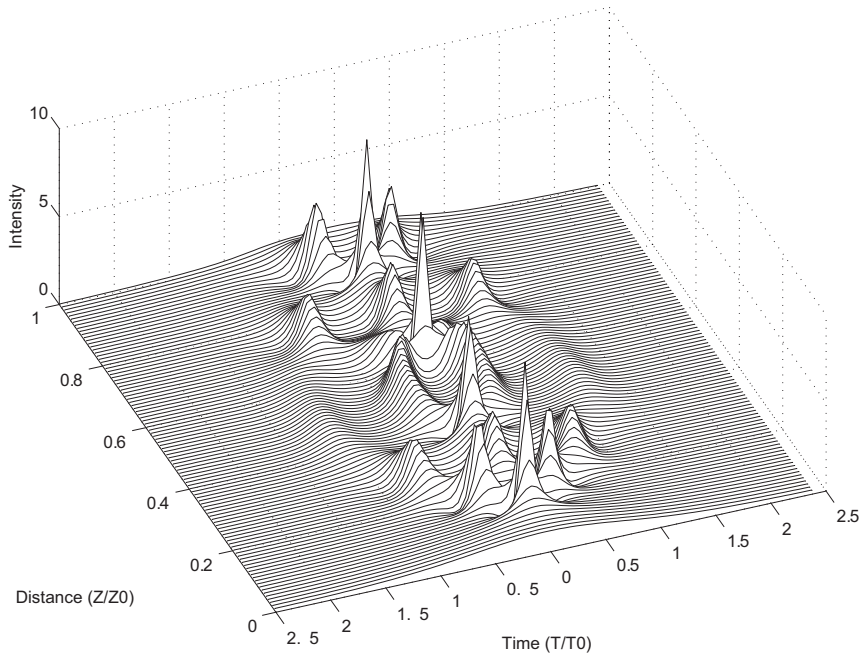

Figure C.1: Propagation of a fifth-order soliton over one soliton period using the Runge-Kutta-Felberg technique.

complexity inherent in coding the Runge-Kutta-Felberg scheme and its divergence issues, it was not used as a primary modeling tool in this work.

C.3 Wavelet Methods

There is clearly no simple way to handle the nonlinear term in Eq. (4.92) in the frequency domain, but one may still wonder if there is any way to treat the dispersion terms in the time domain. Clearly there is as derivatives may always be evaluated in the time domain; this leads us to wavelets and spline methods.

Wavelets are functions that, through scaling and shifting, can be used to decompose a signal into basis functions. Since wavelets can be constructed to span a basis, they

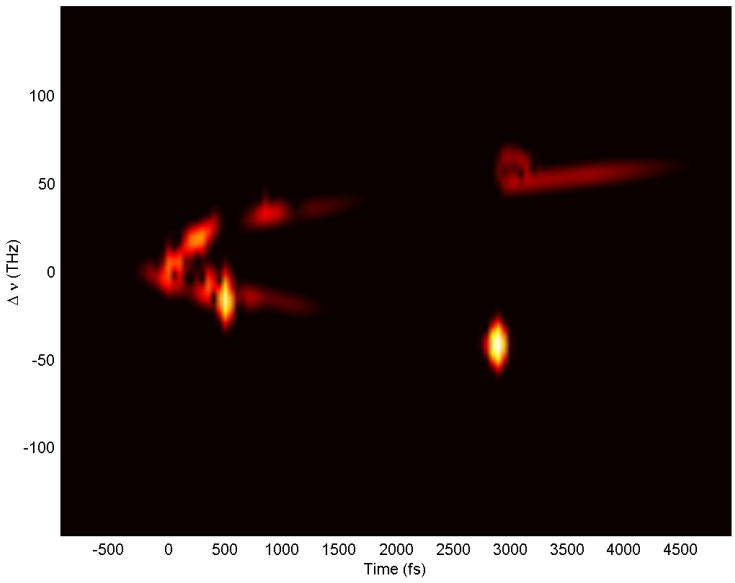

Figure C.2: Propagation of a fifth-order soliton in a photonic crystal fiber whose parameters are given in Ref. [5]. This figure shows the results using a spectrogram. See Appendix F for a discussion of this technique and how to interpret this plot.

have the special property that reconstruction may be accomplished without any loss of information. Since the wavelets themselves can be thought of as well known/behaved functions, differentiation may be performed analytically on these shapes. This offers another way to solve Eq. (4.92) and is referred to as the split-step wavelet method (SSWM) or the split-step wavelet collocation method.[160] As there is an algorithm able to quickly perform the wavelet decomposition, known as the fast wavelet transform (FWT), it is relatively easy to code this approach. A wavelet-based method offers three distinct benefits when compared with the conventional split-step method as follows: The FWT requires $O(n)$ operations as opposed to the FFT which requires $O(n\log(n))$ operations, so it is faster. Since wavelets constitute a time-frequency picture of a signal, they naturally offer a superior visualization space. Finally, for simulations that require short pulses, big temporal windows, and big spectral windows, the wavelet method may offer a way to mitigate the Fourier-transform conundrum (the inverse scaling re-

lationship between the two domains). This is particularly evident in supercontinuum generation where octave spanning spectrum can be created by short pulses that are then temporally delayed. Due to the time-frequency scaling of the FFT, one is limited with what can be modeled as computation times drastically increase. This limit can be mitigated by using wavelets since the information can essentially be processed in the time domain.

With all of these advantages it would seem everyone would use wavelets; however, they are relatively new and they offer choices. Although having choices is generally a good thing, it requires that one make decisions which can negatively impact the results. When working with wavelets, one must choose the mother wavelet which is used to decompose the signal. Unlike the FFT, which offers no choices, a poor choice in which mother wavelet to use will result in poor results. This adds a degree of difficulty to this approach and also means that wavelets cannot be used as universal tools in the way the Fourier transform is. Still, there have been a number of papers which have demonstrated the utility of using wavelets for nonlinear optical pulse propagation, for example see Refs. [160–162].

C.4 Spline Methods

A more simplistic, and purely time-domain, treatment of this problem may also be achieved by locally fitting the field in the time domain to a polynomial. The polynomial may then be analytically differentiated (in the time domain) and the dispersive effects may easily be accounted for. Recent results using this approach have reported that it also requires only $O(n)$ operations and can run faster than either the spit-step or wavelet based approaches.[163]

D Analytic Relations Used to Apply the Moment Method

This appendix provides the mathematical relations that were used to apply the moment method in order to develop our mode-locking rate equations. It includes both integration-by-parts relations as well as the analytic form of various integrals.

D.1 Integration by Parts

By applying the integration-by-parts technique to our results in Chapter 6 they can be simplified. To do this we assume that the optical field is a pulse such that $\lim_{|t|=\infty} A(t,T) \rightarrow 0$. This leads to the following relations, which are needed in our application of the moment method to mode-locked lasers in chapters 6–9:

$$\int_{-\infty}^{\infty} \left[A^* \frac{\partial A}{\partial t} + A \frac{\partial A^*}{\partial t} \right] dt = -\int_{-\infty}^{\infty} \left[A^* \frac{\partial A}{\partial t} + A \frac{\partial A^*}{\partial t} \right] dt = 0 \tag{D.1}$$

$$\int_{-\infty}^{\infty} \left[A^* \frac{\partial^2 A}{\partial t^2} - A \frac{\partial^2 A^*}{\partial t^2} \right] dt = -\int_{-\infty}^{\infty} \left[\frac{\partial A^*}{\partial t} \frac{\partial A}{\partial t} - \frac{\partial A}{\partial t} \frac{\partial A^*}{\partial t} \right] dt = 0, \tag{D.2}$$

and

$$\int_{-\infty}^{\infty} \left[A^* \frac{\partial^3 A}{\partial t^3} - A \frac{\partial^3 A^*}{\partial t^3} \right] dt = -\int_{-\infty}^{\infty} \left[\frac{\partial A^*}{\partial t} \frac{\partial^2 A}{\partial t^2} - \frac{\partial A}{\partial t} \frac{\partial^2 A^*}{\partial t^2} \right] dt. \tag{D.3}$$

Since

$$\int_{-\infty}^{\infty}(t-\xi)\left[A^*\frac{\partial A}{\partial t}+A\frac{\partial A^*}{\partial t}\right]dt = -\int_{-\infty}^{\infty}(t-\xi)\left[A\frac{\partial A^*}{\partial t}+A^*\frac{\partial A}{\partial t}\right]dt - 2\int_{-\infty}^{\infty}|A|^2\,dt, \tag{D.4}$$

we find

$$\int_{-\infty}^{\infty}(t-\xi)\left[A^*\frac{\partial A}{\partial t}+A\frac{\partial A^*}{\partial t}\right]dt = -\int_{-\infty}^{\infty}|A|^2\,dt. \tag{D.5}$$

Using

$$\int_{-\infty}^{\infty}(t-\xi)^2\left[\frac{\partial A^*}{\partial t}\frac{\partial^2 A}{\partial t^2}+\frac{\partial A}{\partial t}\frac{\partial^2 A^*}{\partial t^2}\right]dt = -\int_{-\infty}^{\infty}(t-\xi)^2\left[\frac{\partial^2 A^*}{\partial t^2}\frac{\partial A}{\partial t}+\frac{\partial^2 A}{\partial t^2}\frac{\partial A^*}{\partial t}\right]dt - 4\int_{-\infty}^{\infty}(t-\xi)\left|\frac{\partial A}{\partial t}\right|^2 dt, \tag{D.6}$$

we also find

$$\int_{-\infty}^{\infty}(t-\xi)^2\left[\frac{\partial A^*}{\partial t}\frac{\partial^2 A}{\partial t^2}+\frac{\partial A}{\partial t}\frac{\partial^2 A^*}{\partial t^2}\right]dt = -2\int_{-\infty}^{\infty}(t-\xi)\left|\frac{\partial A}{\partial t}\right|^2 dt \tag{D.7}$$

$$\int_{-\infty}^{\infty}(t-\xi)\left[A^*\frac{\partial^2 A}{\partial t^2}+A\frac{\partial^2 A^*}{\partial t^2}\right]dt = -2\int_{-\infty}^{\infty}(t-\xi)\left|\frac{\partial A}{\partial t}\right|^2 dt - \int_{-\infty}^{\infty}\left[A^*\frac{\partial A}{\partial t}+A\frac{\partial A^*}{\partial t}\right]dt \tag{D.8}$$

By using Eq. (D.1) in Eq. (D.8) we can simplify this result to

$$\int_{-\infty}^{\infty}(t-\xi)\left[A^*\frac{\partial^2 A}{\partial t^2}+A\frac{\partial^2 A^*}{\partial t^2}\right]dt = -2\int_{-\infty}^{\infty}(t-\xi)\left|\frac{\partial A}{\partial t}\right|^2 dt. \tag{D.9}$$

D.1.1 Relations for E

In this subsection we focus on the relations used to obtain the energy moment starting with the integral for β_2 in Eq. (6.13)

$$\int_{-\infty}^{\infty}\left[A^*\frac{\partial^2 A}{\partial t^2}-A\frac{\partial^2 A^*}{\partial t^2}\right]dt = -\int_{-\infty}^{\infty}\left[\frac{\partial A^*}{\partial t}\frac{\partial A}{\partial t}-\frac{\partial A}{\partial t}\frac{\partial A^*}{\partial t}\right]dt = 0, \tag{D.10}$$

The integral for the gain term in Eq. (6.13) may be simplified by noting that

$$\int_{-\infty}^{\infty}\left[A^*\frac{\partial^2 A}{\partial t^2}+A\frac{\partial^2 A^*}{\partial t^2}\right]dt=-2\int_{-\infty}^{\infty}\left|\frac{\partial A}{\partial t}\right|^2 dt. \tag{D.11}$$

The integral involving β_3 in Eq. (6.13) may also be simplified if we use the following relationship:

$$\int_{-\infty}^{\infty}\left[A^*\frac{\partial^3 A}{\partial t^3}+A\frac{\partial^3 A^*}{\partial t^3}\right]dt=-\int_{-\infty}^{\infty}\left[\frac{\partial A^*}{\partial t}\frac{\partial^2 A}{\partial t^2}+\frac{\partial A}{\partial t}\frac{\partial^2 A^*}{\partial t^2}\right]dt. \tag{D.12}$$

If we apply integration-by-parts to Eq. (D.12) a second time, we obtain

$$\int_{-\infty}^{\infty}\left[A^*\frac{\partial^3 A}{\partial t^3}+A\frac{\partial^3 A^*}{\partial t^3}\right]dt=\int_{-\infty}^{\infty}\left[\frac{\partial^2 A^*}{\partial t^2}\frac{\partial A}{\partial t}+\frac{\partial^2 A}{\partial t^2}\frac{\partial A^*}{\partial t}\right]dt. \tag{D.13}$$

By comparing Eqs. (D.12) and (D.13) we find

$$\int_{-\infty}^{\infty}\left[A^*\frac{\partial^3 A}{\partial t^3}+A\frac{\partial^3 A^*}{\partial t^3}\right]dt=0. \tag{D.14}$$

D.1.2 Relations for ξ

The integral involving β_2 can be simplified by using our definition for carrier frequency detuning Ω [See Eq. (6.3)]

$$\int_{-\infty}^{\infty}t\left[A^*\frac{\partial^2 A}{\partial t^2}-A\frac{\partial^2 A^*}{\partial t^2}\right]dt=2i\Omega E. \tag{D.15}$$

Moreover, the integral for g is given by

$$\int_{-\infty}^{\infty}t\left[A^*\frac{\partial^2 A}{\partial t^2}+A\frac{\partial^2 A^*}{\partial t^2}\right]dt=-\int_{-\infty}^{\infty}\left[\frac{\partial(A^*t)}{\partial t}\frac{\partial A}{\partial t}+\frac{\partial(At)}{\partial t}\frac{\partial A^*}{\partial t}\right]dt \tag{D.16}$$

or

$$\begin{aligned}\int_{-\infty}^{\infty}t\left[A^*\frac{\partial^2 A}{\partial t^2}+A\frac{\partial^2 A^*}{\partial t^2}\right]dt\;-\;&\int_{-\infty}^{\infty}\left[A^*\frac{\partial A}{\partial t}+A\frac{\partial A^*}{\partial t}\right]dt\\ &=-2\int_{-\infty}^{\infty}t\left|\frac{\partial A}{\partial t}\right|^2 dt,\end{aligned} \tag{D.17}$$

which can be simplified, if one uses Eq. (D.1), to

$$\int_{-\infty}^{\infty} t\left[A^*\frac{\partial^2 A}{\partial t^2}+A\frac{\partial^2 A^*}{\partial t^2}\right]dt=-2\int_{-\infty}^{\infty} t\left|\frac{\partial A}{\partial t}\right|^2 dt. \tag{D.18}$$

The integral involving β_3 reduces to

$$\int_{-\infty}^{\infty} t\left[A^*\frac{\partial^3 A}{\partial t^3}+A\frac{\partial^3 A^*}{\partial t^3}\right]dt=3\int_{-\infty}^{\infty}\left|\frac{\partial A}{\partial t}\right|^2 dt. \tag{D.19}$$

D.1.3 Relations for Ω

The integral involving β_2 is given by

$$\int_{-\infty}^{\infty}\left[\frac{\partial A^*}{\partial t}\frac{\partial^2 A}{\partial t^2}+\frac{\partial A}{\partial t}\frac{\partial^2 A^*}{\partial t^2}\right]dt=-\int_{-\infty}^{\infty}\left[\frac{\partial A}{\partial t}\frac{\partial^2 A^*}{\partial t^2}+\frac{\partial A^*}{\partial t}\frac{\partial^2 A}{\partial t^2}\right]dt. \tag{D.20}$$

Therefore,

$$\int_{-\infty}^{\infty}\left[\frac{\partial A^*}{\partial t}\frac{\partial^2 A}{\partial t^2}+\frac{\partial A}{\partial t}\frac{\partial^2 A^*}{\partial t^2}\right]dt=0. \tag{D.21}$$

The integral for the β_3 term can also be simplified by integration-by-parts twice where the first application gives

$$\int_{-\infty}^{\infty}\left[A^*\frac{\partial^4 A}{\partial t^4}-A\frac{\partial^4 A^*}{\partial t^4}\right]dt=-\int_{-\infty}^{\infty}\left[\frac{\partial A^*}{\partial t}\frac{\partial^3 A}{\partial t^3}-\frac{\partial A}{\partial t}\frac{\partial^3 A^*}{\partial t^3}\right]dt. \tag{D.22}$$

The second application of integration-by-parts gives us

$$\int_{-\infty}^{\infty}\left[A^*\frac{\partial^4 A}{\partial t^4}-A\frac{\partial^4 A^*}{\partial t^4}\right]dt=\int_{-\infty}^{\infty}\left[\frac{\partial^2 A^*}{\partial t^2}\frac{\partial^2 A}{\partial t^2}-\frac{\partial^2 A}{\partial t^2}\frac{\partial^2 A^*}{\partial t^2}\right]dt, \tag{D.23}$$

which is just

$$\int_{-\infty}^{\infty}\left[A^*\frac{\partial^4 A}{\partial t^4}-A\frac{\partial^4 A^*}{\partial t^4}\right]dt=0. \tag{D.24}$$

Using Eq.'s (D.20) and (D.22), we immediately find that our integral for β_3 is given by

$$\int_{-\infty}^{\infty}\left[\frac{\partial A^*}{\partial t}\frac{\partial^3 A}{\partial t^3}-\frac{\partial A}{\partial t}\frac{\partial^3 A^*}{\partial t^3}\right]dt=0 \tag{D.25}$$

By applying integration-by-parts to the integral for the γ term we obtain

$$\int_{-\infty}^{\infty} |A|^2 \frac{\partial |A|^2}{\partial t} dt = -\int_{-\infty}^{\infty} |A|^2 \frac{\partial |A|^2}{\partial t} dt. \tag{D.26}$$

Therefore,

$$\int_{-\infty}^{\infty} |A|^2 \frac{\partial |A|^2}{\partial t} dt = 0. \tag{D.27}$$

D.1.4 Relations for q

One of the β_2 integrals for the q moment is given by

$$\begin{aligned}\int_{-\infty}^{\infty} (t-\xi) \left[\frac{\partial A^*}{\partial t} \frac{\partial^2 A}{\partial t^2} + \frac{\partial A}{\partial t} \frac{\partial^2 A^*}{\partial t^2} \right] dt \; = & -\int_{-\infty}^{\infty} (t-\xi) \left[\frac{\partial A}{\partial t} \frac{\partial^2 A^*}{\partial t^2} + \frac{\partial A^*}{\partial t} \frac{\partial^2 A}{\partial t^2} \right] dt \\ & - 2\int_{-\infty}^{\infty} \left| \frac{\partial A}{\partial t} \right|^2 dt,\end{aligned} \tag{D.28}$$

hence

$$\int_{-\infty}^{\infty} (t-\xi) \left[\frac{\partial A^*}{\partial t} \frac{\partial^2 A}{\partial t^2} + \frac{\partial A}{\partial t} \frac{\partial^2 A^*}{\partial t^2} \right] dt = -\int_{-\infty}^{\infty} \left| \frac{\partial A}{\partial t} \right|^2 dt. \tag{D.29}$$

The other β_2 integral is given by

$$\begin{aligned}\int_{-\infty}^{\infty} (t-\xi) \left[A^* \frac{\partial^3 A}{\partial t^3} + A \frac{\partial^3 A^*}{\partial t^3} \right] dt = \; & -\int_{-\infty}^{\infty} (t-\xi) \left[\frac{\partial A^*}{\partial t} \frac{\partial^2 A}{\partial t^2} + \frac{\partial A}{\partial t} \frac{\partial^2 A^*}{\partial t^2} \right] dt \\ & - \int_{-\infty}^{\infty} \left[A^* \frac{\partial^2 A}{\partial t^2} + A \frac{\partial^2 A^*}{\partial t^2} \right] dt.\end{aligned} \tag{D.30}$$

By using Eqs. (D.11) and (D.29), we find

$$\int_{-\infty}^{\infty} (t-\xi) \left[A^* \frac{\partial^3 A}{\partial t^3} + A \frac{\partial^3 A^*}{\partial t^3} \right] dt = 3\int_{-\infty}^{\infty} \left| \frac{\partial A}{\partial t} \right|^2 dt. \tag{D.31}$$

Focusing on the gain term, g, we find

$$\begin{aligned}\int_{-\infty}^{\infty} (t-\xi) \left[A^* \frac{\partial^3 A}{\partial t^3} - A \frac{\partial^3 A^*}{\partial t^3} \right] dt = \; & -\int_{-\infty}^{\infty} (t-\xi) \left[\frac{\partial A^*}{\partial t} \frac{\partial^2 A}{\partial t^2} - \frac{\partial A}{\partial t} \frac{\partial^2 A^*}{\partial t^2} \right] dt \\ & - \int_{-\infty}^{\infty} \left[A^* \frac{\partial^2 A}{\partial t^2} - A \frac{\partial^2 A^*}{\partial t^2} \right] dt,\end{aligned} \tag{D.32}$$

which can be further simplified by using Eq. (D.8) to

$$\int_{-\infty}^{\infty}(t-\xi)\left[A^*\frac{\partial^3 A}{\partial t^3}-A\frac{\partial^3 A^*}{\partial t^3}\right]dt=-\int_{-\infty}^{\infty}(t-\xi)\left[\frac{\partial A^*}{\partial t}\frac{\partial^2 A}{\partial t^2}-\frac{\partial A}{\partial t}\frac{\partial^2 A^*}{\partial t^2}\right]dt. \tag{D.33}$$

One of the β_3 integral's can be simplified through

$$\begin{aligned}\int_{-\infty}^{\infty}(t-\xi)\left[\frac{\partial A^*}{\partial t}\frac{\partial^3 A}{\partial t^3}-\frac{\partial A}{\partial t}\frac{\partial^3 A^*}{\partial t^3}\right]dt = & -\int_{-\infty}^{\infty}(t-\xi)\left[\frac{\partial^2 A^*}{\partial t^2}\frac{\partial^2 A}{\partial t^2}-\frac{\partial^2 A}{\partial t^2}\frac{\partial^2 A^*}{\partial t^2}\right]dt \\ & -\int_{-\infty}^{\infty}\left[\frac{\partial A^*}{\partial t}\frac{\partial^2 A}{\partial t^2}-\frac{\partial A}{\partial t}\frac{\partial^2 A^*}{\partial t^2}\right]dt.\end{aligned} \tag{D.34}$$

Noticing that the first term must disappear, we find

$$\int_{-\infty}^{\infty}(t-\xi)\left[\frac{\partial A^*}{\partial t}\frac{\partial^3 A}{\partial t^3}-\frac{\partial A}{\partial t}\frac{\partial^3 A^*}{\partial t^3}\right]dt=-\int_{-\infty}^{\infty}\left[\frac{\partial A^*}{\partial t}\frac{\partial^2 A}{\partial t^2}-\frac{\partial A}{\partial t}\frac{\partial^2 A^*}{\partial t^2}\right]dt. \tag{D.35}$$

The other β_3 integral may be simplified using

$$\begin{aligned}\int_{-\infty}^{\infty}(t-\xi)\left[A^*\frac{\partial^4 A}{\partial t^4}-A\frac{\partial^4 A^*}{\partial t^4}\right]dt = & -\int_{-\infty}^{\infty}(t-\xi)\left[\frac{\partial A^*}{\partial t}\frac{\partial^3 A}{\partial t^3}-\frac{\partial A}{\partial t}\frac{\partial^3 A^*}{\partial t^3}\right]dt \\ & -\int_{-\infty}^{\infty}\left[A^*\frac{\partial^3 A}{\partial t^3}-A\frac{\partial^3 A^*}{\partial t^3}\right]dt.\end{aligned} \tag{D.36}$$

Using Eqs. (D.3) and (D.35) in Eq. (D.36), we find

$$\int_{-\infty}^{\infty}(t-\xi)\left[A^*\frac{\partial^4 A}{\partial t^4}-A\frac{\partial^4 A^*}{\partial t^4}\right]dt=2\int_{-\infty}^{\infty}\left[\frac{\partial A^*}{\partial t}\frac{\partial^2 A}{\partial t^2}-\frac{\partial A}{\partial t}\frac{\partial^2 A^*}{\partial t^2}\right]dt. \tag{D.37}$$

Finally, the integral involving the nonlinear term, γ, is simplified by noting

$$\int_{-\infty}^{\infty}(t-\xi)\left|A\right|^2\frac{\partial\left|A\right|^2}{\partial t}dt=-\frac{1}{2}\int_{-\infty}^{\infty}\left|A\right|^4 dt. \tag{D.38}$$

D.1.5 Relations for τ

Integral for β_2

$$\int_{-\infty}^{\infty}(t-\xi)^2\left[A^*\frac{\partial^2 A}{\partial t^2}-A\frac{\partial^2 A^*}{\partial t^2}\right]dt = -\int_{-\infty}^{\infty}(t-\xi)^2\left[\frac{\partial A^*}{\partial t}\frac{\partial A}{\partial t}-\frac{\partial A}{\partial t}\frac{\partial A^*}{\partial t}\right]dt \\ -2\int_{-\infty}^{\infty}(t-\xi)\left[A^*\frac{\partial A}{\partial t}-A\frac{\partial A^*}{\partial t}\right]dt. \tag{D.39}$$

Therefore, by noting one of the integrals vanishes and using Eq. (6.4), we find

$$\int_{-\infty}^{\infty}(t-\xi)^2\left[A^*\frac{\partial^2 A}{\partial t^2}-A\frac{\partial^2 A^*}{\partial t^2}\right]dt = 2iqE. \tag{D.40}$$

The gain integral can be written as

$$\int_{-\infty}^{\infty}(t-\xi)^2\left[A^*\frac{\partial^2 A}{\partial t^2}+A\frac{\partial^2 A^*}{\partial t^2}\right]dt = -2\int_{-\infty}^{\infty}(t-\xi)\left[A^*\frac{\partial A}{\partial t}+A\frac{\partial A^*}{\partial t}\right]dt \\ -2\int_{-\infty}^{\infty}(t-\xi)^2\left|\frac{\partial A}{\partial t}\right|^2 dt, \tag{D.41}$$

which may be simplified, by using Eqs. (D.5) and (6.1), to

$$\int_{-\infty}^{\infty}(t-\xi)^2\left[A^*\frac{\partial^2 A}{\partial t^2}+A\frac{\partial^2 A^*}{\partial t^2}\right]dt = -2\int_{-\infty}^{\infty}(t-\xi)^2\left|\frac{\partial A}{\partial t}\right|^2 dt+2E. \tag{D.42}$$

The effect of third-order dispersion, β_3, may be simplified via

$$\int_{-\infty}^{\infty}(t-\xi)^2\left[A^*\frac{\partial^3 A}{\partial t^3}+A\frac{\partial^3 A^*}{\partial t^3}\right]dt = -\int_{-\infty}^{\infty}(t-\xi)^2\left[\frac{\partial A^*}{\partial t}\frac{\partial^2 A}{\partial t^2}+\frac{\partial A}{\partial t}\frac{\partial^2 A^*}{\partial t^2}\right]dt \\ -2\int_{-\infty}^{\infty}(t-\xi)\left[A^*\frac{\partial^2 A}{\partial t^2}+A\frac{\partial^2 A^*}{\partial t^2}\right]dt, \tag{D.43}$$

which, using Eqs. (D.7) and (D.9) gives us

$$\int_{-\infty}^{\infty}(t-\xi)^2\left[A^*\frac{\partial^3 A}{\partial t^3}+A\frac{\partial^3 A^*}{\partial t^3}\right]dt = 6\int_{-\infty}^{\infty}(t-\xi)\left|\frac{\partial A}{\partial t}\right|^2 dt. \tag{D.44}$$

D.2 Various Derivatives and Related Terms

In order to apply the moment method to our specific pulse shapes, it is useful to list a few basic derivatives that are useful.

D.2.1 Derivatives Involving Gaussian Pulses

Starting with our perturbed Gaussian pulse shape

$$A = a\exp\left[-\frac{(t-\xi)^2(1+iq)}{2\tau^2} - i\Omega(t-\xi) + ip\right], \tag{D.45}$$

we may determine the derivative relations that will be useful in our work. Obviously,

$$|A|^2 = a^2\exp\left[-\frac{(t-\xi)^2}{\tau^2}\right], \tag{D.46}$$

and

$$\frac{\partial A}{\partial t} = -\left[\frac{(t-\xi)(1+iq)}{\tau^2} + i\Omega\right]\times A. \tag{D.47}$$

The complex conjugate of this result gives us

$$\frac{\partial A^*}{\partial t} = -\left[\frac{(t-\xi)(1-iq)}{\tau^2} - i\Omega\right]\times A^* \tag{D.48}$$

and therefore,

$$\left|\frac{\partial A}{\partial t}\right|^2 = \left[\frac{(t-\xi)^2\left(1+q^2\right)}{\tau^4} + \frac{2\Omega q(t-T)}{\tau^2} + \Omega^2\right]\times|A|^2. \tag{D.49}$$

We also find that

$$A^*\frac{\partial A}{\partial t} = -\left[\frac{(t-\xi)(1+iq)}{\tau^2} + i\Omega\right]\times|A|^2 \tag{D.50}$$

and

$$A\frac{\partial A^*}{\partial t} = -\left[\frac{(t-\xi)(1-iq)}{\tau^2} - i\Omega\right]\times|A|^2, \tag{D.51}$$

which gives

$$A^*\frac{\partial A}{\partial t} - A\frac{\partial A^*}{\partial t} = -2i\left[\frac{q}{\tau^2}(t-\xi) + \Omega\right]\times|A|^2. \tag{D.52}$$

Using the chain rule and Eq. (D.47) gives us

$$\frac{\partial^2 A}{\partial t^2} = \left[-\frac{1+iq}{\tau^2} + \left[\frac{(t-\xi)(1+iQ)}{\tau^2} + i\Omega\right]^2\right]\times A, \tag{D.53}$$

which may be expanded and written as

$$\frac{\partial^2 A}{\partial t^2} = \left[\frac{(t-\xi)^2 (1+iQ)^2}{\tau^4} - \Omega^2 + \frac{1+iq}{\tau^2} \left[2i\Omega (t-\xi) - 1 \right] \right] \times A. \tag{D.54}$$

Finally,

$$\begin{aligned} \frac{\partial A^*}{\partial t} \frac{\partial^2 A}{\partial t^2} = & - \left[\frac{(t-\xi)^3 \left(1+q^2\right) (1+iq)}{\tau^6} + \frac{(t-\xi) \left(1+q^2\right)}{\tau^4} \left[2i\Omega (t-\xi) - 1 \right] \right. \\ & - \frac{\Omega^2 (t-\xi) (1-iq)}{\tau^2} - \frac{i\Omega (t-\xi)^2 (1+iq)^2}{\tau^4} \\ & \left. + \frac{\Omega (1+iq)}{\tau^2} \left[2\Omega (t-\xi) + i \right] + i\Omega^3 \right] \times |A|^2 . \end{aligned} \tag{D.55}$$

This result may be "simplified" somewhat to

$$\begin{aligned} \frac{\partial A^*}{\partial t} \frac{\partial^2 A}{\partial t^2} = & - \left[\frac{(t-\xi)^3 \left(1+q^2\right) (1+iq)}{\tau^6} - \frac{(t-\xi) \left(1+q^2\right)}{\tau^4} \right. \\ & + \frac{i\Omega (t-\xi)^2 (1+iq)}{\tau^4} [1-3iq] + \frac{\Omega^2 (t-\xi)}{\tau^2} [1+3iq] \\ & \left. + \frac{i\Omega (1+iq)}{\tau^2} + i\Omega^3 \right] \times |A|^2 . \end{aligned} \tag{D.56}$$

Recognizing that its complex conjugate gives

$$\begin{aligned} \frac{\partial A}{\partial t} \frac{\partial^2 A^*}{\partial t^2} = & - \left[\frac{(t-\xi)^3 \left(1+q^2\right) (1-iq)}{\tau^6} - \frac{(t-\xi) \left(1+q^2\right)}{\tau^4} \right. \\ & - \frac{i\Omega (t-\xi)^2 (1-iq)}{\tau^4} [1+3iq] + \frac{\Omega^2 (t-\xi)}{\tau^2} [1-3iq] \\ & \left. - \frac{i\Omega (1-iq)}{\tau^2} - i\Omega^3 \right] \times |A|^2 , \end{aligned} \tag{D.57}$$

we obtain

$$\begin{aligned} \frac{\partial A^*}{\partial t} \frac{\partial^2 A}{\partial t^2} - \frac{\partial A}{\partial t} \frac{\partial^2 A^*}{\partial t^2} = & -2i \left[\frac{q (t-\xi)^3 \left(1+q^2\right)}{\tau^6} + \frac{\Omega (t-\xi)^2}{\tau^4} \left[1+3q^2 \right] \right. \\ & \left. + \frac{3q\Omega^2 (t-\xi)}{\tau^2} + \frac{\Omega}{\tau^2} + \Omega^3 \right] \times |A|^2 . \end{aligned} \tag{D.58}$$

D.2.2 Derivatives Involving Autosolitons Pulses

If we assume we have a pulse given by

$$A = a\text{sech}\left(\frac{t-\xi}{\tau}\right)^{1+iq}\exp\left[ip - i\Omega(t-\xi)\right], \tag{D.59}$$

we find

$$|A|^2 = a^2\text{sech}^2\left(\frac{t-\xi}{\tau}\right) \tag{D.60}$$

and

$$\frac{\partial A}{\partial t} = -\left[\frac{(1+iq)}{\tau}\tanh\left(\frac{t-\xi}{\tau}\right) + i\Omega\right]\times A. \tag{D.61}$$

Obviously,

$$\frac{\partial A^*}{\partial t} = -\left[\frac{(1-iq)}{\tau}\tanh\left(\frac{t-\xi}{\tau}\right) - i\Omega\right]\times A^* \tag{D.62}$$

and

$$\left|\frac{\partial A}{\partial t}\right|^2 = \left[\frac{(1+q^2)}{\tau^2}\tanh^2\left(\frac{t-\xi}{\tau}\right) + \frac{2q\Omega}{\tau}\tanh\left(\frac{t-\xi}{\tau}\right) + \Omega^2\right]\times|A|^2. \tag{D.63}$$

Of course by using Eqs. (D.61) and (D.62), we obtain

$$A^*\frac{\partial A}{\partial t} = -\left[\frac{(1+iq)}{\tau}\tanh\left(\frac{t-\xi}{\tau}\right) + i\Omega\right]\times|A|^2 \tag{D.64}$$

and

$$A\frac{\partial A^*}{\partial t} = -\left[\frac{(1-iq)}{\tau}\tanh\left(\frac{t-\xi}{\tau}\right) - i\Omega\right]\times|A|^2, \tag{D.65}$$

which gives us

$$A^*\frac{\partial A}{\partial t} - A\frac{\partial A^*}{\partial t} = -2i\left[\frac{q}{\tau}\tanh\left(\frac{t-\xi}{\tau}\right) + \Omega\right]\times|A|^2. \tag{D.66}$$

By applying the chain rule to Eq. (D.61), we find

$$\begin{aligned}\frac{\partial^2 A}{\partial t^2} = \ & \left[-\frac{1+iq}{\tau^2}\left[1-\tanh^2\left(\frac{t-\xi}{\tau}\right)\right]\right. \\ & \left. + \left[\frac{1+iq}{\tau}\tanh\left(\frac{t-\xi}{\tau}\right) + i\Omega\right]^2\right]\times A,\end{aligned} \tag{D.67}$$

which may be expanded and written as

$$\frac{\partial^2 A}{\partial t^2} = \frac{1}{\tau^2}\left[\left(2-q^2+3iq\right)\tanh^2\left(\frac{t-\xi}{\tau}\right)+2i\Omega\tau\left(1+iq\right)\tanh\left(\frac{t-\xi}{\tau}\right)\right.$$
$$\left. - \left(\Omega^2\tau^2+1+iq\right)\right]\times A. \tag{D.68}$$

Finally, we find that

$$\frac{\partial A^*}{\partial t}\frac{\partial^2 A}{\partial t^2} = -\frac{1}{\tau^3}\left[\left(2-q^2+3iq\right)\left(1-iq\right)\tanh^3\left(\frac{t-\xi}{\tau}\right)\right.$$
$$+ \left[2i\Omega\tau\left(1+iq\right)\left(1-iq\right)-i\Omega\tau\left(2-q^2+3iq\right)\right]\tanh^2\left(\frac{t-\xi}{\tau}\right)$$
$$+ \left[(-i\Omega\tau)2i\Omega\tau\left(1+iq\right)-\left(1-iq\right)\left(\Omega^2\tau^2+1+iq\right)\right]\tanh\left(\frac{t-\xi}{\tau}\right)$$
$$\left. + \; i\Omega\tau\left(\Omega^2\tau^2+1+iq\right)\right]\times|A|^2. \tag{D.69}$$

This result may be "simplified" to

$$\frac{\partial A^*}{\partial t}\frac{\partial^2 A}{\partial t^2} = -\frac{1}{\tau^3}\left[\left(2+iq+2q^2+iq^3\right)\tanh^3\left(\frac{t-\xi}{\tau}\right)\right.$$
$$+ 3\Omega\tau q\left(1+iq\right)\tanh^2\left(\frac{t-\xi}{\tau}\right)$$
$$+ \left[\Omega^2\tau^2\left(1+3iq\right)-1-q^2\right]\tanh\left(\frac{t-\xi}{\tau}\right)$$
$$\left. + \; i\Omega\tau\left(\Omega^2\tau^2+1+iq\right)\right]\times|A|^2. \tag{D.70}$$

Since the complex conjugate of Eq. (D.70) gives us

$$\frac{\partial A}{\partial t}\frac{\partial^2 A^*}{\partial t^2} = -\frac{1}{\tau^3}\left[\left(2-iq+2q^2-iq^3\right)\tanh^3\left(\frac{t-\xi}{\tau}\right)\right.$$
$$+ 3\Omega\tau q\left(1-iq\right)\tanh^2\left(\frac{t-\xi}{\tau}\right)$$
$$+ \left[\Omega^2\tau^2\left(1-3iq\right)-1-q^2\right]\tanh\left(\frac{t-\xi}{\tau}\right)$$
$$\left. - \; i\Omega\tau\left(\Omega^2\tau^2+1-iq\right)\right]\times|A|^2, \tag{D.71}$$

we find

$$\frac{\partial A^*}{\partial t}\frac{\partial^2 A}{\partial t^2}-\frac{\partial A}{\partial t}\frac{\partial^2 A^*}{\partial t^2} = -\frac{2i}{\tau^3}\left[q\left(1+q^2\right)\tanh^3\left(\frac{t-\xi}{\tau}\right)+3\Omega\tau q^2\tanh^2\left(\frac{t-\xi}{\tau}\right)\right.$$
$$\left. + \; 3\Omega^2\tau^2 q\tanh\left(\frac{t-\xi}{\tau}\right)+\Omega\tau\left(1+\Omega^2\tau^2\right)\right]\times|A|^2. \tag{D.72}$$

D.3 Various Integrals

In order to apply the moment method to our specific pulse shapes, it is useful to list a few of the integrals that are needed.

D.3.1 Integrals for Gaussian Pulses

$$\int_{-\infty}^{\infty} |A|^2 \, dt = \sqrt{\pi} a^2 \tau \equiv E \tag{D.73}$$

$$\int_{-\infty}^{\infty} |A|^4 \, dt = \sqrt{\frac{\pi}{2}} a^4 \tau = \frac{E^2}{\sqrt{2\pi}\tau} \tag{D.74}$$

$$\int_{-\infty}^{\infty} (t-\xi)^n |A|^2 \, dt = 0 \quad \text{if n is odd} \tag{D.75}$$

$$\int_{-\infty}^{\infty} (t-\xi)^2 |A|^2 \, dt = \frac{\tau^2}{2} E = \frac{C_1 \tau^2}{2} E \tag{D.76}$$

$$\int_{-\infty}^{\infty} (t-\xi)^4 |A|^2 \, dt = \frac{3\tau^4}{4} E \tag{D.77}$$

$$\int_{-\infty}^{\infty} t |A|^2 \, dt = \xi E \tag{D.78}$$

$$\int_{-\infty}^{\infty} \left| \frac{\partial A}{\partial t} \right|^2 dt = \left[\frac{1}{2\tau^2} \left(1+q^2\right) + \Omega^2 \right] E \tag{D.79}$$

$$\int_{-\infty}^{\infty} t \left| \frac{\partial A}{\partial t} \right|^2 dt = \left[\frac{1}{2\tau^2} \left(1+q^2\right) \xi + q\Omega + \Omega^2 \xi \right] E \tag{D.80}$$

$$\int_{-\infty}^{\infty} (t-\xi) \left| \frac{\partial A}{\partial t} \right|^2 dt = q\Omega E \tag{D.81}$$

$$\int_{-\infty}^{\infty}(t-\xi)^2\left|\frac{\partial A}{\partial t}\right|^2 dt=\left[\frac{3}{4}\left(1+q^2\right)+\frac{\Omega^2\tau^2}{2}\right]E \tag{D.82}$$

$$\int_{-\infty}^{\infty}\left[A^*\frac{\partial A}{\partial t}-A\frac{\partial A^*}{\partial t}\right]dt=-2i\Omega E \tag{D.83}$$

$$\int_{-\infty}^{\infty}(t-\xi)\left[A^*\frac{\partial A}{\partial t}-A\frac{\partial A^*}{\partial t}\right]dt=-iqE \tag{D.84}$$

$$\int_{-\infty}^{\infty}\left[\frac{\partial A^*}{\partial t}\frac{\partial^2 A}{\partial t^2}-\frac{\partial A}{\partial t}\frac{\partial^2 A^*}{\partial t^2}\right]dt=-2i\Omega\left[\frac{\left(1+3q^2\right)}{2\tau^2}+\frac{1}{\tau^2}+\Omega^2\right]E \tag{D.85}$$

$$\int_{-\infty}^{\infty}(t-\xi)\left[\frac{\partial A^*}{\partial t}\frac{\partial^2 A}{\partial t^2}-\frac{\partial A}{\partial t}\frac{\partial^2 A^*}{\partial t^2}\right]dt=-\frac{3iq}{2}\left[\frac{\left(1+q^2\right)}{\tau^2}+2\Omega^2\right]E \tag{D.86}$$

$$\int_{-\infty}^{\infty}\sin\left[\kappa(t-\phi)\right]|A|^2\,dt=\exp\left[-\frac{\kappa^2\tau^2}{4}\right]\sin\left[\kappa(\xi-\phi)\right]E \tag{D.87}$$

$$\int_{-\infty}^{\infty}(t-\xi)\sin\left[\kappa(t-\phi)\right]|A|^2\,dt=\frac{\tau^2\kappa}{2}\exp\left[-\frac{\kappa^2\tau^2}{4}\right]\cos\left[\kappa(\xi-\phi)\right]E \tag{D.88}$$

$$\int_{-\infty}^{\infty}\cos\left[\kappa(t-\phi)\right]|A|^2\,dt=\exp\left[-\frac{\kappa^2\tau^2}{4}\right]\cos\left[\kappa(\xi-\phi)\right]E \tag{D.89}$$

$$\begin{aligned}\int_{-\infty}^{\infty}t\cos\left[\kappa(t-\phi)\right]|A|^2\,dt\;=\;&\xi\exp\left[-\frac{\kappa^2\tau^2}{4}\right]\cos\left[\kappa(\xi-\phi)\right]E\\&-\;\frac{\kappa\tau^2}{2}\exp\left[-\frac{\kappa^2\tau^2}{4}\right]\sin\left[\kappa(\xi-\phi)\right]E\end{aligned} \tag{D.90}$$

$$\int_{-\infty}^{\infty}(t-\xi)\cos\left[\kappa(t-\phi)\right]|A|^2\,dt=-\frac{\kappa\tau^2}{2}\exp\left[-\frac{\kappa^2\tau^2}{4}\right]\sin\left[\kappa(\xi-\phi)\right]E \tag{D.91}$$

$$\int_{-\infty}^{\infty}(t-\xi)^2\cos\left[\kappa(t-\phi)\right]|A|^2\,dt = \left(\frac{\tau^2}{2}-\frac{\kappa^2\tau^4}{4}\right) \times \exp\left[-\frac{\kappa^2\tau^2}{4}\right]\cos\left[\kappa(\xi-\phi)\right]E \quad \text{(D.92)}$$

$$\int_{-\infty}^{\infty}\cos\left[\kappa(t-\phi)\right]\left[A^*\frac{\partial A}{\partial t}-A\frac{\partial A^*}{\partial t}\right]dt = i\left[\kappa q\sin\left[\kappa(\xi-\phi)\right]-2\Omega\cos\left[\kappa(\xi-\phi)\right]\right] \times \exp\left[-\frac{\kappa^2\tau^2}{4}\right]E \quad \text{(D.93)}$$

$$\int_{-\infty}^{\infty}(t-\xi)\cos\left[\kappa(t-\phi)\right]\left[A^*\frac{\partial A}{\partial t}-A\frac{\partial A^*}{\partial t}\right]dt = i\kappa\tau^2\Omega\exp\left[-\frac{\kappa^2\tau^2}{4}\right]\sin\left[\kappa(\xi-\phi)\right]E$$
$$-iq\left(1-\frac{\kappa^2\tau^2}{2}\right)\exp\left[-\frac{\kappa^2\tau^2}{4}\right]\cos\left[\kappa(\xi-\phi)\right]E \quad \text{(D.94)}$$

D.3.2 Integrals for Autosolitons Pulses

$$\int_{-\infty}^{\infty}|A|^2\,dt = 2a^2\tau \equiv E \quad \text{(D.95)}$$

$$\int_{-\infty}^{\infty}|A|^4\,dt = \frac{E^2}{3\tau} \quad \text{(D.96)}$$

$$\int_{-\infty}^{\infty}(t-\xi)^n|A|^2\,dt = 0 \quad \text{if n is odd} \quad \text{(D.97)}$$

$$\int_{-\infty}^{\infty}(t-\xi)^2|A|^2\,dt = \frac{\pi^2\tau^2}{12}E = \frac{C_1\tau^2}{2}E \quad \text{(D.98)}$$

$$\int_{-\infty}^{\infty}(t-\xi)^4|A|^2\,dt = \frac{7\pi^4\tau^4}{240}E \quad \text{(D.99)}$$

$$\int_{-\infty}^{\infty} \tanh^n\left(\frac{t-\xi}{\tau}\right)|A|^2\,dt = \begin{cases} \frac{E}{n+1} & \text{if n is even} \\ 0 & \text{if n is odd} \end{cases} \tag{D.100}$$

$$\int_{-\infty}^{\infty} (t-\xi)\tanh\left(\frac{t-\xi}{\tau}\right)|A|^2\,dt = \frac{\tau}{2}E \tag{D.101}$$

$$\int_{-\infty}^{\infty} (t-\xi)^2\tanh^2\left(\frac{t-\xi}{\tau}\right)|A|^2\,dt = \left(\frac{12+\pi^2}{36}\right)\tau^2 E \tag{D.102}$$

$$\int_{-\infty}^{\infty} (t-\xi)\tanh^3\left(\frac{t-\xi}{\tau}\right)|A|^2\,dt = \frac{\tau}{3}E \tag{D.103}$$

$$\int_{-\infty}^{\infty} (t-\xi)^3\tanh\left(\frac{t-\xi}{\tau}\right)|A|^2\,dt = \frac{\pi^2\tau^3}{8}E \tag{D.104}$$

$$\int_{-\infty}^{\infty} t\,|A|^2\,dt = \xi E \tag{D.105}$$

$$\int_{-\infty}^{\infty} t\tanh\left(\frac{t-\xi}{\tau}\right)|A|^2\,dt = \frac{\tau}{2}E \tag{D.106}$$

$$\int_{-\infty}^{\infty} t\tanh^2\left(\frac{t-\xi}{\tau}\right)|A|^2\,dt = \frac{\xi}{3}E \tag{D.107}$$

$$\int_{-\infty}^{\infty} \left|\frac{\partial A}{\partial t}\right|^2 dt = \left[\frac{1}{3\tau^2}\left(1+q^2\right)+\Omega^2\right]E \tag{D.108}$$

$$\int_{-\infty}^{\infty} t\left|\frac{\partial A}{\partial t}\right|^2 dt = \left[\frac{1}{3\tau^2}\left(1+q^2\right)\xi + q\Omega + \Omega^2\xi\right]E \tag{D.109}$$

$$\int_{-\infty}^{\infty} (t-\xi)\left|\frac{\partial A}{\partial t}\right|^2 dt = q\Omega E \tag{D.110}$$

$$\int_{-\infty}^{\infty} (t-\xi)^2\left|\frac{\partial A}{\partial t}\right|^2 dt = \left[\left(1+q^2\right)\left(\frac{12+\pi^2}{36}\right)+\frac{\Omega^2\pi^2\tau^2}{12}\right]E \tag{D.111}$$

$$\int_{-\infty}^{\infty}\left[A^*\frac{\partial A}{\partial t}-A\frac{\partial A^*}{\partial t}\right]dt=-2i\Omega E \tag{D.112}$$

$$\int_{-\infty}^{\infty}(t-\xi)\left[A^*\frac{\partial A}{\partial t}-A\frac{\partial A^*}{\partial t}\right]dt=-iqE \tag{D.113}$$

$$\int_{-\infty}^{\infty}\left[\frac{\partial A^*}{\partial t}\frac{\partial^2 A}{\partial t^2}-\frac{\partial A}{\partial t}\frac{\partial^2 A^*}{\partial t^2}\right]dt=-\frac{2i\Omega}{\tau^2}\left(1+\Omega^2\tau^2+q^2\right)E \tag{D.114}$$

$$\begin{aligned}\int_{-\infty}^{\infty}(t-\xi)\left[\frac{\partial A^*}{\partial t}\frac{\partial^2 A}{\partial t^2}-\frac{\partial A}{\partial t}\frac{\partial^2 A^*}{\partial t^2}\right]dt\;&=\;-\frac{2iq}{3\tau^2}\left(1+q^2\right)E\\&-\;3i\Omega^2qE\end{aligned} \tag{D.115}$$

$$\int_{-\infty}^{\infty}\sin\left[\kappa(t-\phi)\right]|A|^2\,dt=\frac{\pi\kappa\tau}{2}\operatorname{csch}\left(\frac{\pi\kappa\tau}{2}\right)\sin\left[\kappa(\xi-\phi)\right]E \tag{D.116}$$

$$\begin{aligned}\int_{-\infty}^{\infty}(t-\xi)\sin\left[\kappa(t-\phi)\right]|A|^2\,dt\;&=\;\frac{\pi\tau}{4}\operatorname{csch}^2\left(\frac{\pi\kappa\tau}{2}\right)\left[\pi\kappa\tau\cosh\left(\frac{\pi\kappa\tau}{2}\right)\right.\\&-\;\left.2\sinh\left(\frac{\pi\kappa\tau}{2}\right)\right]\cos\left[\kappa(\xi-\phi)\right]E\end{aligned} \tag{D.117}$$

$$\int_{-\infty}^{\infty}\cos\left[\kappa(t-\phi)\right]|A|^2\,dt=\frac{\pi\kappa\tau}{2}\operatorname{csch}\left(\frac{\pi\kappa\tau}{2}\right)\cos\left[\kappa(\xi-\phi)\right]E \tag{D.118}$$

$$\begin{aligned}\int_{-\infty}^{\infty}(t-\xi)\cos\left[\kappa(t-\phi)\right]|A|^2\,dt\;&=\;-\frac{\pi\tau}{4}\operatorname{csch}\left(\frac{\pi\kappa\tau}{2}\right)\left[\pi\kappa\tau\coth\left(\frac{\pi\kappa\tau}{2}\right)-2\right]\\&\times\;\sin\left[(\kappa(\xi-\phi)\right]E\end{aligned} \tag{D.119}$$

$$\begin{aligned}\int_{-\infty}^{\infty}t\cos\left[\kappa(t-\phi)\right]|A|^2\,dt&=\frac{\pi\kappa\tau}{2}\xi\operatorname{csch}\left(\frac{\pi\kappa\tau}{2}\right)\cos\left[\kappa(\xi-\phi)\right]E\\&-\frac{\pi\tau}{4}\operatorname{csch}\left(\frac{\pi\kappa\tau}{2}\right)\left[\pi\kappa\tau\coth\left(\frac{\pi\kappa\tau}{2}\right)-2\right]\sin\left[\kappa(\xi-\phi)\right]E\end{aligned} \tag{D.120}$$

$$\begin{aligned}\int_{-\infty}^{\infty}(t-\xi)^2\cos\left[\kappa(t-\phi)\right]|A|^2\,dt\;&=\;-\frac{\pi^2\tau^2}{16}\operatorname{csch}^3\left(\frac{\pi\kappa\tau}{2}\right)\left[3\pi\kappa\tau+\pi\kappa\tau\cosh\left(\pi\kappa\tau\right)\right.\\&-\;\left.4\sinh\left(\pi\kappa\tau\right)\right]\cos(\kappa\left[\xi-\phi\right])E\end{aligned} \tag{D.121}$$

$$\int_{-\infty}^{\infty}\cos\left[\kappa\left(t-\phi\right)\right]\tanh\left(\frac{t-\xi}{\tau}\right)|A|^2dt = -\frac{\pi\kappa^2\tau^2}{4}\mathrm{csch}\left(\frac{\pi\kappa\tau}{2}\right) \times \sin\left[\left(\kappa(\xi-\phi)\right]E \tag{D.122}$$

$$\int_{-\infty}^{\infty}\cos\left[\kappa\left(t-\phi\right)\right]\left[A^*\frac{\partial A}{\partial t}-A\frac{\partial A^*}{\partial t}\right]dt = -i\pi\kappa\tau\Omega\mathrm{csch}\left(\frac{\pi\kappa\tau}{2}\right)\cos(\kappa\left[\xi-\phi\right])E + \frac{i\pi\kappa^2\tau}{2}q\mathrm{csch}\left(\frac{\pi\kappa\tau}{2}\right)\sin\left[\left(\kappa(\xi-\phi)\right]E \tag{D.123}$$

$$\int_{-\infty}^{\infty}(t-\xi)\cos\left[\kappa\left(t-\phi\right)\right]\tanh\left(\frac{t-\xi}{\tau}\right)|A|^2dt = -\frac{\pi\kappa\tau^2}{8}\mathrm{csch}\left(\frac{\pi\kappa\tau}{2}\right) \times\left[\pi\kappa\tau\coth\left(\frac{\pi\kappa\tau}{2}\right)-4\right]\cos(\kappa\left[\xi-\phi\right])E \tag{D.124}$$

$$\int_{-\infty}^{\infty}(t-\xi)\cos\left[\kappa\left(t-\phi\right)\right]\left[A^*\frac{\partial A}{\partial t}-A\frac{\partial A^*}{\partial t}\right]dt = \frac{i\pi\kappa\tau}{4}Q\mathrm{csch}\left(\frac{\pi\kappa\tau}{2}\right)\left[\pi\kappa\tau\coth\left(\frac{\pi\kappa\tau}{2}\right)-4\right]\cos(\kappa\left[\xi-\phi\right])E + \frac{i\pi\tau}{2}\Omega\mathrm{csch}\left(\frac{\pi\kappa\tau}{2}\right)\left[\pi\kappa\tau\coth\left(\frac{\pi\kappa\tau}{2}\right)-2\right]\sin\left[\left(\kappa(\xi-\phi)\right]E \tag{D.125}$$

$$\int_{-\infty}^{\infty}\frac{\mathrm{sech}^2(x)}{1+b\mathrm{sech}^2(x)}dt = \frac{2}{\sqrt{b(b+1)}}\coth^{-1}\left(\sqrt{1+\frac{1}{b}}\right) \tag{D.126}$$

$$\int_{-\infty}^{\infty}\frac{x\,\mathrm{sech}^2(x)}{1+b\mathrm{sech}^2(x)}dt = 0 \tag{D.127}$$

$$\int_{-\infty}^{\infty}\frac{\tanh(x)\mathrm{sech}^2(x)}{1+b\mathrm{sech}^2(x)}dt = 0 \tag{D.128}$$

Using Contour integration we find

$$\int_{-\infty}^{\infty}\frac{x\tanh(x)}{b+\cosh^2(x)}dx = \int_0^{\infty}\frac{\ln(z)(z-1)}{z^3+(4b+3)z^2+(4b+3)z+1}dz = \frac{1}{8b}\left\{\ln^2\left[1+2b\left(1-\sqrt{1+\frac{1}{b}}\right)\right] + \ln^2\left[1+2b\left(1+\sqrt{1+\frac{1}{b}}\right)\right]\right\}, \tag{D.129}$$

where we used the change of variables $z = e^{2x}$. Contour integration also allows us to obtain

$$\begin{aligned}\int_{-\infty}^{\infty} \frac{x^2}{b+\cosh^2(x)} dx &= \frac{1}{2}\int_0^{\infty} \frac{\ln^2(z)}{z^2+2(2b+1)z+1} dz \\ &= \frac{1}{12\sqrt{\gamma^2-1}}\left[\ln^3\left(-\gamma-\sqrt{\gamma^2-1}\right) - \ln^3\left(-\gamma+\sqrt{\gamma^2-1}\right)\right. \\ &+ \left. 16\pi^2 \coth^{-1}\left(\sqrt{1+\frac{1}{b}}\right)\right], \end{aligned} \tag{D.130}$$

where we used the change of variables $z = e^{2x}$ and simplified the appearance of the result by introducing $\gamma = 2b+1$.

E Solving Systems of Nonlinear Algebraic Equations

E.1 The Newton–Raphson Technique

In the course of our work it became necessary to solve systems of coupled equations in order to get the steady-state values predicted by the application of the moment method to the mode-locked lasers in chapters 7, 8, and 9. Moreover, these equations were nonlinear and so, unfortunately, they could not be solved using the well-known approach of Gaussian elimination. As a consequence, simple analytic solutions could not be obtained and numerical techniques were required. The Newton-Raphson technique is the most common approach one can use to solve such problems since it is easy to implement and converges quickly.

This approach is easily derived from the multivariate Taylor expansion, which is given for a function of many variables $F(x_0, x_1, x_2, \cdots, x_n)$

$$F(x_0+\delta_0, x_1+\delta_1, \cdots, x_n+\delta_n) = \frac{\partial F(x_0, x_1, \cdots, x_n)}{\partial x_0}\delta_0 + \frac{\partial F(x_0, x_1, \cdots, x_n)}{\partial x_1}\delta_1 + \cdots + \frac{\partial F(x_0, x_1, \cdots, x_n)}{\partial x_n}\delta_n + H.O.T. \tag{E.1}$$

It is instructive to apply the multivariate Taylor expansion, seen in Eq. (E.1), to a system of (presumably) coupled equations allowing us to write

$$\begin{bmatrix} 0 \\ 0 \\ \vdots \\ 0 \end{bmatrix} = \begin{bmatrix} f_0 \\ f_1 \\ \vdots \\ f_n \end{bmatrix} + \begin{bmatrix} \frac{\partial f_0}{\partial x_0} & \frac{\partial f_0}{\partial x_1} & \cdots & \frac{\partial f_0}{\partial x_n} \\ \frac{\partial f_1}{\partial x_0} & \frac{\partial f_1}{\partial x_1} & \cdots & \frac{\partial f_1}{\partial x_n} \\ \vdots & \vdots & \ddots & \vdots \\ \frac{\partial f_n}{\partial x_0} & \frac{\partial f_n}{\partial x_1} & \cdots & \frac{\partial f_n}{\partial x_n} \end{bmatrix} \begin{bmatrix} \delta_0 \\ \delta_1 \\ \vdots \\ \delta_n \end{bmatrix} \tag{E.2}$$

where f_n represents the n^{th} coupled equation. Solutions to the system are obtained by iteratively applying Eq. (E.2) after an initial guess is made for each parameter. Generally a system of coupled equations can have more than one unique solution. Fortunately, all possible solutions may be obtained through varying the initial conditions, but this approach can diverge and will get stuck in local minima so one must apply it wisely.

F Time Frequency Analysis

F.1 The Short-Time Fourier Transform

Although individually visualizing optical phenomena in both the time-domain and the frequency-domain is probably still the most widely used approach, it does not provide a comprehensive picture. Since the Fourier transform decomposes a function into an infinite set of sines and cosines, it provides no temporal resolution when applied to a signal of duration T. To be more exact, we know that the frequencies obtained by the Fourier transform had to exist somewhere within the signal; so they are, in fact, restricted to the time interval T.

The short-time Fourier transform (STFT) uses this restriction to its advantage to create a spectrogram or a time-frequency map of a signal. Since the temporal window over which the Fourier transform is applied localizes the frequencies contained therein to its width, we can temporally split our signal into multiple sub-windows as depicted by Eq. (F.1)

$$STFT(\omega, T) = \int_{-\infty}^{\infty} h(t,T)A(t)e^{i\omega t}dt, \tag{F.1}$$

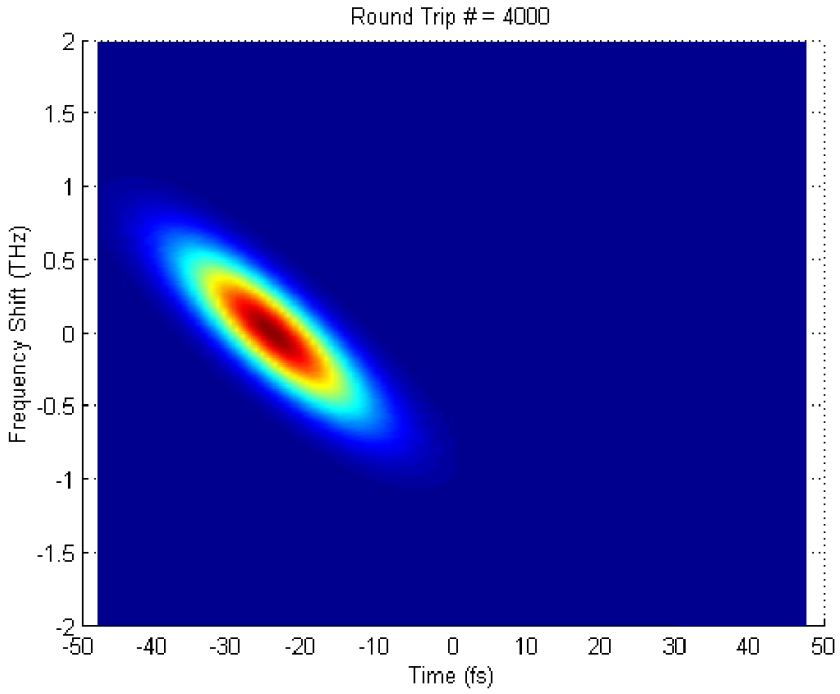

Figure F.1: A sample spectrogram showing the secondary solution for a FM mode-locked laser from chapters 5 and 9.

where $h(t,T)$ represents the windowing function. In this work a Gaussian windowing function was used which had the form $h(t,T) = \exp\left[-(t-T)^2/(2T_0^2)\right]$ where T_0 represents the temporal width of the window. Although these windows must each have a finite width, they act to temporally gate the original signal. By individually applying the Fourier transform to each of these gated sub-signals, we obtain a spectrum for each window. Since each resulting spectra corresponds to a different time, we obtain a time-frequency picture of our signal. Figure F.1 is a sample spectrogram that shows a heavily chirped (and ultimately unstable) mode-locked pulse inside a FM mode-locked laser. Note that the chirp manifests itself by tilting the ellipse in this figure.

Another example which really illustrates the strength of the spectrogram comes from the supercontinuum generation simulation from appendix C. This figure shows the spectrogram of Fig. C.2; however this time we display the final "pulse" intensity in the time and frequency domains along side the spectrogram.

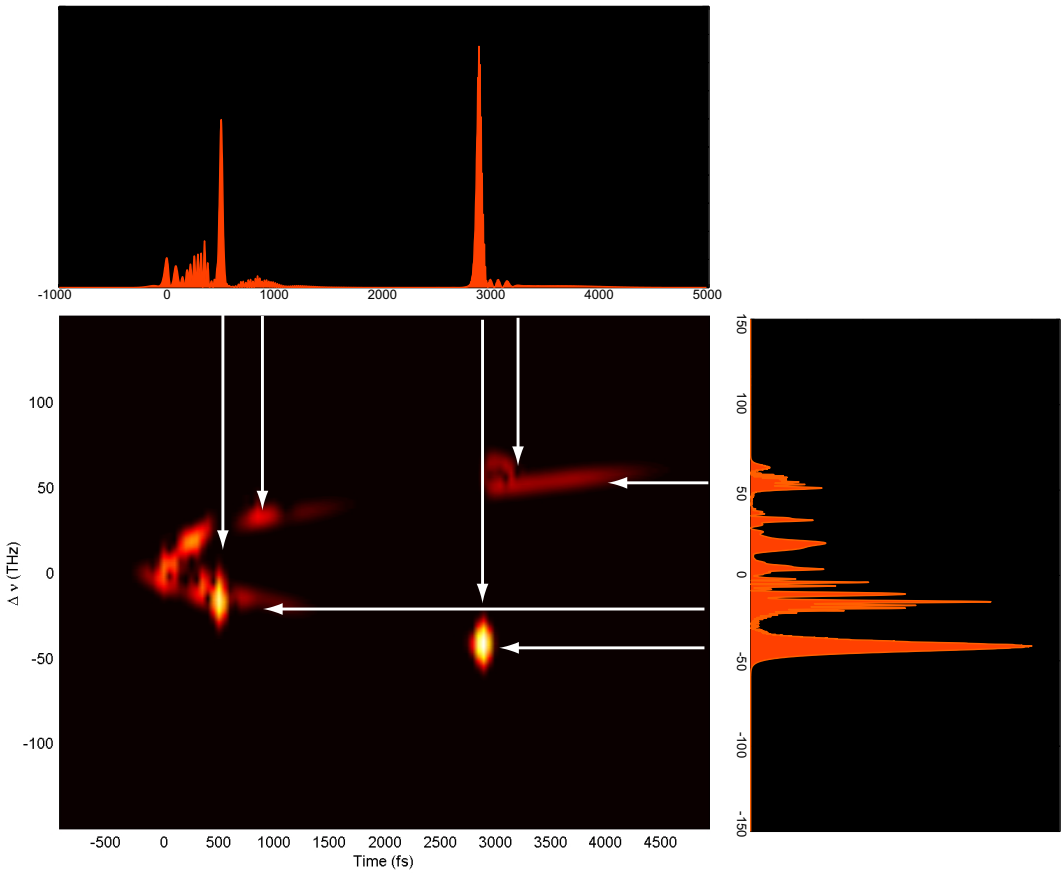

Figure F.2: Propagation of a fifth-order soliton in a photonic crystal fiber whose parameters are given in Ref. [5]. This figure shows the results using a spectrogram. See appendix C for a discussion of the numerical technique used to solve this problem.

The arrows shown in Fig. F.2 show where the various temporal/spectral components manifest themselves in the spectrogram. This figure also illuminates the point that neither a time-domain nor a frequency-domain plot of the field intensity provides a full picture as to what is occurring. Moreover, even with both time-domain and frequency-domain plots one is not able to determine what parts of the temporal pulse correspond to what part of its spectrum. Because the STFT takes the Fourier transform of the full field, both amplitude and phase, within a restricted temporal location, it is able to produce a spectrogram that provides more information than either of the two individually. We should point out that if one compared four plots consisting of the temporal inten-

sity and phase to the spectral intensity and phase it would also be possible to extract this information, however spectrograms provide a convenient and intuitive visualization tool.

F.2 Wavelets

By construction, wavelets create a sort of time-frequency map although its interpretation is not as physical as that of the spectrogram. Since the wavelet transform works by decomposing a signal into higher and higher frequency coefficients, the strengths of these different coefficients provide information as to the frequency components of a signal. If one considers the computer environment where a signal is represented in an array it can contain no higher frequency content than that which corresponds to $1/2$ the number of cells. The wavelet transform decomposes a signal into its DC component and then higher and higher frequency components, ultimately ending at the Nyquest limit.